

INVESTIGATION ON LOCAL STRUCTURES OF OXIDE THIN FILMS BY EXAFS STUDY

By

SK MAIDUL HAQUE

PHYS01201304003

Bhabha Atomic Research Centre, Visakhapatnam

*A thesis submitted to the
Board of Studies in Physical Sciences
in partial fulfillment of requirements
for the Degree of*

DOCTOR OF PHILOSOPHY

of

HOMI BHABHA NATIONAL INSTITUTE

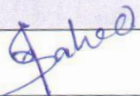
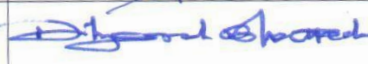
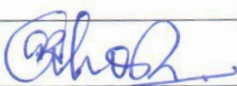
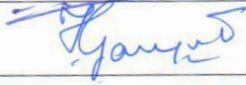

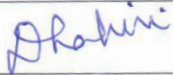


June, 2018

HOMI BHABHA NATIONAL INSTITUTE

Recommendations of the Viva Voce Committee

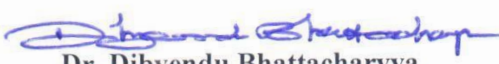
As members of the Viva Voce Committee, we certify that we have read the dissertation prepared by **Sk Maidul Haque** entitled “Investigation on local structures of oxide thin films by EXAFS study” and recommend that it may be accepted as fulfilling the thesis requirement for the award of Degree of Doctor of Philosophy.

Sr.No.	Name	Designation	Signature	Date
1.	Dr. N.K. Sahoo	Chairman		23/5/2018
2.	Dr. D. Bhattacharyya	Guide & Convener		28/5/18
3.	Prof. A. Ghosh	Examiner		23.5.2018
4.	Dr. T. Ganguli	Member		23/5/2018
5.	Dr. A. Das	Member		23.5.18
6.	Dr. D. Lahiri	Technology Advisor		23.5.18

Final approval and acceptance of this thesis is contingent upon the candidate's submission of the final copies of the thesis to HBNI.

I hereby certify that I have read this thesis prepared under my direction and recommend that it may be accepted as fulfilling the thesis requirement.

Date: 28/5/18
Place: Mumbai


Dr. Dibyendu Bhattacharyya
(Guide)

STATEMENT BY AUTHOR

This dissertation has been submitted in partial fulfillment of requirements for an advanced degree at Homi Bhabha National Institute (HBNI) and is deposited in the library to be made available to borrowers under rules of the HBNI.

Brief quotations from this dissertation are allowable without special permission, provided that accurate acknowledgement of source is made. Requests for permission for extended quotation from or reproduction of this manuscript in whole or in part may be granted by the Competent Authority of HBNI when in his or her judgment the proposed use of the material is in the interests of scholarship. In all other instances, however, permission must be obtained from the author.

Sk Maidul Haque

DECLARATION

I, hereby declare that the investigation presented in the thesis has been carried out by me. The work is original and has not been submitted earlier as a whole or in part for a degree /diploma at this or any other Institution / University.

Sk Maidul Haque

List of Publications arising from the Thesis

Journal Publications:

1. Sk. Maidul Haque, Pankaj R. Sagdeo, Shanmugam Balaji, Kalavathi Sridhar, Sanjiv Kumar, Debarati Bhattacharyya, Dibyendu Bhattacharyya and Naba K. Sahoo, "Effect of substrate bias and oxygen partial pressure on properties of RF magnetron sputtered HfO₂ thin films," **J. Vac. Sci. Technol. B** **32(3)** **2014**.
2. S. Maidul Haque, Pankaj R. Sagdeo, Archana Sagdeo, S. N. Jha, D. Bhattacharyya, And N. K. Sahoo, "Effect of oxygen partial pressure on properties of asymmetric bipolar pulse DC magnetron sputtered TiO₂ thin films", **Applied Optics** **54 (2015)** **3817**.
3. S. Maidul Haque, Pankaj R. Sagdeo, D. D. Shinde, J.S. Misal, S.N. Jha, D. Bhattacharyya and N.K. Sahoo, "Extended X-ray Absorption Fine Structure (EXAFS) measurements on Asymmetric Bipolar Pulse direct current magnetron sputtered Ta₂O₅ thin films," **Applied Optics** **54 (2015)** **6744**.
4. S. Maidul Haque, C. Nayak, D. Bhattacharyya, S.N. Jha and N.K. Sahoo, "EXAFS measurements on RF magnetron sputtered HfO₂ thin films deposited with different oxygen partial pressures," **Applied Optics** **55, 2175(2016)**.
5. S. Maidul Haque, S. Tripathi, S.N. Jha, D. Bhattacharyya and N. K. Sahoo, "EXAFS studies on Gd doped ZrO₂ thin films deposited by RF magnetron sputtering," **Applied Optics** **55, 7355(2016)**.
6. S. Maidul Haque, Rajnarayan De, S. Tripathi, C. Mukherjee, A. K. Yadav, Dibyendu Bhattacharyya, S.N. Jha And N.K. Sahoo, "Effect of oxygen partial pressure in deposition ambient on the properties of RF magnetron sputter deposited Gd₂O₃ thin films," **Applied Optics** **56, 6114-6125(2017)**.

Conference Publications:

- 1 S. Maidul Haque, D. D. Shinde, J. S. Misal, D. Bhattacharyya, N. K. Sahoo, "Study of Optical Properties of Asymmetric Bipolar Pulse DC Magnetron Sputtered Ta₂O₅ Thin Film as a function of Oxygen Content in Deposition Ambient" , **AIP Conf. Proc.** **1591 (2014)** **858**.
- 2 S. Maidul Haque, D. D. Shinde, J. S. Misal, S.N. Jha, D. Bhattacharyya and N. K. Sahoo, "Optical And Local Structural Study Of Gd Doped ZrO₂ Thin Films Deposited By RF Magnetron Sputtering Technique," **AIP Conf. Proc.** **1665 (2015)** **080056**.

List of other journal publications:

1. S. Maidul Haque, A. Biswas, Debarati Bhattacharya, R. B. Tokas, D. Bhattacharyya, N. K. Sahoo, "Surface roughness and interface width scaling of magnetron sputter deposited Ni/Ti multilayers", **J. Appl. Phys.** **114, 103508 (2013)**.
2. S. Maidul Haque, K. Divakar Rao, J.S. Misal, R.B. Tokas, D.D. Shinde, J.V. Ramana, Sanjay Rai, N.K. Sahoo, "Study of hafnium oxide thin films deposited by RF magnetronsputtering under glancing angle deposition at varying target to substrate distance," **Applied Surface Science** **353, 459 (2015)**.
3. A. Biswas, S. Maidul Haque, S. Tripathi, Rajnarayan De, S. Rai, D. Bhattacharyya and N. K. Sahoo, "Study of interface correlation in W/C multilayer structure by specular and nonspecular grazing incidence X-ray reflectivity measurements", **J. Appl. Phys.** **118, 165312 (2015)**.

4. Ashok Kumar Yadav, Sk Maidul Haque, Dinesh Shukla, Ram Janay Choudhary, S. N. Jha and D. Bhattacharyya, "X-ray absorption spectroscopy of Mn doped ZnO thin films prepared by RF sputtering technique," **AIP Advances** **5**, 117138 (2015).
5. S. Tripathi, S. Maidul Haque, K. Divakar Rao, Rajnarayan De, T. Shripathi, U. Deshpande, V. Ganesan, N.K. Sahoo, "Investigation of optical and microstructural properties of RF magnetron sputtered PTFE films for hydrophobic applications," **Applied Surface Science** **385**, 289(2016).
6. Rajnarayan De, S. Maidul Haque, S. Tripathi, K. Divakar Rao, C. Prathap, Mohit Kumar, T. Som, N.K. Sahoo, Surface characterization of magnesium fluoride thin films prepared by a fluorine trapping based non-reactive sputtering technique, **Vacuum** **134**, 110-119 (2016).
7. Ashok Kumar Yadav, Sk Maidul Haque, Shilpa Tripathi, Dinesh Shukla, Md. A. Ahmed, D. M. Phase, S. Bandyopadhyay, S. N. Jha and D. Bhattacharyya, "Investigation of Fe doped ZnO thin films by X-ray absorption spectroscopy," **RSC Adv.** **6**, 74982–74990(2016).
8. S. Jena, R.B. Tokas, P. Sarkar, J.S. Misal, S. Maidul Haque, K.D. Rao, S. Thakur, N.K. Sahoo, Omnidirectional photonic band gap in magnetron sputtered TiO₂/SiO₂ one dimensional photonic crystal, **Thin Solid Films** **599**, 138 (2016).
9. S. Maidul Haque , K. Divakar Rao, S. Tripathi, Rajnarayan De, D.D. Shinde, J.S. Misal, C. Prathap, Mohit Kumar, T. Som, U. Deshpande, N.K. Sahoo, "Glancing angle deposition of SiO₂ thin films using a novel collimated magnetron sputtering technique," **Surface & Coatings Technology** **319** 61–69(2017).

List of other conference Publications:

1. Sekh Maidul, D. D. Shinde, J. S. Misal, Nisha Prasad, P. R. Sagdeo and N. K. Sahoo, "Simulation of thickness and optical constants from transmission spectrum of thin film by envelope method: Practical constraints and their solution", **AIP Conf. Proc.** **1451**(2012)**160**.
2. P.R. Sagdeo, Sekh Maidul, D.D. Shinde, J.S. Misal, S. Thakur, N.K. Sahoo, A. Sagdeo, S. Rai, C. Mukherjee, K. Rajiv, V.G. Sathe and M. Gupta, "Crystallographic phase control of TiO₂ in thin films deposited by asymmetric bipolar pulsed DC sputtering", **AIP Conf. Proc.** **1451** (2012) **121**.
3. S. Maidul Haque, P. R. Sagdeo, D. Bhattacharyya, D. D. Shinde, J. S. Misal, Nisha Prasad, N. K. Sahoo, "Comparison of Spectral Performance of HfO₂/SiO₂ and TiO₂/SiO₂ Based High Reflecting Mirrors", **AIP Conf. Proc.** **1512** (2013) **480**.
4. S. Maidul Haque, A. Biswas, J. S. Misal, D.D. Shinde, D. Bhattacharyya, S. Singh, S. Basu, D. Bhattacharyya, S.L. Chaplot, N.K. Sahoo, "Design, development and characterization of RF magnetron sputter deposited Ni/Ti multilayer super-mirrors for thermal neutron wavelengths", **International Symposium on Neutron Scattering, Mumbai, Jan. 14-17, 2013**.
5. S. Maidul Haque, K. Divakar Rao, N. K. Sahoo, "Modelling of lateral inhomogeneity of dielectric thin film by simulated annealing optimization algorithm", **National Symposium of Optical Society of India, Pondicherry, 2013**.
6. D. Bhattacharyya, A. Biswas, A.K. Poswal, Sk. Maidul Haque, K. D. Lagoo, R.D. Veerapur, M. Padmanabhan, R.K. Puri and N.K. Sahoo, "Development of a large area magnetron coating system for fabrication of thin film multilayer X-ray/Neutron Mirrors and Super Mirrors", **Synergy in Physics and Industry (SPI-2013), Mumbai, Jan. 21-22, 2013**.
7. A. Biswas, Sk. Maidul Haque, J. Misal, K. D. Lagoo, R. D. Veerapur, M. Padmanabhan, R. K. Puri, R. Sampathkumar, Ajaykumar, Debarati Bhattacharyya, D. Bhattacharyya and N. K. Sahoo, "Installation and commissioning of a large area coating system for neutron and X-ray optical devices", **AIP Conf. Proc.** **1591** (2014) **985**.

8. S. Tripathi, S. Maidul Haque, J. S. Misal, D.D. Shinde, K. Divakar Rao and N. K. Sahoo, "Refractive Index Tailoring Of Morphology Engineered SiO₂ Thin Films By Collimated Glancing Angle RF Magnetron Sputtering," **AIP Conf. Proc. 1665 080046 (2015).**
9. S Jena, R B Tokas, P Sarkar, S. Maidul Haque, J S Misal, K D Rao, S Thakur and N K Sahoo, "Achieving Omnidirectional Photonic Band Gap in Sputter Deposited TiO₂/SiO₂ One Dimensional Photonic Crystal," **AIP Conf. Proc. 1665 060018 (2015).**
10. R. B. Tokas, Shuvendu Jena, S. Maidul Haque, K. Divakar Rao, S. Thakur and N. K. Sahoo, "Spectroscopic ellipsometry investigations of optical anisotropy in obliquely deposited hafnia thin films," **AIP Conf. Proc. 1731, 060007(2016).**
11. S. Tripathi, S. Maidul Haque, K. Divakar Rao, J. S. Misal, C. Pratap and N. K. Sahoo, "Oxygen partial pressure dependent optical properties of glancing angle deposited (GLAD) Ta₂O₅ films deposited by magnetron sputtering," **AIP Conf. Proc. 1731, 080076 (2016).**
12. A. K. Yadav, S. Maidul Haque, D. Shukla, D. M. Phase, S. N. Jha and D. Bhattacharyya, "Local structure investigation of Co doped ZnO thin films prepared by RF sputtering technique," **AIP Conf. Proc. 1731, 060008(2016).**
13. Rajnarayan De, S. Maidul Haque, S. Tripathi, C. Prathap, K. Divakar Rao and N. K Sahoo, "Effect of sputtering power on MgF₂ thin films deposited by sputtering technique under fluorine trapping," **AIP Conf. Proc. 1731, 080078(2016).**
14. S. Maidul Haque, S. Tripathi, Rajnarayan De, J. S. Misal, D. D. Shinde, K. Divakar Rao, and N. K. Sahoo, "The effect of pulse width on asymmetric bipolar pulse DC sputtered tantalum pentoxide thin films," **AIP Conference Proceedings 1832, 080047(2017).**
15. S. Tripathi, Rajnarayan De, K. Divakar Rao, S. Maidul Haque, J. S. Misal, C. Prathap, S.C. Das, V. Ganesan, and N. K. Sahoo, "Annealing induced morphological modifications in PTFE films deposited by magnetron sputtering,," **AIP Conference Proceedings 1832, 080044 (2017).**
16. Rajnarayan De, S. Tripathi, S. C. Naidu, C. Prathap, J. Tripathi, J. Singh, S. Maidul Haque, K. Divakar Rao, and N. K. Sahoo, "Investigation on optical properties of spin coated TiO₂/Co composite thin films,," **AIP Conference Proceedings 1832, 080038 (2017).**

Sk Maidul Haque

Dedicated
To
My Parents
(Sk Tajem Ali & Parsina Begum)

ACKNOWLEDGEMENTS

At first I would like to wholeheartedly thank Dr. Dibyendu Bhattacharyya, Head Synchrotron Science & Multilayer Physics Section, Atomic & Molecular Physics Division, BARC, who is my guide for this thesis work. I consider myself to be highly privileged that I have got opportunity to work with him. I am deeply grateful to Dr. N.K. Sahoo, Associate Director, Physics Group and Head, Atomic & Molecular Physics Division, BARC for his continuous encouragement throughout this thesis work. I would like to express special thanks to all my colleagues in our group in Atomic & Molecular Physics Division at BARC, Visakhapatnam including Dr. K. Divakar Rao, Dr. Shilpa Tripathi, Rajnarayan De, J. S. Misal, D. D. Shinde for their continuous support in my research activity. I would like to express my deepest gratitude and appreciation to my collaborators Dr. C. Mukherjee (Mechanical and Optical Support Section, RRCAT, Indore), Dr. Sanjiv Kumar (National Centre for Compositional Characterization of Materials, Hyderabad), Dr. S. N. Jha (Atomic and Molecular Physics Division, Bhabha Atomic Research Center, Mumbai), Dr. Kalavathi Sridhar (Condensed Matter Physics Division, India Gandhi Centre for Atomic Research, Kalpakkam), Dr. Debarati Bhattacharyya (Solid State Physics Division, Bhabha Atomic Research Centre, Mumbai), Shri Shanmugam Balaji (Material Physics Division, India Gandhi Centre for Atomic Research, Kalpakkam), Dr. Archana Sagdeo (Indus Synchrotron Utilization Division, Raja Raman Center for Advanced Technology, Indore) and their group members. I would like to express my wholehearted thanks to Dr. P. R. Sagdeo (formerly at Atomic & Molecular Physics Division at BARC, Visakhapatnam and now at Discipline of Physics & Discipline of Surface Science & Engineering, Indian Institute of Technology, Indore) for his continuous support and encouragement throughout my scientific career. I would like to heartfully thank all the group members in Synchrotron Science & Multilayer Physics Section, Atomic & Molecular Physics Division, BARC including Ashok Kumar Yadav, Chandrani Nayak, Nidhi Tiwari and Dr. Parasmani Rajput.

I would also like to express sincere thanks to members of my doctoral committee for their input and valuable discussions. I acknowledge all my teachers, friends and family members for their inspiration and silent support during the course of this thesis work. Last but not the least; I heartfully thank my wife, Jyoti Begam for all her sacrifices, moral supports and encouragement without which it would have been impossible for me to complete the thesis.

CONTENTS

Contents	Page number
❖ Synopsis	xiii
❖ List of Figures	xxi
❖ List of Tables	xxxi
❖ Chapter 1	1
Introduction and motivation	1
❖ Chapter 2	14
Experimental Techniques	14
2.1 Introduction	14
2.2 Thin Film Deposition Technique	15
2.2.1 DC Sputtering	19
2.2.2 RF Sputtering	21
2.2.3 Pulse DC sputtering	23
2.2.4 Reactive sputtering	24
2.2.5 Magnetron sputtering	25
2.2 Deposition systems used in this thesis work	27
2.3.1 In-House Built DC/RF Magnetron Sputtering System	28
2.3.2 Custom Made DC/RF/Pulse DC Magnetron Sputtering System	29
2.4 Thin film characterization techniques	31
2.4.1 Grazing incidence X-ray diffraction	32
2.4.2 Grazing incidence X-ray reflectivity	35
2.4.3 Transmission spectrophotometry	39
2.4.4 Spectroscopic Ellipsometry	44
2.4.5 Atomic force microscopy	52
2.4.6 Rutherford Backscattering Spectrometry	54
2.4.7 X-ray Absorption Spectroscopy	58
2.4.7.1 EXAFS	64
2.4.7.2 XANES	70

2.4.7.3 Two modes of XAFS measurement	72
2.4.7.4 EXAFS data analysis	76
2.4.7.5 EXAFS experimental facility	78
❖ Chapter 3	82
Study on HfO ₂ samples deposited at various oxygen partial pressures and the effect of substrate biasing	82
3.1 Introduction	82
3.2 Preparation of samples	85
3.3 Grazing Incidence X-ray Diffraction measurements	85
3.4 Rutherford Backscattering measurements	86
3.5 Grazing Incidence X-ray Reflectivity measurements	88
3.6 Optical Transmission measurements	90
3.7 Spectroscopic ellipsometric measurements	93
3.8 EXAFS measurements	97
3.9 Conclusions	110
❖ Chapter 4	114
Study on TiO ₂ samples deposited at various oxygen partial pressures	114
4.1 Introduction	114
4.2 Preparation of samples	116
4.3 Grazing Incidence X-ray Diffraction measurements	117
4.4 Optical Transmission measurements	120
4.5 EXAFS and XANES measurements	123
4.6 Conclusions	132
❖ Chapter 5	133
Study on Ta ₂ O ₅ samples deposited at various oxygen partial pressures	133
5.1 Introduction	133
5.2 Preparation of samples	134
5.3 Grazing Incidence X-ray Diffraction measurements	135
5.4 Spectroscopic ellipsometry measurements	136
5.5 Extended X-ray absorption fine structure (EXAFS) measurements	140

5.6 Rutherford Back scattering (RBS) measurements	143
5.7 Conclusions	146
❖ Chapter 6	147
Study on Gd ₂ O ₃ samples deposited at various oxygen partial pressures	147
6.1 Introduction	147
6.2 Preparation of samples	148
6.3 Grazing Incidence X-ray Diffraction (GIXRD) measurements	149
6.4 Rutherford Back scattering (RBS) measurements	153
6.5 Grazing Incidence X-ray reflectivity (GIXR) measurements	155
6.6 Atomic Force Microscopy (AFM) measurements	158
6.7 Transmittance spectrophotometry measurements	161
6.8 Spectroscopic Ellipsometry measurements	163
6.9 Extended X-ray Absorption Fine Structure measurements	166
6.10 Conclusion	170
❖ Chapter 7	172
Study of Gd doped ZrO ₂ samples	172
7.1 Introduction	172
7.2 Preparation of samples	174
7.3 Grazing Incidence X-ray reflectivity (GIXR) measurements	175
7.4 Spectroscopic Ellipsometry measurements	177
7.5 Extended X-ray Absorption Fine Structure measurements	180
7.5.1 Zr K-edge data	181
7.5.2 Gd L ₃ -edge data	187
7.6 Conclusion	192
❖ Chapter 8	194
Local structural investigation of refractory oxide thin films near to laser damage threshold	194
8.1 Introduction	194
8.2 Preparation of samples	196
8.3 Laser irradiation of samples	196
8.4 Characterization of laser irradiated samples	199

8.5 Results and discussions	201
8.5.1 Titanium di-oxide samples	201
8.5.2 Tantalum pentoxide samples	205
8.5.3 Hafnium di-oxide samples	211
8.5.4 Gadolinium oxide samples	218
8.6 Conclusion	225
❖ Chapter 9	226
Summary and future work plan	226
9.1 Introduction	226
9.2 Summary on study of HfO₂ samples	227
9.3 Summary on study of TiO₂ set samples	229
9.4 Summary on study of Ta₂O₅ samples	230
9.5 Summary on study of Gd₂O₃ samples	231
9.6 Summary of study made with the variation of oxygen partial pressure	232
9.7 Summary on study of Gd doped ZrO₂ set of samples	233
9.8 Summary on study of local structure investigation on refractory oxide thin films near laser damage threshold	234
9.9 Future work plan	235
❖ References	237
❖ Appendices	250
• Appendix-A: Swanepoel method	250
• Appendix-B: Tauc-Lorentz dispersion model	255
• References	257

SYNOPSIS

Investigation on local structures of oxide thin film by EXAFS study

The materials studied in this thesis work are sputter deposited thin films of oxide materials viz., HfO_2 , TiO_2 , Ta_2O_5 , Gd_2O_3 and ZrO_2 which are important for use as high refractive index material in optical thin film multilayers [1,2] and are also used as high k dielectric in electronic devices [3] or as ion conductors in Solid Oxide Fuel Cells [4]. The films have been deposited at different sputtering conditions like changing oxygen partial pressure or substrate bias. It is well known that the properties of these films like refractive index, band gap, dielectric constant etc. can be tuned by varying the deposition conditions, which is useful to prepare tailor made materials for their fruitful applications.

However, to establish proper correlation of the macroscopic optical properties of the films with their preparation conditions, detail microscopic structural characterization of the films is essential. Conventionally, structural characterizations of thin film samples are carried out by grazing incidence X-ray diffraction (GIXRD) technique, where X-rays are made incident on the thin film samples at a narrow grazing angle of incidence to enhance the interaction of X-rays with the thin film. However, in most of the cases it is very difficult to get good GIXRD data from these thin film samples which are mostly amorphous or polycrystalline in nature with small crystallites size. In this regard, X-ray Absorption Spectroscopy (XAS) qualifies to be a good alternative technique since it only probes the short range order in the samples and presence of long range order in the sample is not an essential requirement [5]. Due to its element specific and short range nature, X-ray absorption spectroscopy (XAS) is increasingly been useful for local structural investigation of complex, disordered materials in a variety of scientific fields such as physics, chemistry, bioscience, materials science and engineering, energy science, environmental science, geoscience, metallurgy, mineralogy etc. In this thesis work thus synchrotron radiation based XAS, which consists of both extended X-ray absorption fine structure (EXAFS) and X-ray absorption

near edge structure (XANES) measurements have been extensively used for structural characterization of optical thin films. The methodology followed in the present work is as follows: (i) determination of macroscopic overall optical constants of the samples by transmission spectrophotometry, (ii) obtaining morphological information of the films from atomic force microscopy (AFM) and/or grazing incidence X-ray reflectivity (GIXR), and (iii) using these data to fit the spectroscopic ellipsometry results which yield information regarding the intrinsic optical properties of the thin film material. The variation of these intrinsic properties of the films with deposition conditions are then correlated with the structural information obtained from XAS measurements on the samples. The results have also been correlated with other complementary measurement techniques like Rutherford back scattering spectroscopy (RBS) wherever needed.

Chapter-1 of the thesis gives a brief introduction to the work carried out under this Ph.D programme and addresses the motivation behind the work. Initially the various important properties of optical thin films and their significance in thin film multilayer optical devices have been discussed. Subsequently, the necessities of detail microstructural characterization of the samples in explaining their macroscopic properties have been discussed. Since these films are mostly amorphous or polycrystalline, the importance of using a local structure analysis tool like X-ray absorption spectroscopy, instead of X-ray diffraction has been emphasized. Subsequently, optical and local structural properties of the various thin film systems discussed in this thesis in subsequent chapters have been described briefly. In summary the contents of this chapter provides the basis for the works presented in subsequent chapters.

Chapter-2 deals with various experimental techniques used in this thesis work. In the beginning of the chapter various deposition techniques used for preparation of thin film samples have been discussed. It is started with listing out of different types of physical vapor deposition techniques and the advantage of sputtering technique, particularly magnetron sputtering technique that has been extensively used for

preparation of thin film samples in this present study has been discussed. Subsequently different sputtering processes like DC magnetron, RF magnetron and Asymmetric Bipolar Pulse DC sputtering techniques have been shortly described. In the second part of this chapter, various thin film characterization techniques that have been employed to investigate the properties of thin films in this thesis have been briefly discussed. The techniques of grazing incidence X-ray diffraction (GIXRD), grazing incidence X-ray reflectivity (GIXR), transmission spectrophotometry, spectroscopic ellipsometry (SE), atomic force microscopy (AFM) and Rutherford backscattering (RBS) techniques have been described shortly. Finally the XAS technique, including both EXAFS and XANES, which has been used in this thesis work extensively have been discussed in details. It is started with the various types of interactions of X-rays with matter and the theoretical basis of XANES and EXAFS techniques have been discussed in brief. The experimental procedures of carrying out XAS measurements using synchrotron radiation has then been described including the two modes (transmittance and fluorescence) of XAS measurements with a brief description of the Energy Scanning EXAFS Beam line (BL-09) of Indus-2 synchrotron source, RRCAT, Indore, India [6]. Finally, the analysis procedure of the EXAFS data starting with data normalization, transformation to k space, Fourier transformation and finally choice of appropriate model to fit the EXAFS data has been thoroughly described with a mention of the software codes used for the above purpose [7,8].

In the following chapters (chapter 3-8) the main results of the thesis work on the correlation of local structural and optical properties of refractory oxide thin films of HfO_2 , Ta_2O_5 , TiO_2 , Gd_2O_3 and Gd doped ZrO_2 deposited under different conditions by sputtering techniques have been described.

In chapter-3, correlation of local structure and optical properties of HfO_2 thin films have been discussed. Two sets of HfO_2 thin films at varying oxygen partial pressures in the range of 0 to 56% have been deposited by RF magnetron sputtering technique; one set without putting any electrical bias to the

substrate i.e. connecting the substrate holder to the ground and the other set keeping the substrate under 50W of pulse DC biasing. The characterizations of the samples by GIXRD, GIXR, RBS, optical transmission spectrophotometry and spectroscopic ellipsometry measurements have been reported. The variation of effective refractive index as obtained from optical transmission measurement could be explained in the light of the variation of atomic density obtained from RBS measurement and variation of void fraction estimated from spectroscopic ellipsometry measurement. Finally with local structural probing through XAS, it was found that for the set of HfO_2 films deposited without substrate bias, the variation of intrinsic refractive index of the films with oxygen partial pressure could be explained in terms of the variation of Hf-Hf bond lengths and for the set of film deposited with substrate biasing, the trend of intrinsic refractive index could be explained in terms of oxygen coordination surrounding Hf sites [9.10].

In chapter-4, the studies on a set of TiO_2 thin films have been reported. A set of TiO_2 thin films has been deposited by asymmetric bipolar pulsed DC (ABPDC) technique in the range of 0 to 21% oxygen partial pressure. The refractive index of TiO_2 films varies in a non-linear fashion with increase in O_2 partial pressure in the sputtering ambient. GIXRD measurements show that the anatase phase fraction in the films increases slowly and monotonically as oxygen partial pressure is increased which cannot explain the observed non-linear variation of refractive index of the films with increase in oxygen partial pressure. However, local structure investigation by EXAFS measurements shows that anatase phase fraction also varies in a nonlinear fashion with increase in oxygen partial pressure and almost follows an opposite trend observed for the variation of refractive index of the films [11].

In chapter-5, the studies on a set of Ta_2O_5 thin films have been reported which were deposited by asymmetric bipolar pulsed DC (ABPDC) technique in the range of 0 to 50% oxygen partial pressure. The intrinsic refractive index obtained from spectroscopic ellipsometry techniques have been explained in the light of change in average Ta-O bond lengths and oxygen coordination around Ta sites as obtained from

EXAFS measurements. The trend of variation in oxygen co-ordination as estimated from EXAFS measurements has been found to follow the variation in oxygen to tantalum ratio in the films as estimated from RBS measurement, while the variation in physical density of the films obtained from RBS measurements is found to be similar with the variation in Ta-O bond lengths obtained from EXAFS measurements [12].

In chapter-6, the studies on a set of Gd_2O_3 thin films have been reported which were deposited by RF magnetron sputtering technique in the range of 0 to 50% oxygen partial pressure. GIXRD measurements show that all the thin film samples are grown in cubic phases. Spectroscopic ellipsometry measurements show that the low density of the sample prepared with 9.1% oxygen partial pressure is due to the presence of high concentration of voids in this sample. Comparing the nature of variation of Gd-Gd bond length of the samples obtained from EXAFS measurements, as a function of oxygen partial pressure, with that of the intrinsic refractive index of the Gd_2O_3 material, as obtained from the spectroscopic ellipsometric measurements, it could be concluded that these films assume $ia-3$ space group of cubic crystalline structure. Thus by applying complementary characterization techniques, it has been possible to explain several macroscopic properties of this technologically important thin film system from microscopic structural information [13].

In chapter-7, the study on Gd doped ZrO_2 thin films samples with varying Gd doping concentration from 0 to 13%, prepared by RF magnetron sputtering technique, has been described. It has been observed from spectroscopic ellipsometry and optical transmission measurements that the void fraction present in the films increases significantly beyond Gd doping concentration of 11% causing a decrease in the effective refractive index of the films. It has also been observed from GIXRD measurements that though the undoped ZrO_2 film is having monoclinic structure, Gd doping stabilises the films in cubic structure, which is different from the results obtained earlier by our group on bulk ZrO_2

samples prepared by co-precipitation route. The observed optical properties of the thin films that Gd doping beyond 11% yields samples with higher void fraction, lower band gap and lower effective refractive index has been found to be corroborated with the results from EXAFS measurements on the samples at both Zr- K edge and Gd L3 edges [14].

Study of laser induced damage mechanism and effort to increase the damage threshold of the above oxide thin films is of immense technological importance because as improved laser damage-resistant optical materials and better fabrication technologies are developed, laser designers can increase the system operating energies and powers to the limits of these new materials. The study of these materials under laser irradiation is also important from the point of view of tailoring of material properties by purposeful laser irradiation. Although, many efforts have been made to investigate how stoichiometry or long range order structure plays a role in describing the laser damage process, to the best of our knowledge, efforts to understand the local structural changes in the materials due to laser irradiation near around the damage threshold has not been made so far. In chapter-S, results of EXAFS and XANES measurements on laser irradiated refractory oxide samples near the damage threshold have been described. The above studies have been carried out on r.f. sputter deposited dielectric refractory oxide thin film samples of TiO_2 , Ta_2O_5 , HfO_2 and Gd_2O_3 each of approximately 200 nm thicknesses. For TiO_2 , Ta_2O_5 and HfO_2 samples, the laser fluence was optimized to 0.95 J/cm^2 , 2.06 J/cm^2 and 5.58 J/cm^2 respectively and different locations on the samples were irradiated with varying number of pulse shots. On the other hand, for Gd_2O_3 samples, the number of shots were kept constant at 5 and the fluence was varied from $\sim 13\text{-}35 \text{ J/cm}^2$ in order to study the damage mechanism around the damage threshold. Apart from XAS measurements, various other characterization techniques such as optical microscopic imaging, grazing incidence X-ray reflectivity and grazing incidence X-ray diffraction have also been employed to study the laser irradiated zones, Using these above studies, several interesting correlations between the laser

irradiation process near the damage threshold with various macro/micro structural properties of the samples could be established which have been described in this chapter.

Finally in chapter-9 the conclusions drawn in all the previous chapters in the different set of thin films have been summarized and future directions of the works have been mentioned. As a future prospective it is proposed to carry out grazing incidence XAS measurements on optical multilayers using the recently commissioned high precision goniometer at BL-09 Energy Scanning EXAFS beam line at Indus-2 SRS understanding wave conditions so that the interfaces of the thin film optical multi layers can be studied. It is also proposed to study the structural evolution of these optical thin films during their growth by employing a sputtering system in the experimental station of BL-09 which will be placed on the above goniometer. Finally it is proposed to carry out the EXAFS measurements on the samplers under in-situ laser irradiation conditions so that further insight into the local structural changes in the materials under laser irradiation near the damage threshold can be obtained.

References

1. Laurent Gallais and Mireille Commandre, "Laser-induced damage thresholds of bulk and coating optical materials at 1030 nm, 500 fs," *Applied Optics* 53, A186-A196 (2014).
2. Ivan B. Angelov, Maximilian von Pechmann, Michael K. Trubetskov, Ferenc Krausz and Vladimir Pervak, "Optical breakdown of multilayer thin-films induced by ultrashort pulses at MHz repetition rates," *Optics Express* 21, 31453(2013).
3. Davinder Rathee Mukesh Kumar Sandeep K. Arya, " CMOS Development and Optimization, Scaling Issue and Replacement with High-k Material for Future Microelectronics," *International Journal of Computer Applications* 8, 0975 - 8887(2010).
4. P. D. L. Mercera, I. G. van Ommen, E. B. M. Doesburg, A. J. Burggraaf, and J. R. H. Ross, "Stabilized tetragonal zirconium oxide as a support for catalysts: evolution of the texture and structure on calcination in static air," *Appl. Catal.* 78, 79-96 (1991).
5. L. Properzi, A. Di Cicco, L. Nataf, F. Baudelet & T. Irifune, "Short-range order of compressed amorphous GeSe₂," *Scientific Reports* 5, 1 (2015).
6. S. Basu, C. Nayak, A.K. Yadav, A. Agrawal, A.K. Poswal, D. Bhattacharyya, S.N. Jha, and N. K. Sahoo, A comprehensive facility for EXAFS measurements at the INDUS-2 synchrotron source at RRCAT, Indore, India, 1. *Phys.: Conf. Ser.* 493, 012032(2014).
7. D.C. Konigsberger and R. Prince, *X-ray absorption: principles, applications, techniques of EXAFS, SEXAFS, and XANES*. Wiley, New York, 1988.

8. M. Newville, B. Ravel, D. Haskel, I.I. Rehr, E.A. Stern, and Y. Yacoby, Analysis of multiple scattering XAFS data using theoretical standards, *Physica B* 154, 1208(1995).
9. Sk. Maidul Haque, Pankaj R. Sagdeo, Shanmugam Balaji, Kalavathi Sridhar, Sanjiv Kumar, Debarati Bhattacharyya, Dibyendu Bhattacharyya and Naba K. Sahoo, *Vac. Sci. Technol. B* 32, 03D104-1 (2014).
10. S. Maidul Haque, C. Nayak, Dibyendu Bhattacharyya, S. N. Jha, And N. K. Sahoo, *Applied Optics* 55, 2175 (2016).
11. S. Maidul Haque, Pankaj R. Sagdeo, Archana Sagdeo, S. N. Jha, D. Bhattacharyya, And N. K. Sahoo, *Applied Optics* 54, 3817 (2015).
12. S. Maidul Haque, Pankaj R. Sagdeo, D. D. Shinde, I.S. Misal, S.N. Jha, D. Bhattacharyya and N.K. Sahoo, *Applied Optics* 54, 6744 (2015).
13. S. Maidul Haque, Rajnarayan De, S. Tripathi, C. Mukherjee, A. K. Yadav, Dibyendu Bhattacharyya, S.N. Jha And N.K. Sahoo, *Applied Optics* 56, 6114-6125(2017).
14. S. Maidul Haque, S. Tripathi, S.N. Jha, D. Bhattacharyya and N. K. Sahoo, *Applied Optics* 55, 7355 (2016).

List of Figures

Fig. No.	Figure Captions	Page No.
Fig. 1.1:	Photographs of optical devices made out of thin film deposition.	2
Fig. 1.2:	The Stack of multilayer on transparent substrate.	2
Fig. 1.3:	Flowchart of this thesis work	9
Fig. 2.1:	Schematic representation of sputter deposition technology	16
Fig. 2.2:	Collision cascade in sputtering process	17
Fig. 2.3:	Sputtering yield for several materials as a function of Ar ion energy	18
Fig. 2.4:	Different electric discharge regime in DC glow discharge	19
Fig. 2.5:	Dependence of deposition rate on gas pressure for non-magnetron sputtering	20
Fig. 2.6:	Formation of self bias sheath on target during RF Discharge (a) net current/zero self-bias voltage (b) Zero current/nonzero self bias voltage	22
Fig. 2.7:	Applied field and electron motion in planer magnetron	26
Fig. 2.8:	Magnetic field lines of balanced and unbalanced magnetrons	27
Fig. 2.9:	In -house built DC/RF Magnetron Sputtering System at AMPD, BARC-Visakhapatnam Laboratory	28
Fig. 2.10:	Custom Made DC/RF/Pulse DC Magnetron Sputtering System at AMPD, BARC-Visakhapatnam Laboratory	29
Fig. 2.11:	Waveform of ABPDC power supply installed in sputtering system	31
Fig. 2.12:	Photograph of GIXRD instrument in AMPD, BARC, Visakhapatnam laboratory	32
Fig. 2.13:	Schematic of GIXRD set-up in 2 θ scan mode	33
Fig. 2.14:	Typical GIXRD spectrum of thin film sample	34
Fig. 2.15:	Reflectivity vs. grazing angle of incidence curve	35
Fig. 2.16:	Screen shot of 'Global Fit' analysis software	38
Fig. 2.17:	Photograph of Jasco (V-630) spectrophotometer at AMPD lab, BARC, Visakhapatnam	39
Fig. 2.18:	Block Diagram of Spectrophotometer [Jasco (V-630)]	40
Fig. 2.19:	Representative transmission spectra of bare substrate and thin film coated	41

substrate

Fig. 2.20: Screenshot of indigenously developed computer program for determination of thickness and dispersion relation of thin film from transmission spectrum	42
Fig. 2.21: Tauc plot of sputter deposited tantalum pentoxide thin films	43
Fig. 2.22: Schematic of reflection of plane polarized light from sample	45
Fig. 2.23: Photograph of spectroscopic ellipsometer (SOPRA GES5E) at AMPD, BARC, Visakhapatnam.	46
Fig. 2.24: Schematic of rotating polarizer type spectroscopic ellipsometer	47
Fig. 2.25: Photograph of phase modulated spectroscopic ellipsometer at AMPD, BARC, Trombay	49
Fig. 2.26: Microscopically inhomogeneous medium to be treated under effective medium approximation (EMA).	50
Fig. 2.27: Actual photograph of AFM set up located at Mechanical and Optical Support Section, RRCAT, India and used for AFM characterization of the samples in this thesis.	53
Fig. 2.28: Backscattering event following collision between two different masses.	54
Fig. 2.29: Kinematical factors versus target masses for different projectiles	55
Fig. 2.30: Representative RBS spectrum measured by proton beam for a Ta ₂ O ₅ coated glass substrate	56
Fig. 2.31: Screenshot of the SIMNRA program.	57
Fig. 2.32: Different energy regime of whole electromagnetic spectrum	58
Fig. 2.33: The X-ray and Auger electron emission following photoelectric effect	59
Fig. 2.34: The Compton scattering of X-ray	60
Fig. 2.35: Diagram showing the process of electron-positron pair production	61
Fig. 2.36: X-ray to matter interaction cross section at different energy range of X-ray	62
Fig. 2.37: The typical absorption cross section vs. X-ray energy of any materials	63
Fig. 2.38: Basic phenomenon of XAFS	64
Fig. 2.39: Typical absorption spectrum around absorption edge	65
Fig. 2.40: Typical characteristic of photoelectron mean free path vs. wave number	69
Fig. 2.41: XANES spectra of standard Fe metal and oxides	71
Fig. 2.42: Block diagram of XAFS measurement set-up	72
Fig. 2.43: Physical filtering of scattered X-rays using 'Z-1' filter	74
Fig. 2.44: Optical layout of scanning EXAFS beam line (BL-09) at INDUS-2, RRCAT,	79

Fig. 2.45: Experimental set-up for transmission mode of XAFS measurement	80
Fig. 2.46: Experimental set-up for fluorescence mode of XAFS measurement	81
Fig.3.1: GIXRD spectrum of HfO ₂ films deposited (a) without and (b) with pulsed DC substrate bias and at various oxygen flow rates (Ar flow rate has been kept at 20 sccm in each case)	86
Fig. 3.2: (a)RBS spectrum of a representative HfO ₂ sample deposited without substrate bias and at 9.1 % oxygen partial pressure. (b)Variation of atom number density of HfO ₂ films, estimated from RBS spectra, as a function of oxygen partial pressure.	88
Fig.3.3 (a)Grazing incidence x-ray reflectivity spectra of HfO ₂ samples deposited without substrate bias and at various oxygen flow rates. (b)Variation of density estimated from GIXR spectra as a function of oxygen partial pressure (in percentage) used during deposition for HfO ₂ films deposited without substrate bias.	89
Fig. 3.4: (a)Transmission spectrum of a representative HfO ₂ sample deposited without substrate bias and at zero oxygen partial pressure. (b)Variation of deposition rates of HfO ₂ films, obtained from transmittance measurements, as a function of oxygen partial pressure. (c)Variation of refractive index of HfO ₂ films at 550 nm, obtained from transmittance measurements, as a function of oxygen partial pressure (in percentage) used during deposition. (d)Variation of band gap of HfO ₂ films, obtained from transmittance measurements, as a function of oxygen partial pressure (in percentage) used during deposition.	90 91
Fig.3.5: Experimental ψ and Δ versus wavelength along with best-fit theoretical curve for a representative HfO ₂ film deposited without substrate bias and at 23.1% oxygen partial pressure (in percentage). oooo: Experimental Data; ———: Theoretical fit.	93
Fig.3.6: Sample structure and the fitting parameters of used TL model along with the dispersion of refractive index for a representative HfO ₂ thin film deposited with substrate bias and at 23.1 % oxygen partial pressure.	94
Fig.3.7: (a)Variation of effective void percentage present in the HfO ₂ films as a function of oxygen partial pressure used during deposition. (b)Variation of intrinsic refractive index of HfO ₂ at 550 nm as a function of oxygen partial pressure used during deposition.	95
Fig.3.8: Experimental $\mu(E)$ vs. E spectra of HfO ₂ thin films deposited under different oxygen partial pressures for the set of samples deposited without substrate bias (a) and with pulsed DC substrate bias (b).	99

Fig.3.9: Fourier transformed EXAFS spectra of HfO ₂ films deposited under different oxygen partial pressures for the set of samples deposited without any substrate bias along with best fit theoretical plots.	103
o-o-o-o: Experimental Data	
(a) -----: Theoretical fitting with monoclinic structure.	
(b) -----: Theoretical fitting with orthorhombic structure.	
Fig.3.10: Fourier transformed EXAFS spectra of HfO ₂ films deposited under different oxygen partial pressures for the set of samples deposited with pulsed DC substrate bias along with best fit theoretical plots.	104
o-o-o-o: Experimental Data	
(a) -----: Theoretical fitting with monoclinic structure.	
(b) -----: Theoretical fitting with orthorhombic structure.	
Fig. 3.11: Comparison of R_{factor} values of EXAFS fitting for HfO ₂ thin film samples fitted with monoclinic and orthorhombic structure.	105
(a) Films deposited without any substrate bias.	
(b) Films deposited with pulsed DC substrate bias.	
Fig.3.12: Variation of (a) Hf-O bond length (R_o) & (b) oxygen coordination (N_o) of nearest neighbor oxygen shell, (c) Hf-Hf distance (R_{Hf}) & (d) Hf coordination (N_{Hf}) of next nearest neighbor Hf shell, and (e) intrinsic refractive index (n) of HfO ₂ thin films at 550 nm as obtained from spectroscopic ellipsometry measurements, as a function of oxygen partial used during deposition, for the set of films deposited without substrate bias.	107
Fig.3.13: Variation of (a) Hf-O bond length (R_o) & (b) oxygen coordination (N_o) of nearest neighbor oxygen shell, (c) Hf-Hf distance (R_{Hf}) & (d) Hf coordination (N_{Hf}) of next nearest neighbor Hf shell, and (e) intrinsic refractive index (n) of HfO ₂ thin films at 550 nm as obtained from spectroscopic ellipsometry measurements, as a function of oxygen partial used during deposition, for the set of films deposited with pulsed DC substrate bias.	109
Fig.4.1: GIXRD plots of TiO ₂ films deposited at various oxygen partial pressure (in percentage) used during deposition.	117
Fig.4.2: Variation of anatase phase fraction as a function of oxygen partial pressure used during deposition obtained from GIXRD and EXAFS measurements.	119
Fig. 4.3: Transmission spectra of two samples deposited at 0% (without any extra oxygen) and with 21% oxygen partial pressure in sputtering ambient.	120
Fig.4.4: Variation of (a) refractive index @ 550 nm, (b) band gap and (c) deposition rate as obtained from transmittance measurements as a function of oxygen partial pressure (in percentage) used during deposition.	122
Fig.4.5: Absorption coefficient (μ) versus incident X-ray energy (E) of TiO ₂ films	124

deposited at different oxygen partial pressures

Fig.4.6:	(a) XANES spectra of TiO ₂ films showing various absorption peaks. (b) XANES spectra of two TiO ₂ samples prepared at 0% and 21% oxygen partial pressures shown in expanded scale.	125
Fig.4.7:	(a) $k\chi(k)$ versus k plots of the samples deposited with 2% and 21% oxygen partial pressures. (b) $\chi(r)$ versus r plots of the samples deposited with 2% and 21% oxygen partial pressures.	126
Fig.4.8:	Experimental $\chi(r)$ versus r plot along with best fit theoretical plots of the TiO ₂ film deposited at zero oxygen partial pressure: ooooooo: Experimental data; -----: Theoretical fit with rutile structure.	127
Fig. 4.9:	Experimental $\chi(r)$ versus r plot along with best fit theoretical plots of TiO ₂ films deposited at different oxygen partial pressures: ooooooo : Experimental data : Theoretical fit assuming only anatase phase	128
Fig.4.10:	Variation of R_{factor} factor of fitting in both the cases (assuming pure anatase phase and mixed phase of anatase and rutile) as a function of oxygen partial pressure used during deposition.	130
Fig.5.1:	GIXRD pattern of Ta ₂ O ₅ thin films deposited under various oxygen partial pressures used in the ambient during deposition.	136
Fig.5.2:	Spectroscopic ellipsometry data along with best fit theoretical simulation for a representative Ta ₂ O ₅ film deposited with 37.5% oxygen partial pressure.	137
Fig.5.3:	The best fit sample structure and the best fit parameters of the TL model as obtained by the fitting along with the dispersion of intrinsic refractive index generated with the best fit parameters for the representative Ta ₂ O ₅ film deposited with 37.5% oxygen partial pressure.	137
Fig.5.4:	(a) Variation of intrinsic refractive index (r.i.) of Ta ₂ O ₅ @ 550 nm as a function of oxygen partial pressure used during deposition. (b) Variation of band gap of Ta ₂ O ₅ films as a function of oxygen partial pressure used during deposition. (c) Variation of deposition rate of Ta ₂ O ₅ films as a function of oxygen partial pressure used during deposition. (d) Variation of void percentage of Ta ₂ O ₅ as a function of oxygen partial pressure used during deposition.	139
Fig.5.5:	Experimental $\mu(E)$ vs. E spectra of Ta ₂ O ₅ thin films.	141
Fig. 5.6:	$\chi(R)$ versus R plots for experimental and fitted EXAFS data of Ta ₂ O ₅ thin films	141
Fig.5.7:	(a) Variation of average Ta-O bond length as a function of oxygen partial pressure used during deposition as obtained from EXAFS data analysis of	142

Ta₂O₅ thin films.

(b) Variation of total oxygen co-ordination number around Ta sites as a function of oxygen partial pressure used during deposition as obtained from EXAFS data analysis of Ta₂O₅ thin

Fig.5.8:	Experimental and simulated RBS spectra of Ta ₂ O ₅ samples deposited under 0%, 28.57%, 37.5% and 50% oxygen partial pressure. The RBS front edge of different constituent elements of the film (F) and substrate (S) are indicated in the figure.	144
Fig.5.9:	(a) Variation of oxygen to tantalum ratio obtained from RBS measurement as a function of oxygen percentage used during deposition. (b) Variation of physical density data estimated combining RBS and ellipsometry measurements as a function of oxygen percentage used during deposition.	145
Fig.6.1:	(a) GIXRD plot of all Gd ₂ O ₃ samples deposited under different oxygen partial pressure. (b) Positions of XRD peaks for space group I2 ₁ 3, (c) Positions of XRD peaks for space group Ia-3.	150
Fig.6.2:	Variation of estimated crystallite size obtained from GIXRD measurement as a function of oxygen partial pressure.	152
Fig.6.3:	Experimental and simulated RBS spectra of Gd ₂ O ₃ samples deposited under 0%, 16.7% and 37.5% oxygen partial pressure. The RBS front edge of different constituent elements of the film and substrate are indicated in the figure.	153
Fig. 6.4:	Variation of oxygen-to-gadolinium ratio obtained from RBS measurement as a function of oxygen partial pressure.	154
Fig.6.5:	Measured GIXR curves of all Gd ₂ O ₃ samples deposited under different oxygen partial pressures. (Inset shows the layer structure model employed to fit the experimental GIXR spectra).	155
Fig.6.6:	Experimental GIXR curve along with best fit theoretical simulation for a representative Gd ₂ O ₃ sample deposited at 16.7% oxygen partial pressure. (Inset shows layer structure model obtained by analyzing the GIXR data of the same sample).	156
Fig. 6.7:	(a) Variation of (a) main (bottom) layer density obtained from GIXR fitting, (b) Surface roughness obtained from GIXR fitting, (c) Surface roughness (RMS) estimated from AFM measurement as a function of oxygen partial pressure.	157
Fig.6.8:	3D AFM micrographs of all the Gd ₂ O ₃ samples deposited under different oxygen partial pressures (x and y axes are in μ m, z axis is in nm unit).	160
Fig.6.9:	Experimental transmission spectrum of bare fused silica substrate and of one	161

representative Gd_2O_3 sample deposited on fused silica substrate under 16.7% oxygen partial pressure. (Inset shows $(\alpha h\nu)^2$ vs. $h\nu$ curve for the sample.)

- Fig.6.10: Variation of (a) deposition rate (b) refractive index at 550 nm (c) direct band gap estimated from transmission measurement as a function of oxygen partial pressure. (a) also shows the variation of deposition rate obtained from spectroscopic ellipsometry measurement and in-situ measurement by quartz crystal monitor. 162
- Fig.6.11: Variation of (a) intrinsic refractive index @ 550 nm (b) interface layer thickness and (c) interface layer void percentage estimated from spectroscopic ellipsometry data as a function of oxygen partial pressure. 165
- Fig.6.12: (a) Experimental EXAFS spectrum (μ vs. E), (b) Reduced $k^2\chi(k)$ vs k plot, (c) Fourier transformed EXAFS spectrum ($\chi(R)$ versus R) along with best-fit theoretical simulation assuming body centered cubic Gd_2O_3 phase having space group $I2_13$, (d) Fourier transformed EXAFS spectrum ($\chi(R)$ versus R) along with best-fit theoretical simulation assuming body centered cubic Gd_2O_3 phase having space group $ia-3$ for a representative Gd_2O_3 sample deposited at 9.09% oxygen partial pressure, (e) theoretical paths of $I2_13$ space group and (f) theoretical paths of $ia-3$ space group. 166
- Fig. 6.13: Variation of R_{factor} assuming body centered cubic Gd_2O_3 phase having space group $I2_13$ and $ia-3$ model as a function of oxygen partial pressure. 169
- Fig.6.14: Variation of (a) average Gd-O bond length (b) average Debye-Waller factor of Gd-O bonds (c) average Gd-Gd bond length and (d) average Debye-Waller factor of Gd-Gd bonds as a function of oxygen partial pressure as obtained from EXAFS data analysis assuming Gd_2O_3 cubic phase having space group $I2_13$ (left panel) and space group $ia-3$ (right panel). 170
- Fig. 7.1: (a) GIXRD plot of fused silica substrate, (b) GIXRD plot of undoped ZrO_2 thin film and (c) GIXRD plots of 7%, 9%, 11% and 13% Gd doped ZrO_2 thin films. 176
- Fig. 7.2: (a) Variation of void percentage of interface layer in all the samples obtained from spectroscopic ellipsometry measurement. 177
(b) Variation of main layer refractive index of all the samples at 550 nm obtained from ellipsometry measurement.
- Fig. 7.3: (a) Absorption coefficient (α) versus energy ($h\nu$) plots in optical region obtained from transmission measurement for all the samples. 179
(b) Variation of direct band gap calculated from absorption spectra as a function of Gd doping concentration.
(c) Variation of effective refractive index of all the samples at 550 nm obtained from transmittance measurement.
- Fig. 7.4: (a) Absorption coefficient ($\mu(E)$) versus incident X-ray energy (E) of undoped as well as Gd doped ZrO_2 thin films measured at Zr K-edge. Inset: 180

$k^2 \chi(k)$ vs. k plots of the samples.

(b) Absorption coefficient ($\mu(E)$) versus incident X-ray energy (E) of all Gd doped ZrO_2 thin films measured at Gd L_3 -edge. Inset: $k^2 \chi(k)$ vs. k plots of the samples.

Fig. 7.5: (a) Experimental $\chi(R)$ versus R plots along with best fit theoretical plots of undoped as well as Gd doped ZrO_2 samples measured at Zr K-edge assuming Monoclinic Phase of ZrO_2 . 183

o-o-o-o: Experimental Data; -----: Theoretical fit.

(b) Experimental $\chi(R)$ versus R plots along with best fit theoretical plots of undoped as well as Gd doped ZrO_2 samples measured at Zr K-edge assuming Cubic Phase of ZrO_2 . o-o-o-o: Experimental Data; -----: Theoretical fit

Fig. 7.6: Variation of R_{factor} in case of fitting of Zr K-edge data assuming Monoclinic and Cubic phase of ZrO_2 as a function of Gd doping concentration. 184

Fig. 7.7: (a) Variation of average Zr-Zr distance as a function of Gd doping concentration (b) Variation of total oxygen co-ordination number around core Zr sites as a function of Gd doping concentration.(c) Variation of average Debye Waller factors of Zr-O bonds as a function of Gd doping concentration. 186

Fig.7.8: (a):Experimental versus plots along with best fit theoretical plots of Gd doped ZrO_2 samples measured at Gd L_3 -edge assuming Cubic Phase of ZrO_2 , core Zr site being replaced by Gd. o-o-o-o: Experimental Data; -----: Theoretical fit. 188

(b): Experimental versus plots along with best fit theoretical plots of Gd doped ZrO_2 samples measured at Gd L_3 -edge assuming Cubic Phase of Gd_2O_3 . o-o-o-o: Experimental Data; -----: Theoretical fit.

Fig. 7.9: Variation of R_{factor} in case of fitting of Gd L_3 -edge data as a function of Gd doping concentration assuming (i) Cubic Phase of ZrO_2 , core Zr site being replaced by Gd, (ii) Cubic Phase of Gd_2O_3 ,and (iii) mixed phase for the 9% and 11% Gd doped samples 189

Fig.7.10: Experimental $\chi(R)$ versus R plots along with best fit theoretical plots of (a) 9% Gd doped ZrO_2 sample and (b) 11% Gd doped ZrO_2 sample measured at Gd L_3 -edge assuming mixed phase model. 190

o-o-o-o: Experimental Data; -----: Theoretical fit.

Fig.7.11: (a) Variation of Gd-O bond length as a function of Gd doping concentration. (b) Variation of oxygen co-ordination around Gd site as a function of Gd doping concentration. (c) Variation of Debye Waller factors of Gd-O bonds as a function of Gd doping concentration 191

Fig. 8.1: Schematic of marked zones on sample surface. 196

Fig.8.2: (a) Photograph and (b) schematic of Laser irradiation experimental set-up.	197
Fig.8.3: Optical microscopic images of laser irradiated TiO ₂ sample spots after undergoing laser irradiation of 0.95 J/cm ²	201
Fig. 8.4: GIXR spectra of as-deposited and all laser irradiated TiO ₂ sample spots.	202
Fig. 8.5: GIXRD spectra of all the laser irradiated TiO ₂ sample spots along with that of the as deposited sample spot.	203
Fig. 8.6: (a) XANES spectra of as deposited and laser irradiated TiO ₂ sample spots. (b) Expanded XANES spectra in the region of 4980–5000 eV.	204
Fig. 8.7: (a) Pre-edge region of the XANES spectra of as-deposited and laser irradiated TiO ₂ sample spots.	205
Fig.8.8: Optical microscopic images of laser irradiated Ta ₂ O ₅ sample spots after undergoing laser irradiation of 2.06 J/cm ² .	206
Fig. 8.9: GIXR spectra of as deposited and all laser irradiated Ta ₂ O ₅ sample spots	207
Fig. 8.10: GIXRD spectra of as deposited and all laser irradiated Ta ₂ O ₅ sample spots.	207
Fig. 8.11: Measured normalized EXAFS spectra of as-deposited and all laser irradiated Ta ₂ O ₅ sample spots.	208
Fig. 8.12: Experimental and fitted FT-EXAFS spectra for all the laser irradiated Ta ₂ O ₅ samples.	209
Fig. 8.13: Plot of (a) average Ta-O bond length, (b) oxygen co-ordination number and (c) average disorder of Ta-O bonds obtained from EXAFS.	210
Fig.8.14: Optical microscopic images of laser irradiated HfO ₂ sample spots after undergoing laser irradiation of 5.58 J/cm ² .	211
Fig. 8.15: Measured GIXR spectra of as-deposited and all laser irradiated HfO ₂ samples.	212
Fig. 8.16: Variation of roughness of laser irradiated spots of HfO ₂ as obtained analyzing the GIXR data.	212
Fig. 8.17: Measured GIXRD spectra of as-deposited as well as laser irradiated HfO ₂ sample spots.	213
Fig. 8.18: (a) Representative Williamson-Hall plot for as deposited HfO ₂ sample. (b) Plot of variation of crystallite size with increase in number of pulse shots as obtained from GIXRD.	214
Fig. 8.19: Measured EXAFS spectra for all the laser irradiated HfO ₂ sample spots	215
Fig. 8.20: Experimental and fitted FT-EXAFS spectra for all the laser irradiated HfO ₂ sample spots.	217

Fig. 8.21: Plot of estimated bond parameters for Hf-O co-ordination shell	218
Fig. 8.22: Plot of estimated bond parameters for Hf-Hf co-ordination shell	218
Fig. 8.23: Optical microscopic images of laser irradiated Gd ₂ O ₃ sample spots after undergoing laser irradiation of varying fluencies.	219
Fig. 8.24: GIXR spectra of all the laser irradiated Gd ₂ O ₃ samples along with the as-deposited sample.	220
Fig. 8.25: GIXRD spectra of all the laser irradiated Gd ₂ O ₃ samples along with the as-deposited sample spots.	220
Fig. 8.26: Measured normalized EXAFS spectra of as deposited and all laser irradiated Gd ₂ O ₃ sample spots	221
Fig. 8.27: Experimental and fitted FT-EXAFS spectra for all the laser irradiated Gd ₂ O ₃ samples.	223
Fig. 8.28: R-factor of fitting using I2 ₁ 3 and ia-3 space group model.	224
Fig. 8.29: Plot of estimated bond parameters for Gd-O co-ordination shell	224
Fig. 8.30: Plot of estimated bond parameters for Gd-Gd co-ordination shell.	224

List of Tables

Table No.	Table Title	Page No.
Table-3.1	Scattering paths used for simulating EXAFS spectra of monoclinic HfO ₂ samples.	100
Table-3.2	Scattering paths used for simulating EXAFS spectra of orthorhombic HfO ₂ samples.	101
Table-4.1	Thickness of all the TiO ₂ samples deposited under different oxygen partial pressures as estimated from transmission spectra.	121
Table-6.1	Scattering paths used for fitting assuming BCC crystal structure having space group I2 ₁ 3.	167
Table-6.2	Scattering paths used for fitting assuming BCC crystal structure having space group ia-3.	167
Table-7.1	Scattering paths used for fitting Zr K-edge data with Monoclinic Phase of ZrO ₂ .	182
Table-7.2	Scattering paths used for fitting Zr K-edge data with cubic phase of ZrO ₂ .	182
Table-7.3	Scattering paths used for fitting Gd L ₃ -edge data with Cubic Phase of ZrO ₂ , core Zr being replaced by Gd.	187
Table-7.4	Scattering paths used for fitting Gd L ₃ -edge data with cubic Gd ₂ O ₃ structure.	188
Table-8.1	Experimental condition (Pulse repetition rate was 1 Hz for all the experiments) Diameter of laser illumination zone, D; Laser peak energy E _p .	198
Table-8.2	Scattering paths used for fitting Ta ₂ O ₅ EXAFS data assuming orthorhombic crystal structure having β-Ta ₂ O ₅ phase (space group: Pccm).	208
Table-8.3	Scattering paths used for fitting HfO ₂ EXAFS data assuming monoclinic crystal structure (space group: P2 ₁ /c).	216
Table-8.4	Scattering paths used for fitting Gd L ₃ -edge $\chi(R)$ versus R data assuming BCC crystal structure having space group I2 ₁ 3.	222
Table-8.5	Scattering paths used for fitting Gd L ₃ -edge $\chi(R)$ versus R data assuming BCC crystal structure having space group ia-3.	222

CHAPTER-1

Introduction and motivation

Starting from 20th century especially in last few decades, thin film deposition technology has become an increasingly popular subject primarily due to the fact that all microelectronic solid state devices are based on thin film. Owing to their small thickness, thin films are almost invisible to the naked eye or buried below other surface layers. Nevertheless, this field of science and technology has so much impact on electronic, optical, mechanical or biological applications that modern life, as we experience today, would have not been possible without thin film and coating technology. The usage of thin films for decorative coatings is probably one of the oldest applications of thin film. To name some of the areas where thin films are greatly applied are as diffusion barrier, stain repellent, anti-microbial, anti-fogging, anti-corrosive, photo catalytic, photovoltaic, thin film batteries, thermally or electrically insulating, conductive, optical, low friction and wear resistant etc.

Out of all these wide variety of applications of thin film, optical thin film caters a major area of application. Optical thin film based devices have applications to various field of science and technology starting from laser technology to astronomy. Numerous optical devices are made out of thin film technology such as anti reflection (A.R.) coating, high reflecting (H.R.) dielectric mirrors, beam reflectors, beam combiners, beam dividers, band pass or edge pass filters, broadband A.R. or H.R. coatings, electro-optical devices [1], active[2] and passive[3] waveguides so on and so forth. Fig. 1.1 shows photographs of handsome of optical devices made out of modern thin film technology. The advancement of

all these important devices is the main driving force for carrying out research and development in thin film technology.



CD/DVD



Camera lens coating[4]



Solar cells[5]

Fig. 1.1: Photographs of optical devices made out of thin film deposition.

Fig. 1.2 depicts a general design of interferometry based optical devices. It consists of multilayer stack of several thin film layers of different materials or very often two alternate materials.

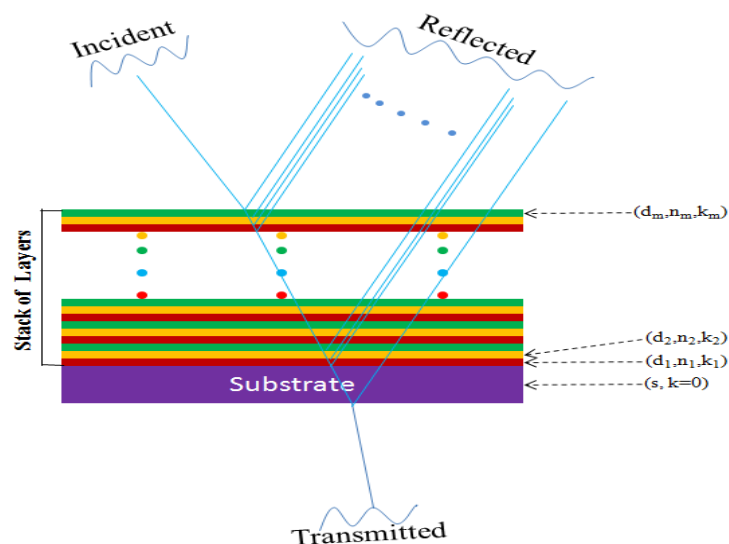


Fig. 1.2: The Stack of multilayer on transparent substrate.

The successful fabrication and operation of all these devices requires appropriate design in one hand and in other hand it relies upon selection of right optical materials, method of preparation and optimization of process parameters in order to achieve desired optical and other associated properties. Optical properties characterize the response of materials to incident electromagnetic radiation. For each material, the incident radiation is partially transmitted, partially reflected and partially absorbed and the percentage of each one is dictated by two of the most important optical properties namely the refractive index n and the extinction coefficient K , which are generically called *optical constants*. Since many of these devices are made for utilization in high power laser system and in extreme environmental conditions, apart from optical constants, other associated properties such as thermal expansion coefficient, mechanical properties, stress, birefringence etc. are also important which needs to be assessed before adopting fabrication methodology or process parameters. Also the inter-relation among these properties and the dependence of these properties on micro structural behavior of the materials in thin film form is of fundamental interest. Below mentioned are few important properties of thin film that one needs to care for while designing and fabricating thin film based optical devices.

(i) Homogeneity:

When a thin film based optical device is fabricated it is expected that different spatial locations of the thin film exhibits similar characteristics. To satisfy this, what is required in the first hand is that the ingredients are mixed uniformly and distributed in all locations in the similar fashion. This is called homogeneity of the thin film samples. For example, when a polished lens with a diameter of approximately 4 inches is installed into an optical system, the lens is expected to perform consistently across its entire aperture, that is to say light

passing through its center will refract consistently with light passing near the edge. It is the ability to limit localized variations in the refractive index and dispersion that opticians define as a material's homogeneity.

(ii) Refractive index:

In simpler language refractive index of any medium is defined as the ratio of the phase velocity of the light in vacuum to that in the medium. It is an important optical constant firstly because the change in phase of the light in traversing a certain distance in a medium is determined by the optical path length which is the product of refractive index and the physical path length traversed by the light. Secondly, when light moves from one medium to another, the change in direction at the boundary of the two medium is dictated by the refractive indices of the two medium. Usually, refractive index of any medium is intimately related to the density of the medium. The theoretical basis for relationship between density and refractive index is embedded in the relationship between macroscopic dielectric (optical/electric) properties with microscopic molecular properties (e.g. molecular polarizability) known as Clausius Mossotti relationship [6]. In terms of refractive index (n) the relationship reads as

$$\frac{n^2 - 1}{n^2 + 2} = \frac{N\alpha}{3M} \rho_M \quad (1.1)$$

where, N is the Avogadro's number, α is the molecular polarizability, M is the molecular weight and ρ_M is the mass density.

The refractive index may also be related to the crystallographic structure of a material. Depending upon the method of preparation or process parameters of preparation technology a thin film of a particular composition may grow in different crystallographic structure or

phase. Since the packing density of different crystallographic structure are different, the structure is directly linked with the physical mass density of the thin film and hence with optical properties. For example, rutile phase of TiO_2 being denser than anatase phase of TiO_2 rutile phase exhibits higher refractive index (~ 2.6) compared to the anatase phase refractive index (~ 2.4) at 550 nm. Crystallographic structure or phase of grown thin film decides the density and hence optical properties of the samples.

(iii) Attenuation coefficient:

Attenuation coefficient of a medium dictates the amount of absorption of light when it interacts with the medium and this is linked with absorption coefficient (α) at any wavelength (λ), with a relation $\alpha = 4\pi k/\lambda$. Although for the development of interferometry based optical devices it is always preferred to choose almost fully transparent material, some amount of absorption of light is inevitable in a medium. Apart from fundamental absorption due to electronic transition from valence band to conduction band the absorption can take place due to free carriers, phonons, excitons and impurities [7]. Free carrier absorption takes place due to the presence of free electrons and holes, an effect that decreases with increasing photon energy. Exciton is an electron and hole pair excited by a photon and bound together through their attractive Coulombic interaction. Exciton absorption peaks are usually observed at low temperatures and are close to the fundamental absorption edge. Impurity absorption, which is usually related to the presence of ionized impurities or dopants, arises below fundamental (band-to band) and excitonic absorption. In addition, lattice absorption may take place due to the vibrations of the crystal ions. So, absorption coefficient of thin film largely depends upon various structural and compositional intricacies of thin film.

(iv) Dispersion:

The refractive index of materials varies with the wavelength (and frequency) of light. This is called dispersion and causes prisms and rainbows to divide white light into its constituent spectral colors. Dispersion also causes the focal length of lenses to be wavelength dependent.

For optics in the visual range, the amount of dispersion of a lens material is often quantified by the Abbe number [8].

$$V = \frac{n_{yellow} - 1}{n_{blue} - n_{red}} \quad (1.2)$$

Because of dispersion, it is usually important to specify the vacuum wavelength of light for which a refractive index is measured. Dispersion of material is an important factor which needs to be taken into account in every optical design which involves spectral range instead of single wavelength.

(v) Optical Band Gap:

Optical band gap refers to the absorption of light in a medium due to the fundamental electronic transition from valence band to the conduction band of the lattice in the medium. In a defect free crystalline semiconductor, there exists a well-defined energy gap between valence band and conduction band, which arises from the periodicity of the crystal. This gives rise to fundamental absorption edge in this kind of material. In contrast, in amorphous semiconductor, the valence band and conduction band of electronic states do not terminate in sharp edge rather tail states appear within the energy gap. In addition to the tail states, localized electronic states may appear due to the existence of defects [7]. Optical band gap of a material is a very primary property to be considered for qualifying the material to be a

constituent part of any optical device. For example, TiO_2 which has typical band gap of ~ 3.5 eV can not be a comprising layer of any UV mirror as TiO_2 itself will absorb all wavelength below ~ 365 nm.

(vi) Birefringence:

Birefringence is the optical property of a material having a refractive index that depends on the polarization and propagation direction of light. These optically anisotropic materials are said to be birefringents. Even though there are lots of applications of birefringent materials, the birefringence may be undesirable in various interferometry based optical devices. Crystallographic structural anisotropy is one of the reason that leads to optical anisotropy or birefringence in a medium.

(vii) Linkage of local structure with optical properties:

From so far discussion it is clear that the optical properties of nano structured thin film and hence the performance of thin film based optical devices are intimately related to the various physical properties of the thin films such as density, morphology, defects, crystallographic structure etc. So far as probing crystallographic structure is concerned, conventionally it is carried out by grazing incidence X-ray diffraction (GIXRD) technique, where X-rays are made incident on the thin film samples at a narrow grazing angle of incidence to enhance the interaction of X-rays with the thin film. However, in most of the cases it is very difficult to get good GIXRD data from these thin film samples which are mostly amorphous or polycrystalline in nature with small crystallites size. In this regard, X-ray Absorption Spectroscopy (XAS) qualifies to be a good alternative technique since it only probes the short range order in the samples and presence of long range ordering in the sample

is not required [9]. For example, the local structural information about crystallographic phase of thin film might be related with density and hence refractive index for poly crystalline or amorphous thin films. Secondly, expansion or contraction of bond distance, as determined by local structural probe, might be responsible for lower or higher density and hence refractive index of any material. Thirdly, local coordination number may give idea about the stoichiometry or compositional defect which determines the optical loss in the thin films system. Thus such investigation to find out any possible correlation among the optical and other macroscopic properties with the local structural behavior of the thin films seems absolutely sensible and important in research domain of thin film science and technology, which becomes feasible due to the advent of high intensity synchrotron radiation sources in recent time.

In this thesis work thus synchrotron radiation based XAS, which consists of both extended X-ray absorption fine structure (EXAFS) and X-ray absorption near edge structure (XANES) measurements have been extensively used for structural characterization of optical thin films. The methodology followed in the present work is as follows: (i) determination of macroscopic overall optical constants of the samples by transmission spectrophotometry, (ii) obtaining morphological information of the films from atomic force microscopy (AFM) and/or grazing incidence X-ray reflectivity (GIXR), and (iii) using these data to fit the spectroscopic ellipsometry results which yield information regarding the intrinsic optical properties of the thin film material. The variation of these intrinsic properties of the films with depositions conditions are then correlated with the structural information obtained from XAS measurements on the samples. The results have also been correlated with other complementary measurement techniques like Rutherford back scattering spectroscopy (RBS) wherever needed. The above scheme is pictorially depicted in fig. 1.3.

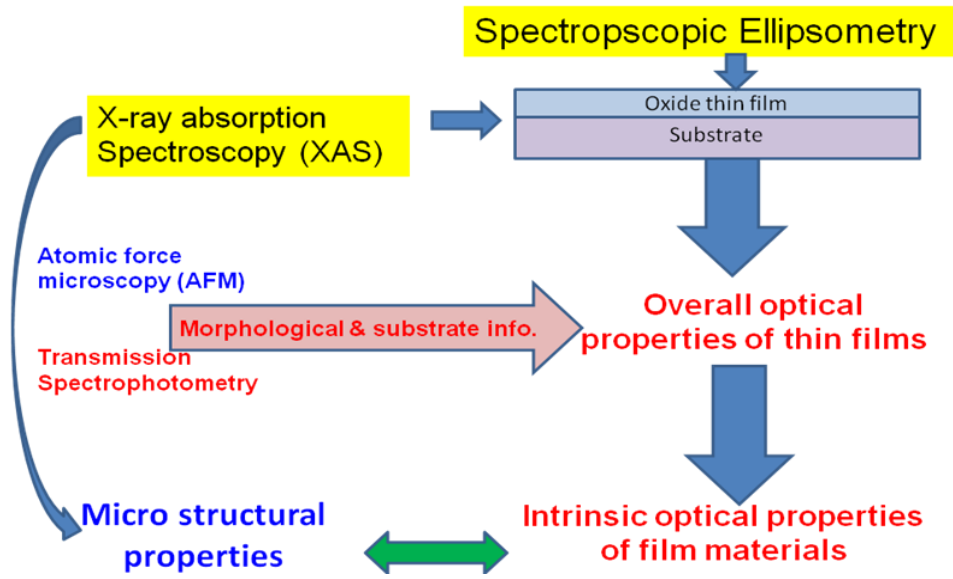


Fig. 1.3: Flowchart of this thesis work

In this thesis work, correlation of local structural and optical properties of refractory oxide thin films of HfO_2 , Ta_2O_5 , TiO_2 , Gd_2O_3 and Gd doped ZrO_2 deposited by sputtering techniques under different conditions have been described.

Hafnium oxide (HfO_2), is one of the most promising high k dielectric materials to replace SiO_2 in metal oxide semiconductor transistors [10-12]. Apart from its excellent high- k dielectric properties, hafnium oxide also qualifies to be an excellent optical coating material in the extended spectral region for high power laser applications. HfO_2 is fairly transparent in UV-Visible-near IR spectral range and has got considerably high band gap (~ 5.7 eV). Over the years, HfO_2 has been preferred as a high index coating material for fabrication of multilayer thin film devices [13] primarily due to its superior thermal and chemical stability [14-15] in contact with silicon and silicon oxides. Titanium dioxide (TiO_2) being a large band gap and high index material has also been of wide research interest for its application in multilayer optical interference coatings [16-17]. Excellent chemical stability of TiO_2 makes it an important choice for high index material in multilayer interference coatings

[18]. It has also been used in various semiconductor devices like in sensors [19], photo catalysts [20] and transistors [21-22]. Tantalum pentoxide (Ta_2O_5) has been the focus of research for optical and electronic devices due to its excellent refractive index and dielectric properties. Depending upon the process of preparation Ta_2O_5 exhibits optical band gap ~ 4 -4.2 eV and refractive index in the range 1.9-2.2 @ 550 nm. Tantalum pentoxide can be prepared in thin film form which exhibit a very low attenuation coefficient ($\sim 10^{-4}$) in the visible wavelength region of light i.e. they are optically transparent. Due to such excellent optical properties of Ta_2O_5 and its chemical compatibility with other optical materials it also finds applications as a comprising thin film layer in various types of multilayer thin film based optical devices [23]. Gadolinium oxide (Gd_2O_3) belongs to lanthanide rare-earth sesquioxide group which, in one hand is a potential gate oxide material due to its good chemical compatibility, lesser interface diffusion with silicon and higher dielectric constant ($k=14$) and on other hand is an excellent optical material covering a transmitting region from 190 nm to 1600 nm and having bulk high refractive index of ~ 1.80 @ 550 nm. Similarly, zirconia (ZrO_2) has been extensively studied in various forms due to its diverse applications such as a refractory material, oxygen sensor, bioceramic, or thermal barrier coating, amongst others [24-25]. Doped zirconia systems are especially important in catalytic applications, either as supports or as electrolytes in solid oxide fuel cells (SOFCs) [26-27]. Along with many other alternate dopants, Gadolinium (Gd) is one of the most promising dopants in ZrO_2 system on which several works have already been reported [28-29]. Due to its high transparency in the entire visible and near infrared region and stability with other refractory materials, ZrO_2 is also often used as a comprising layer in multilayer interference coating based optical devices [30] such as in anti-reflection coating, broadband interference filters and active electro-optical devices.

Several deposition techniques have been adopted to deposit optical films of desired optical and electronic properties including sputtering [31] sol-gel [32], atomic layer deposition (ALD) [33] etc. Ion beam assisted deposition (IBAD) [34] has also been used in a number of studies aimed to obtain high-quality optical films. Optical films produced by evaporation processes, barring ion assisted deposition, are generally porous [35] and therefore absorption of moisture in the voids causes refractive index to change under humid condition. Again, ion assisted deposition also poses limitation in developing large area coatings due to restriction in the sizes of available ion sources [36]. Magnetron sputtering, on the other hand, has got several advantages in achieving improved morphology, microstructure and interfaces [37-39] and thus is a highly preferred technique for surface sensitive deposition like of metal oxide semiconductors for device application. Compared to the RF magnetron sputtering technique which is generally adopted for sputtering of insulating oxide materials, the asymmetric bipolar pulsed DC (ABPDC) magnetron sputtering technique makes it possible to overcome the problem of accumulation of space charge through a relatively simpler way that does not need any critical impedance matching of the load and the power supply and helps in producing high-quality, low-defect oxide dielectric films required for precise coating processes [39-41]. Thus in this thesis work the optical thin films have been prepared using the above two deposition techniques. In a typical sputtering deposition technique, the percentage of oxygen present with respect to argon i.e. oxygen partial pressure acts as an important controlling parameter since it controls the stoichiometry of the deposited oxide samples and the deposition rate. Oxygen partial pressure decides the average sputtering efficiency since the sputtering efficiency of oxygen is less compared to argon. Apart from the above it also monitors energy of the sputtered species [42] reaching the substrate surface and thus in turn determines morphology and crystallinity of the films. Substrate biasing has also

considerable influence on the energy of ionic species present in the magnetron plasma and thus on the total energy delivered to the substrate [43] during deposition, thereby changing the growth process and thus may result in determining the optical and micro structural properties. Thus in this thesis work the oxide samples have been deposited under various oxygen partial pressures and with substrate biasing (in some cases) and their dependence on the structural and optical properties of the films have been investigated in detail.

Chapter-2 of the thesis deals with various experimental techniques used in this thesis work including the description of magnetron sputtering and Asymmetric Bipolar Pulse DC sputtering techniques. Apart from this, the various characterization techniques, their principles and the description of the equipments used including grazing incidence X-ray diffraction (GIXRD), grazing incidence X-ray reflectivity (GIXR), transmission spectrophotometry, spectroscopic ellipsometry (SE), atomic force microscopy (AFM) and Rutherford backscattering (RBS) techniques have also been described shortly in this chapter. Finally the synchrotron radiation based XAS technique, including both EXAFS and XANES, which has been used in this thesis work extensively have been discussed in details. In the following chapters (chapters 3-7) of the thesis the findings of the above characterizations on the HfO_2 , TiO_2 , Ta_2O_5 , Gd_2O_3 and ZrO_2 thin films prepared under various deposition conditions have respectively been described.

Study of laser induced damage mechanism and effort to increase the damage threshold of the above oxide thin films is of immense technological importance because as improved laser-damage-resistant optical materials and better fabrication technologies are developed, laser designers can increase the system operating energies and powers to the limits of these new materials. The study of these materials under laser irradiation is also important from the point of view of tailoring of material properties by purposeful laser

irradiation. Although, many efforts have been made to investigate how stoichiometry or long range order structure plays a role in describing the laser damage process, to the best of our knowledge, efforts to understand the local structural changes in the materials due to laser irradiation near around the damage threshold has not been made so far. In chapter-8 of the thesis, results of EXAFS and XANES measurements on laser irradiated refractory oxide samples near the damage threshold have been described. The above studies have been carried out on RF sputter deposited dielectric refractory oxide thin film samples of TiO_2 , Ta_2O_5 , HfO_2 and Gd_2O_3 each of approximately 200 nm thicknesses. Apart from XAS measurements, various other characterization techniques such as optical microscopic imaging, grazing incidence X-ray reflectivity and grazing incidence X-ray diffraction have also been employed to study the laser irradiated zones. Using these above studies, several interesting correlations between the laser irradiation processes near the damage threshold with various macro/micro structural properties of the samples could be established.

CHAPTER-2

Experimental Techniques

2.1 Introduction:

This chapter deals with various experimental techniques used in this thesis work. In the beginning of the chapter various deposition techniques used for preparation of thin film samples have been discussed. It is started with listing out different types of physical vapor deposition techniques and the advantage of sputtering technique, particularly magnetron sputtering technique that has been extensively used for preparation of thin film samples in the present study has been discussed. Subsequently different sputtering processes like DC magnetron, RF magnetron and Asymmetric Bipolar Pulse DC sputtering techniques have been shortly described. In the second part of this chapter, various thin film characterization techniques that have been employed to investigate the properties of thin films in this thesis have been briefly discussed. The techniques of grazing incidence X-ray diffraction (GIXRD), grazing incidence X-ray reflectivity (GIXR), transmission spectrophotometry, spectroscopic ellipsometry (SE), atomic force microscopy (AFM) and Rutherford backscattering (RBS) techniques have been described shortly. Finally the XAS technique, including both EXAFS and XANES, which has been used in this thesis work extensively have been discussed in details. It is started with various types of interactions of X-rays with matter and the theoretical basis of XANES and EXAFS techniques have been discussed in brief. The experimental procedures of carrying out XAS measurements using synchrotron radiation has

then been described including the two modes (transmittance and fluorescence) of XAS measurements with a brief description of the Energy Scanning EXAFS Beamline (BL-09) of INDUS-2 synchrotron source, RRCAT, Indore, India [44]. Finally, the analysis procedure of the EXAFS data starting with data normalization, transformation to k space, Fourier transformation and finally choice of appropriate model to fit the EXAFS data has been thoroughly described with a mention of the software codes used for the above purpose [45-46].

2.2 Thin Film Deposition Techniques

Since last many decades, thin film deposition technology has been increasingly popular subject primarily due to the fact that all microelectronic solid state devices are based on thin film deposition [47]. The successful applications of the technology to mitigate the requirements have been possible because of the improved understanding of the physics and chemistry of thin films, surfaces, interfaces, and microstructures. Over the time several dozens of deposition technologies have emerged out which can be classified broadly into four groups [47] such as evaporative, glow discharge, gas-phase chemical and liquid-phase chemical processes.

Sputtering technology falls under the group of glow discharge process. The electrode and gas phase phenomenon in various kinds of glow discharge forms the basis of such deposition technology. Apart from sputtering various other deposition technologies such as ion beam deposition, reactive ion plating, plasma enhanced chemical vapor deposition (PECVD), plasma oxidation, Microwave ECR plasma CVD etc. falls in this category of deposition technology. Sputtering is a phenomenon in which when an energetic ion bombards

on target surface it ejects atoms or molecules from the target surface by the process of momentum transfer.

All the samples in this thesis work have been prepared by a variant of sputtering technique called magnetron sputtering technique. Before going into the details of different variants of sputtering, it is important to understand the mechanism of sputtering process. Fig. 2.1 gives schematic representation of sputter deposition technology in its simplest form. As shown in this figure, the deposition material (called target) is subjected to high electric field in a closed chamber having evacuation facility by vacuum pump. During the process, the chamber is filled with inert gas like Argon (Ar). Ar gas ions, under the strong electric field applied between the two electrodes, collide with the target material and knock out the target species which traverse up side and settle on the substrate surface. This is how the whole

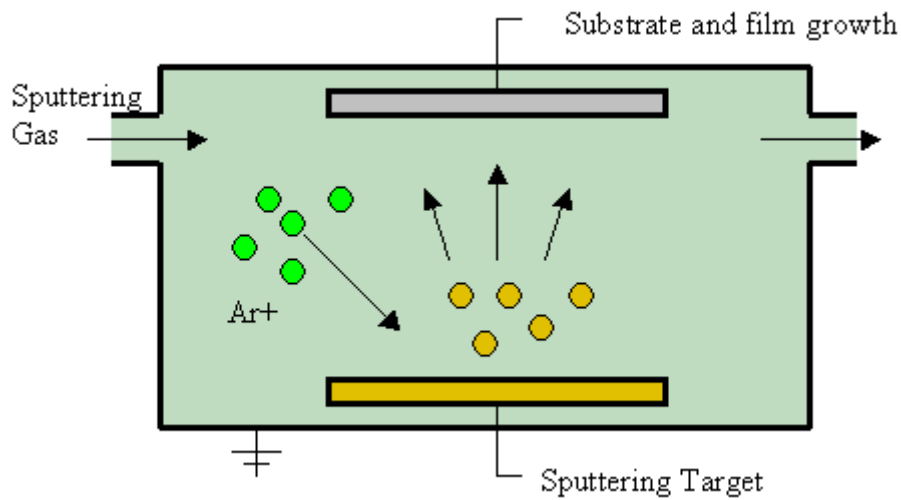


Fig. 2.1: Schematic representation of sputter deposition technology [48]

deposition process works. The physics of sputtering is perhaps best understood by momentum transfer theory [49]. According to this theory, the kinetic momentum of the incident ions are transferred to target surface atoms upon collision and a collision cascade (shown in fig. 2.2)

takes place within the top few layers in the material so that some of the target surface species get emitted out which is called sputtering.

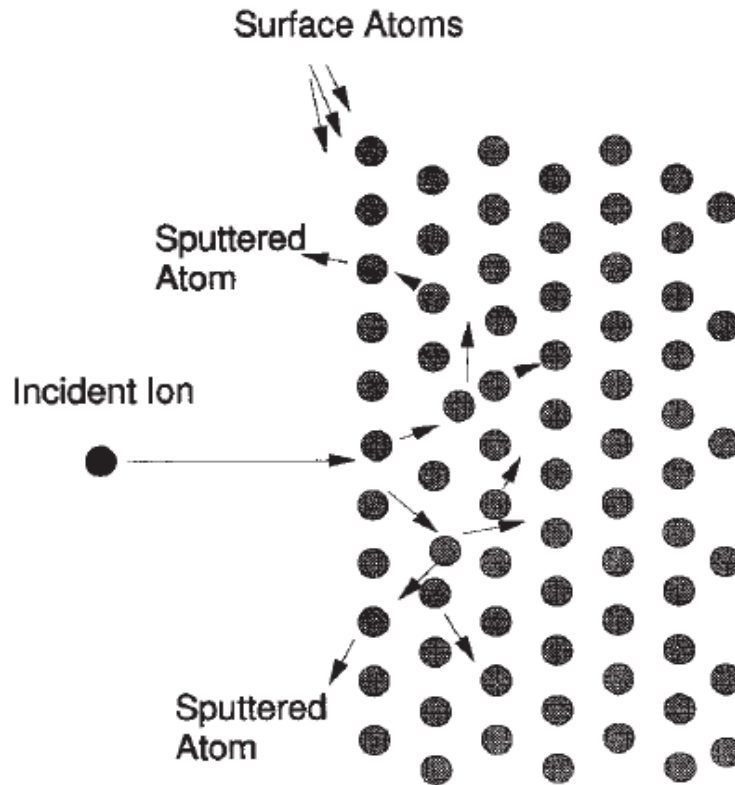


Fig. 2.2: Collision cascade in sputtering process [50].

The efficiency of sputtering is quantified by a term called *sputtering yield* which is defined as the average number of ejected target atoms/molecules per single ion hitting the target. The yield of sputtering depends upon several factors such as: (i) Ion and target atomic mass, (ii) ion energy, (iii) target crystallinity and (iv) angle of incidence.

The dependence of sputtering yield of several materials as a function of Ar ion energy is displayed in fig. 2.3.

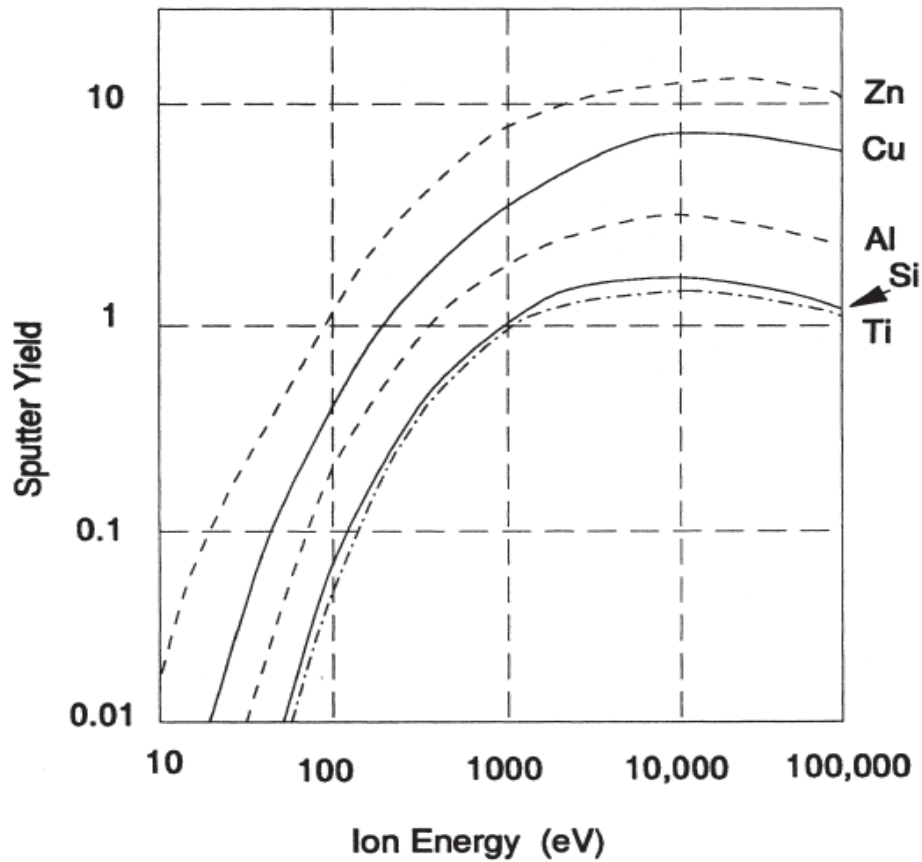


Fig. 2.3: Sputtering yield for several materials as a function of Ar ion energy [50].

The sequences of events in thin film deposition by sputtering process [51] are-

- (i) Generation of ions in plasma, (ii) Acceleration of ions in electric field between target (cathode) and substrate (anode), (iii) Sputtering of target through momentum transfer, (iv) Transport of sputtered material, (v) Adsorption of sputtered species to the substrate, (vi) Surface diffusion in substrate and (vii) Nucleation and thin film formation.

Generally a base pressure of $\sim 10^{-6}$ mbar is achieved prior to deposition and actual sputtering deposition is accomplished at pressure of $\sim 10^{-2}$ - 10^{-3} mbar. Here it should be mentioned that apart from thin film deposition, the concept of sputtering is also exploited in

Etching of targets: Microelectronics patterning, Depth profiling microanalysis etc.

Surface treatment: Hardening, Corrosion treatment etc.

There are various types of sputtering, viz., (i) DC sputtering or diode sputtering, (ii) radio frequency (RF) sputtering, (iii) pulse DC sputtering, (iv) reactive sputtering and (v) magnetron sputtering

2.2.1 DC Sputtering:

In DC sputtering the target is held with constant negative DC potential and the corresponding positive terminal is grounded and the substrate as well as the chamber wall is also grounded. So, the DC sputtering process is similar to DC glow discharge. Fig. 2.4 displays voltage current characteristic in entire electric discharge regime which can be distinguished from each other in three regions namely dark discharge, glow discharge and arc discharge. The abnormal glow discharge region as shown in this figure is exploited in the process of DC sputtering.

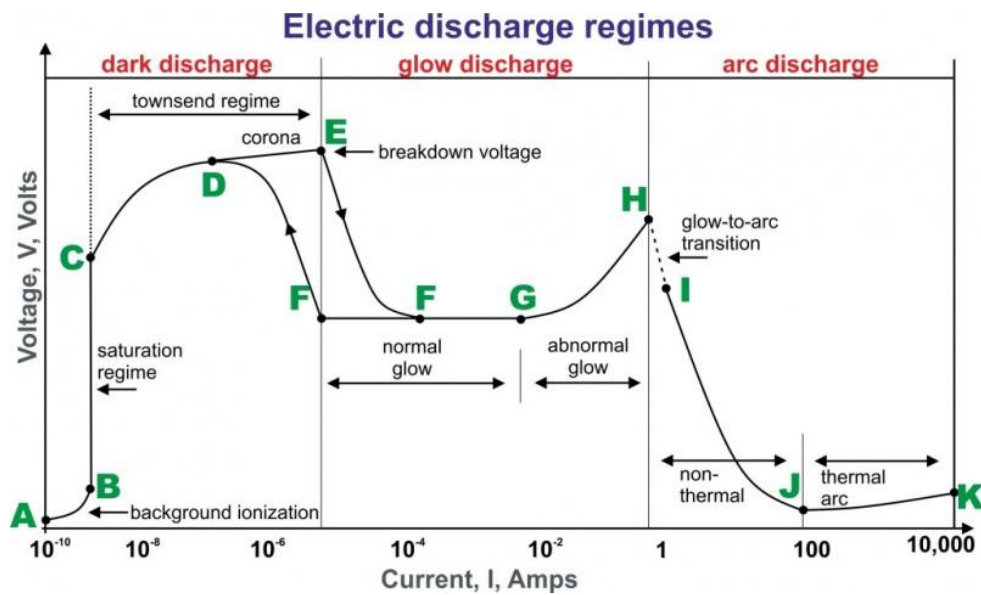


Fig. 2.4: Different electric discharge regime in DC glow discharge [52].

The deposition rate in DC sputtering is very much affected by the pressure of gas in chamber. As the pressure increases, the electron mean free path decreases, more ions get generated, cathode sheath becomes narrower; the chance of ions getting absorbed in the wall

reduces. All these causes discharge current to increase with increasing gas pressure which in turn favors high deposition rate. On the other hand, due to increased collisional scattering of sputtered atoms with the increase in pressure, the deposition rate decreases. Therefore, the combined effect is, the deposition rate is maximum in a defined range of gas pressure for a given system. In general, deposition rate is proportional to the power consumed and the square of current density and inversely dependent on the electrode spacing. Fig. 2.5 shows the dependence of deposition rate on gas pressure which bears the combined effect due to discharge current and sputtering yield.

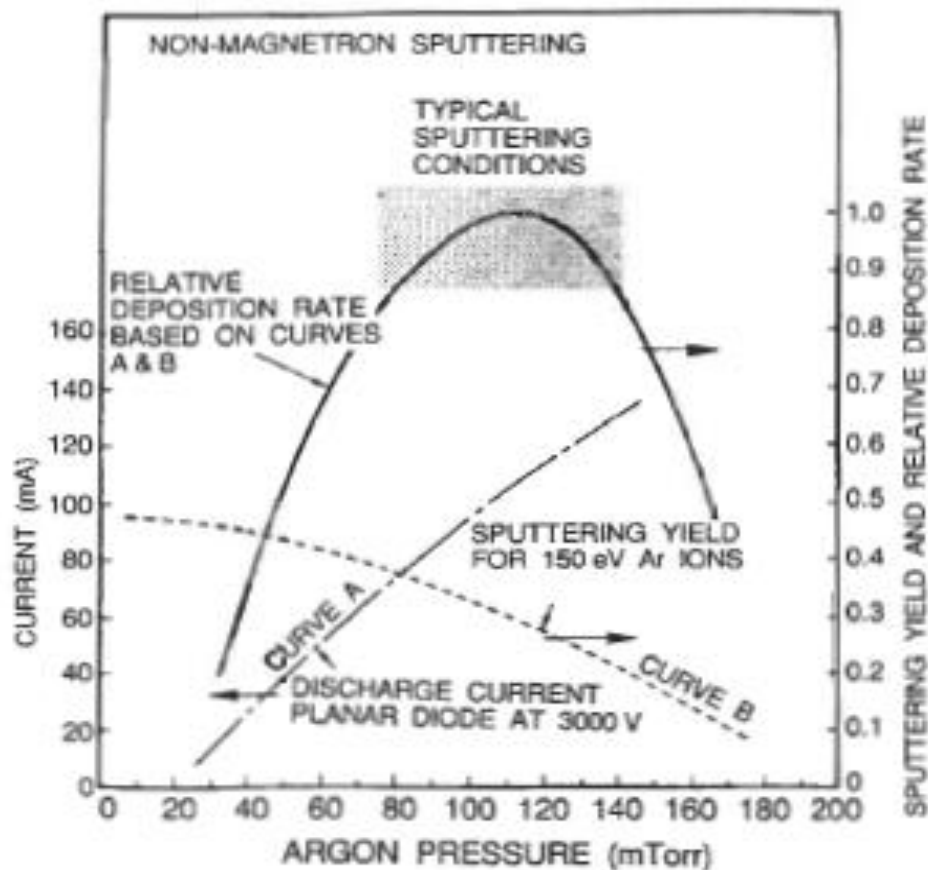


Fig. 2.5: Dependence of deposition rate on gas pressure for non-magnetron sputtering [53].

In DC sputtering, there is a low concentration of secondary electrons. So, there will be fewer collisions in the plasma and large voltage is required to sustain the plasma. DC sputtering is only effective for deposition of conductive materials. Typical ion currents striking the cathode are on the order of 1 mA. cm^{-2} . To draw a current density, J through a target of thickness, t and resistivity, ρ the cathode needs a voltage given by $V = \rho t J$ [53]. Hence, if we want to deposit quartz, even if we use a very thin quartz target of thickness 1 mm, quartz resistivity of $10^{16} \Omega\text{-cm}$ would require applying as high as 10^{12} Volts to create 1 mA. cm^{-2} current. This cannot be achieved in practice. This is why DC sputtering cannot be used for deposition of quartz or any insulator. For the same reason, for a given cathode voltage DC sputtering requires higher chamber ambient pressure for the sustenance of the plasma.

2.2.2 RF Sputtering:

The problem of DC sputtering of insulating material is solved in RF sputtering by a mechanism called the ‘self bias’ mechanism. In this process, an alternative electric field of megahertz frequency is applied to the target. In the presence of this alternating field both electrons and ions in the plasma oscillate and alternatively hit the target surface. However due to the fact that electrons are lighter in mass than ions, during positive cycle of RF field more numbers of electrons reach the target surface than ions in the negative half cycle. As a consequence, a net negative potential is produced in front of the target surface which drives positive ions towards the target surface and repels electrons in opposite way. This is called self biasing of the target. Once this happens, it behaves as a DC target where positive ions continuously bombard the target surface and sputtering takes place. In fig. 2.6, the development of self bias has been demonstrated from current-voltage characteristic of

plasma. It can be seen from fig. 2.6(a), the RF signal being applied to the target would create a net current through the plasma which is not possible through the capacitor. As a consequence, the operating point in the I-V characteristic shifts to the negative voltage (as shown in Fig. 2.6 (b)) so that net current becomes zero.

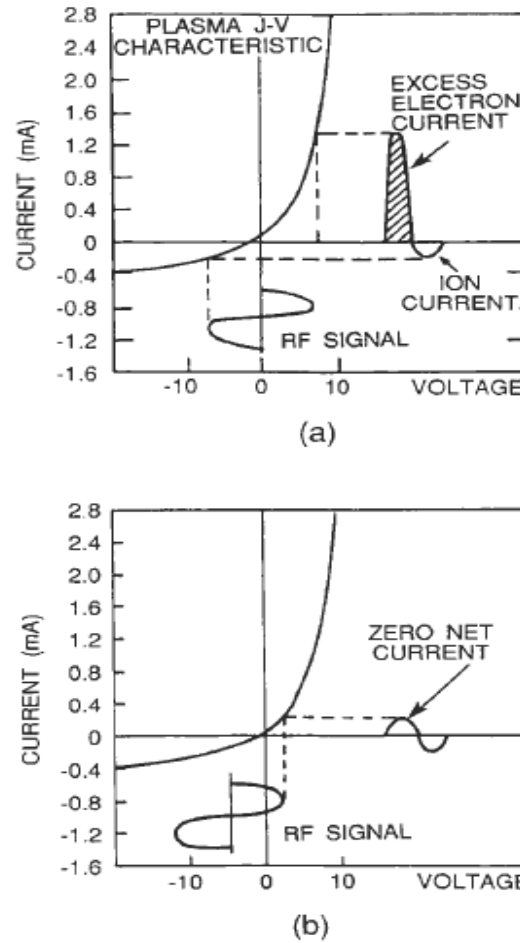


Fig. 2.6: Formation of self bias sheath on target during RF Discharge (a) net current/zero self-bias voltage (b) Zero current/nonzero self bias voltage [53].

For AC field of frequency less than 50 kHz, both electrons and ions can follow the switching of the anode and cathode and no self bias gets produced. Essentially below 50 kHz frequency, the DC sputtering conditions prevail at both the electrodes. On the other hand, above ~50 kHz, two important things happen. At high frequencies, electrons oscillating in the glow region acquire sufficient energy so that requirement of secondary electron is reduced to

sustain the plasma. Secondly, it becomes possible to couple RF to any high impedance without requiring the electrodes to be conductor. Typical RF frequency exploited for this purpose is in the range of 5-30 MHz. In practice, 13.56 MHz is used due to government communications regulations (International Telecommunications Union).

One notable point here is, the sheath potential get developed on both the electrodes. But since the surface area of target electrode is much less than the opposite electrode consisting of substrate, base plate, chamber wall etc., the self bias potential developed near target surface is much greater than the other. In principle, the self bias developed near any electrode is inversely proportional to the forth power of electrode surface area i.e. $V \propto A^{-4}$.

2.2.3 Pulse DC sputtering:

This is a relatively new and novel technique [54] in which the target is powered by an alternative DC power supply in mid frequency range. The power supply offers a rectangular waveform with its negative cycle having amplitude of typically few hundred volts and positive cycle having amplitude of typically 25-50 volts. The negative cycle is responsible for attracting the positive sputtering ions and ejecting the target species in atomic, molecular and ionic forms as usual like DC sputtering. In the process, some of the ions while colliding with target may leave their positive charges on the target surface. These positive charges being accumulated on the target surface over some time would create an electric field so as to repel further positive ions to reach to target surface and ultimately stops the sputtering. This process of positive charge accumulation on the target surface is known as surface poisoning. The positive cycle of the applied power plays an important role in overcoming the problem of target surface poisoning by showering the target with electrons which neutralizes the charge

buildup [55]. This also inhibits the possibility of formation of arc. Usually the required time period of positive cycle for removing the charge build up is not same as the time period of negative cycle in which the sputtering phenomenon takes place. That's why, an asymmetric form of power supply with varying pulse on/off time and pulse frequency is employed for this purpose, also called asymmetric bipolar pulsed DC (ABPDC) sputtering. As the ABPDC discharges target in mid-frequency ranges up to few hundred kHz and uses a positive voltage of only 25–50V for target surface neutralization, it prevents back sputtering and thus results in relatively smoother films as compared to that of the other deposition processes. Bipolar pulsed DC sputtering technology also offers larger degree of freedom due to available tunability features of pulse frequency, pulse width, pulse power etc. of the bipolar pulsed DC power supply and does not have stringent requirement of impedance matching as is required in case of RF power supply.

2.2.4 Reactive sputtering:

Reactive Sputtering [57] is a variant of sputtering technique in which a target of one chemical composition (e.g. Ti) is sputtered in the presence of a gas or a mixture of gasses (e.g. Ar + O₂) that will react with the target material to form a coating of a different chemical composition (e.g. compound TiO₂). Argon is in most cases the primary gas responsible for sputtering and the amount of a reactive gas introduced into a process chamber is controlled either to achieve certain amount of doping or produce a fully reacted compound. Reactive gas is a type of gas which undergoes chemical reactions with materials in contact. Gases that are inert in ambient conditions (e.g. molecular N₂) become reactive when present in a plasma discharge due to collisions with energetic particles and subsequent dissociation into atomic neutral (e.g. N) and charged (e.g. N⁺, N⁻, N₂⁺) components. Most often used reactive gasses

are oxygen (O_2), nitrogen (N_2), carbon dioxide (CO_2), acetylene (C_2H_2), methane (CH_4). Several reactive gasses can also be mixed (e.g. $O_2 + N_2$) in order to deposit multi-component functional thin films, such as oxy-nitrides (e.g. Cr-O-N) or oxy-carbides (e.g. Si-O-C).

2.2.5 Magnetron sputtering:

In DC, RF or PDC sputtering process discussed above, the secondary electrons have relatively longer mean free path (10's cm) and that's why the processes suffer from inefficient secondary electron process and thereby low ionization levels. This leads to slow etching of target surface and therefore lower deposition rate. To increase the efficiency of secondary electron generation, in magnetron sputtering a magnetic field is applied parallel to the target surface which helps in increasing the deposition rate dramatically. Typically in magnetron sputtering an order of magnitude higher deposition rate can be achieved in compared to conventional sputtering technique and presently, magnetron sputtering is the most widely commercially practiced sputtering technique.

As shown in fig. 2.7, in planer magnetron configuration the magnetic field is applied parallel to the target surface i.e. perpendicular to the applied electric field. When the secondary electrons near the target surface encounters this crossed electric and magnetic field, the field drives the electrons in helical motion and electrons hop on the target surface as shown in the figure. In absence of magnetic field these electron would have escaped from the target and reach to the plasma bulk or hit the anode surface. These revolving electrons will collide with the ions in the cathode dark space for a longer time and increases the ionizing efficiency and in turn causes more sputtering and thus increases the deposition rate. Usually, a magnetic field of $\sim 200 - 500$ G is applied to contain the secondary electrons, and therefore the plasma, close to the cathode. Deposition rate increases up to 10-100 times higher than

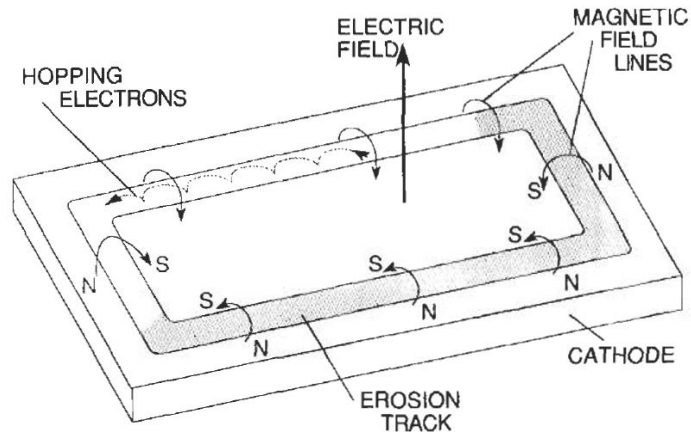


Fig. 2.7: Applied field and electron motion in planer magnetron [53]

without magnetron configuration and deposition rate as high as $1 \mu\text{m/min}$ [53] has been possible to achieve in magnetron sputtering. The advantages of magnetron sputtering compared to conventional sputtering are (i) Increased ionization ($n_i/n \sim 10^{-4}$ to 10^{-2}), (ii) higher plasma density ($n_i \sim 10^{11} \text{ cm}^{-3}$), (iii) increased ion bombardment ($4\text{--}60 \text{ mA/cm}^2$), (iv) higher deposition rates ($\sim 1 \mu\text{m/min}$ for Al), (v) lower Ar pressures ($0.5 - 30 \text{ mT}$), (vi) lower DC ($300 - 700 \text{ V}$) or RF voltages ($< 500 \text{ V}$ amplitude).

Depending upon the distribution of magnetic field on target there can be two types of magnetron sputtering-, viz., balanced and unbalanced magnetron sputtering technique. In balanced magnetron configuration the central pole magnet and ring magnet below the target surface has equal strength and there is no resultant magnetic lines of force along the perpendicular to the target surface where as in unbalanced magnetron configuration, the two magnets are intentionally kept of unequal strength so that there is resultant magnetic lines of force along perpendicular to the target surface. Fig. 2.8 shows the typical distribution of magnetic field lines in balanced and unbalanced magnetron configurations. In unbalanced magnetron, the resultant magnetic lines of force along perpendicular to the target surface

helps in extending the plasma length towards the substrate surface which increases the substrate current and improves the coating quality.

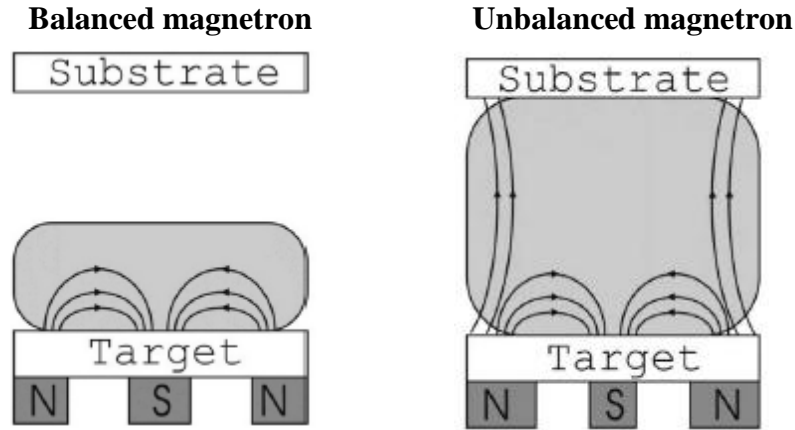


Fig. 2.8: Magnetic field lines of balanced and unbalanced magnetrons [57]

Finally, the main advantages of sputtering compared to other thin film deposition techniques are (i) higher energy of sputtered particles compared to energy of evaporated adatoms, (ii) higher surface mobility in condensing particles, (iii) possibility of large area deposition, (iv) feasibility of alloy sputtering with required stoichiometry due to smaller difference in sputtering yields among elements of alloys compared to the difference in vapor pressure, (v) lower substrate temperature, (vi) feasibility of sputtering the materials with high melting point and (vii) better adhesion.

2.3 Deposition systems used in this thesis work:

For all depositions of thin film samples studied in this thesis work one in-house built DC/RF magnetron sputtering system and another custom made DC/RF/Pulse DC sputtering system present in AMPD, BARC, Visakhapatnam Centre have been used. In all cases, prior to deposition a base vacuum of $\sim 10^{-6}$ mbar was archived while the actual deposition has been commenced at Ar/O₂ gas pressure of $\sim 10^{-3}$ mbar. The target to substrate distance is kept at 60

mm. The substrates are kept at ambient during deposition. However, it has been observed that substrate temperature reaches up to 60-80°C during the process of deposition. Both the deposition systems are briefly discussed below with mention of technical specifications of major components.

2.3.1 In-House Built DC/RF Magnetron Sputtering System:



Fig. 2.9: In -house built DC/RF Magnetron Sputtering System at AMPD, BARC-Visakhapatnam Laboratory

This system consists of two magnetrons cathodes (make-Edwards) of 3” diameter, each of which can be powered by either RF power supply (Make-Huttlinger, Max 1.5 kW) or DC power supply (Make-Millman, Max. 2.5 KW). The vacuum chamber is evacuated using a turbo molecular pump (Make:Alcatel) with backing Rotary pump (Make: Alcatel). The vacuum chamber is equipped with one pirani (Make:HHV) and penning gauge (Make:Pfeiffer) for monitoring the chamber pressure. A quartz crystal thickness monitor (Make: Inficon) is provided to monitor deposited thickness online. Cold water supply is provided with a custom made chiller in order to cool power supply, magnetron, quartz crystal

head etc. Fig. 2.9 shows the picture of this dual magnetron in-house built sputtering system. This system can be used for the deposition of both metallic and dielectric samples.

2.3.2 Custom Made DC/RF/Pulse DC Magnetron Sputtering System:



Fig. 2.10: Custom Made DC/RF/Pulse DC Magnetron Sputtering System at AMPD, BARC-Visakhapatnam Laboratory

This system (Make: M/s., Advance Process Technology (APT), Pune, India) consists of three numbers of 3 inch magnetron cathodes and two numbers of 6 inch magnetron cathodes each having pneumatic control shutter assembly. It is equipped with a rotating substrate assembly having multi-position substrate holder including heating arrangement inside it. Quartz crystal monitor has been provided to each cathode to measure film thickness deposited on the substrate and all these quartz crystal monitors are connected with a Maxtek make MDC 360 thickness controller. The system is provided with turbo molecular pump backed by a rotary pump and the pumping system is isolated from the chamber with a stepper motor driven gate valve. The system is also equipped with a Pirani Gauge (Make: HHV,

India), one compact capacitance gauge (Make: Pfeiffer, Germany) and one full range gauge (Make: Pfeiffer, Germany). Cooling system is provided with chiller to cool each magnetron, each quartz crystal, turbo molecular pump and vacuum chamber. One heater tank is also provided with P-U Tubing connections to heat the vacuum chamber for baking to achieve high vacuum. The actual photograph of the system is shown in fig. 2.10.

It has got three mass flow controllers (make-MKS) for argon, oxygen and nitrogen gas and has facility to heat the substrate up to 400⁰C. Cathodes can be powered with a bipolar pulsed DC power supply (10KW max.), a DC power supply (3KW max.) or a RF power supply (1KW max). The bi-polar pulsed DC power supply (MKS/ENI make, model RPG-100) installed in this system has maximum power output of 10 kW and it has a fixed reverse bias of +37V, whereas the negative voltage can be varied from 0 to -800V. That's why it is called Asymmetric Bi-polar Pulse DC (ABPDC) power supply. DC or RF sputtering has only one key parameter to change the sputtering rate by its power to the cathode whereas in bi-polar pulsed DC sputtering system one has pulse frequency, pulse width and power as controlling parameters.

The waveform of the power supply is shown in fig. 2.11 where pulse frequency can be varied in the range of 50 to 250 kHz and pulse width can be varied from 496 to 8016 ns at 50 kHz pulse frequency and from 496 to 1536 ns at 250 kHz pulse frequency. So, overall, the duty cycle (defined in the inset of fig. 2.11) can be varied in the range of ~2 to 40 % to tune the deposition dynamics and control the arcing and deposition rate. The arc free and high sputtering rates for TiO₂, SiO₂ and other oxide targets could be achieved by varying the negative voltage in the typical range of -400 to -700V. The system also has the flexibility to use any power supply to not only cathodes for sputtering but also to the substrate assembly for biasing.

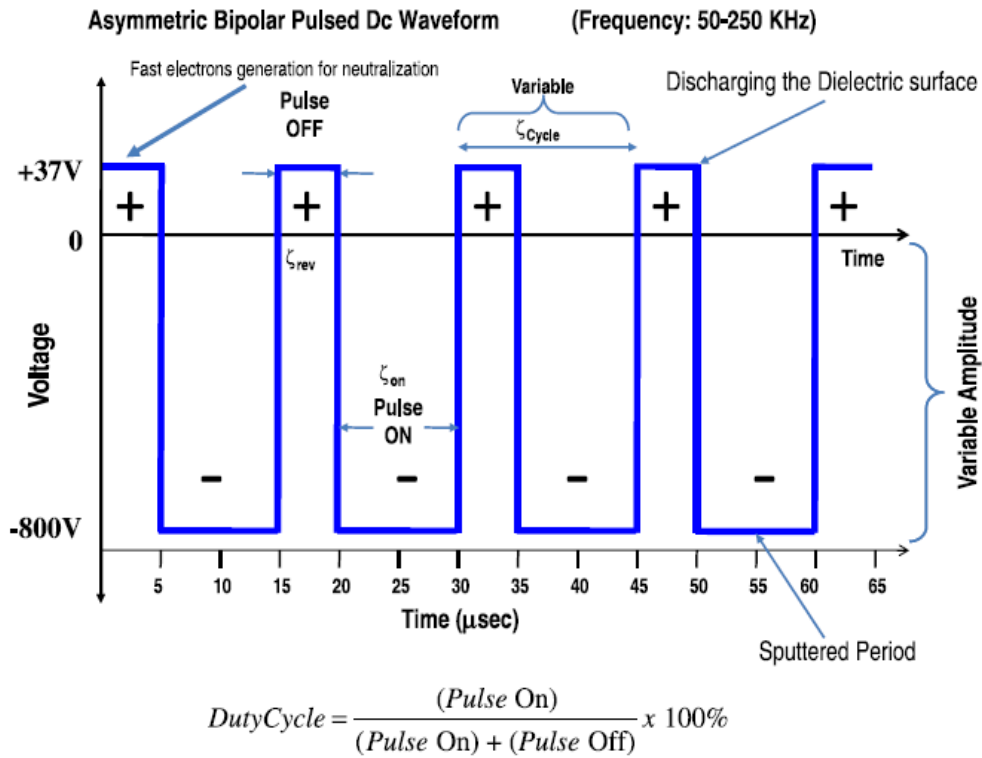


Fig. 2.11: Waveform of ABPDC power supply installed in sputtering system [36]

2.4 Thin film characterization techniques:

In this thesis, the deposited thin film samples have been characterized by grazing incidence X-ray diffraction (GIXRD), grazing incidence X-ray reflectivity (GIXR), transmission spectrophotometry, spectroscopic ellipsometry (SE), atomic force microscopy (AFM) and Rutherford backscattering (RBS) apart from synchrotron radiation based extended X-ray absorption fine structure (EXAFS) and X-ray absorption near edge structure (XANES) techniques. In the following, the above techniques are discussed briefly.

2.4.1 Grazing incidence X-ray diffraction:

Grazing incidence X-ray diffraction (GIXRD) is specifically used for investigating structural properties of thin films coated on bulk substrates. In contrast to wide angle X-ray

diffraction where angle of incidence $>10^\circ$, here the X-ray beam is made incident on the sample at a fixed grazing angle of incidence. This is to ensure that the penetration depth of incident X-ray lies almost within the thickness of the thin film so that X-rays will interact mostly with the thin film and not with the underlying substrate. To collect the GIXRD pattern for thin film, the grazing angle of incidence of X-rays is kept fixed and the diffracted X-ray is measured in the wide angular range by rotating the detector arm across the intended angular range. This is often called as detector scan mode of measurement. One of the prime difference of detector scan mode with conventional θ - 2θ mode of XRD measurement is that in θ - 2θ mode, only the family of crystallographic planes which are parallel to the sample surface can take part in diffraction whereas in detector scan mode (2θ mode), all the crystallographic planes in the sample takes part in diffraction. Fig. 2.12 shows the photograph



Fig. 2.12: Photograph of GIXRD instrument in AMPD, BARC, Visakhapatnam laboratory

of GIXRD instrument in AMPD, BARC, Visakhapatnam laboratory. The schematic of grazing incidence X-ray diffraction measurement configuration is shown in fig. 2.13. One of the prerequisite for recording noise free GIXRD measurement is that incident X-ray beam should be sufficiently collimated. Otherwise the X-ray beam will have spread of incident angle rather than having a definite well-defined angle of incidence. Monochromatic Cu K $_{\alpha}$ X-ray being originated from X-ray tube is collimated using collimating mirror by cross beam optics (CBO) technique. X-rays diffracted from the sample is passed through a soller slit and

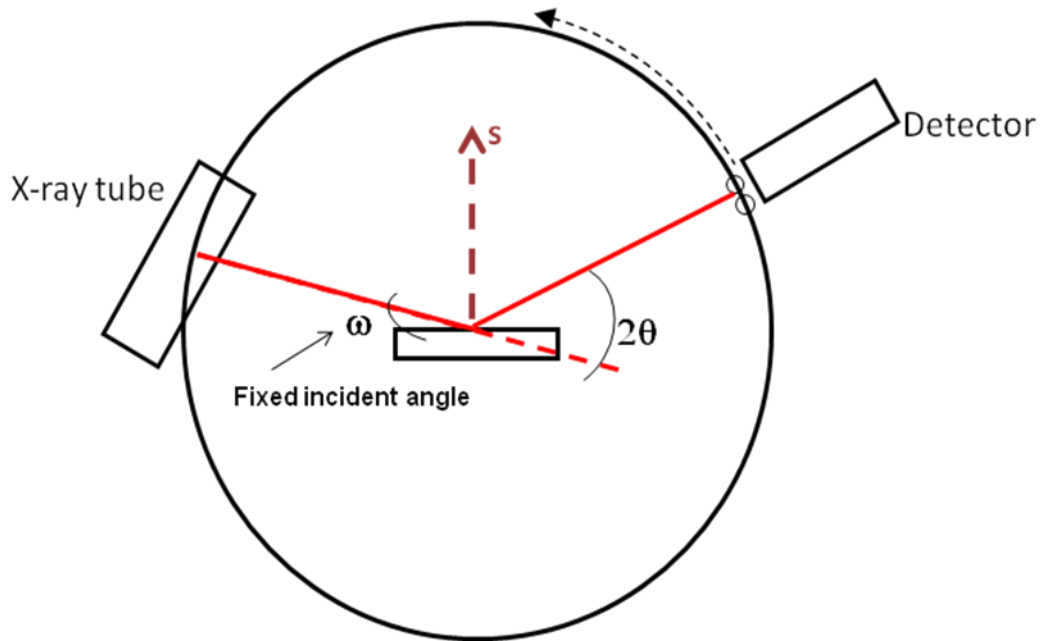


Fig. 2.13: Schematic of GIXRD set-up in 2θ scan mode

detected by a scintillation detector followed by photomultiplier tube. During scan in the detector scan mode, all the parallel planes of atoms, with interplanar spacing d_{hkl} , will form constructive interference when the following law (known as Bragg's law) is satisfied

$$2d \sin \theta_{hkl} = n\lambda \quad (2.1)$$

Here X-ray wavelength λ is fixed and n is a positive integer and represents the order of diffraction. So, the diffraction angle θ_{hkl} gives the knowledge of all the family of crystallographic planes in the specimen or in other words will give the specimen's crystallographic structure. In practice, as shown in fig. 2.14 the GIXRD pattern of thin film samples consist of broad peaks instead of being very sharp peaks which arises predominately

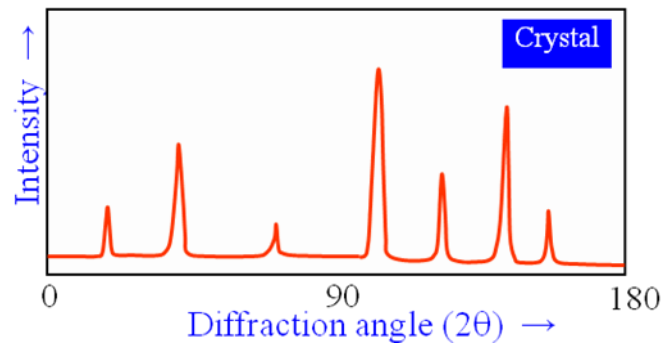


Fig. 2.14: Typical GIXRD spectrum of thin film sample

due to finite size of crystals or ordering present in the thin film sample. Of course peak broadening can be due to lattice strain or due to the instrumental error also. After proper elimination of the contribution from other factors for peak broadening, the corrected peak angular width can be utilized for computing the average crystallite sizes present in the specimen using Debye Sherrer formula [58] as given below:

$$L = \frac{0.9\lambda}{B \cos \theta} \quad (2.2)$$

Where, B is the peak FWHM in radian, θ is the Bragg angle and λ is the wavelength of incident X-ray.

2.4.2 Grazing incidence X-ray reflectivity:

Grazing incidence X-ray reflectivity (GIXR) is another important X-ray based technique used for precise determination of thin film thickness, density and surface and interface roughness. The basic principle of the technique is to measure the specular reflectivity of X-ray in the range of grazing incidence angle (typically between 0-3°). The measurement is carried out in grazing angle of incidence since the reflectivity of any material gets reduced dramatically beyond a small grazing angle, known as critical angle as shown in fig. 2.15. GIXR measurements are generally carried out in same equipments where GIXRD measurements are done.

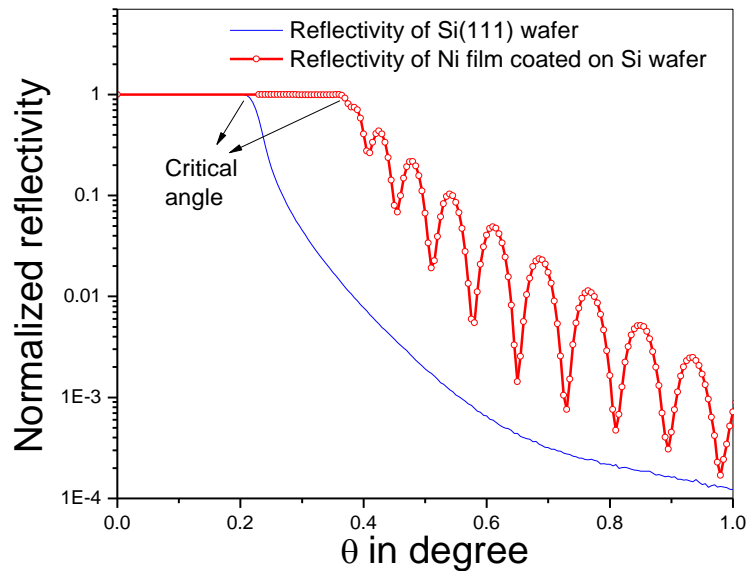


Fig. 2.15: Reflectivity vs. grazing angle of incidence curve

The basic theory of X-ray reflectivity is derived from classical optics and Fresnel theory, modified slightly for X-ray. The complex refractive index (η) of an element in the X-ray region is given by [59]-

$$\eta = 1 - \delta - i\beta \quad (2.3)$$

where,

$$\delta = \{(r_0 \lambda^2) / 2 \pi\} N_A (\rho Z / A_w) \quad (2.4)$$

and $\beta = (\mu \lambda / 4 \pi) \quad (2.5)$

where, r_0 is the classical electron radius (2.82×10^{-13} cm), N_A is the Avogadro number, ρ is the density, Z is the atomic number and A_w is the atomic weight of the element and μ is the linear absorption coefficient of the material at the particular wavelength λ . The quantity $[N_A (\rho Z / A_w)]$ actually gives the number of electrons per cm^3 of the particular element.

Since for all materials in the X-ray regime, $\eta < 1$, at very low grazing angle of incidence, X-ray suffers total external reflection from any surface and the reflectivity is almost ~ 1 . However, for the grazing angle of incidence above the critical angle (θ_c), X-ray starts to penetrate inside the layer and reflectivity starts to fall off rapidly. The critical angle is approximately given by the following expression:

$$\theta_c = \sqrt{2\delta} \quad (2.6)$$

$$\text{or, } \theta_c = \sqrt{\frac{r_0 \lambda^2}{\pi} N_A \frac{\rho Z}{A_w}} \quad (\text{combining equation (2.4) and (2.6)})$$

So with an apriori knowledge of the atomic number and atomic mass of the sample it is possible to estimate the physical density of the sample by measuring critical angle. If the

sample is a thin film coated on a thick substrate, the reflectivity tail shows oscillatory behavior (as shown in Fig. 2.15) due to interference between X-ray reflected from top surface with that reflected from film-substrate interface. By carefully analyzing these interference oscillations, the thickness of the thin film can be estimated.

Beyond critical angle, X-rays start penetrating inside the layer and the reflectivity falls off at a rate defined by the absorption of the sample. However, if there is any surface roughness, the Fresnel's reflectivity gets modified by a “Debye-Waller-like” factor as follows:

$$R_0 = R_p \exp\left(-\frac{q^2 w^2}{2}\right) \quad (2.7)$$

where, q is the momentum transfer factor ($=4\pi\sin\theta/\lambda$), R_0 is the reflectivity of the rough surface, R_p is the reflectivity of an otherwise identical smooth surface and w is the r.m.s. roughness of the surface. In case of an interface, the above quantity (w) is called the interface width which includes the contribution of both interfacial roughness and interfacial diffusion.

Thus by analyzing X-ray reflectivity data measured at grazing angle of incidence over a range of angle (typically $0-4^\circ$ in 2θ) it is possible to estimate thickness, density, surface and interface roughness of thin films. Displayed in fig. 2.16 is the screenshot of commercially available grazing incidence X-ray reflectivity data analysis software, Global Fit [60] which has been used to compute various quantities from GIXR data measured in the context of this thesis work.

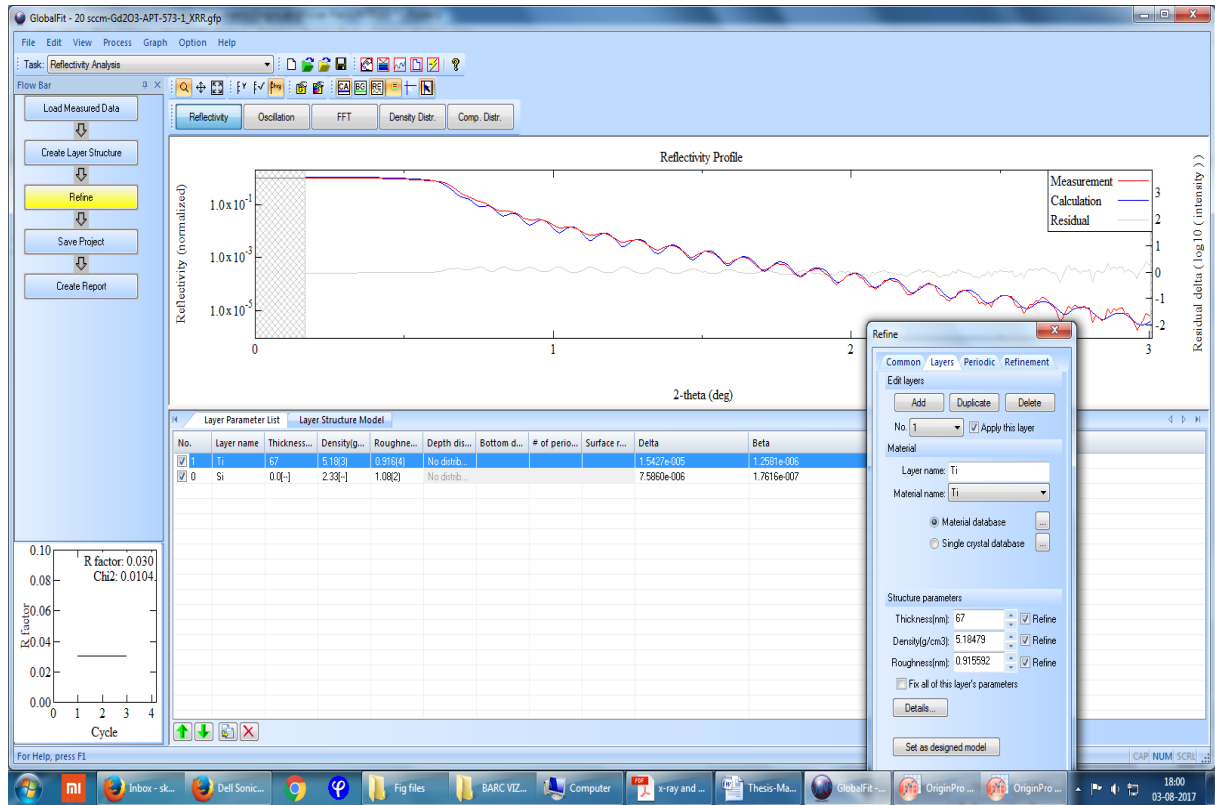


Fig. 2.16: Screen shot of 'Global Fit' analysis software

In few cases in this thesis, the X-ray reflectivity data has been analyzed using the IMD computer program [61]. IMD is a computer code that can calculate specular and non specular reflectivity of single layer and multilayer structure of any number of layers and for any material, whose optical constants are known, using Parratt formalism. This program works under XOP (X-ray Oriented Programming) platform and it can also fit the experimentally measured X-ray reflectivity spectrum of a sample and estimate the optical parameters and sample structure [61]. Under the Parratt's formalism [62] the reflectivity of X-rays from a plane boundary between two media can be obtained using Fresnel's boundary conditions of continuity of the tangential components of the electric field vector and its derivative at the interface.

2.4.3 Transmission spectrophotometry:

Transmission spectrophotometry relies on the measurement of ratio of transmitted to incident light intensity over a given spectral range. Usually the measurement is carried out at 90° angle of incidence. The transmission spectrum of semi transparent thin film samples coated on transparent substrate such as glass substrate usually yields spectral interference oscillations and shows several maxima and minima within the spectral range which is used to estimate thickness and optical constants of such thin film.



Fig. 2.17: Photograph of Jasco (V-630) spectrophotometer at AMPD lab, BARC, Visakhapatnam

Fig. 2.17 shows the photograph of spectrophotometer equipment at AMPD, BARC, Visakhapatnam laboratory while the schematic of the equipment is shown in fig. 2.18. It operates in the wavelength range of 190 to 1100 nm. In this equipment, two light sources namely deuterium lamp (190 to 350 nm) and halogen lamp (330 to 1100 nm) is used to cover the whole spectral range and silicon photodiode detector is used to measure the output light intensity. A single monochromator of concave grating (1200 lines/mm) is used to scan the wavelength.

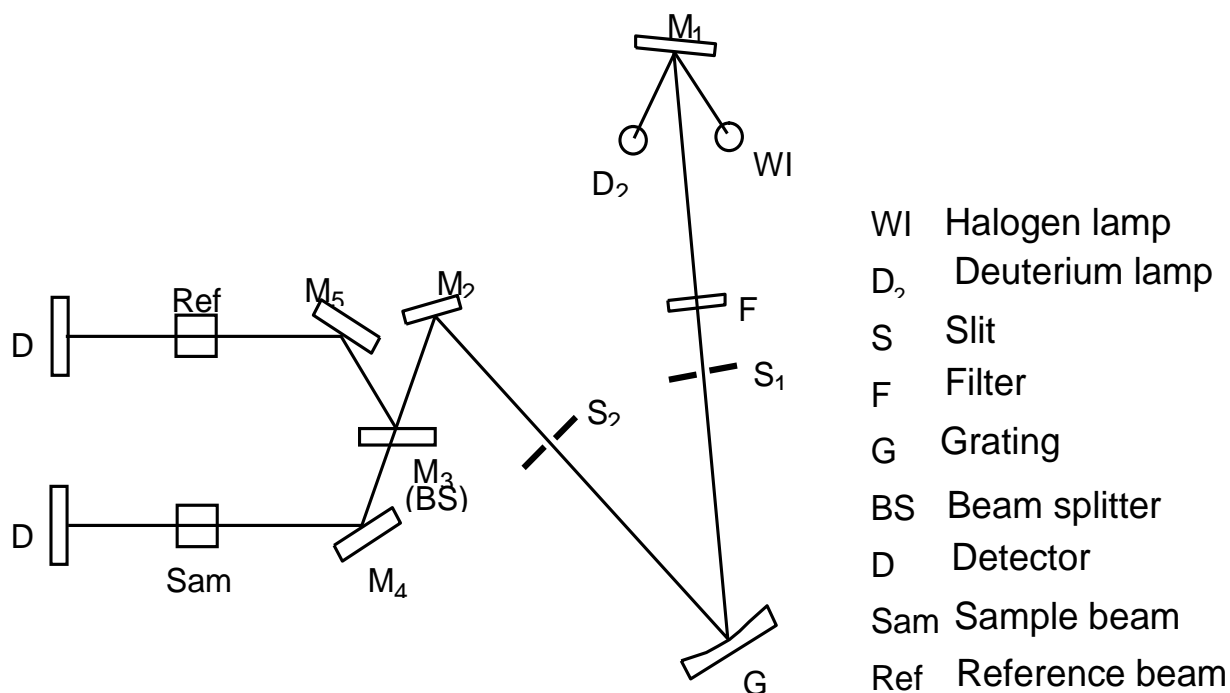


Fig. 2.18: Block Diagram of Spectrophotometer [Jasco (V-630)]

Accurate measurement of transmission spectrum requires simultaneous measurements of incident and transmitted light intensities for a given wavelength of light at the same instant as there could be error due to the fluctuation of brightness of light source. To ensure this, the incident light is generally split into two components and one component is sent through the reference arm and another through sample arm as shown in fig.2.18.

The required quantity to be measured is given by:

$$T_{sample} = \frac{I_{sample}}{I_{blank}} \quad (2.8)$$

However, I_{blank} cannot be measured directly when the sample is placed in the sample arm for measuring I_{sample} . For this reason the ratio β ($= I_{blank}/I_{reference}$), which is independent of source brightness, is measured initially. During the actual sample transmittance

measurement I_{sample} and $I_{reference}$ is measured and I_{blank} is derived from know value of β and measured $I_{reference}$. That is mathematically-

$$T_{sample} = \frac{I_{sample}}{I_{blank}} = \frac{I_{sample}}{\beta \times I_{reference}} \quad (2.9)$$

Fig. 2.19 shows typical transmission spectra of bare transparent substrate and semitransparent dielectric thin film coated on transparent substrate. The difference between transmission maxima and minima depends on the refractive index of the thin film and the spectral width of the interference fringes depends on the thickness and refractive index of the thin film sample.

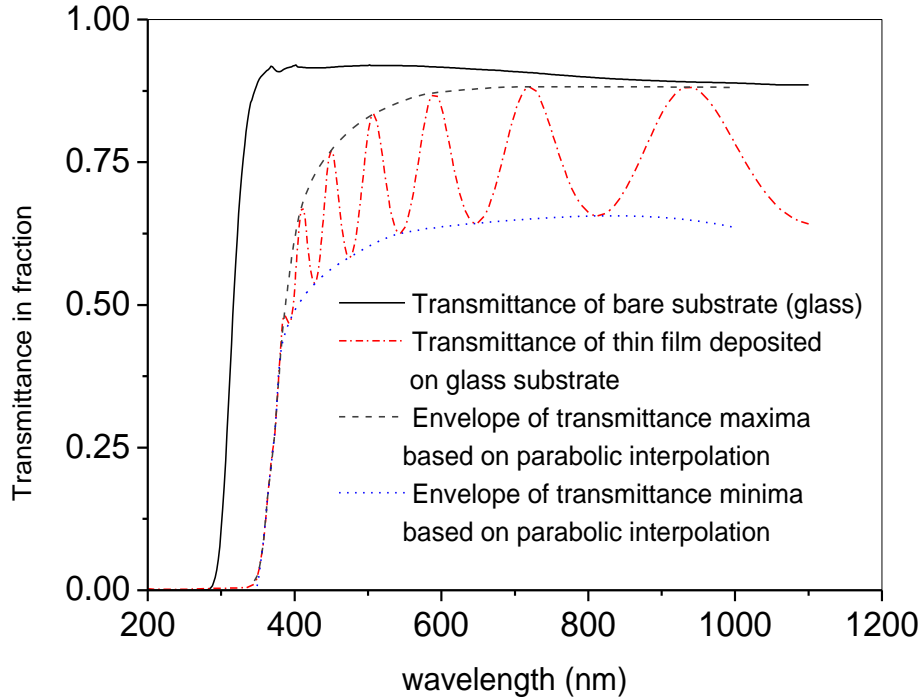


Fig. 2.19: Representative transmission spectra of bare substrate and thin film coated substrate

These facts and additional measurements of bare substrate transmission spectrum are exploited to estimate the thickness and complex refractive indices of the thin film sample using envelope method, originally proposed by Manifacier et al. [63] and later on upgraded

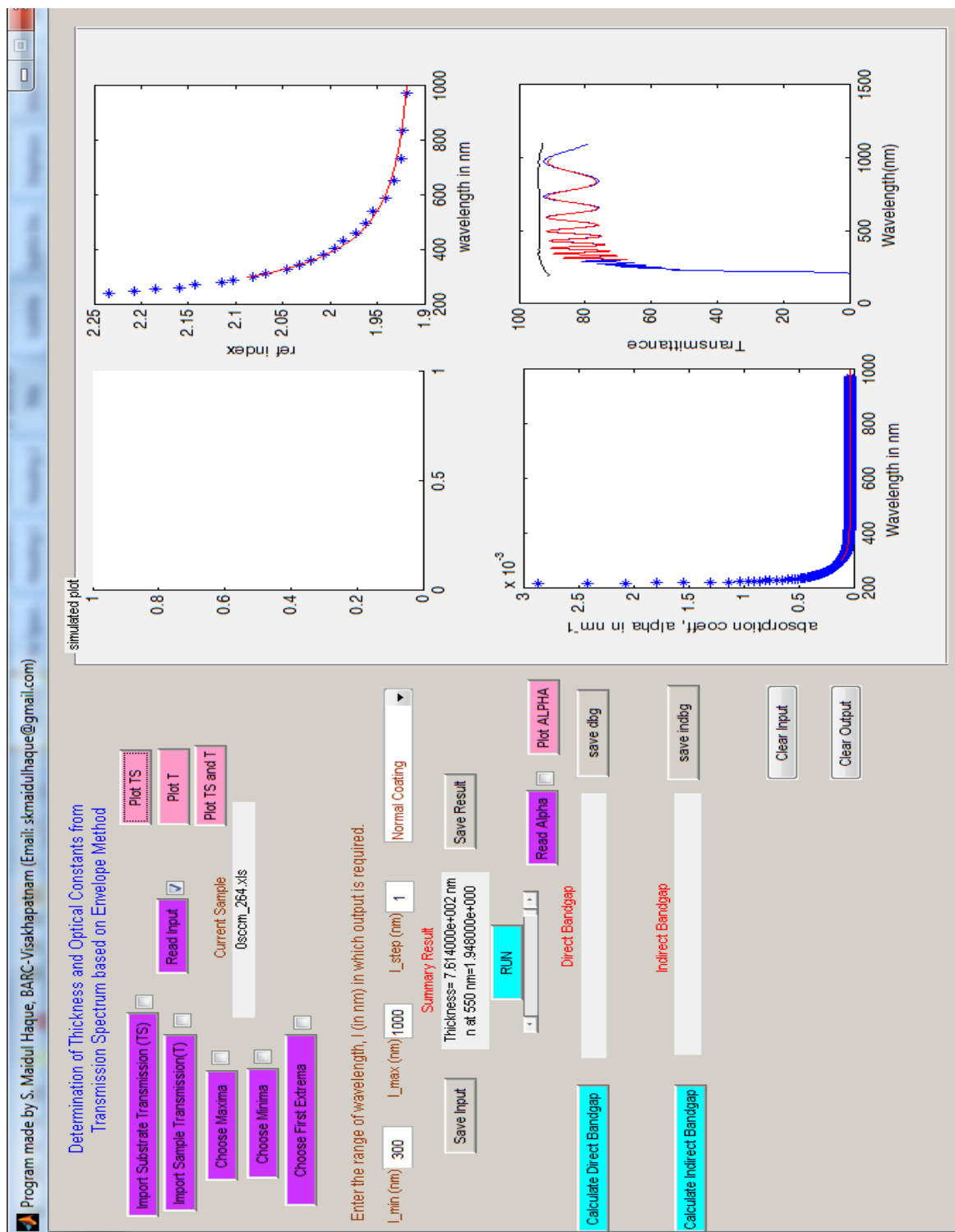


Fig. 2.20: Screenshot of indigenously developed computer program for determination of thickness and dispersion relation of thin film from transmission spectrum

by Swanepoel [64]. A brief account of Swanepoel method has been described in the Appendix-A of this thesis. A graphical user interface (GUI) based user friendly computer program (screenshot shown in Fig. 2.20) has been developed during the course of this thesis work using MATLAB to conveniently select the interference maxima/minima and compute thickness and wavelength dependent complex refractive index of the thin film from transmittance spectrum using Swanepoel method.

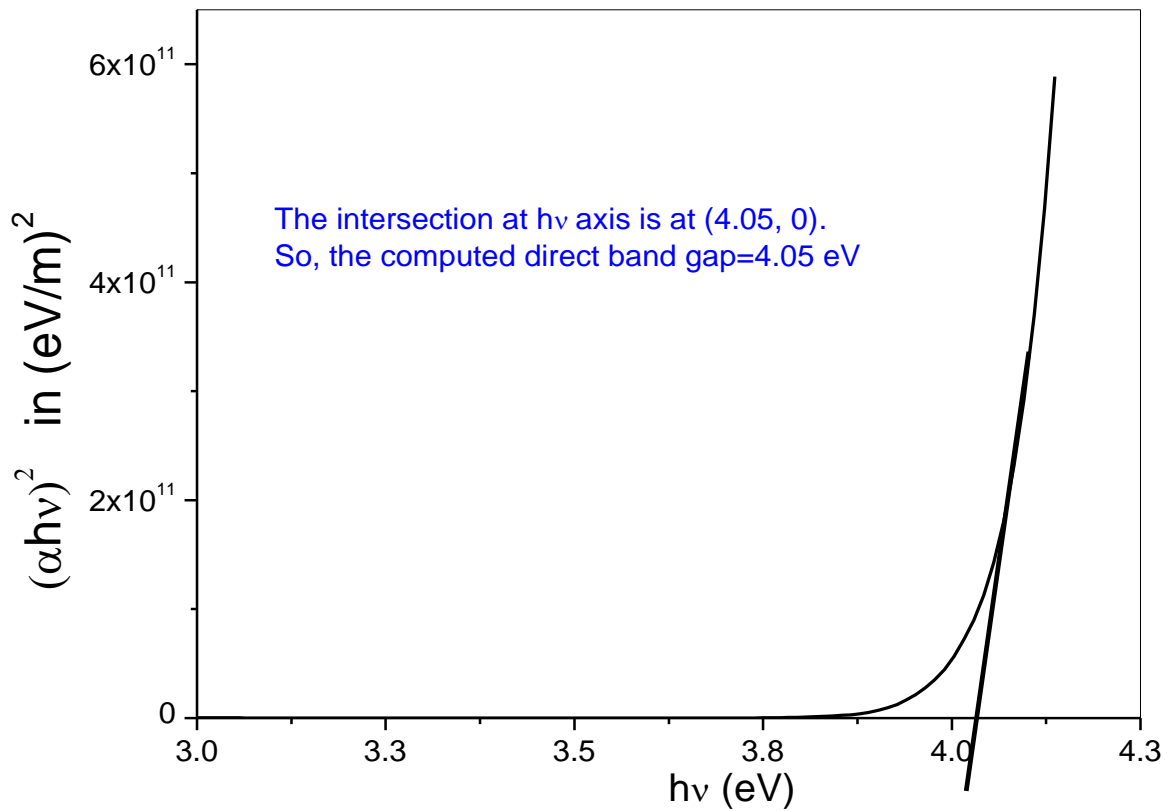


Fig. 2.21: Tauc plot of sputter deposited tantalum pentoxide thin films

The obtained wavelength dependent imaginary part of refractive index i.e. attenuation coefficient can be further utilized to calculate optical band gap of the thin film. Typically for semi-transparent thin films, in regime $\alpha > 10^4 \text{ cm}^{-1}$ of absorption coefficient (α) obeys Tauc relation [7] given by-

$$\alpha h\nu = B(h\nu - E_g)^p \quad (2.10)$$

where, B is a constant which depends upon the transition probability between the concerned states. E_g is the band gap and p is the index that characterizes the optical absorption process. ' p ' is theoretically equal to 2, 1/2, 3 or 3/2 for indirect allowed, direct allowed, indirect forbidden and direct forbidden transitions respectively. If an appropriate value of the index p is chosen and $(\alpha h\nu)^{(1/p)}$ is plotted against $h\nu$, the plot asymptotically tends to a linear plot, the interception of which on $h\nu$ axis gives the value of band gap, E_g .

Fig. 2.21 shows a Tauc plot for a representative ABPDC sputtered tantalum pentoxide thin films and estimated direct band gap is 4.05 eV. The error in estimated thickness and refractive index of our samples is ~ 1 % as estimated by R. Swanepoel [64] for the envelope method. The typical error in band gap value is ± 0.01 eV as calculated based on the wavelength resolution of the spectrophotometer in transmission measurement.

2.4.4 Spectroscopic Ellipsometry:

Spectroscopic ellipsometry is a widely used optical characterization technique to precisely measure optical properties of materials in bulk form, and thickness and optical properties of materials in thin film form. In this technique, the change in state of polarization of light upon reflection from the specimen is measured. Usually a plane polarized light is shined on the sample at 45° angle of incidence. The light being incident on the sample will have electric field vectors parallel (p) and perpendicular (s) to the plane of incidence as shown in fig.2.22. Upon reflection, the p and s components of light undergo different amplitude and phase shift so that when they come out of the specimen and recombine to form

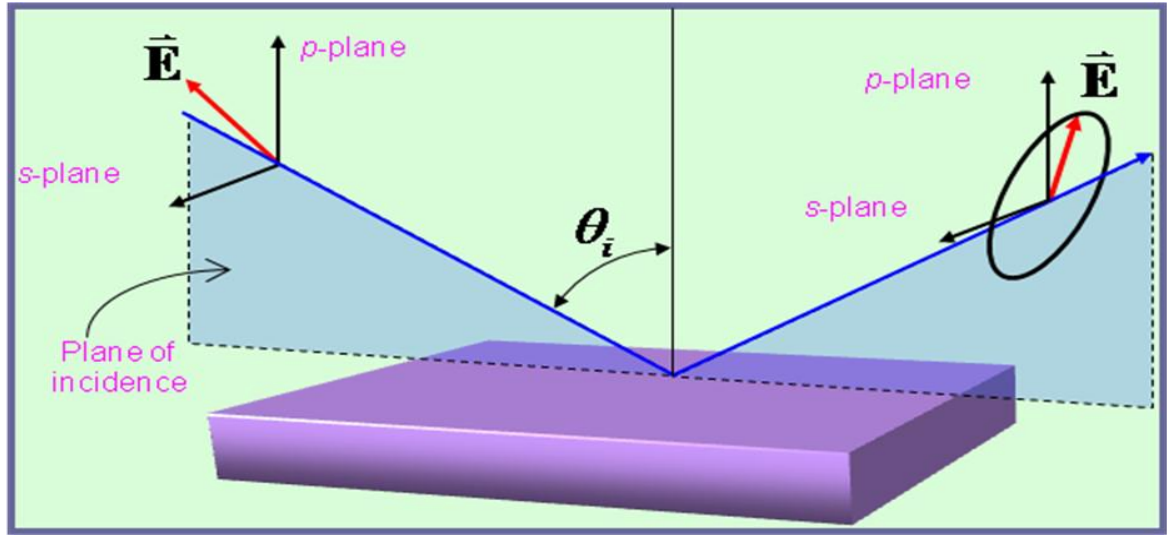


Fig. 2.22: Schematic of reflection of plane polarized light from sample

reflected light, in general, they produce elliptically polarized light. To assess the change in state of polarization of light upon reflection, a quantity ρ [65] defined as follows is evaluated in this context.

$$\rho = \frac{r_p}{r_s} = \tan(\Psi) \exp(i\Delta) \quad (2.11)$$

where r_p and r_s are the complex reflection coefficients for the p and s component of the waves respectively. In this thesis a variant of ellipsometer called rotating polariser type ellipsometer (photograph and schematic shown in fig.2.23 and 2.24 respectively) has been employed for optical characterization of most of the thin film samples.

The instrument consists of one polarizer and another analyzer arm that are mounted on a precision goniometer which allows the measurements at incidence angles continuously varying from 12 to 90°. The accuracy of the position of the goniometer arms is 0.01°. At the entrance of the polariser arm, there is a light source of 75 W Xenon arc lamp fed by a Stabilised Power Supply. Light from xenon lamp passes through a collimation optics which

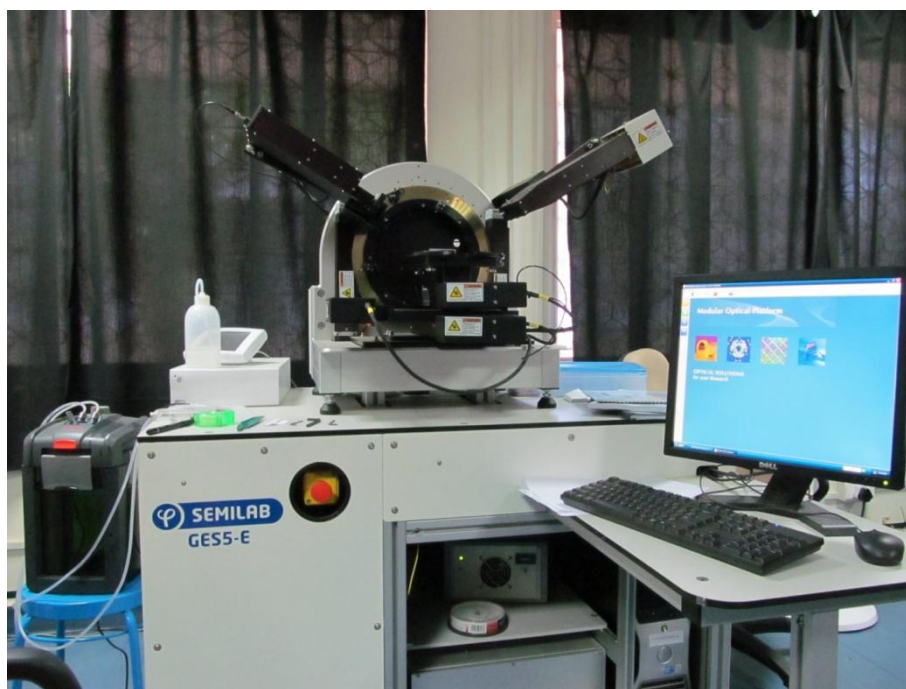


Fig. 2.23: Photograph of spectroscopic ellipsometer (SOPRA GES5E) at AMPD, BARC, Visakhapatnam.

consists of a combination of one concave mirror and flat mirror to transform the source emitted diverging beam into parallel beam. Similarly, in the analyzer arm, there is a focussing optics which consists of one flat mirror followed by a concave mirror to focus the parallel beam into the optical fibre. This ellipsometer is rotating polarizer type in which the polarizer in the source arm rotates with a fixed frequency while the analyser in the detector arm is oriented at fixed angle while measuring the ellipsometry data at a particular wavelength. Rotating polarizer and fixed analyzer, both consists of Rochon (quartz) polarizer having extinction ratio at 632.5 nm is $>10^4$. The focussed beam from analyzer arm falls on the entrance of an optical fibre of 3 m length, core diameter 1 mm and numerical aperture of 0.37 and at the other end of the optical fibre there is a monochromator based on ruled plane grating having focal length of 250 mm with two 58x58 ruled plane gratings with 1200 gr/mm (for UVVIS range) and 600 gr/mm (for IR range) respectively. The beam detector consists of PMT (for 190-900 nm) and an InGaAs IR detector (for 750-1700) nm.

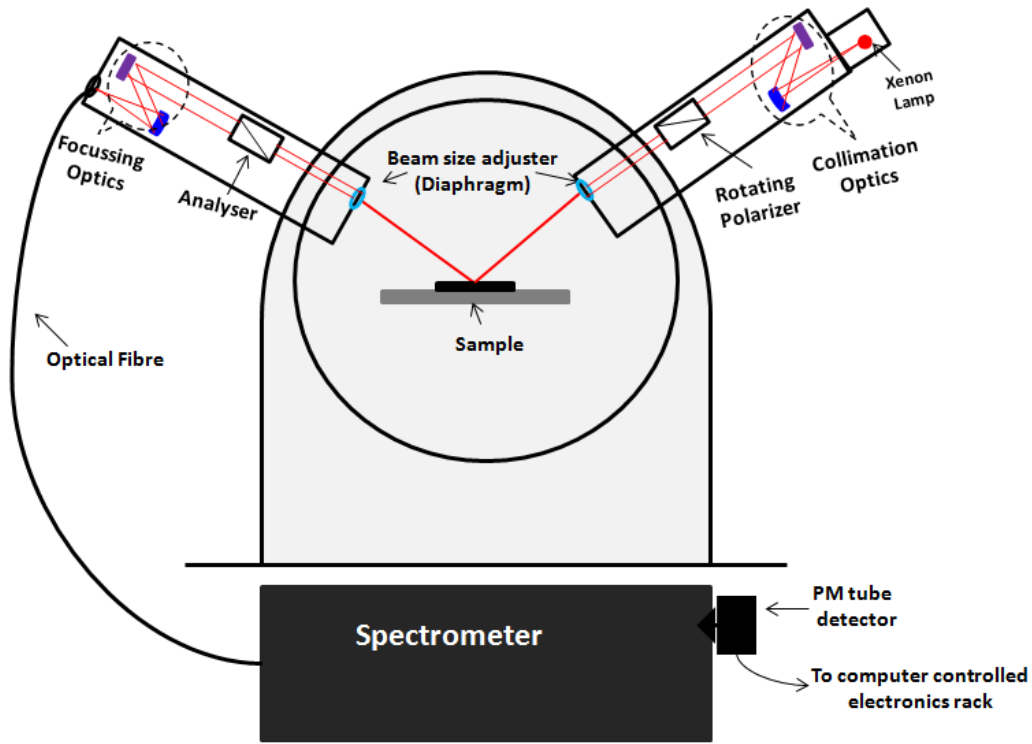


Fig. 2.24: Schematic of rotating polarizer type spectroscopic ellipsometer

In this type of ellipsometer, the polarizer in the source arm is constantly rotated at uniform frequency in order to introduce a periodic time varying modulation to the reflected signal which helps in evaluation of $\tan(\psi)$ (which measures the amplitude ratio) and $\cos(\Delta)$ (which measures the phase shift) as described above. From rigorous calculation [66], it can be shown that the time varying reflected intensity in this type of ellipsometry is given by:

$$I(t) = I_0 \left\{ 1 + \left(\frac{\tan^2 \psi - \tan^2 A}{\tan^2 \psi + \tan^2 A} \right) \cos(2P) + \frac{2 \tan \psi \cos \Delta \tan A}{\tan^2 \psi + \tan^2 A} \sin(2P) \right\} \quad (2.12)$$

Where, 'A' is the fixed analyzer angle and 'P' is the polarizer angle which is a periodic function of time. The measured periodic time dependent signal $I(t)$ at each wavelength can be Fourier transformed to write it in the form [66]:

$$I(t) = I_0 (1 + \alpha \cos(2\omega t) + \beta \sin(2\omega t)) \quad (2.13)$$

where, ω is the rotational frequency of the polarizer and α and β are the normalized Fourier coefficients which can be determined comparing equation (2.12) and (2.13) and it is found that they are linked through the following expressions:

$$\alpha = \frac{\tan^2 \psi - \tan^2 A}{\tan^2 \psi + \tan^2 A} \quad ; \quad \beta = \frac{2 \tan \psi \cos \Delta \tan A}{\tan^2 \psi + \tan^2 A} \quad (2.14)$$

where, A is the angle of the analyzer. Even though ψ and Δ are physically more meaningful ellipsometric parameters, the more directly obtained ellipsometric parameters α and β (at analyser angle of 45°) are also used for ellipsometry data analysis. Therefore, measured ellipsometry data consists of either the normalized Fourier coefficients α and β or derived from the measured data $\tan \psi$ and $\cos \Delta$ as a function of wavelength. In either of the case, the data needs to be fitted with the theoretical spectra generated using an appropriate model assuming a realistic sample structure and a suitable dispersion of optical constants of the materials of the layers. Various parameters of the sample layer structure and dispersion relations are varied in the analysis software and the simulated ellipsometry parameters are fitted with the measured ellipsometric spectra by minimizing the Root Mean Squared Error (RMSE) value between the measured and calculated values of the ellipsometric parameters (α and β) given by:

$$\text{RMSE} = [\{1/(2N-P)\} \sum_i^N \{(\alpha_i^{\text{exp}} - \alpha_i^{\text{cal}})^2 + (\beta_i^{\text{exp}} - \beta_i^{\text{cal}})^2\}]^{1/2} \quad (2.15)$$

where, N is the number of data points and P is the number of model parameters.

Apart from rotating polariser type ellipsometer, another variant of ellipsometer called phase modulated spectroscopic ellipsometer (photograph shown in fig. 2.25) has also been employed for optical characterization of few samples in this thesis. In phase modulated



Fig. 2.25: Photograph of phase modulated spectroscopic ellipsometer at AMPD, BARC, Trombay

ellipsometry technique [67], the reflected light is modulated by a photo-elastic modulator, which introduces a sinusoidal phase shift $\delta(t)$ between the two waves polarized parallel and perpendicular to the strain axis and the modulated signal takes the general form :

$$I(\lambda, t) = I_0 + I_s \sin \delta(t) + I_c \cos \delta(t) \quad (2.16)$$

where, $\delta(t) = A_0 \sin \omega t$ and A_0 is the modulation amplitude which is proportional to V_m / λ , V_m being the excitation voltage, λ is the wavelength of light and ω is the modulation frequency (50 kHz in our case) and for the present set of measurements with $M=0^\circ$, $P=45^\circ$ and $A=45^\circ$,

$$\left. \begin{aligned} I_0 &= 1 \\ I_s &= \sin 2\psi \sin \Delta \\ I_c &= \sin 2\psi \cos \Delta \end{aligned} \right\} \quad (2.17)$$

A , P and M being the respective orientations of the analyzer, polarizer and modulator with respect to the plane of incidence. The detected signal is Fourier analyzed to determine the parameters I_s and I_c , which in turn generate the parameters of interest, viz., ψ and Δ .

Since the thin film samples investigated under the scope of the thesis have been deposited by physical vapour deposition technique, most of the films are prone to have void in whole or in part of thin film layer structure. This has been accounted in ellipsometry modelling by assuming the thin film layer as an effective medium of mixture of bulk-like material and void. The refractive index of bulk like material is called intrinsic refractive index as opposed to the effective refractive index of the mixture of void and bulk material. Such effective medium model is applied under the assumption that the medium is microscopically inhomogeneous and macroscopically homogeneous i.e. each separate region (shown in fig. 2.26) in the medium is large enough to possess their own dielectric identities, but small compared to wavelength of light i.e. $L_1, L_2, L_3 \ll \lambda$.

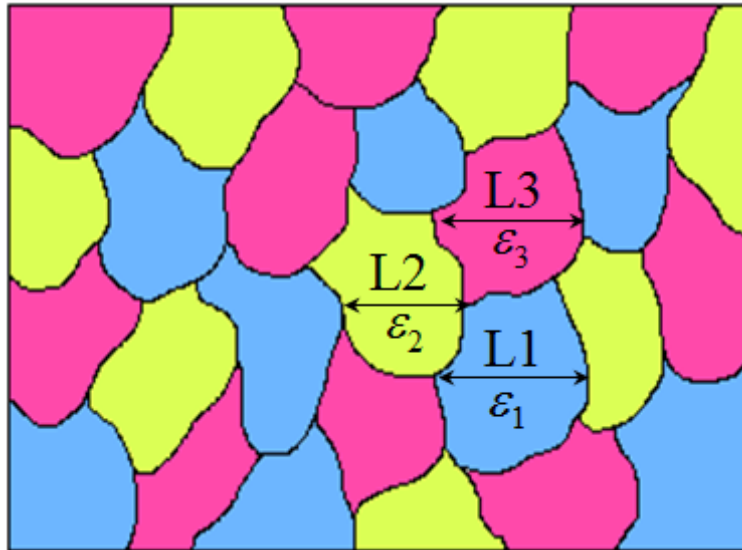


Fig. 2.26: Microscopically inhomogeneous medium to be treated under effective medium approximation (EMA).

Under this approximation, the constituent separate regions with different complex dielectric constants $\epsilon_1, \epsilon_2, \epsilon_3, \dots$ are considered to be embedded in a host medium

having complex dielectric constant of ε_h and the effective complex dielectric function, ε of the whole medium takes the general form given by-

$$\frac{\varepsilon - \varepsilon_h}{\varepsilon + 2\varepsilon_h} = v_1 \frac{\varepsilon_1 - \varepsilon_h}{\varepsilon_1 + 2\varepsilon_h} + v_2 \frac{\varepsilon_2 - \varepsilon_h}{\varepsilon_2 + 2\varepsilon_h} + \dots \quad (2.18)$$

v_1, v_2, \dots represents the volume fraction of material having dielectric constants of $\varepsilon_1, \varepsilon_2, \dots$. There are various effective medium approximation (EMA) models and in different EMA model, the dielectric constant of host material is considered differently. For example, in Lorentz-Lorentz (LL) EMA model vacuum is considered as host material i.e ε_h is considered to be 1. In Maxwell Garnett (MG) EMA model any one of the inclusions is considered as host material. In Bruggeman EMA model the effective medium itself is considered as host material, i.e. ε_h is considered to be same as ε .

Since the materials that have been studied in this thesis exhibit optical band gaps in the far UV or near visible wavelength range, a suitable dispersion relation, called Tauc Lorentz dispersion relation has been assumed to represent the intrinsic refractive index in the model. A brief account of Tauc-Lorentz dispersion [68] model has been given in Appendix-B.

There are several advantages of spectroscopic ellipsometry technique as compared to many other characterization techniques as long as optical characterization of thin film or bulk slab is concerned.

1. It measures the ratio of two values, so it is highly accurate and reproducible, does not need a reference sample, and is not so susceptible to the fluctuations in light source intensity.
2. Since it measures phase, it is highly sensitive to the presence of ultrathin films (<10 nm).

3. It provides two data at each wavelength viz., intensity ratio and phase change and hence more unknown parameters can be determined regarding the optical properties of the films. On the other hand, transmission measurement by a spectrophotometer measures only changes in amplitude or intensity at each wavelength.

The typical practical error bar in spectroscopic ellipsometry technique of estimated thickness is ± 0.5 nm and that of refractive index is ± 0.001 .

2.4.5 Atomic force microscopy:

Atomic Force Microscopy (AFM) provides surface morphological quantitative idea by using a sharp tip which is scanned over the specimen to sense surface forces. The microscopic image produced by AFM is basically locus of points of constant force between the tip and the specimen. Though in principle, either attractive or repulsive forces between the tip and surface can be used for imaging, in practice, the repulsive force mode is predominantly used because it is more stable. Although functionally similar to a stylus surface profilometer, AFM utilizes much smaller forces between tip and surface (typically $0.1 \mu\text{N}$) and the small radius of curvature of the tip ($0.03 \mu\text{m}$) which gives better spatial resolution. The tip is usually held stationary and the sample is scanned using piezoelectric transducers. An important feature of AFM is its ability to image non-conducting surfaces, whereas the Scanning Tunneling Microscope (STM) requires a conducting surface capable of sustaining a stable tunneling current. The sample is scanned by a small Si cantilever holding a sharp pyramidal tip at its end. This sharp tip senses attractive or repulsive forces while scanned on the surface of a sample and maintains the constant force with the surface through deflection during scanning.



Fig. 2.27: Actual photograph of AFM set up located at Mechanical and Optical Support Section, RRCAT, India and used for AFM characterization of the samples in this thesis.

The deflection is most often detected by the laser beam reflected from the back side of the cantilever onto a position sensitive detector. During the measurement the sample or cantilever is moved in X–Y plane by piezoelectric actuators and the locus of point of constant force forms the surface image in the computer by putting the line–scans together. In this work, AFM measurements have been carried out by Atomic force microscope (NT-MDT, SOLVER-PRO) using Si cantilever tips (resonant frequency $\sim 190\text{kHz}$) in non-contact mode. Fig. 2.27 shows the actual photograph of AFM set up used for AFM characterization of the samples in this thesis. The acquired AFM images have been used to extract surface statistical parameters such as surface roughness, average grain sizes etc. after a required software correction from the measured images.

2.4.6 Rutherford Backscattering Spectrometry:

Rutherford backscattering spectrometry (RBS) technique is based on the measurement of the number and energy of the backscattered ions/particles from a specimen's near surface region when the sample is bombarded with high energy particles/ions typically in the MeV

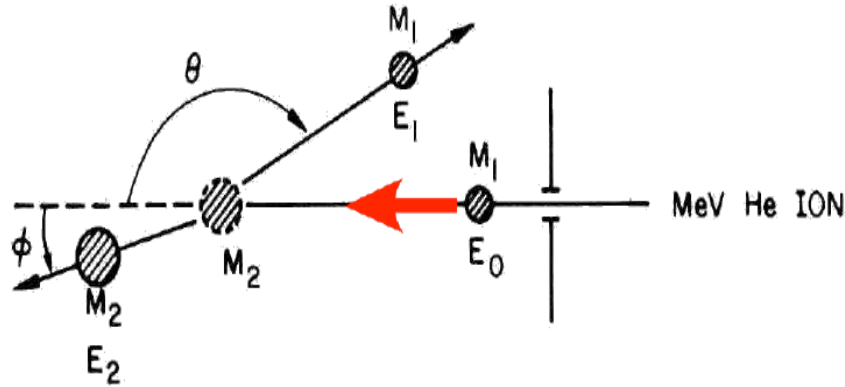


Fig. 2.28: Backscattering event following collision between two different masses.

energy range (0.5-4 MeV). This information enables one to determine atomic mass and elemental concentration along the depth of a sample. Out of all the particles bombarding the sample in this energy range, the vast majority get impinged into the sample and very few escapes due to scattering. This is due to the fact that the diameter of the atomic nucleus ($1e^{-15}$ m) is much less compared to the spacing between nuclei ($2e^{-10}$ m). The ratio of kinetic energy of the backscattered particle with respect to that of the incident particle is called Kinematical factor and can be derived from simple consideration of conservation of energy and momentum. If a particle of mass M_1 is backscattered from mass M_2 ($M_1 < M_2$) at angle θ (as shown in fig. 2.29), the kinematical factor [69] turns out to be

$$K_{M_2} = \frac{E_1}{E_0} = \left[\frac{(M_2^2 - M_1^2 \sin^2 \theta)^{1/2} + M_1 \cos \theta}{M_2 + M_1} \right]^2 \quad (2.19)$$

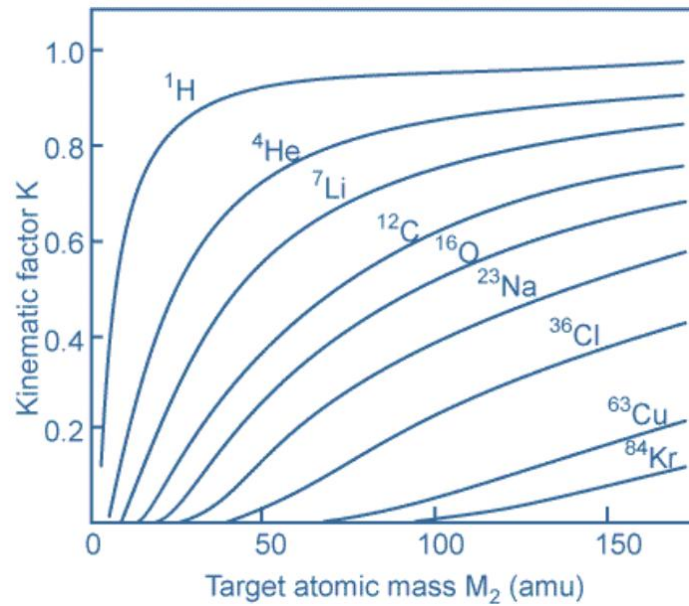


Fig. 2.29: Kinematical factors versus target masses for different projectiles [70].

This follows that as the mass of the target atom increases, less momentum is transferred to the target atom. This is why RBS has good mass resolution for light elements, but poor mass resolution for heavy elements. Fig. 2.29 shows the typical variation of kinematical factor with respect to target mass for different projectiles which show that the energy of the backscattered particle for all projectiles asymptotically approaches the incident particle energy. Again, it follows from equation (2.19) that for small difference in target mass (ΔM_2) the sensitivity becomes maximum for $\theta=180^\circ$. This is why the energy of the backscattered particles is measured at $\sim 170^\circ$ angle (to accommodate the detector). There are two more important terminologies in the context of this technique, namely ‘Stopping power’ and ‘scattering cross section’. A particle which backscatters from an element at some depth in a sample suffers from extra energy loss compared to that backscattered from a surface element. The energy loss of the projectile per unit of depth in a sample is called the stopping power. The energy loss depends upon the density and composition of the samples, a fact that enables RBS to be suitable for depth profiling. The scattering cross section is a term that relates to the

relative number of particles backscattered from a target atom into a given solid angle for a given number of incident particles. The scattering cross section is basically proportional to the square of the atomic number of the target atom.

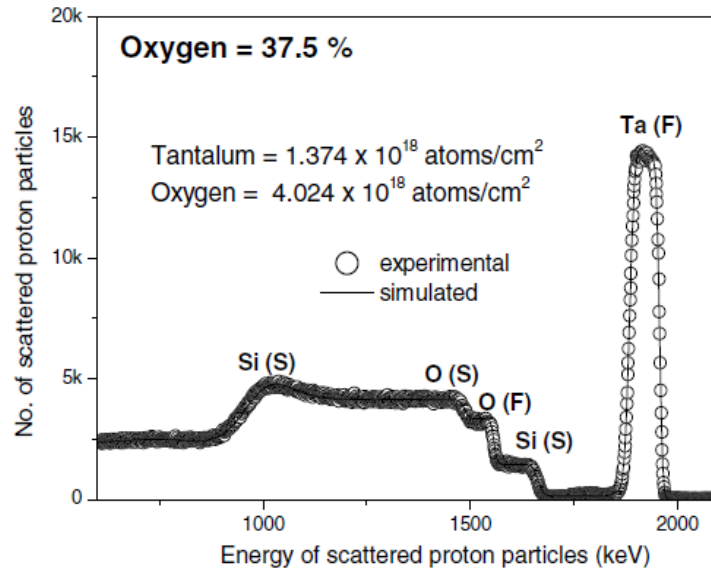


Fig. 2.30: Representative RBS spectrum measured by proton beam for a Ta₂O₅ coated glass substrate [55].

Fig. 2.30 shows a typical RBS spectrum [55] measured for Ta₂O₅ thin film coated on fused silica substrate. The RBS peak arising from different constituent elements in film and substrate have been marked in the same figure. By measuring the height of Ta and O peaks of film and normalizing by respective scattering cross section, the ratio of Ta and O can be obtained. Peak width, i.e., the difference in energy between front edge and the back edge of any peak gives the measurement of energy loss of the alpha particle scattered while traveling through the sample. Dividing this energy width by the stopping power of the material (energy loss in traversing the unit areal density of the sample), one can estimate the areal density of the sample. The areal density is defined as the number of atoms present in the unit area of the sample throughout the depth of the sample and basically depends upon the physical density

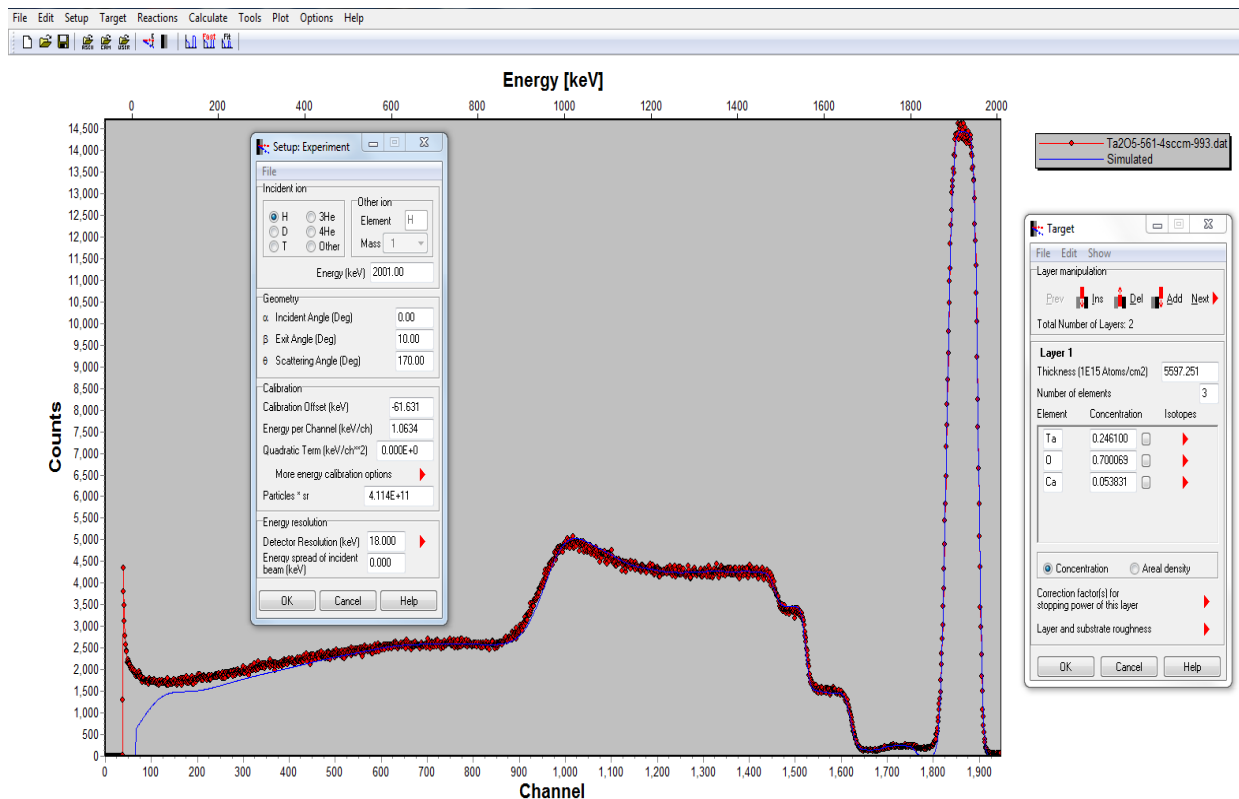


Fig. 2.31: Screenshot of the SIMNRA program.

and thickness of the sample under investigation. After estimating areal density from RBS, one can calculate the physical density of the samples if there is apriori knowledge of thickness and vice versa.

To analyze the RBS data presented in this thesis, a microsoft window based program SIMNRA has been used. SIMNRA can calculate spectra for any ion-target combination including incident heavy ions and any geometry including transmission geometry. Arbitrary multi-layered foils in front of the detector can be used. Many different stopping power data sets are also available. Calculation of scattering kinematics, stopping, peak integrals, positions of elements etc. is possible by this program. Data fitting (layer thicknesses, compositions etc.) can be done within the program using simplex algorithm. A screenshot of the program taken during data analysis is given in fig. 2.31.

2.4.7 X-ray Absorption Spectroscopy:

X-rays are short wavelength electromagnetic wave (Fig. 2.32) ranging from 25 Å to ~0.25 Å or energy from 500 eV to 500 KeV.

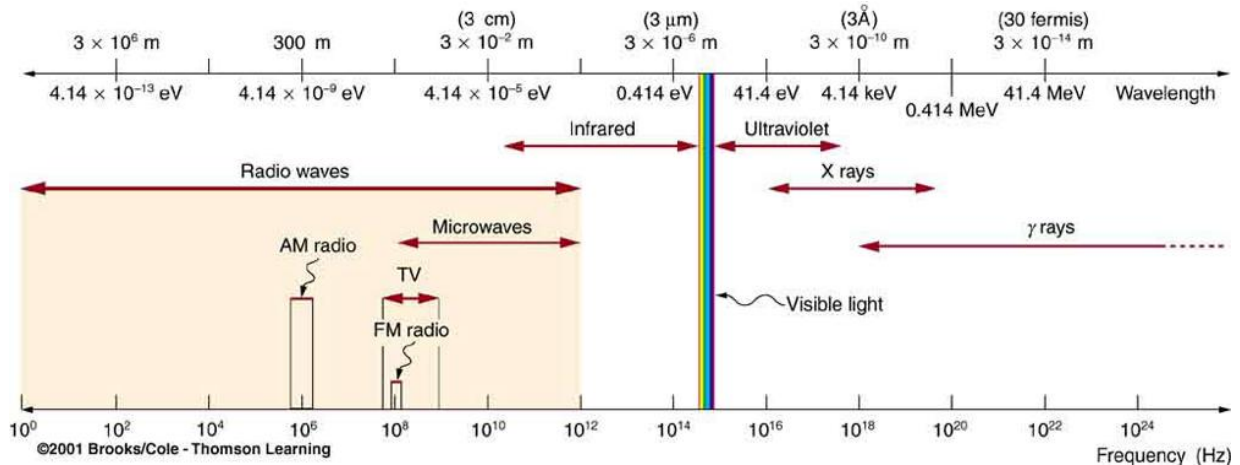


Fig. 2.32: Different energy regime of whole electromagnetic spectrum [68].

The different types of phenomena through which X-rays interact with matter are briefly discussed below. There are primarily four types of X-ray interaction with matter, viz., (i) Thomson scattering, (ii) Photoelectric effect, (iii) Compton scattering and (iv) Electron positron pair production, which are described in brief in the following:

(i) Thomson scattering

It is the elastic scattering of photons by the free or bound charged particles (electrons) in the medium. For most of the materials Thomson scattering is dominant when the energy of the photon is less. In terms of electromagnetic theory, when an electromagnetic wave is incident on a charged particle, the electric field of the wave exerts a Lorentz force on the particle, setting it into motion. Since the electric field is periodic in time, so is the motion of the particle. Thus, the particle is accelerated and, consequently, emits radiation. It can be envisaged as a process in which energy is absorbed from the incident wave by the particle and re-emitted as electromagnetic radiation of same frequency.

(ii) Photoelectric effect

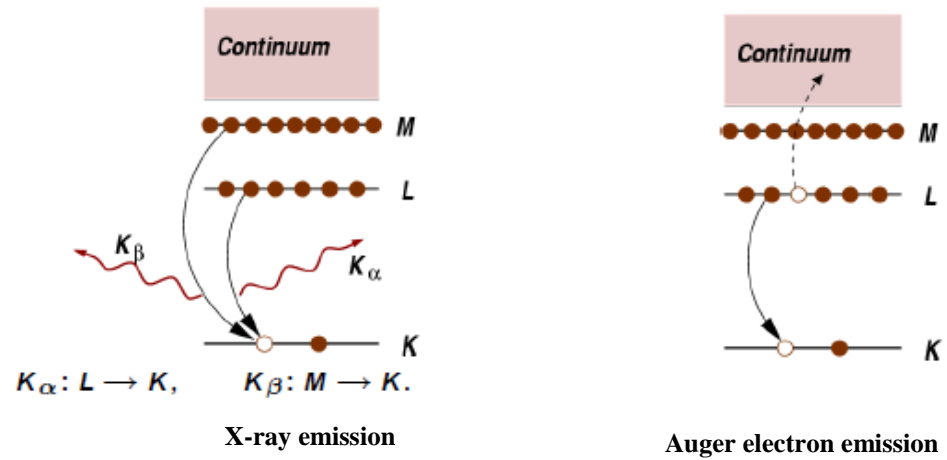


Fig. 2.33: The X-ray and Auger electron emission following photoelectric effect [71].

In this process an X-ray is absorbed by an atom promoting a core level electron (K, L or M shell) out of the atom and into the continuum. The atom is then left in an excited state with an empty electronic level (a core hole). The electron ejected from the atom is called the photo electron and this phenomenon is known as photo electric effect. There can be two secondary effects (fig. 2.33) following the photoelectric effect. The excited core hole will relax back to a ground state by another core level electron jumping into the ground level. This can be accompanied by either (i) emission of x-ray in which excess energy of electron is emitted as X-ray called fluorescence or (ii) ejection of electron in which excess energy is transferred to another core level electron and prompting that electron to emit out of the material is called Auger emission. In the hard x-ray regime (> 2 keV), X-ray fluorescence is more likely to occur than Auger emission [72], but for lower energy X-ray absorption, Auger processes dominate. Either of these processes can be used to measure the absorption coefficient μ , though the use of fluorescence is somewhat more common.

(iii) **Compton effect**

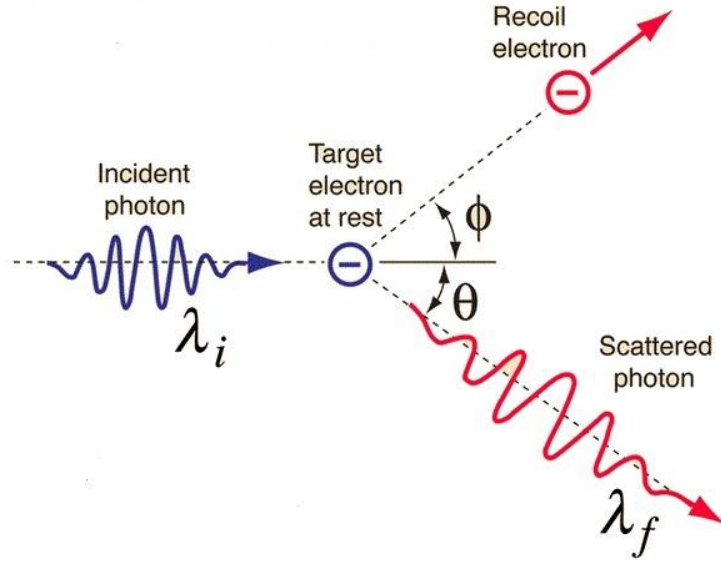


Fig. 2.34: The Compton scattering of X-ray [73].

The Compton effect (also called *Compton scattering*) is the result of a high-energy photon colliding with a free electron or with an atom having loosely bound electrons. The scattered radiation experiences a wavelength or energy shift due to transfer of momentum to the electron. Essentially the effect is an example of inelastic scattering of light and it demonstrates that light cannot be explained purely as a wave phenomenon. Compton successfully explained and modeled the data by assuming a particle (photon) nature for light and applying conservation of energy and conservation of momentum to the collision between the photon and the electron. The phenomenon is pictorially represented in fig. 2.34. The shift of the wavelength varies with scattering angle according to the Compton formula [74]:

$$\lambda_f - \lambda_i = \Delta\lambda = \frac{h}{mc} (1 - \cos \theta) \quad (2.20)$$

where h is the Planck constant, m is the mass of electron, θ is the scattering angle of photon and c is the speed of light. Compton's experiment convinced physicists that light can be

treated as a stream of particle-like objects (quanta called photons), whose energy is proportional to the light wave's frequency.

(iv) Pair Production

This phenomenon occurs when high energy ($\geq \sim \text{MeV}$) X-ray photon interacts with the electric field of a heavy nucleus. In this process, as pictorially represented in fig. 2.35, the heavy nucleus breaks down to form an electron and its anti-particle, called a positron. Since both electron and positron have a rest mass energy equivalent of 0.511 MeV, the minimum energy of the photon required for pair production is 1.022 MeV. In the pair production process the momentum is conserved by the recoiling nucleus. Pair production is an example of energy to mass conversion process.

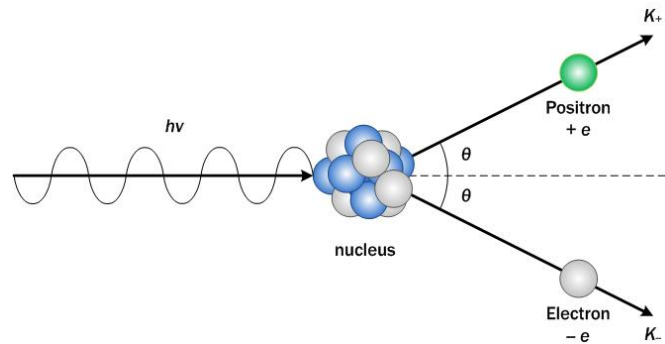


Fig. 2.35: Diagram showing the process of electron-positron pair production [75].

In different energy regime of X-ray, the probabilities of occurrence of the above processes are different. In this regard, one defines cross section to represent the probability of a specific type of X-ray interaction such as absorption or scattering with matter. Operationally the cross section can be defined in terms of a uniform beam of particles interacting with an object, such as a collection of atoms. If the number of interactions (e.g. absorption or scattering events) per unit time R (the rate) is divided by the incident beam intensity (particles/time/area) then it gives the measure of that interaction probability which is

also called total cross section of the target particles. Fig. 2.36 depicts the cross section of different processes mentioned above along with the total cross-section for Cu.

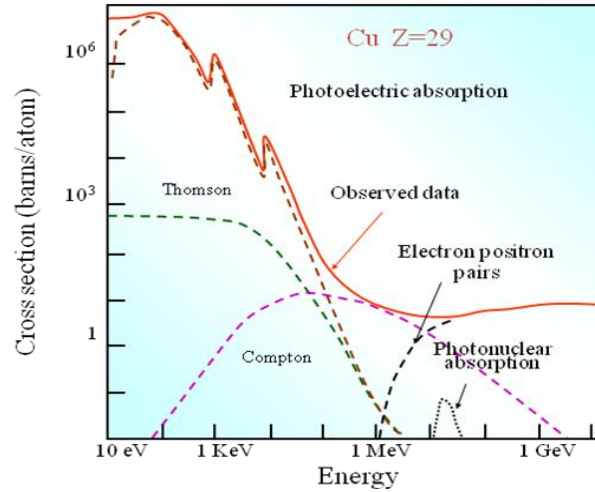


Fig. 2.36: X-ray to matter interaction cross section at different energy range of X-ray [76].

X-ray Absorption Fine Structure (XAFS) spectroscopy is a unique tool for studying the local structure around selected elements that are contained within a material. The basic quantity that is measured in XAFS technique, is the linear absorption coefficient $\mu(E)$. The absorption coefficient is defined as the fraction of incident X-ray intensity which gets absorbed per unit thickness of the material. As has been shown in fig. 2.37, generally X-ray absorption coefficient smoothly decreases as the energy increases (approximately as $1/E^3$), i.e. the X-rays become more penetrating with the increase in energy. However, at specific energies that are characteristic of the elements present in the material, there are sudden increases in the absorption cross section which are called X-ray absorption edges (as shown in fig. 2.37). The absorption edges occur at the on-set of photoelectric effect described above when X-ray photon has sufficient energy to liberate electrons from the core level of the atoms.

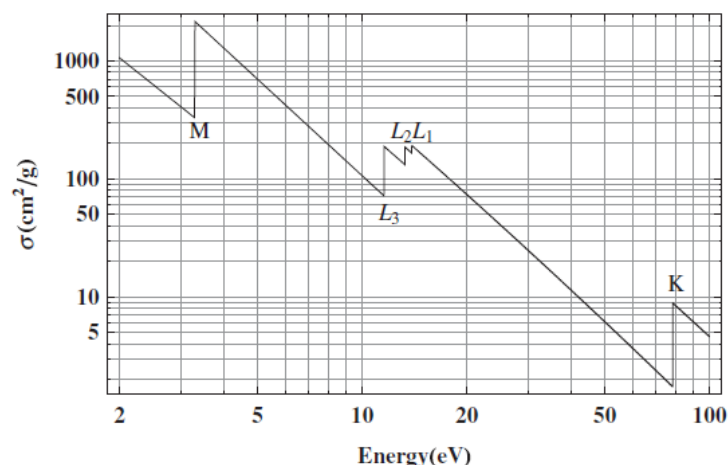


Fig. 2.37: The typical absorption cross section vs. X-ray energy of any materials [77].

A closer look near the absorption edge reveals that the absorption spectra just above the absorption edge are characterized by fine structure oscillations due to modulation of the absorption probability of X-ray by number of factors pertaining to the physical and chemical state of the specific element. X-ray absorption fine structure (XAFS) measurement is all about investigating these oscillations and thereby extraction of various information like formal oxidation state, coordination chemistry, and the distances, coordination number and species of the atoms immediately surrounding the selected element. The X-ray absorption fine structure spectrum is typically divided into two regimes: X-ray absorption near-edge spectroscopy (XANES) and extended X-ray absorption fine-structure spectroscopy (EXAFS). Though the two have the same physical origin, there are few fundamental differences between the two techniques. XANES is strongly sensitive to formal oxidation state and coordination chemistry (e.g., octahedral, tetrahedral coordination) of the absorbing atom, while EXAFS is used to determine the distances, coordination number and disorders (both static and thermal) disorders in the neighborhood of the absorbing atom.

2.4.7.1 EXAFS:

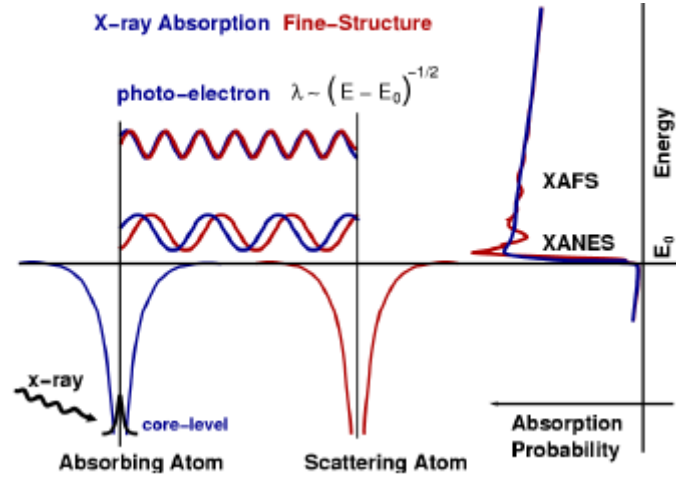


Fig. 2.38: Basic phenomenon of XAFS [72].

In the photoelectric absorption process, discussed above when a neighboring atom is present near to the absorbing atom (shown in fig. 2.38), the photo-electron can scatter from the electrons of this neighboring atom, and the scattered photo-electron can return to the absorbing atom. These scattered photo electrons at the location of absorbing atom alters the available electronic energy state and thereby modulates the functional behavior of absorption coefficient with energy near to edge energy. Thus by studying these modulation in the absorption spectra above the absorption edge one can find out quantitative information regarding the distances, coordination number and species of the atoms in the immediate surrounding the selected element. The typical experimentally measured absorption spectrum shows the plot as shown in fig. 2.39.

EXAFS formalism is concerned with the oscillations beyond the absorption edge. Thus one conveniently defines EXAFS fine-structure function as:

$$\chi(E) = \frac{\mu(E) - \mu_0(E)}{\Delta\mu_0(E)} \quad (2.21)$$

where, $\mu(E)$ is the measured absorption coefficient, $\mu_0(E)$ is a smooth background function representing the absorption of an isolated atom, and $\Delta\mu_0(E)$ is the measured jump in the absorption $\mu(E)$ at the threshold energy E_0 (Fig 2.39).

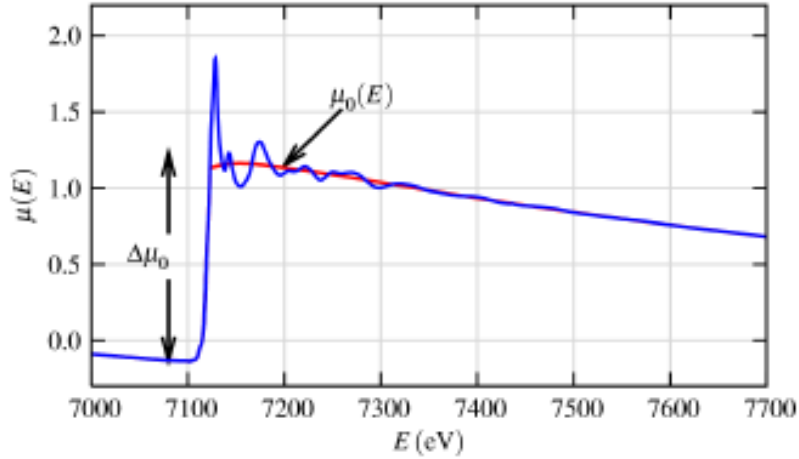


Fig. 2.39: Typical absorption spectrum around absorption edge [72].

As discussed previously, XAFS is governed by the transition between two quantum states visualizing from an initial state $\langle i |$ with an X-ray, a core electron, and no photo-electron to a final state $| f \rangle$ with no X-ray, a core hole, and a photo-electron [72]. The transition probability and thus the absorption coefficient is described by Fermi's golden rule given by-

$$\mu \propto |\langle i | H | f \rangle|^2 \quad (2.22)$$

The initial state $\langle i |$ does not alter due to the presence of neighboring atom. On the other hand the final state $| f \rangle$ gets affected by the scattered photo electron and can be considered as the summation of $| f_0 \rangle$, the bare atom contribution and $| \Delta f \rangle$, the neighboring atom's contribution, i.e. $| f \rangle = | f_0 \rangle + | \Delta f \rangle$ Thus,

$$\mu(E) \propto (\langle i | H | f_0 \rangle + \langle i | H | \Delta f \rangle) \times (\langle i | H | f_0 \rangle + \langle i | H | \Delta f \rangle)^*$$

$$\begin{aligned} &\propto \left| \langle i|H|f_0 \rangle \right|^2 + \left| \langle i|H|\Delta f \rangle \right|^2 + \langle i|H|f_0 \rangle \times \langle i|H|\Delta f \rangle^* + \langle i|H|\Delta f \rangle \times \langle i|H|f_0 \rangle^* \\ &\propto \left| \langle i|H|f_0 \rangle \right|^2 + 2 \operatorname{Re} \left[\langle i|H|\Delta f \rangle \times \langle i|H|f_0 \rangle^* \right] \end{aligned}$$

Neglecting the small contribution due to $\left| \langle i|H|\Delta f \rangle \right|^2$ term, one gets-

$$\mu(E) \propto \left| \langle i|H|f_0 \rangle \right|^2 \left[1 + \frac{2 \operatorname{Re} \left[\langle i|H|\Delta f \rangle \times \langle i|H|f_0 \rangle^* \right]}{\left| \langle i|H|f_0 \rangle \right|^2} \right] \quad (2.23)$$

Comparing this equation with equation (2.22) we can write-

$$\chi(E) \propto \langle i|H|\Delta f \rangle \quad (2.24)$$

As per quantum radiation theory, the interaction term H is proportional to e^{ikr} . The initial state is a tightly bound core level which can be approximated as a delta function. The change in final state is same as the wave function of scattered photo electron $\Psi_{scatt}(r)$.

Putting all these terms, one can write the expression for EXAFS as-

$$\chi(E) \propto \int \delta r e^{ikr} \psi_{scatt}(r) dr = \psi_{scatt}(0) \quad (2.25)$$

To say it in words, the EXAFS function is proportional to the scattered photoelectron at the site of absorbing atom.

EXAFS is usually understood in terms of the wave behavior of the photo-electron created in the absorption process. Thus it is common to convert the X-ray energy to wave vector k , of the photo-electron, which has dimensions of 1/distance and is defined as

$$k = \sqrt{\frac{2m(E - E_0)}{\hbar^2}} \quad (2.26)$$

where E_0 is the absorption edge energy and m is the electron mass. The primary quantity for EXAFS is then $\chi(k)$ and this is why the subsequent section, it will be tried to derive EXAFS

function in terms of wave vector instead of energy. EXAFS function is basically the amplitude of scattered photo electron at absorbing atom,

Treating the outgoing photo electron wave function $\psi(k, r)$ as spherical wave, we can write-

$$\psi(k, r) = \frac{e^{ikr}}{kr} \quad (2.27)$$

This generated photo electron traverses a distance R to the neighboring atom, gets scattered from neighboring atoms and then traverses back to the absorbing atom. The amplitude of scattered photo electron at the position of absorbing atom then becomes

$$\psi_{scatt}(k, r = 0) = \frac{e^{ikR}}{kR} \left[2kf(k)e^{i\delta(k)} \right] \frac{e^{ikR}}{kR} + C.C. \quad (2.28)$$

where, $f(k)$ and $\delta(k)$ are scattering amplitude and scattering phase shift due to the scattering atom. The scattering factors $f(k)$ and $\delta(k)$ depend upon the atomic number, Z of the neighboring atom. These scattering factors make EXAFS sensitive to the presence of neighboring atoms. Combining equation 2.25 and 2.28 we get, after few more simplification

$$\chi(k) = \frac{f(k)}{kR^2} \sin[2kR + \delta(k)] \quad (2.29)$$

This represents EXAFS equation considering one pair of absorbing atom and scattering atoms. However, in real scenario, often there is large number of scattering atoms and we need to average over their contribution to EXAFS taking into account the effect of thermal or static disorder in the bond distances. As a first approximation i.e. assuming one type of neighboring atoms and Gaussian distributions of neighboring atom's disorder, the EXAFS equation becomes-

$$\chi(k) = \frac{Ne^{-2k^2\sigma^2} f(k)}{kR^2} \sin[2kR + \delta(k)] \quad (2.30)$$

where, N is the coordination number and σ^2 is the mean-square-displacement in the bond distance R . Summing over the contribution due to different types of neighboring atoms, EXAFS equation becomes

$$\chi(k) = \sum_j \frac{N_j e^{-2k^2 \sigma_j^2} f_j(k)}{k R_j^2} \sin[2k R_j + \delta_j(k)] \quad (2.31)$$

where, j stands for the individual coordination shell of identical atoms at approximately the same distance from the central atom. In principle there could be many such shells, but as shells of similar Z become close enough (i.e., within a 0.05 \AA of each other), they become difficult to distinguish from one another and they are often represented by a single shell having equivalent multiple degeneracy.

Before applying the EXAFS equation (2.31) to any practical case, it needs an important correction. At the start of the derivation, we assumed that photoelectron wave traverses the distance between absorbing and neighboring atom as spherical wave. In reality, these photoelectrons can undergo inelastic scattering with the conduction electrons; phonons etc. and its energy may get changed. The criteria for a photo electron to participate in the XAFS is that the photo-electron has to scatter from the neighboring atom and return to the absorbing atom elastically (i.e., at the same energy) as the outgoing photo-electron and also, the photoelectron has to return back before the excited state decays. To take inelastic scattering and the core-hole lifetime into account one should rather use a damped spherical wave like:

$$\psi(k, r) = \frac{e^{ikr} e^{-2r/\lambda(k)}}{kr} \quad (2.32)$$

where, λ is the mean free path that represents the distance that a photoelectron can traverse without undergoing inelastic scattering and before the core hole is filled. The mean free path

typically falls in the range of 5-30 Å and has a fairly universal functional relationship with photo electron wave number, k as shown in fig. 2.40.

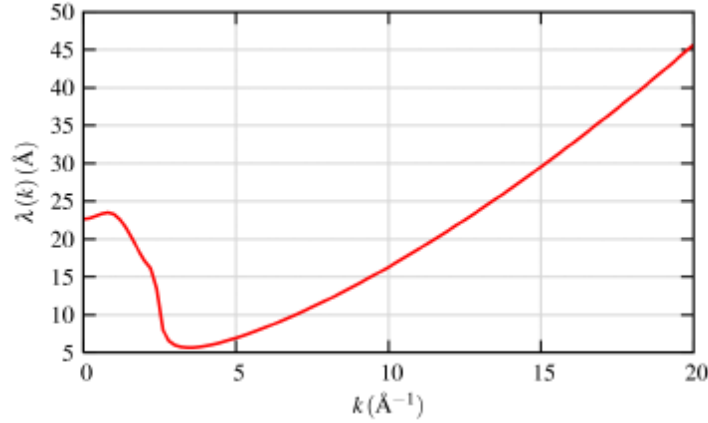


Fig. 2.40: Typical characteristic of photoelectron mean free path vs. wave number [72].

Taking the mean free path correction into account, the EXAFS equation becomes-

$$\chi(k) = \sum_j \frac{N_j e^{-2k^2\sigma_j^2} e^{-2R_j/\lambda(k)} f_j(k)}{kR_j^2} \sin[2kR_j + \delta_j(k)] \quad (2.33)$$

This is the EXAFS equation which widely used for simulating theoretical EXAFS spectra of any species in order to carry out the analysis of experimental EXAFS data. Certainly, this requires apriori knowledge about scattering factors $f(k)$ and $\delta(k)$. These scattering factors are function of atomic number Z and are usually calculated theoretically with very high accuracy rather than taking them from any experimental database. One important corollary that can be drawn from EXAFS equation follows that because of $\lambda(k)$ term and R^{-2} term in the equation, EXAFS is inherently a local probe i.e. EXAFS cannot see much further than ~ 5 Å. In this regard, this is to be recollected that X-ray diffraction (XRD) which relies on long range ordering of atomic planes, probe crystalline structure at a much larger length scale. On the other hand, X-ray absorption spectroscopy probes the immediate environment of the selected element, within about 6 Å, and its theory and interpretation does not rely on any

assumption of symmetry or periodicity in the samples. So EXAFS work even if there is no long range periodicity in the sample. The above characteristic along with the fact that EXAFS is an element specific tool, makes EXAFS a powerful structural local probe. With the advent of modern bright synchrotron radiation sources, this technique has emerged out to be most powerful for local structure determination which can be applied to any type of material viz. amorphous, polycrystalline, polymers, surfaces, solutions, nanomaterials and thin films.

2.4.7.2 XANES:

The region typically up to 50 eV above the absorption edge is called the XANES region where the interaction of the ejected photoelectron with the potential of the neighboring atoms is still strong so the simplifying single scattering assumption leading to EXAFS is not possible. The EXAFS equation breaks down at low- k , due to the $1/k$ term and the increase in the mean-free-path at very low k . In the near-edge (XANES) region the muffin-tin approximation is less satisfactory for quantitative analysis. Thus the interpretation of XANES is complicated since there is no simple analytic description of XANES. However, much information regarding the chemical environment can be obtained from the XANES region. The absorption edge position and shape is sensitive to formal valence state, ligand type, and coordination geometry and can be used as a fingerprint to identify phases.

The final states of K and L1 edges are p -states, and the final states in L2 and L3 edges are a mixture of d and s character. The p final states of K and L1 edges are more diffuse than the localized d final state of L2 and L3 edges. All of these edges may show strong peaks at the top of the edge (the “principal maximum”). Historically these were called “white lines,” because that was how they appeared on photographic plates. Transition metal oxides, for example, usually have many unfilled $3d$ electrons near the Fermi level, and a filled $3p$ band.

There are empty $2p$ electron states from the oxygen, but these are too far away to appreciably overlap with the metal $1s$ band. Therefore, the metal $3d$ electrons do not normally participate in the absorption process unless there is a strong hybridization of the O $2p$ and metal $3d$ levels. The XANES spectra are especially sensitive to such hybridization. For ions with unfilled d -electron bands, the pd hybridization is dramatically altered depending on the coordination environment, with much stronger hybridization for tetrahedral coordination than for octahedral coordination. Another important and common application of XANES is to use the shift of the edge position to determine the valence state.

Fig. 2.41 shows the valency dependence of Fe metal and oxides of Fe^{2+} and Fe^{3+} (and a mixture of these two). With good model spectra, $\text{Fe}^{3+}/\text{Fe}^{2+}$ ratios can be determined with very good precision and reliability. The heights and positions of pre-edge peaks can also be reliably used to empirically determine oxidation states and coordination chemistry. For

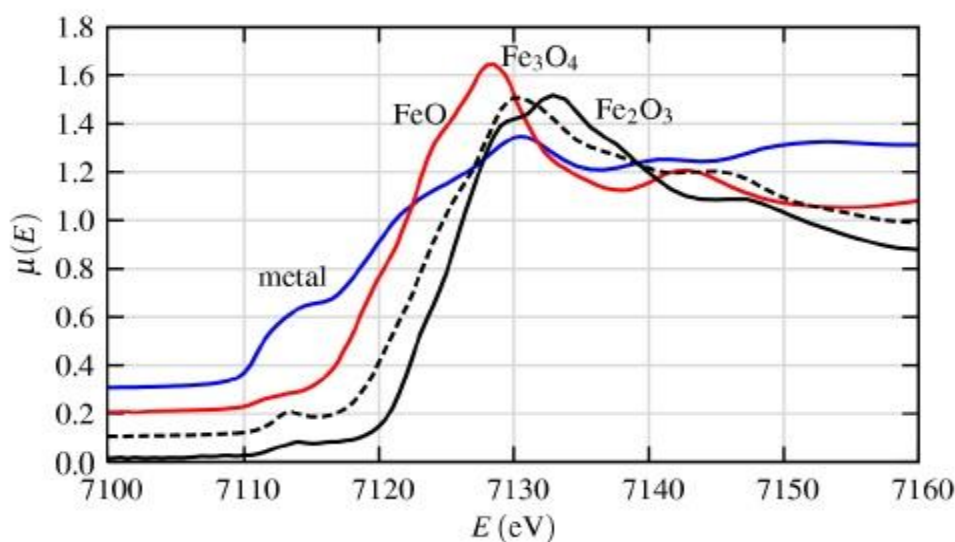


Figure 2.41: XANES spectra of standard Fe metal and oxides [72].

many systems, XANES analysis based on linear combinations of known spectra from “model compounds” is sufficient to tell ratios of valence states and/or phases. More sophisticated linear algebra techniques such as Principle Component Analysis and Factor Analysis can also

be applied to XANES spectra. Some materials, such as the spinel and inverse spinel structures have metal ions in inequivalent sites: 2/3 of the sites are octahedral, and 1/3 are tetrahedral. Despite the dilution due to octahedral sites, the 3d pre-edge peaks are noticeably larger than the pure octahedral case. In some cases the states associated with pre-edge transitions are full ($3d^{10}$ configuration) in one charge state, but have a hole ($3d^9$) in another charge state. For example, the presence or absence of the 3d pre-edge transition can be used to detect the difference between Cu^+ and Cu^{2+} . Correlating formal charge state with absorption edge shifts is obvious from simple physical arguments that shifts of a few eV can indeed occur by transferring charge.

2.4.7.3 Two modes of XAFS measurement:

EXAFS requires measurement of energy dependent X-ray absorption coefficient with high accuracy, typically of $\sim 10^{-3}$. Experimentally this can be accomplished in either of following two ways (fig. 2.42).

- (i). Transmission mode of measurement
- (ii). Fluorescence mode of measurement

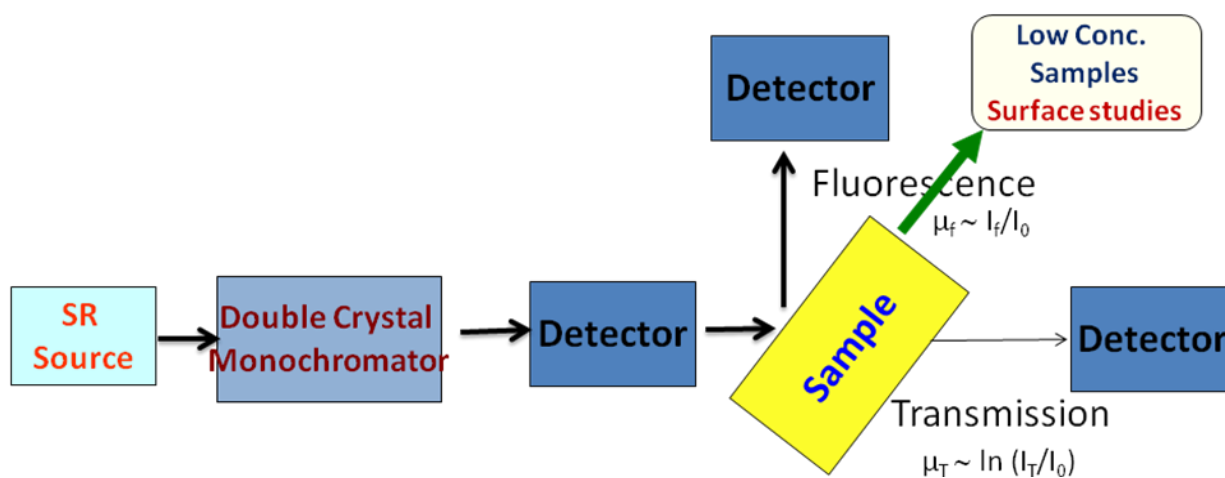


Fig. 2.42: Block diagram of XAFS measurement set-up.

(i) Transmission mode of measurement

In transmission mode, X-ray is made to transmit through the sample and the intensity of incident (I_0) and transmitted (I) X-ray beam is measured and the ratio $\log(I_0/I)$ gives the measure of absorption coefficient, μ . Often for concentrated samples, EXAFS is required to be carried out in transmission mode in order to avoid high background in fluorescence mode. However, for transmission mode measurement, the sample amount has to be properly optimized. The sample should sufficiently absorb to give a good EXAFS signal over a strong I_0 background, and also it should not be too absorbing. The rule of thumb followed for this purpose is to maintain the sample thickness, t such that $\mu t \sim 2.5$ above edges step and the edge step $\Delta\mu t \sim 1$. This thickness calculates to be few microns for metals, few tens of microns for solid oxide metals to few millimeters for dilute solutions. This measurement technique also requires that the sample is homogeneous and free from pinholes. The method is usually appropriate for model compounds and elements with concentrations greater than 10%.

(ii) Fluorescence mode of measurement

In fluorescence mode, instead of measuring the X-rays transmitted through the samples, intensity of the fluorescence X-ray emitted from the sample following the absorption of incident X-ray is measured. For thicker bulk samples, thin film samples deposited on thick substrate through which X-ray cannot pass. Fluorescence mode is also preferred in case of samples with very low concentrations of the absorber like doped samples since in this case it is very difficult to detect very weak absorption over a strong signal of transmitted beam. In fluorescence mode measurement stringent condition of sample uniformity is not there as required in transmission mode measurement, however, there

are two important concerns for experimentally measuring fluorescence X-ray efficiently i.e. energy discrimination and solid angle selection.

Energy discrimination: The emitted X-ray will not only be the fluorescence lines of element of interest but will also include fluorescence lines of other elements in the sample. In addition there can be elastically and inelastically scattered X-rays etc. In order to pick up the fluorescence X-ray of interest out of all these, the unwanted X-rays are filtered out either physically before it gets to the detector or electronically after it is detected through energy discrimination.

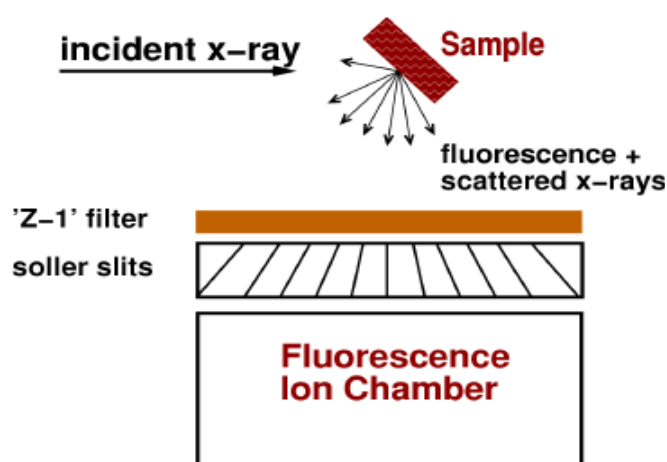


Fig. 2.43: Physical filtering of scattered X-rays using 'Z-1' filter [72].

As a physical technique to filter scatter X-rays, a material of atomic number 'Z-1' is used in between the sample (atomic number: Z) and the detector. 'Z-1' material will preferably absorb the scatter peaks pass the fluorescence lines. To avoid re-radiation from the filter itself, a set of slits (Soller slits) is often used to preferentially collect emission from the sample and block the emission from the filter, as shown in fig. 2.43. Such arrangement is very effective especially when the signal is dominated by scatter. Energy discrimination can also be done electronically after the X-ray emission is collected in the detector. A common

example of this approach uses a solid-state Si or Ge detector, which can achieve energy resolutions of about 200 eV or better.

Dead time: The electronic energy discrimination takes a finite amount of time, which restricts the total amount of signal that can be processed over a given time. Typically when count rate exceeds $\sim 10^5$ Hz or so, the detector is effectively unable to count the entire fluorescence signal, and is said to be “dead” for some fraction of the time. It is common to use ten (or more!) such detectors in parallel. Even then, the limit of total intensity incident on these detectors can limit the quality of the measured XAFS signal.

The selection of right solid angle for the measurement of fluorescence emission measurement is another important aspect. The fluorescence is emitted isotropically. However, since X-rays from a synchrotron are polarized in the plane of the synchrotron, the scattering is least at 90° to the incident beam. This is why the detectors are usually placed at right angle to the incident beam.

Self absorption: In XAFS measurement it is usually assumed that XAFS signal is proportional to the X-ray absorption. However, the fluorescence intensity that we measure has to travel back up to the detector by penetrating the sample medium. In the process, the portion of fluorescence intensity might get absorbed by the element of interest itself, the phenomenon is usually known as self-absorption. The self absorption essentially dampens the XAFS oscillation and requires proper correction before proceeding for analysis. The self absorption is especially an important consideration for thick pure sample.

It should be noted here that in fluorescence mode EXAFS, though the signal emitting from the front of the sample is collected at the detector, it is not really a surface sensitive technique because of large escape depth of fluorescence X-rays. On the contrary, electrons have much less escape depth (\sim less than a micron) compared to X-ray. That’s why XAFS

measurement by Auger electron spectroscopy is much more surface sensitive compared to X-ray absorption spectroscopy.

2.4.7.4 EXAFS data analysis:

Whether the EXAFS measurement has been carried out in transmission mode or fluorescence mode, the procedure for EXAFS data analysis is the same. EXAFS data analysis consists of primarily two parts called (1) Data reduction and (2) Data modeling.

(i) Data reduction

(i) Fluorescence intensity is converted to $\mu(E)$ after taking care of any possible experimental corrections such as self absorption effects, detector dead time etc.

(ii) The measured energy range is calibrated to take care of any shift in energy. For example, during measurement if there is any offset of the Double Crystal Monochromator (DCM) it can be corrected by measuring absorption edge of some known metallic foil and then calibrating it with the DCM energy scale.

(iii) A smooth pre-edge function is subtracted from $\mu(E)$ to get rid of any instrumental background and absorption from other edges. The corrected absorption spectrum is normalized by absorption edge energy step as we are interested in the EXAFS oscillations.

Thus EXAFS function $\chi(E)$ is derived as

$$\chi(E) = \frac{\mu(E) - \mu_0(E)}{\Delta\mu_0(E_0)} \quad (2.34)$$

Where, E_0 is the absorption edge, $\mu_0(E)$ is the bare atom background, and $\Delta\mu_0(E_0)$ is the step in the $\mu(E)$ value at the absorption edge.

(iv) The energy scale is subsequently converted to the wave number scale k , given by:

$$k = \sqrt{\frac{2m(E - E_0)}{\hbar^2}} \quad (2.35)$$

The function $\chi(k)$ is called the EXAFS function.

(v) $\chi(k)$ is then weighted by k^n to amplify the oscillations at high k value. Because the measured EXAFS function is in the finite range of k and since Fourier transform is defined for a spectrum that extends from $-\infty$ to $+\infty$, to reduce Fourier transform ripple caused due to the abrupt termination at both ends of EXAFS spectra, a gradual window function is multiplied. The k weighted EXAFS function $k^n \chi(k)$ is then Fourier transformed to generate the Fourier transformed EXAFS (FT-EXAFS) spectra or $\chi(R)$ versus R plots in terms of real distances from the centre of the absorbing atom.

(ii) Data Modeling:

In this stage, the experimentally derived $\chi(R)$ versus R plots are fitted with theoretically generated plots to find the local structural parameters around absorbing atoms.

Theoretically, EXAFS function is derived for a given local structure model using following formula [72].

$$\chi(k) = \sum_j \frac{N_j e^{-2k^2 \sigma_j^2} f_j(k)}{k R_j^2} \sin[2k R_j + \delta_j(k)] \quad (2.36)$$

where, j represents the individual coordination shell of identical atoms; R_j , N_j and σ_j^2 represents respectively the bond length (Å), coordination number and Debye-Waller factor (Å²) of the j^{th} shell and $f_j(k)$ and $\delta_j(k)$ give the scattering properties of the neighbouring atoms in the j^{th} shell. So for EXAFS data analysis of any system, first a crystallographic structure and space group is assumed based on apriori knowledge of the system and subsequently the EXAFS function for the structure is simulated using equation (2.36) with some initial guess value of R_j , N_j and σ_j^2 parameters. Later on the values of these parameters are varied to achieve best fitting between the experimentally derived $\chi(R)$ versus R plot with that of the simulated one. For all the EXAFS data analysis of the samples under

this thesis work, a set of EXAFS data analysis program available within the IFEFFIT software package [46] have been used for reduction and fitting of the experimental EXAFS data. The goodness of the fit in the above process is generally expressed by the R_{factor} which is defined [78] as:

$$R_{factor} = \sum \frac{[\text{Im}(\chi_{dat}(R_i) - \chi_{th}(R_i))]^2 + [\text{Re}(\chi_{dat}(R_i) - \chi_{th}(R_i))]^2}{[\text{Im}(\chi_{dat}(R_i))]^2 + [\text{Re}(\chi_{dat}(R_i))]^2} \quad (2.37)$$

where, χ_{dat} and χ_{th} refer to the experimental and theoretical $\chi(R)$ values respectively and Im and Re refer to the imaginary and real parts of the respective quantities.

If there is multiple possibility of the structure of any system, fitting is tried with all the structure models and R_{factor} of each fitting is evaluated. The lesser value of R_{factor} signifies the better possibility of the system to belong to the corresponding structure.

2.4.7.5 EXAFS experimental facility

EXAFS measurements described in this thesis have been carried out at scanning EXAFS beam line (BL-09) at INDUS-2 synchrotron source at Raja Ramanna Centre for Advanced Technology (RRCAT), Indore [44]. The X-ray flux of the beam line is typically 10^{11} ph/sec/0.1% band width @2.5 GeV, 200 mA. This bending magnet beam line can probe elements having X-ray absorption edge within the energy range of 4-25 KeV. The optical layout of the beam line is shown in fig. 2.44. The divergent beam from bending magnet source is vertically collimated using a 1.3 m long meridional cylindrical mirror with radius of fixed exit type double crystal monochromator (DCM). The DCM consists of two Si (111) curvature 11.2 kms. The vertically collimated X-ray beam is made to fall on first crystal of a

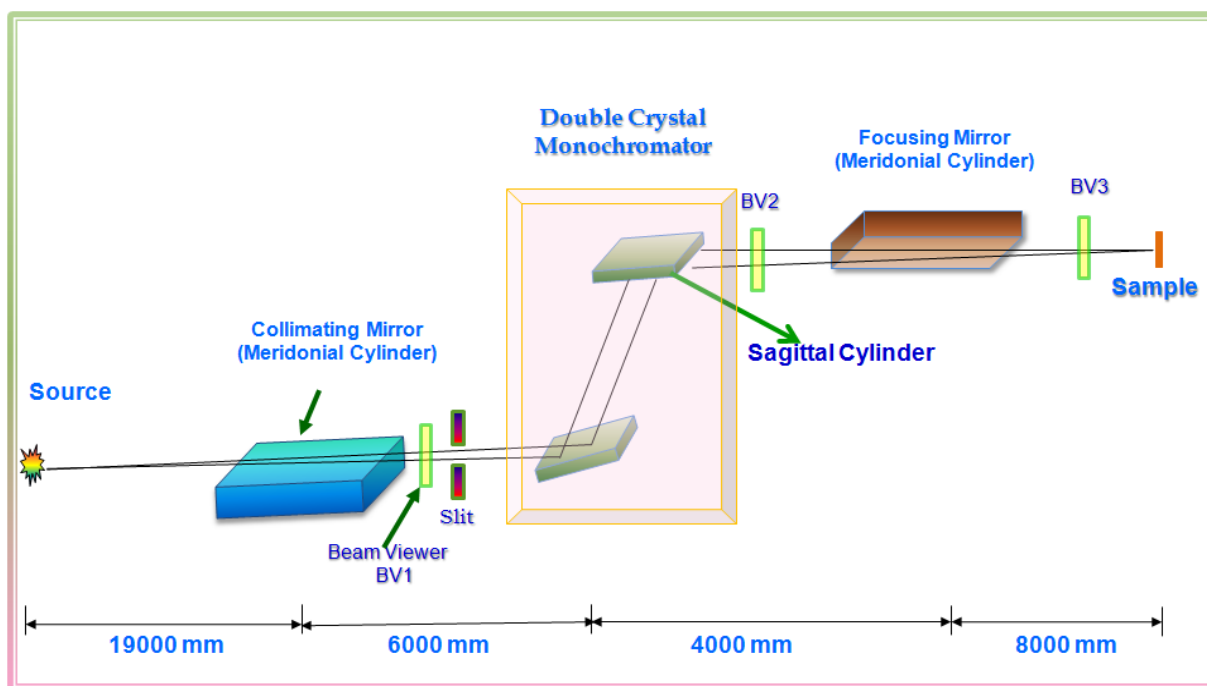


Fig. 2.44: Optical layout of scanning EXAFS beam line (BL-09) at INDUS-2, RRCAT, Indore [79].

crystals with $2d=6.2709\text{\AA}$ and narrow Darwin widths. The fixed exit is achieved by varying the relative lateral and vertical distances between the two crystals at each energy setting, maintaining parallelism between them. The second crystal of the DCM is bendable in sagittal direction with variable radius of curvature, which provides horizontal focusing to the beam. Higher harmonics are rejected by detuning the parallelism of two crystals in DCM by compromising on the photon flux to some extent. The energy resolution of DCM is $\sim 10^4$ @ 10 KeV. After the DCM, a Rh/Pt coated mirror with meridional curvature and facing downward is used for vertical focusing of the beam at the sample position. The focal spot size of X-ray at the sample location can be made up to $2.0\text{ mm} \times 0.75\text{ mm}$. Each of the two cylindrical mirrors has two coating strips, viz., of Platinum (Pt) and Rhodium (Rh). To cover the energy range of 4-25 keV, coatings of Rh and Pt are used since Rhodium has the absorption edge at 23.2 KeV (K-edge) and Pt has L1, L2 and L3 absorption edges between 11.5 KeV to 13.9

KeV. The entire optics is maintained at 10^{-9} torr vacuum and separated by front end and experimental hutch using 200 μ m thick beryllium windows.

For recording the X-ray absorption spectra in transmission mode, the sample is placed between two 30 cm long ionization chamber detectors as shown in fig. 2.45. The first ionization chamber measures the incident flux (I_0) and the second ionization chamber measures the transmitted intensity (I_t). Absorption (μ) is calculated using formula, $\mu = \log(\frac{I_0}{I_t})$. A third ionization chamber is also used after the second ionization chamber where reference metal foils are measured for energy calibration. Appropriate gas or gas mixture is filled at atmospheric pressure in each of the ionization chamber depending on energy range to be probed.



Fig. 2.45: Experimental set-up for transmission mode of XAFS measurement.

For recording the X-ray absorption spectra in fluorescence mode, the sample is placed at 45° to the incident X-ray beam. For measuring the fluorescence spectrum from the sample, a single channel Si drift detector is placed in front of the sample at 45° .

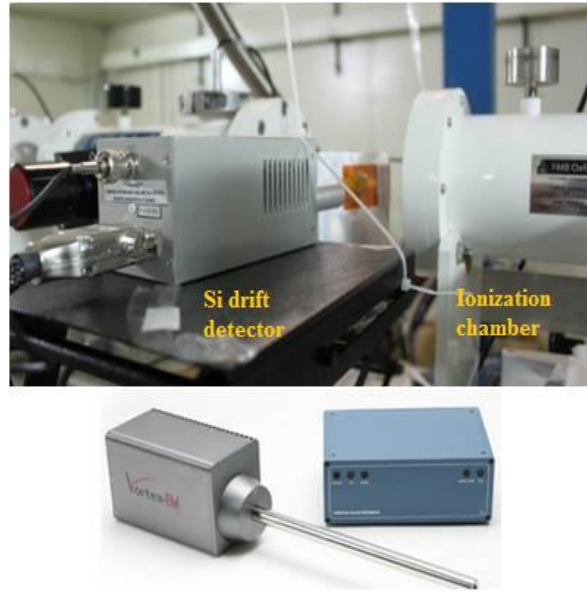


Fig. 2.46: Experimental set-up for fluorescence mode of XAFS measurement.

The detector is placed at right angle to the incident beam as shown in fig. 2.46 so that the scattered X-ray is largely suppressed as the incident X-ray is polarized in the plane of synchrotron. An ionization chamber filled with a pre-defined gas mixture to absorb 10-20% of the incident beam was placed prior the sample stage to measure the incident beam (I_0). A proper region of interest (ROI) is selected in the detector output to selectively measure the fluorescence intensity of the absorbing atomic species (I_f). Thus the absorption co-efficient of the sample was determined by the relation ($\mu = I_f / I_0$) and the spectrum was obtained as a function of the energy by scanning the DCM of the beam line over the specified energy range.

CHAPTER-3

Study on HfO₂ samples deposited at various oxygen partial pressures and the effect of substrate biasing

3.1 Introduction:

Hafnium oxide (HfO₂), which is more popularly known as hafnia, is recognized as one of the most promising high k dielectric materials to replace SiO₂ in metal oxide semiconductor transistors [10-12]. Apart from its excellent high-k dielectric properties, hafnium oxide also qualifies to be an excellent optical coating material in the extended spectral region for high power laser applications. HfO₂ is fairly transparent in UV-Visible-near IR spectral range and has got considerably high band gap (~5.7 eV). Over the period, HfO₂ has been preferred as a high index coating material for fabrication of multilayer thin film devices [13] primarily due to its superior thermal and chemical stability [14-15] in contact with silicon and silicon oxides. Several deposition techniques have been adopted to deposit HfO₂ films of desired optical and electronic properties including sputtering [31], sol-gel [32], atomic layer deposition (ALD) [33] etc. Ion beam assisted deposition (IBAD) [34] has also been used in a number of studies aimed to obtain high-quality HfO₂ optical films.

HfO₂ films produced by evaporation processes, barring ion assisted deposition, are generally porous [35] and therefore absorption of moisture in the voids causes refractive index to change under humid condition. Again, ion assisted deposition also poses limitation

in developing large area coatings due to restriction in the sizes of available ion sources [36]. Magnetron sputtering, on the other hand, has got several advantages in achieving improved morphology, microstructure and interfaces [37-39]. Ma et al. [40] have used pulse sputtering to produce high quality HfO_2 thin films, having refractive index of ~ 2.0 at 550 nm. There are number of sputtering techniques e.g. reactive sputtering, diode sputtering, etc., being experimented to achieve superior microstructure and morphology. However, compared to other sputtering techniques, magnetron sputtering, which has been discussed in details in Chapter-2, is preferred since in this case the electrons emitted from the cathode execute helical motions and strike back to the target surface which enhances the sputtering efficiency. Generally, magnetron sputtering yields a deposition rate which is an order of magnitude higher than that obtained by conventional sputtering technique. Also since in this technique, the secondary electrons are trapped near the target they don't contribute to the substrate heating [41]. Due to such inherent advantages, magnetron sputtering is a highly preferred technique for surface sensitive deposition like of metal oxide semiconductors for device application. For oxide targets which are insulating RF magnetron sputtering is used instead of DC sputtering.

In a typical RF magnetron sputtering deposition technique, the percentage of oxygen present with respect to argon i.e. oxygen partial pressure acts as an important controlling parameter since it controls the stoichiometry of the deposited oxide samples and the deposition rate. Oxygen partial pressure decides the average sputtering efficiency since the sputtering efficiency of oxygen is less compared to argon. Apart from the above it also monitors energy of the sputtered species [42] reaching the substrate surface and thus in turn determines morphology and crystallinity of the films. Systematic study of reactive sputtered HfO_2 thin film with different oxygen to argon ratio has been investigated by Aygun et al.

[80]. Substrate biasing has also considerable influence on the energy of ionic species present in the magnetron plasma and thus on the total energy delivered to the substrate [43] during deposition, thereby changing the growth process and thus may result in determining the optical and micro structural properties. Mohan Babu et al.. [81] have demonstrated experimentally that the deposited indium oxide thin films shift from amorphous to polycrystalline structure when they are deposited by substrate biasing as compared to floating substrate. For diamond-like carbon films deposited by inductively coupled plasma assisted CVD process, Kim et al.. [82] have reported that with increasing bias voltage, the hardness of the films increased to a maximum value and then decreased. Systematic study of chemical binding configuration, crystallographic structure, dielectric and optical properties of Ta₂O₅ thin film with respect to substrate biasing has also been reported [83]. For RF sputter-deposited amorphous silicon films, it has been demonstrated [84] that DC substrate bias produces denser a-Si film with fewer defects as compared to that of the unbiased deposition. However, to best of our knowledge the effect of biasing in case of deposition of HfO₂ films by magnetron sputtering has been reported [85] by us for the first time.

In the above study we have investigated the evolution of micro-structural, optical and other physical properties of hafnium oxide thin films deposited under different oxygen partial pressures and with and without pulse DC bias on the substrate. The samples have been characterized by grazing incidence X-ray diffraction (GIXRD) to probe the crystallinity of the films. Grazing incidence X-ray reflectivity (GIXR) and Rutherford Back Scattering (RBS) spectrometry techniques have been used to study the mass density aspects of the samples. Further, optical transmission spectrophotometry and spectroscopic ellipsometry (SE) have been employed to investigate the optical properties of the films. Finally EXAFS

measurement has been carried out in order to investigate any possible correlation between local structural properties of HfO₂ films with the optical properties of the same.

3.2 Preparation of samples:

HfO₂ thin films have been deposited on fused silica substrate by RF magnetron sputtering technique in the home-built magnetron sputtering system described in Chapter-2. For the present investigations, HfO₂ films were sputter deposited at seven different oxygen flow rates, namely 0, 2, 4, 6, 12, 20, 25 standard cubic centimeters per minute (sccm) (corresponding to oxygen partial pressure of 0%, 9.1%, 16.6%, 23.1%, 37.5%, 50% and 56% respectively) vis-a-vis a constant argon flow rate of 20 sccm. One set of samples was deposited without substrate bias and other set was deposited with bias of 50 watt pulse DC. The pulse DC bias was provided using the pulsed DC source (MKS/ENI make, model RPG-100) described in Chapter-2. The pulse shape was rectangular with pulse frequency of 250 kHz and pulse width or pulse on time of 1456 ns. The amplitude of the pulse was -98 V during one half-cycle and +37 V during the other half-cycle. The detailed pulse shape has been given in Chapter-2. The deposition rate obtained in in-situ crystal monitor was $\sim 1 \text{ \AA sec}^{-1}$ for samples deposited under mixed argon and oxygen ambient and $\sim 6 \text{ \AA sec}^{-1}$ for films deposited without oxygen.

3.3 Grazing Incidence X-ray Diffraction measurements:

GIXRD measurements were carried out using a STOE diffractometer using Cu K _{α} X-ray radiation (1.54 Å) and 2 θ detector scan with the incident beam kept fixed at a constant grazing angle of incidence. GIXRD measurements were carried out to investigate structural

changes in the samples and the GIXRD patterns are shown in Figures 3.1(a) and (b) respectively for the samples deposited at different oxygen partial pressure and without and with substrate bias. The comparison of GIXRD spectra of the samples, with the standard data (PCPDF), suggests that all the samples exhibit monoclinic phase. It can be seen that in both the cases (i.e., with and without substrate biasing), the sample deposited without additional oxygen has got preferred orientation along $(\bar{1}11)$ direction and with the increase of oxygen partial pressure, polycrystallinity of the samples is increased. However, no significant change in the crystallinity of the samples due to substrate biasing has been observed.

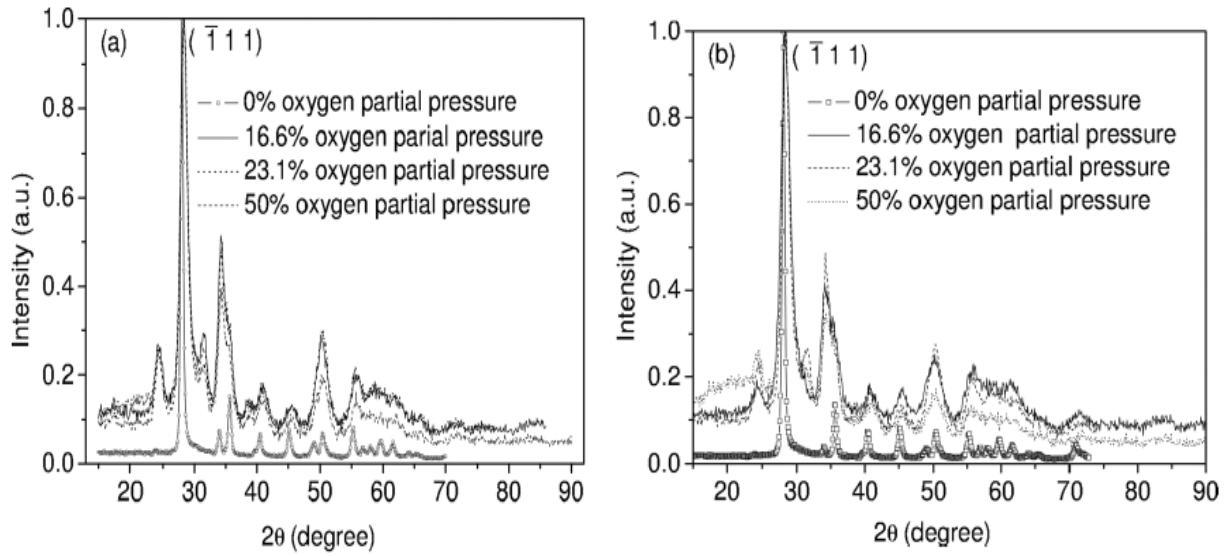


Fig.3.1: GIXRD spectrum of HfO₂ films deposited (a) without and (b) with pulse DC substrate bias and at various oxygen flow rates (Ar flow rate has been kept at 20 sccm in each case).

3.4 Rutherford Backscattering measurements:

Atomic concentrations of the films have also been estimated by RBS measurements carried out with He ions (α particles) of 3.5 MeV energy from a 1.7 MV Tandemron accelerator at IGCAR, Kalpakkam, India. RBS spectra were recorded with the help of a detector kept at 165° scattering angle and a charge of 27 micro coulombs were collected for

each RBS spectra. The spectra were calibrated using gold and silicon edges for the corresponding He ion energy. RBS spectrum (no. of scattered α particles as a function of energy of α particles) of a representative HfO_2 sample which was deposited without any substrate bias and at $\sim 9.1\%$ oxygen partial pressure is shown in Fig. 3.2(a). Peak width i.e. the difference in energy between front edge and the back edge of any peak gives the measurement of energy loss of alpha particle scattered while travelling through the sample. As has been discussed in details in Chapter-2, dividing this energy width by the stopping power of the material (energy loss in traversing the unit areal density of the sample), one can estimate the areal density of the sample. In case of the present samples, the areal density was estimated by fitting the hafnium peak of the spectrum presuming stoichiometric sample. Subsequently dividing the areal density by the respective thickness obtained from optical transmittance measurement, as discussed later, we have calculated atom density (no. of atoms/cm³) of the films and have shown in fig.3.2 (b). The typical accuracy of determination of composition of thin films by RBS technique is $\sim 1\%$ [86-87].

It can be seen that for both the set of films, atomic densities of the films deposited without oxygen partial pressure are high and densities become lower for films deposited with 9.1% oxygen partial pressure or more and in general, films deposited with substrate bias are found to have higher density than the films deposited without any bias. It can be seen from Fig. 3.2(b) that for both the set of films, atomic densities of the films deposited without oxygen partial pressure are high which might be due to high metal content in the films. Densities become lower for films deposited with 9.1% oxygen partial pressure or more which indicate realisation of relatively more stoichiometric films and in general, films deposited with substrate bias are found to have higher density than the films deposited without any bias. For the films deposited with pulsed substrate bias enhanced bombardment of Ar^+ ions on the

growing films takes place in the negative half cycle of the pulsed bias. This gives higher mobility to the ad atoms enabling their reorganisation on the growing surface, thus leading to more compact and denser films. However, as oxygen partial pressure is increased, bombardment of the growing films by negative oxygen ions in the positive half cycle of the bias is increased leading to oxygen rich low density films. Hence as can be seen from fig. 3.2(b), for films deposited at >15% oxygen partial pressure without any substrate bias, density shows an increasing trend with increase in oxygen partial pressure, while for the other set deposited with substrate bias, density of the films does not increase, rather decreases slightly.

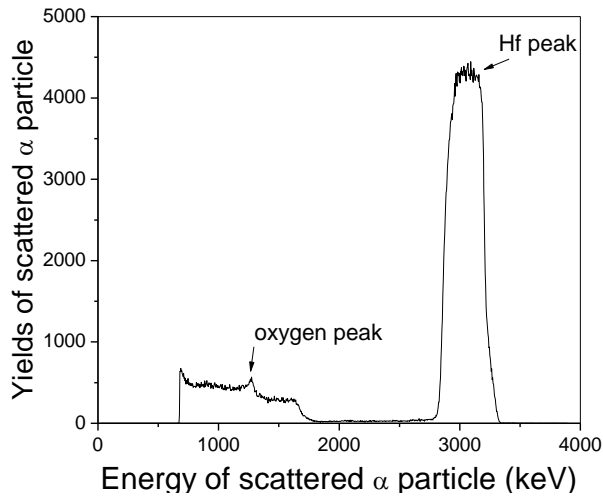


Fig. 3.2(a): RBS spectrum of a representative HfO_2 sample deposited without substrate bias and at 9.1 % oxygen partial pressure.

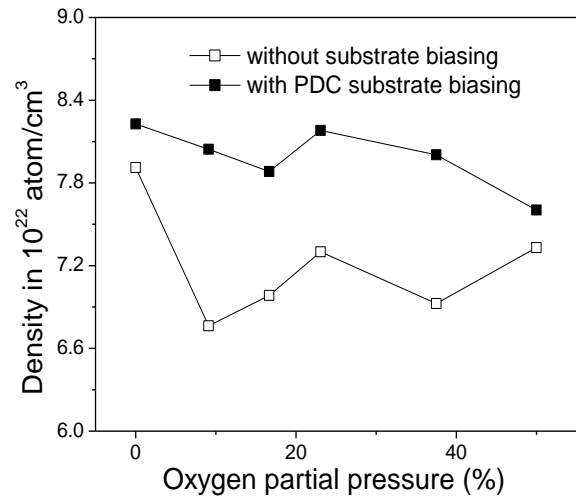


Fig. 3.2(b): Variation of atom number density of HfO_2 films, estimated from RBS spectra, as a function of oxygen partial pressure.

3.5 Grazing Incidence X-ray Reflectivity measurements:

Densities of the films have been estimated by GIXR measurements carried out in an X-ray reflectometer. The measurements have been carried out with a Cu K_α (1.54\AA) source by varying the grazing angle of incidence in the range of $0-2^\circ$ with an angular resolution of

0.001°. Rocking curve measurements have been done prior to each measurement for aligning the sample.

Figure 3.3(a) shows the GIXR spectra of HfO_2 films deposited without substrate bias at different oxygen partial pressures. The density estimated from GIXR data employing the method described in Chapter-2, are shown in Fig. 3.3(b). The errors involved in the measurements are quite low ($\sim 0.1\%$) since critical angles can be measured very accurately due to the high precision goniometer of the GIXR system. It can be seen from fig. 3.3(b) that the decreasing trend for the density of the films deposited with substrate bias, with increasing oxygen partial pressure, as obtained from RBS measurements and shown in fig. 3.2(b) has also been reflected in the density of the films as obtained from GIXR measurements.

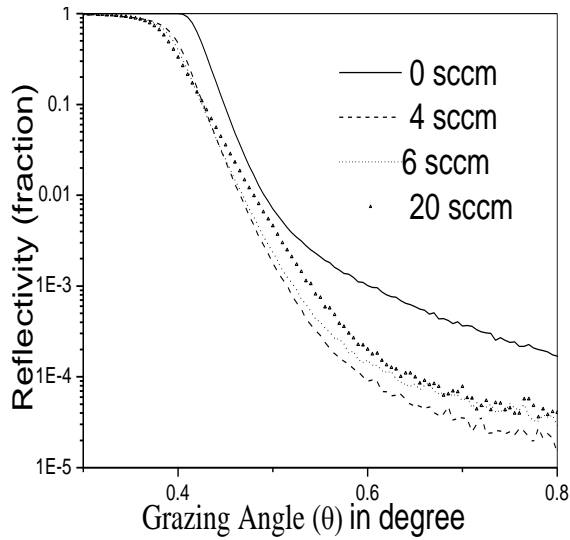


Fig.3.3 (a): Grazing incidence x-ray reflectivity spectra of HfO_2 samples deposited without substrate bias and at various oxygen flow rates.

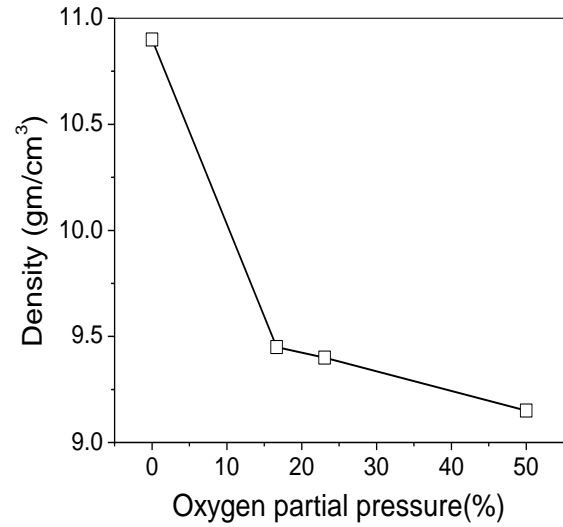


Fig.3.3 (b): Variation of density estimated from GIXR spectra as a function of oxygen partial pressure (in percentage) used during deposition for HfO_2 films deposited without substrate bias.

3.6 Optical Transmission measurements:

The refractive index, band gap and thickness of the films were estimated by optical transmission measurements using the Jasco V-630 UV-VIS-NIR spectrophotometer as described in Chapter-2 in the range of 190 nm to 1100 nm Figure 3.4(a) shows the transmission spectrum of a representative HfO_2 film deposited under pure argon ambient (i.e., without oxygen) and without any substrate bias. The transmission spectra of the samples were analyzed using the method described in Chapter-2, proposed by Swanepoel [64] to estimate thickness and wavelength dispersion of refractive index (n) and extinction coefficient (k). Typical error involved in the above spectrophotometric measurements of n and thickness for transparent oxide films like HfO_2 is $\sim 1\%$ [64, 88]. Deposition rates, as shown in Fig. 3.4(b), were calculated by dividing the estimated thickness of the films with the duration of depositions and are found to agree well with that obtained from the in-situ crystal monitor

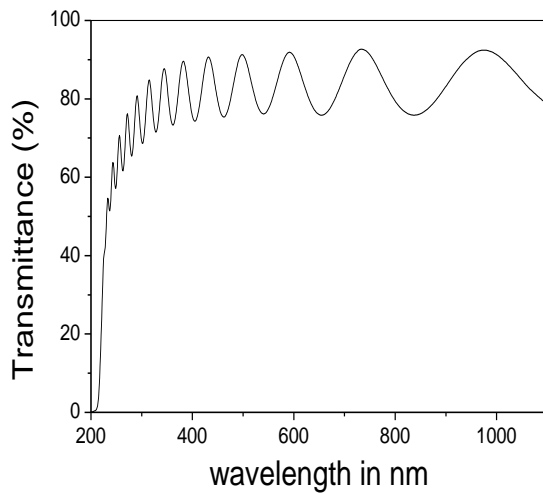


Fig. 3.4(a): Transmission spectrum of a representative HfO_2 sample deposited without substrate bias and at zero oxygen partial pressure.

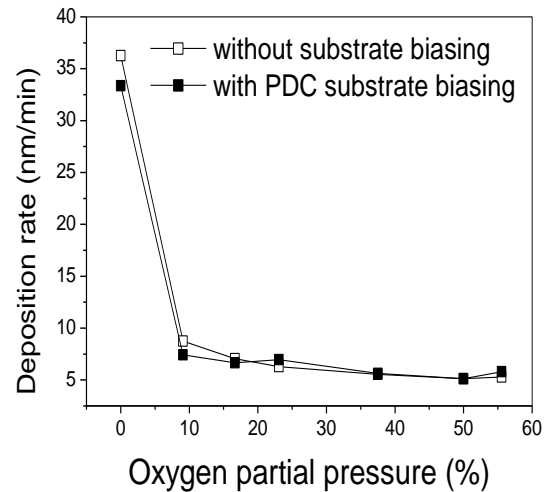


Fig. 3.4(b): Variation of deposition rates of HfO_2 films, obtained from transmittance measurements, as a function of oxygen partial pressure.

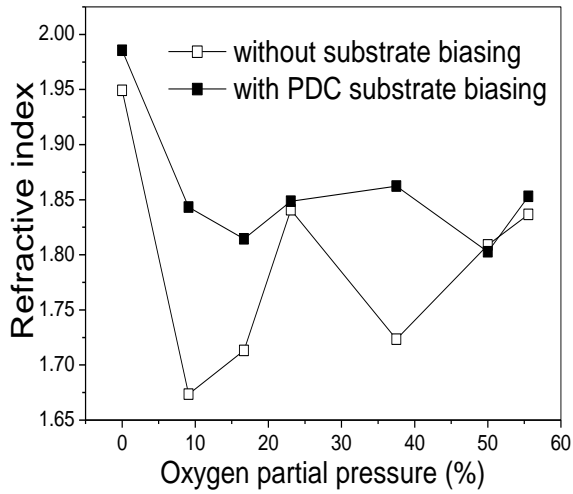


Fig. 3.4(c): Variation of refractive index of HfO₂ films at 550 nm, obtained from transmittance measurements, as a function of oxygen partial pressure (in percentage) used during deposition.

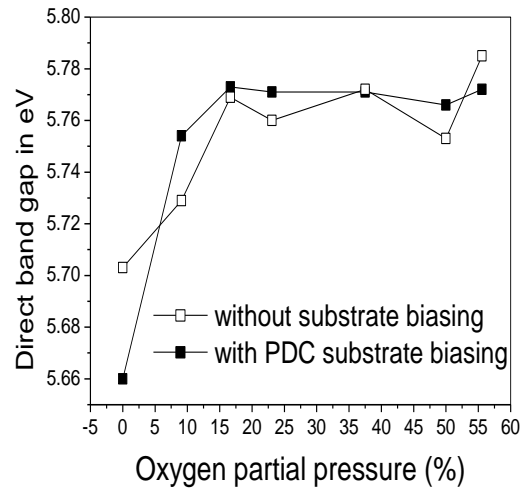


Fig. 3.4(d): Variation of band gap of HfO₂ films, obtained from transmittance measurements, as a function of oxygen partial pressure (in percentage) used during deposition.

measurements. It can also be seen that the deposition rate of the films decreases drastically with the onset of oxygen in the sputtering ambient and then decreases further slowly with increase in oxygen partial pressure. The gradual decrease in sputtering rate, as shown in fig. 3.4(b), with increase in oxygen partial pressure (for >10% oxygen partial pressure) might be due to the fact that sputtering efficiency of oxygen is less than that of argon. However, the large decrease in sputtering rate with onset of oxygen ambient cannot be solely due to the lower sputtering efficiency with oxygen. This can be attributed to reaction on the target surface leading to oxygen-rich compound formation that would result in sputtering of HfO₂ compound compared to preferential sputtering of Hf in oxygen-free ambient leading to metal-rich films. Drastic reduction in sputtering rate due to chemical reaction on target surface and compound formation is a typical characteristic of reactive sputtering [89].

The refractive indices of the films at 550 nm, as obtained from the transmission measurements, have been plotted in Fig.3.4(c), while the band gap of the films, as obtained

by plotting $(\alpha h\nu)^2$ vs. $h\nu$, (where $\alpha (=4\pi k/\lambda)$, k being the extinction coefficient, while λ and ν are the wavelength and frequency of photon) are shown in Fig. 3.4(d), with an error bar of ± 0.03 eV, which is typical of such high band gap dielectric films[90].

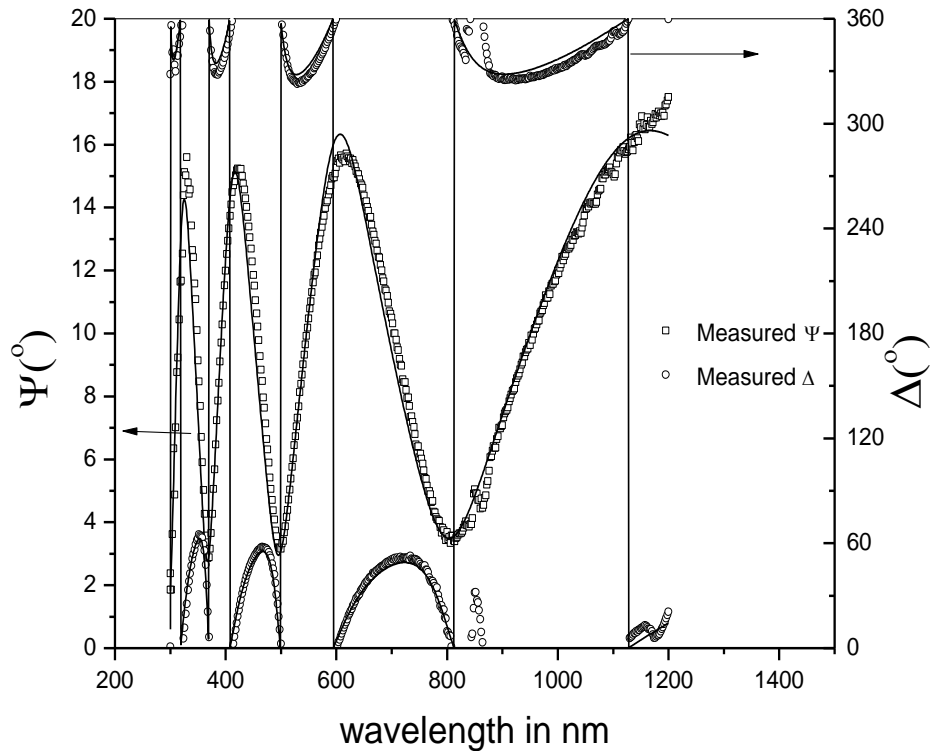
The refractive index of the samples @ 550 nm, as can be seen from Fig. 3.4(c), lies in the range of 1.7-2.0. This agrees well with the refractive index values reported by other workers for HfO₂ films deposited by various techniques viz., MOCVD, magnetron sputtering, e-beam evaporation etc. [91-94]. It can also be seen from the above figure that the refractive index of the films deposited without oxygen is very high due to high metal content in these films. The refractive index decreases for both set of the films when deposited with 9.1% oxygen partial pressure due to realisation of more stoichiometric films. In general, the refractive index of the films deposited with substrate bias is higher than that deposited without substrate bias, because of the realisation of denser and more compact films in the later case due to the reasons discussed above. It can also be seen from this figure that with increase in oxygen partial pressure, refractive index shows an increasing trend for films deposited without substrate bias, while it remains more or less constant for films deposited with substrate bias. The observed difference in the variation of refractive index with oxygen partial pressure in the two set of films will however be explained at the end of this section.

The band gap of the films, as can be seen from fig.3.4(d), deposited without oxygen or at oxygen partial pressure of 9.1% are considerably low manifesting high Hf content in these films which is corroborated with our observations of high density of these films by RBS and GIXR measurements also. The band gap of the films achieves higher value appropriate for stoichiometric HfO₂ films when deposited at oxygen partial pressure of 15% or above. The band gap values remain more or less constant for these films irrespective of oxygen partial

pressure or biasing used during deposition and agrees well with that reported by other workers [95-96].

3.7 Spectroscopic ellipsometric measurements:

Detailed optical characterisation of the films was subsequently carried out by spectroscopic ellipsometric measurements in the phase-modulated spectroscopic ellipsometer (ISA JOBIN-YVON SPEX, France), as described in Chapter-2, in the wavelength range of 300-1200 nm [67, 97]. Figure 3.5 shows the experimental ellipsometric (Ψ and Δ) spectra over a wavelength range of 300-1200 nm for a representative HfO_2 films deposited at ~23.1 % oxygen partial pressure without substrate bias.



**Fig.3.5: Experimental Ψ and Δ versus wavelength along with best-fit theoretical curve for a representative HfO_2 film deposited without substrate bias and at 23.1% oxygen partial pressure (in percentage).
oooo: Experimental Data; ———: Theoretical fit.**

The measured ellipsometry spectra are then fitted with an appropriate model assuming a realistic sample structure for an oxide film with two layers, one bulk layer on the substrate and another void-prone thinner layer at the top which takes care of the surface roughness of the film[90]. The optical constants of the quartz substrates have been supplied from standard reference [98] and the Tauc-Lorentz (TL) model [68] as described in Chapter-2, has been used to describe wavelength dispersion of the optical constants of the HfO₂ layers.

Since thin film deposition by physical vapour deposition processes is in general characterized by presence of voids in the layers, some amount of void has been assumed to be present homogenously in the bulk layer also and the calculation of the effective dielectric constant of the layers has been done using the Bruggeman Effective Medium Approximation (EMA) model [99] as mentioned in Chapter-2.

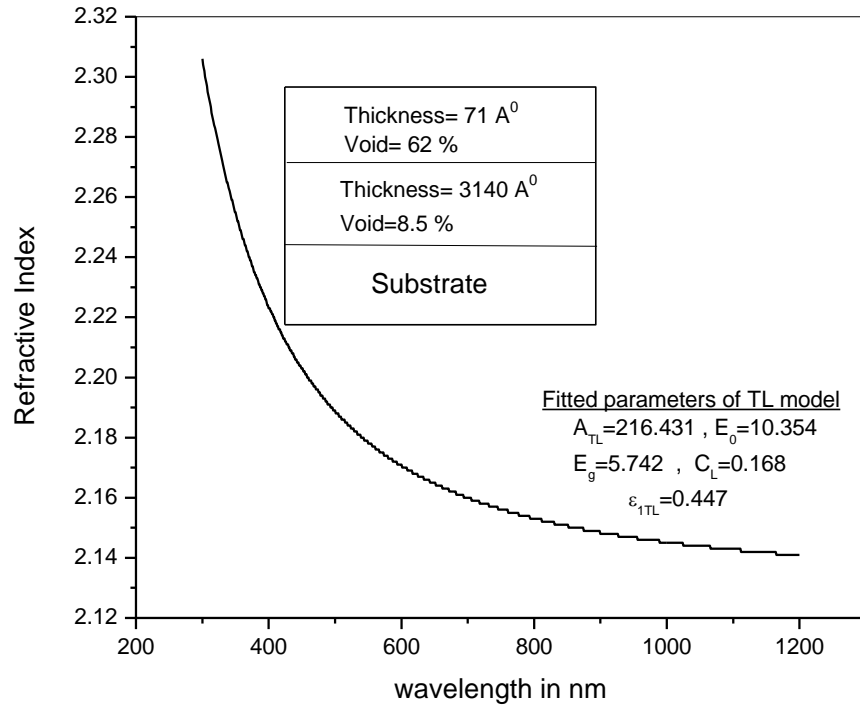


Fig.3.6: Sample structure and the fitting parameters of used TL model along with the dispersion of refractive index for a representative HfO₂ thin film deposited with substrate bias and at 23.1 % oxygen partial pressure.

Assuming the above sample structure, with trial thicknesses, void fractions and parameters of dispersion relation for HfO_2 as fitting parameters, the measured ellipsometric spectra are fitted with that of the simulated spectra and the best fitted spectra for a representative sample is shown in fig. 3.5. Fig. 3.6 shows the sample layer structure model and the dispersion of refractive index generated with the best fit parameters for the representative sample with an accuracy of ± 0.003 which is typical for spectroscopic ellipsometric measurements[14]. After carrying out the above exercise on all the HfO_2 samples under study, the obtained void fractions present in the bulk layer and refractive index of the bulk layer of the films (at 550 nm) are shown in Fig. 3.7(a) and (b) respectively. It should be noted that voids present in the bulk layers are true representation of the void fractions present in the films since the bulk layers constitute $\sim 98\%$ of the total thickness of the films. It can be seen that void fraction in the films, does not show any particular trend of change for films

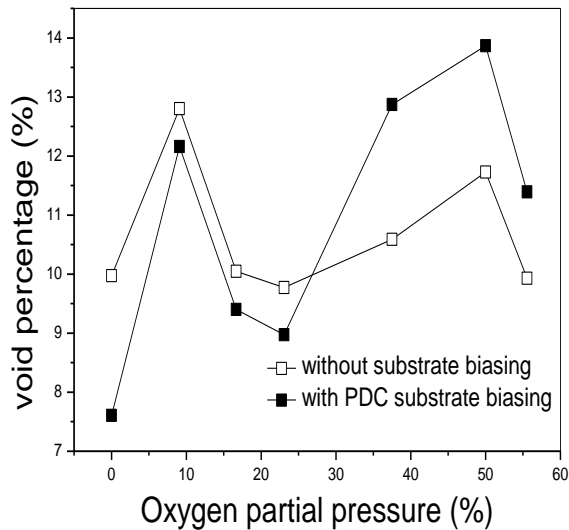


Fig.3.7 (a): Variation of effective void percentage present in the HfO_2 films as a function of oxygen partial pressure used during deposition.

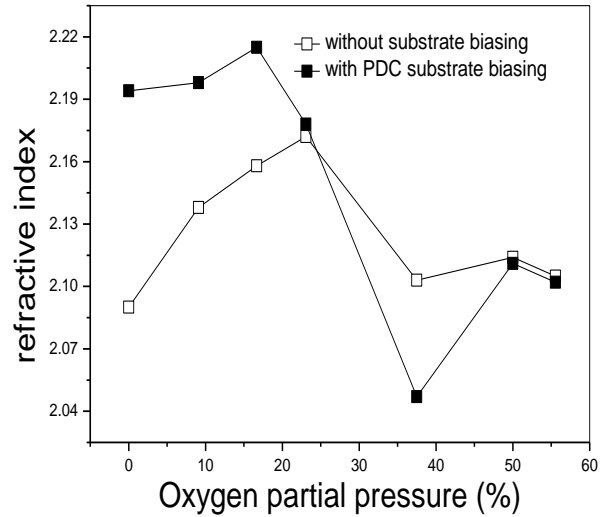


Fig.3.7 (b): Variation of intrinsic refractive index of HfO_2 at 550 nm as a function of oxygen partial pressure used during deposition.

deposited without substrate bias though it shows an upward trend for the other set of films deposited with substrate bias. The refractive index of bulk HfO_2 layer is found to initially increase with an increase in oxygen partial pressure used during deposition, which however decreases again, with increase in oxygen partial pressure beyond 20%. It can be seen from Fig. 3.7(a) that the void fraction of HfO_2 films as obtained from the ellipsometric analysis lies in the range of 7.5% to 13.9%. Zaharescu et al. [100] have compared the porosity in HfO_2 films prepared from different precursor by sol-gel method where they got minimum porosity of 4.35% when prepared from Hf-pentadionate and maximum porosity of 56.80% when prepared from Hf-chloride precursor. Lu et al. [101] have studied the effect of annealing on the void percentage of HfO_2 thin film deposited by MOCVD, where they found 9.29% void for as-deposited film which decreases after annealing to 5%. Void fraction in the films, as can be seen from Fig. 3.7(a), does not show any particular trend of change for films deposited without substrate bias. For films deposited with substrate bias and low oxygen partial pressure void fraction is found to be less because of the compactness resulted from bombardment by Ar^+ ions on the growing films during the negative half cycle of the pulsed bias. However, for these films deposited with substrate bias, void fraction shows an overall increasing trend with increase in oxygen partial pressure due to enhanced bombardment of the growing films by negative oxygen ions in the other half cycle of the pulse.

It can be further observed that the refractive index values of the films as obtained from transmission measurements and shown in Fig. 3.4(c) are less compared to that obtained from ellipsometry measurements and shown in Fig. 3.7(b). This is due to the fact that the refractive index obtained from ellipsometry measurement is that of the HfO_2 material present in the sample, while that obtained from the transmission measurement is that of the whole film which will have lower refractive index because of the presence of voids in it.

Finally, if we exclude the films deposited at 0 and 9.1% oxygen partial pressure which are low band gap Hf-rich films, the variation of density and void content in the films, as shown in Figs. 3.2(b) and 3.7(a) respectively, has a direct correlation with the variation of overall refractive index of the films as obtained from transmission measurements and shown in Fig. 3.4(c). For films deposited without substrate bias, the void fraction does not show any particular trend of change and hence the refractive index of the films shows an overall increasing trend with increase in oxygen partial pressure due to increase in density of the films. However, for the other set of films deposited with substrate bias, refractive index does not increase significantly with increase in oxygen partial pressure, since void content in the films shows an overall increase hindering density to increase at higher oxygen partial pressure.

Finally, since the refractive index of the films deposited with substrate bias is generally higher than that obtained for films deposited without substrate bias, it can be concluded that better quality HfO₂ films with lower void fraction and higher refractive index can be obtained in case of deposition with substrate bias at lower oxygen partial pressure in the range of 15-30%.

3.8. EXAFS measurements:

The variation of intrinsic refractive index of the deposited material excluding the effect of void, as estimated from spectroscopic ellipsometry and shown in fig. 3.7(b), remains so far unexplained. The two main features of this variation are that the intrinsic or void-free refractive index for the set of samples deposited without substrate biasing case shows a peak around 23% oxygen partial pressure. On the other hand, void-free refractive index for the set of samples deposited with substrate biasing case shows a deep at ~37% oxygen partial

pressure. Structural study by GIXRD probe could not help in explaining these observations. This is why, we have carried out Extended X-ray Absorption Fine Structure (EXAFS) study on few representative samples from both the sets, namely the samples deposited at 0, 6, 12 and 25 sccm oxygen flow rates i.e. at 0%, 23.1%, 37.5% and 56% oxygen partial pressures to investigate whether these observations are linked to the local structural properties of the films.

The EXAFS measurements have been carried out at the Energy-Scanning EXAFS beam line (BL-9) at the INDUS-2 Synchrotron Source (2.5 GeV, 100 mA) at Raja Ramanna Centre for Advanced Technology (RRCAT), Indore, India [44, 79] following the procedures described in details in Chapter-2. Figures 3.8 (a) and (b) show the experimental EXAFS spectra (μ vs. E) of HfO₂ films deposited by RF magnetron sputtering under various oxygen partial pressures for the set of samples deposited without and with pulse DC substrate bias respectively. Although HfO₂ can exist in cubic (Fm-3m), tetragonal (P4₂/nmc), monoclinic (P2₁/c) and orthorhombic (Pbca and Pnma) phases; cubic and tetragonal phase stabilization is only possible [102] either by doping or by synthesizing at higher temperature (>1700°C). Therefore, to analyze the EXAFS spectra of present HfO₂ samples, which were prepared from 99.99% pure HfO₂ target and at relatively lower substrate temperature, possibility of having monoclinic and orthorhombic phases have been explored. The theoretical standards for monoclinic and orthorhombic HfO₂ crystal structure was created using lattice parameters and Wyckoff positions obtained in the literatures [103-104]. The scattering paths used for simulating EXAFS spectra of monoclinic HfO₂ samples have been tabulated in Table-3.1. While fitting with the monoclinic model, paths 1 to 7, which represent the first few oxygen shells were combined and were represented by a single scattering path with degeneracy 7. Similarly, path-8 to path-21 were represented by a single Hf-Hf scattering path of degeneracy

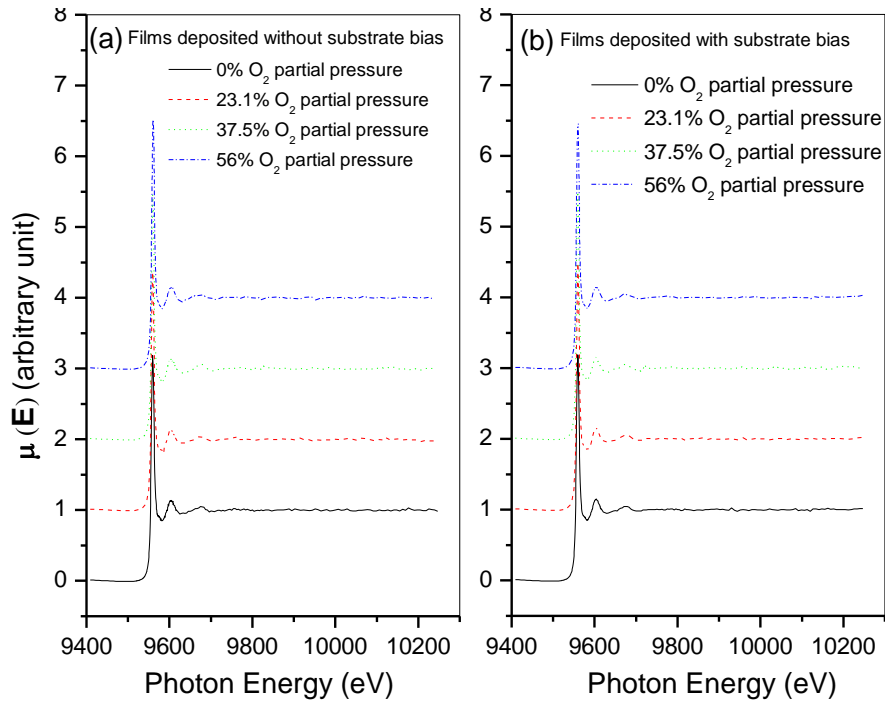


Fig.3.8: Experimental $\mu(E)$ vs. E spectra of HfO_2 thin films deposited under different oxygen partial pressures for the set of samples deposited without substrate bias (a) and with pulsed DC substrate bias (b).

7 and paths 45 and 51 were represented by another single Hf-Hf scattering path of degeneracy 4. As for orthorhombic phase model, the scattering paths used for simulating EXAFS spectra have been tabulated in Table-3.2. While fitting, paths 1 to 7, which represent the first few oxygen shells were combined and were represented by a single Hf-O scattering path with degeneracy 7. Similarly, path-8 and path-9 were represented by another single Hf-O scattering path of degeneracy 2 and path-10 and path-11 were represented by a single Hf-Hf scattering path of degeneracy 3.

Table-3.1: Scattering paths used for simulating EXAFS spectra of monoclinic HfO₂ samples.					
Model of structure	Path No.	Degeneracy	Distance (Å)	Amplitude	Scattering paths considered
Monoclinic	Path-1	1	2.054	100	[+] O1_1 [+]
	Path-2	1	2.063	99.01	[+] O1_2 [+]
	Path-3	1	2.138	90.78	[+] O2_1 [+]
	Path-4	1	2.147	89.91	[+] O1_3 [+]
	Path-5	1	2.162	88.34	[+] O2_2 [+]
	Path-6	1	2.213	83.45	[+] O2_3 [+]
	Path-7	1	2.217	83.08	[+] O2_4 [+]
	Path-8	1	3.346	35.91	[+] Hf_1 [+]
	Path-11	2	3.398	69.59	[+] Hf_2 [+]
	Path-12	2	3.404	69.32	[+] Hf_3 [+]
	Path-14	1	3.425	34.23	[+] Hf_4 [+]
	Path-21	1	3.528	32.15	[+] Hf_5 [+]
	Path-45	2	3.929	50.47	[+] Hf_6 [+]
	Path-51	2	4.017	47.90	[+] Hf_7 [+]

Table-3.2: Scattering paths used for simulating EXAFS spectra of orthorhombic HfO₂ samples.					
Model of structure	Path No.	Degeneracy	Distance (Å)	Amplitude	Scattering paths considered
Orthorhombic	Path-1	1	2.05	100	[+] O1_1 [+]
	Path-2	1	2.105	93.8	[+] O1_2 [+]
	Path-3	1	2.155	88.6	[+] O2_1 [+]
	Path-4	1	2.163	87.81	[+] O1_3 [+]
	Path-5	1	2.166	87.5	[+] O2_2 [+]
	Path-6	1	2.188	85.36	[+] O2_3 [+]
	Path-7	1	2.192	84.98	[+] O2_4 [+]
	Path-8	1	3.331	28.17	[+] O1_4 [+]
	Path-9	1	3.352	27.66	[+] O1_5 [+]
	Path-10	2	3.393	68.76	[+] Hf1_1 [+]
	Path-11	1	3.402	34.19	[+] Hf1_2 [+]

The above exercise has been carried out to keep the number of independent parameters that can be varied during fitting, less than the maximum number of independent data points available (N_{in}) as defined by Nyquist criterion [78]:

$$N_{in} = \frac{2 \cdot \Delta k \cdot \Delta R}{\pi} + 1 . \quad (3.1)$$

where, we have taken the Fourier transform range in k space as $2-9 \text{ \AA}^{-1}$ ($\Delta k = 7$) and fitting in R space as $1-3.5 \text{ \AA}$ ($\Delta R = 2.5$) respectively. As has been stated earlier, only three parameters viz., R , N and σ^2 of the different paths have been varied during the fitting process and the ΔE_0 and passive electron reduction factor (S_0^2) values have been taken from fitting of EXAFS data of commercial powder HfO_2 samples and have not been varied during fitting of EXAFS data of the thin film samples. Figure 3.9 (a) shows the Fourier transformed EXAFS (FT-EXAFS) spectra or $\chi(R)$ versus R plots of the HfO_2 films deposited at various oxygen partial pressures for the set of samples deposited without substrate bias along with the best fit theoretical plots generated using the monoclinic crystal structure. Similarly Fig. 3.9(b) shows the EXAFS fitting results for the above films using orthorhombic crystal structure. Corresponding plots for the set of films deposited with substrate bias are shown in Figs. 3.10(a) and (b) respectively. The qualities of fit in each case were assessed through estimation of R_{factor} as already been defined in equation (3). The R_{factor} values are shown in Figs. 3.11 (a) and (b) for the above two cases. As seen from Figs. 3.11 (a) and (b), R_{factor} values of monoclinic phase are less compared to that of the orthorhombic phase for both the set of samples manifesting that all the HfO_2 samples prepared for this study predominantly exhibit monoclinic phase. GIXRD pattern as displayed in fig. 3.1 for both set of samples also showed monoclinic crystal structure. It should be noted here that we have also carried out the fitting of the FT-EXAFS data assuming presence of mixed phases of monoclinic and orthorhombic structures also. The procedure adopted for mixed phase analysis is similar to that described in Chapter-5 of this thesis in case of TiO_2 films [105]. However, we have found that the R_{factor} values in that case are close to that obtained in case of fitting with monoclinic phase only and the relative contributions of the monoclinic phase as estimated from mixed phase fitting is

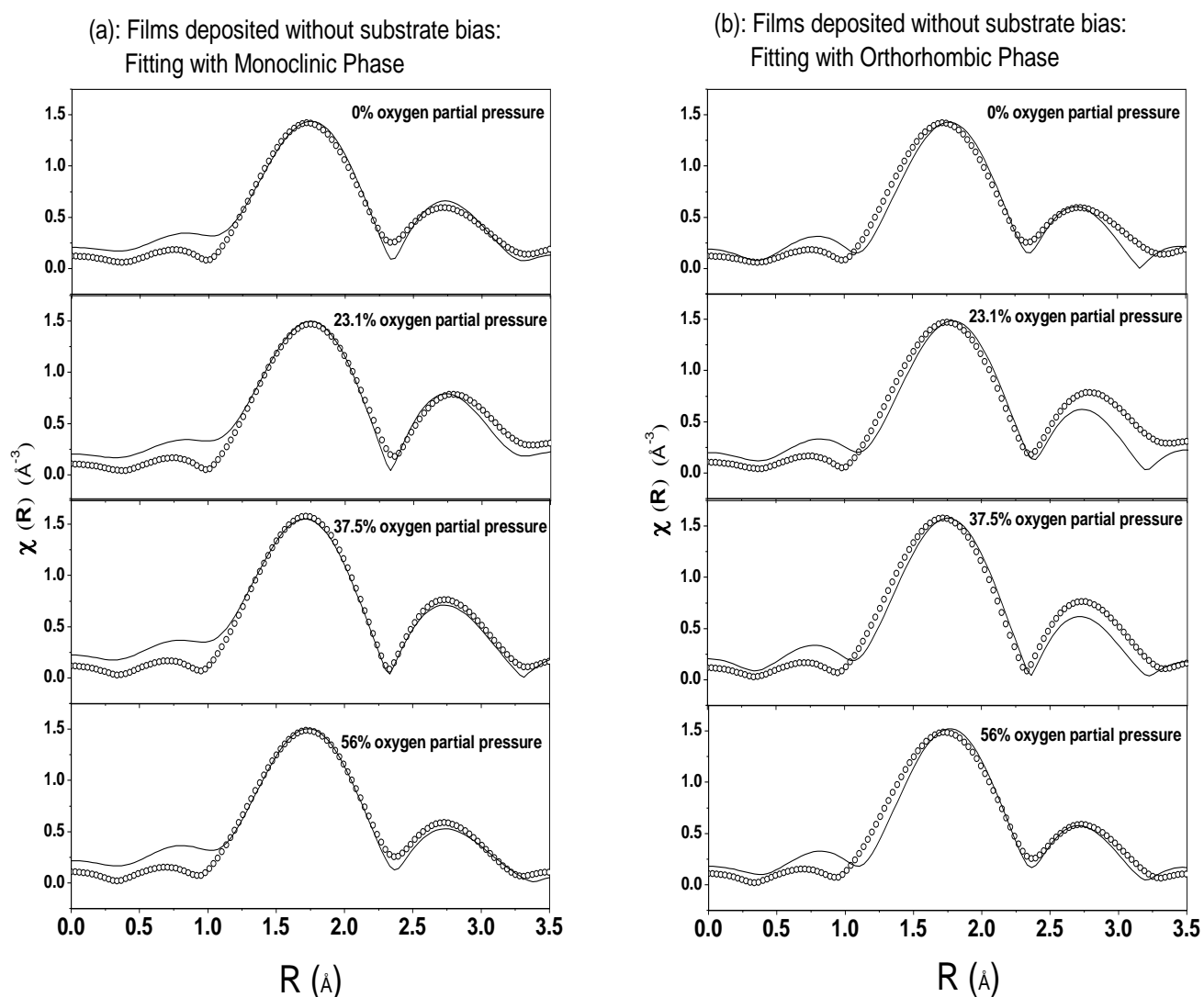


Fig.3.9: Fourier transformed EXAFS spectra of HfO_2 films deposited under different oxygen partial pressures for the set of samples deposited without any substrate bias along with best fit theoretical plots.

o-o-o-o: Experimental Data

- (a) -----: Theoretical fitting with monoclinic structure.
 (b) -----: Theoretical fitting with orthorhombic structure.

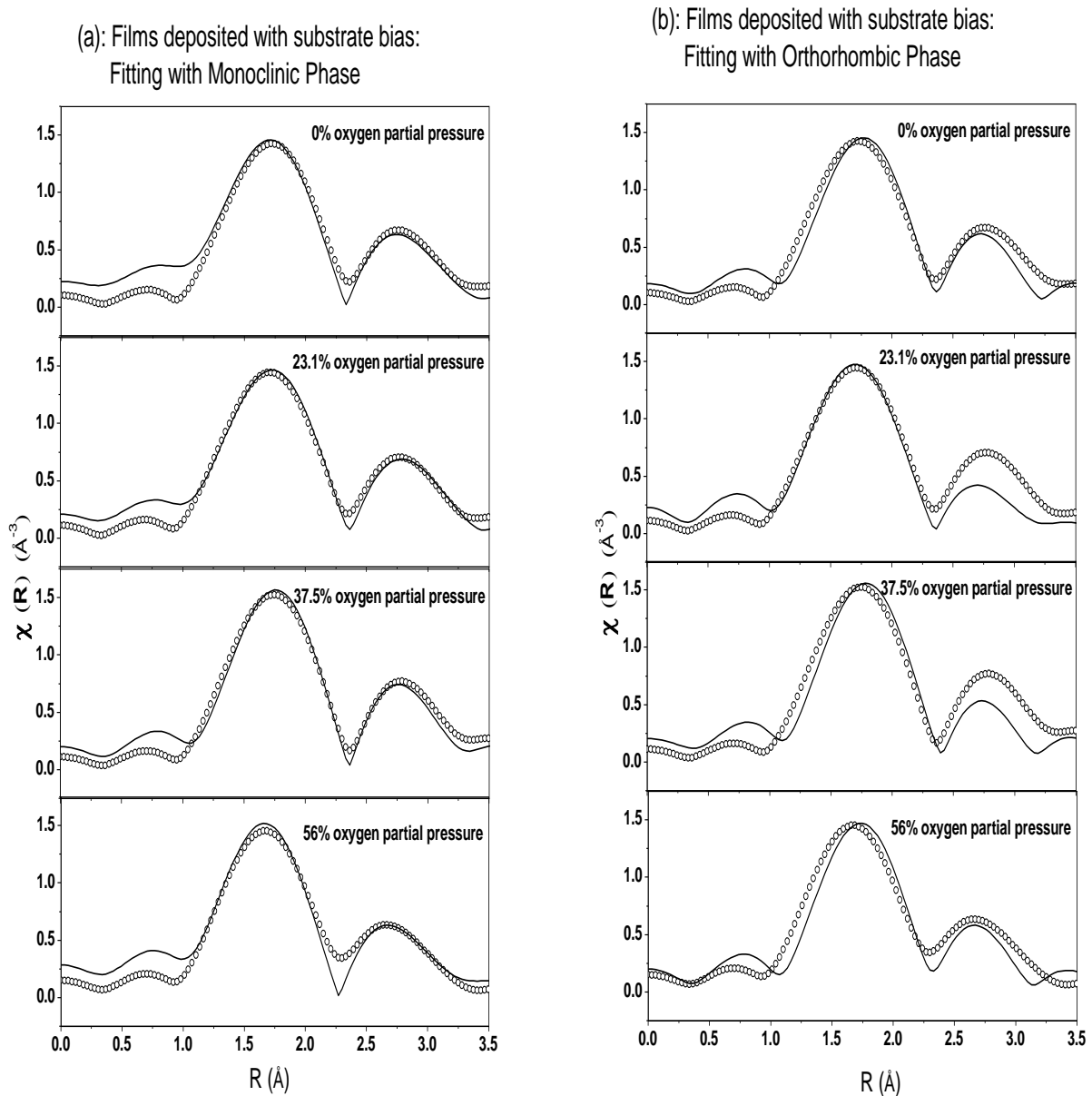


Fig.3.10: Fourier transformed EXAFS spectra of HfO_2 films deposited under different oxygen partial pressures for the set of samples deposited with pulsed DC substrate bias along with best fit theoretical plots.

o-o-o-o: Experimental Data

(a) -----: Theoretical fitting with monoclinic structure.

(b) -----: Theoretical fitting with orthorhombic structure.

almost 100% in the samples. Thus the rest of the results of the samples have been described based on the best fit parameters obtained in case of fitting with monoclinic phase only. It should also be noted here that HfO_2 thin films obtained by RF magnetron sputtering by

Vargas et. al [106] are amorphous in nature when deposited at substrate temperature below 200°C, while the films grown at substrate temperatures higher than 200°C are nanocrystalline

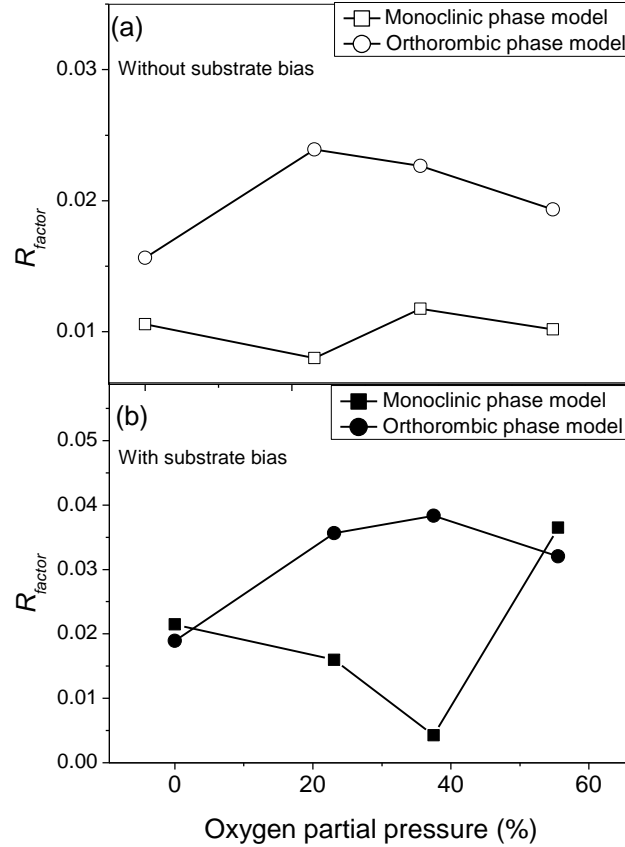


Fig. 3.11: Comparison of R_{factor} values of EXAFS fitting for HfO_2 thin film samples fitted with monoclinic and orthorhombic structure.

(a) Films deposited without any substrate bias.

(b) Films deposited with pulsed DC substrate bias.

in nature and exhibit monoclinic crystal structure. On the contrary, we have obtained monoclinic crystal structure in the samples prepared even when the substrate temperatures were in the range of 60-80°C. One of the reasons behind the different results obtained by us and Vargas et al.. [106] could be the higher target to substrate distance (80 mm) used by the later group compared to us (58 mm). Degradation in crystallinity with the increase in target to substrate distance due to the corresponding reduction in ad atom kinetic energy has been

reported by Thaveedetrakul et al. [107] also. This is to be noted that Ma et al. [40] have also obtained monoclinic HfO₂ thin films by reactive magnetron sputtering technique using pulsed power at 50 mm of target to substrate distance and ambient substrate temperature. Another reason why Vargas et al.[106] obtained amorphous films could be that they have used 100 W of magnetron power in contrast to 250 W of power in our case. Higher magnetron power increases kinetic energy of ejected adatoms which helps in realizing better crystallinity in the films [108]. Figs. 3.12(a)-(d) show the variation of the bond length and co-ordination numbers corresponding to the nearest Hf-O shell (R_o, N_o) and next nearest Hf-Hf shell (R_{Hf}, N_{Hf}) of the HfO₂ samples as a function of oxygen partial for the set of samples deposited without substrate biasing. Figs.3.13 (a)–(d) show the corresponding plots for the films deposited with substrate bias. The trend of variation of intrinsic refractive index of the HfO₂ films (n) as obtained from spectroscopic ellipsometry measurements and shown in fig. 3.7(b) for both the sets are reproduced again in fig. 3.12(e) and 3.13(e) respectively for the set of films deposited without and with substrate biasing. The uncertainties involved in measurement of bond length ($\pm 0.01 \text{ \AA}$), co-ordination number (± 0.1) and refractive index (± 0.003) are also shown in the above figures as error bars. As can be seen from Fig. 3.12(a), Hf-O bond length (R_o) is $\sim 2.16 \text{ \AA}$ throughout the whole oxygen partial pressure range except for the sample deposited at 37.5% oxygen partial pressure where it is 2.13 \AA . Thus the variation of R_o for the set of samples deposited without substrate bias, is not so significant considering the uncertainty in determination of bond length being $\pm 0.01 \text{ \AA}$. However, from Fig. 3.12(b) it is seen that, with the increase in oxygen partial pressure up to 37.5%, oxygen co-ordination around hafnium (N_o) increases from 6.4 to 6.9 which is significant w.r.t. the uncertainty involved in the measurement of coordination number (± 0.1), though with further

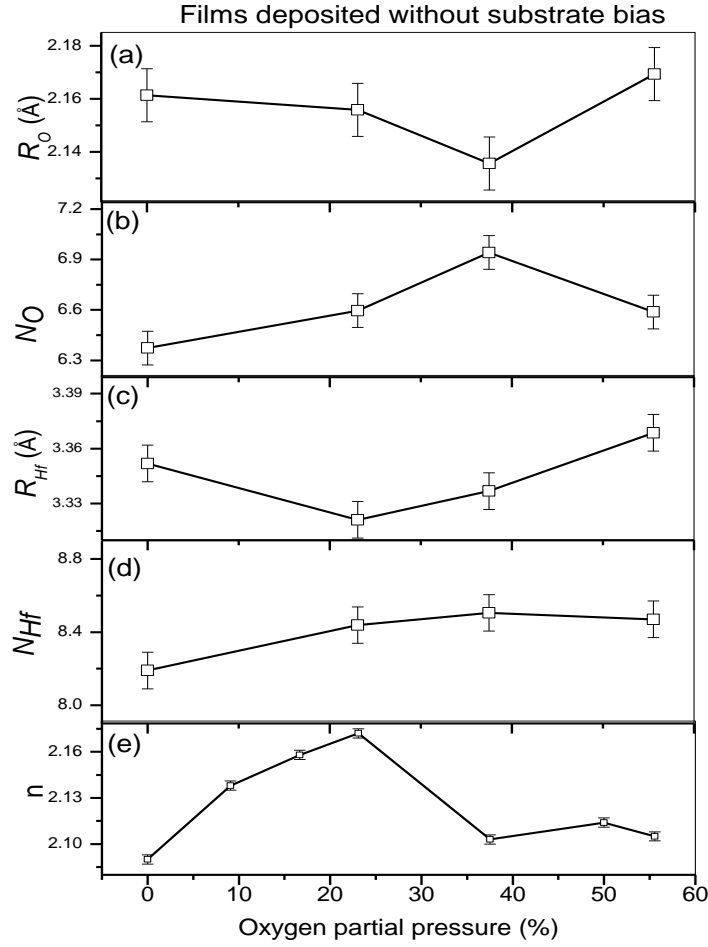


Fig.3.12: Variation of (a) Hf-O bond length (R_o) & (b) oxygen coordination (N_o) of nearest neighbor oxygen shell, (c) Hf-Hf distance (R_{Hf}) & (d) Hf coordination (N_{Hf}) of next nearest neighbor Hf shell, and (e) intrinsic refractive index (n) of HfO₂ thin films at 550 nm as obtained from spectroscopic ellipsometry measurements, as a function of oxygen partial used during deposition, for the set of films deposited without substrate bias.

increase in oxygen partial pressure, oxygen co-ordination does not increase, rather decreases.

The reduction in oxygen coordination with increase in oxygen partial pressure beyond ~40% in sputtering ambient has also been observed by us in case of bipolar pulsed DC sputter deposited Ta₂O₅ films which had been corroborated by RBS measurement also [55]. This might be related to reduction in reactive sputtering rate due to the presence of excess oxygen compared to argon atoms in the sputtering ambient.

As can be seen from Fig. 3.12(c), Hf-Hf bond length (R_{Hf}) decreases from 3.35Å to 3.32Å with an increase in oxygen partial pressure in the range of 0-23%, however with further increase in oxygen partial pressure beyond 23%, bond length increases to 3.37Å. The variation is significant considering the uncertainty in bond length determination of ± 0.01 Å. This trend of variation of R_{Hf} is almost reverse to the variation of intrinsic refractive index (n) of the samples as displayed in Fig.3.7 (b) and reproduced in Fig. 3.12(e). The reverse trend of variation in the intrinsic refractive index with respect to Hf-Hf bond length is due to the fact that reduction in Hf-Hf bond length can cause significant increase in density of the sample which in turn increases its refractive index. Mass of Hf atom (mass no 178) being about eleven times higher than O atom (mass no 16), it is likely that any change in Hf-Hf bond length will have more dominant effect on density or refractive index of the samples than change in Hf-O bond length. Similar increase in refractive index due to decrease in bond lengths have also been observed earlier in several other oxide systems [15, 109]. However, in case of the HfO₂ films deposited with substrate bias, as can be seen from Figs. 13(c) and (e), intrinsic refractive index (n) is not maximum for the sample deposited with 37.5% oxygen partial pressure, which has minimum Hf-Hf bond length (R_{Hf}), rather the n value is quite low for this sample. This is due to the fact that the oxygen coordination (N_o) is also very low for this sample as can be seen from Fig. 13(b). Thus the intrinsic refractive index of this set of samples deposited with substrate bias, does not follow the opposite trend of variation in the Hf-Hf bond length for the samples, unlike the case for the set of samples deposited without substrate bias.

It should be noted here that the variation of oxygen coordination with increase in oxygen partial pressure, for the set of films deposited without substrate bias, as shown in Fig.

12(b), follows the same trend as observed by us in case of sputter deposited Ta₂O₅ thin films [55]. However, as can be seen from Fig. 13(b), similar variation for the set of films deposited with substrate bias shows an opposite trend. As has been mentioned earlier and described in detail in chapter-2, the substrate bias used for the preparation of this set of samples is a pulsed

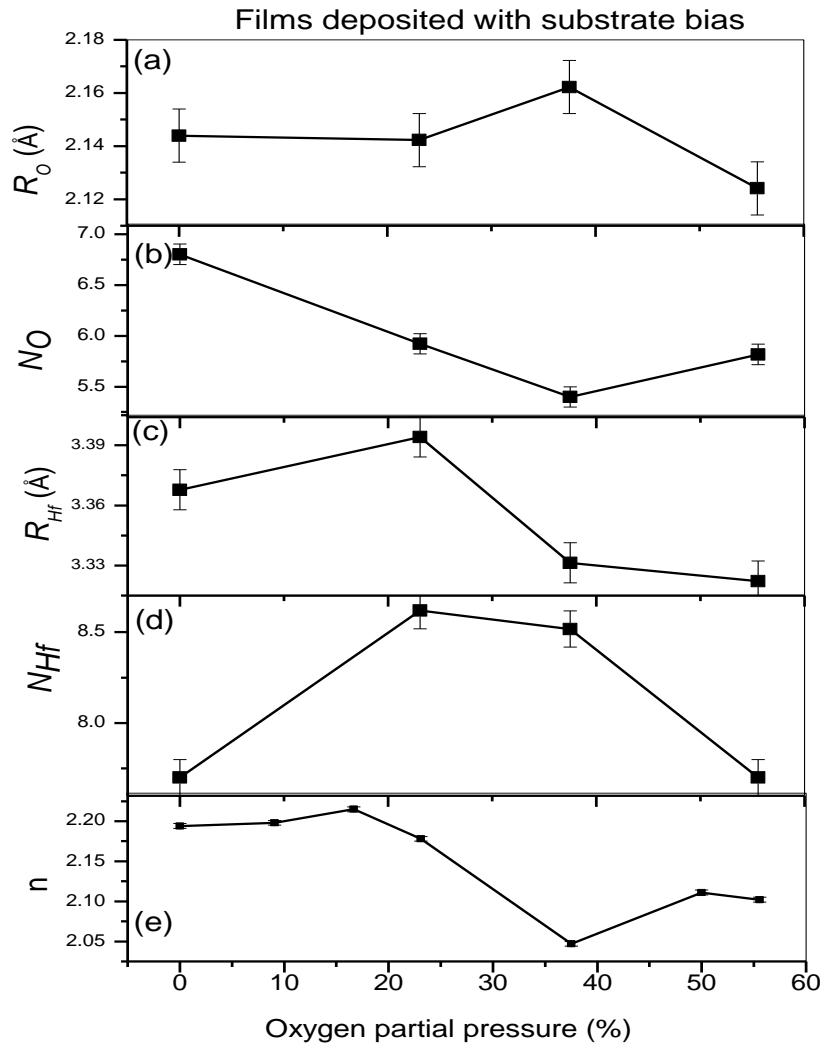


Fig.3.13: Variation of (a) Hf-O bond length (R_o) & (b) oxygen coordination (N_o) of nearest neighbor oxygen shell, (c) Hf-Hf distance (R_{Hf}) & (d) Hf coordination (N_{Hf}) of next nearest neighbor Hf shell, and (e) intrinsic refractive index (n) of HfO₂ thin films at 550 nm as obtained from spectroscopic ellipsometry measurements, as a function of oxygen partial pressure used during deposition, for the set of films deposited with pulsed DC substrate bias.

DC bias of 50Watt having a rectangular pulse shape with pulse frequency of 250 kHz and pulse width or pulse-on time of 1456 ns. The amplitude of the pulse is -98 V during -ve half-cycle (when the growing film on the substrate is bombarded with Ar^+ ions) and +37 V during the +ve half-cycle (when the growing film on the substrate is bombarded with O^- ions). The variation of oxygen coordination shows that for films deposited at lower oxygen partial pressure (20-40%), bombardment by Ar^+ ions is predominant resulting in oxygen loss from the films which yields non-stoichiometric films with low refractive index. However, for films deposited with oxygen partial pressure higher than 40%, oxygen ion bombardment on the growing films is significant which results in realisation of more stoichiometric and oxygen-rich films and refractive index of the films also increase. Thus the intrinsic refractive index of the films deposited with substrate bias is found to be governed by oxygen stoichiometry of the films rather than Hf-Hf bond length.

3.9 Conclusions:

HfO_2 thin films have been deposited on fused silica substrates by RF magnetron sputtering under mixed ambient of argon and oxygen. One set of films have been deposited at varying oxygen partial pressure in the range of 0-60% without any substrate bias. Another set was deposited with same ratios of argon to oxygen with pulse DC bias on the substrate. The films have been characterised by GIXRD, GIXR, RBS, Optical Transmission and Spectroscopic Ellipsometry (SE) measurements. For local structural characterizations, the samples have also been probed by EXAFS technique. The data were analysed and the following observations have been made:

- (i) HfO_2 films were found to be polycrystalline with predominantly monoclinic crystal

structure and crystallinity of the films gets degraded with increase in oxygen partial pressure during deposition.

(ii) For films deposited without oxygen and with 9.1% oxygen partial pressure, the densities are high but band gaps are low and overall refractive index as obtained from optical transmission measurements are high manifesting oxygen deficiency and high Hf content in the films.

(iii) Films deposited at 15% oxygen partial pressure achieve reasonably high band gap values and densities and over-all refractive indices of the films become lower showing realisation of stoichiometric films.

(iv) The SE measurements show that films deposited in the regime of 15-20% oxygen partial pressure have higher refractive indices compared to the films deposited at both lower and higher oxygen partial pressures which might be due to the non-stoichiometry effect. It is also observed that the refractive index of HfO_2 films deposited with substrate bias is in general higher than that deposited without substrate bias.

(v) In general, the density of the films deposited with substrate bias is found to be higher than that for the films deposited without substrate bias since enhanced bombardment of Ar^+ ions on the growing films in the negative half cycle of the pulsed bias leads to more compact and denser films. For films deposited at >15% oxygen partial pressure without any substrate bias, density shows an overall increasing trend with oxygen partial pressure, however for the other set deposited with substrate bias, density does not increase, rather decreases slightly. This is attributed to the fact that for the later set of films, as oxygen partial pressure is increased, enhanced bombardment of the growing films by negative oxygen ions in the positive half cycle leads to oxygen rich low density films.

(vi) The above observation is corroborated by the variation of void fraction in the films as obtained from SE measurements which shows that void fraction shows an overall increase with increase in oxygen partial pressure in the range of 15-60% for films deposited with substrate bias but it does not increase significantly for films deposited without substrate bias.

(vii) The variation of density and void content in the films finally get reflected in the variation of overall optical properties of the HfO_2 films as obtained from transmission measurements. Refractive index of the films deposited with >15% oxygen partial pressure and without substrate bias show an overall increasing trend with increase in oxygen partial pressure, due to increase in density. However, for the set of films deposited with substrate bias, refractive index does not increase significantly since density does not increase due to enhancement of void content in the films.

(viii) Finally we conclude that stoichiometric HfO_2 films with high band gap and refractive index and with low void content can be obtained with 15-30% oxygen partial pressure and with a substrate bias of 50 watt pulse DC on the substrate.

(ix) The information obtained from EXAFS measurement has been found to be correlated with the variation of intrinsic refractive index of the deposited material. For the set of HfO_2 films deposited without substrate bias, the variation of intrinsic refractive index of the films with oxygen partial pressure could be explained in terms of the variation of Hf-Hf bond lengths estimated from the EXAFS modelling. It has been observed that the film having lowest Hf-Hf bond length manifests the highest refractive index due to increase in compactness and density. However, for the set of films deposited with substrate bias it has been observed that refractive index does not follow the trend of variation of Hf-Hf bond length. Rather for this set of films, oxygen coordination surrounding Hf sites plays a major role. In this case, Ar^+ ion bombardment -ve cycle of PDC substrate bias causes oxygen loss

from the sample resulting in lower refractive index in the range of 20-40%, where as beyond 40% oxygen partial pressure, oxygen ion bombardment predominates which results in improved stoichiometric and high refractive index film. Thus EXAFS measurement and analysis provides a microscopic explanation of the macroscopic behaviour of intrinsic refractive index of the oxide films.

CHAPTER-4

Study on TiO₂ samples deposited at various oxygen partial pressures

4.1 Introduction:

Titanium dioxide being a large band gap and high index material has been of wide research interest for its application in multilayer optical interference coatings [110-111]. Excellent chemical stability of TiO₂ makes it an important choice for high index material in multilayer interference coatings [112]. It has also been used in various semiconductor devices like in sensors [113], photo catalysts [114] and transistors [115-116]. Several deposition techniques have been adopted to deposit TiO₂ films of the desired optical and electronic properties including sputtering [117], sol-gel [118], atomic layer deposition (ALD) [119], plasma enhanced chemical vapor deposition [120] etc. There are plenty of reports on structural investigation of TiO₂ thin films prepared by various methods, which reveal realization of the films in three major crystalline phases namely, rutile, anatase and brookite, even though brookite form of TiO₂ is comparatively less studied than the more common rutile and anatase polymorphs [121]. Addamo et al.. [122] demonstrated an easy way to prepare thin films of all three TiO₂ phases (anatase, rutile, brookite) starting from aqueous dispersions of TiO₂ obtained by hydrolysis of TiCl₄. Lin et al.. [123] identified anatase type TiO₂ nanoparticles prepared by sol gel synthetic route. An interesting study by Ohara et al. [124] showed that TiO₂ films prepared by sol suspension on silicon substrate shows pure anatase

phase whereas the one prepared on soda glass substrate is the mixture of anatase and brookite phases due to the Na diffusion from the substrate to the film. Reactive RF sputter-deposited undoped and Fe doped TiO_2 thin films [125] showed that undoped TiO_2 films crystallize in a mixed rutile/anatase phase whereas Fe-doped films exhibit the rutile phase only. Moret et al. [126] found that pulse laser deposited TiO_2 films on silicon and other substrates are brookite. In many cases formation of nano-crystalline and amorphous TiO_2 thin films have also been reported [127]

Even though electron beam (EB) evaporation technique [128] has been most widely employed for preparation of TiO_2 thin films, the method generally produces films with significant amount of voids. This drawback of EB evaporation technique encourages one to deposit dense TiO_2 films using ion assisted deposition (IAD), IAD though has limitation in producing large area multilayer thin films due to its inherent limitation pertaining to unavailability and high cost of large area ion sources [129]. As has been discussed in detail in earlier chapters, magnetron sputtering, on the other hand, has got several advantages in achieving improved morphology, microstructure and interfaces [37-39] of oxide thin films. Singh et al., for example, have used DC magnetron sputtering [130] to produce high quality TiO_2 thin films, having refractive index in the range of 2.24 to 2.5. Compared to the RF magnetron sputtering technique which is generally adopted for sputtering of insulating oxide materials, the asymmetric bipolar pulsed DC (ABPDC) magnetron sputtering technique makes it possible to overcome the problem of accumulation of space charge through a relatively simpler way that does not need any critical impedance matching of the load and the power supply and helps in producing high-quality, low-defect oxide dielectric films required for precise coating processes [34, 38-39, 130].

In the present study, a set of TiO₂ (titanium di-oxide) thin films has been deposited by asymmetric bipolar pulsed DC (ABPDC) sputtering technique using different oxygen partial pressures in the sputtering ambient. The samples have been characterized by grazing incidence X-ray diffraction (GIXRD) technique to probe the long range order in the films, while synchrotron-based extended X-ray absorption fine structure (EXAFS) measurements have been employed to investigate the local structure surrounding Ti atoms in the films and structural information obtained by the above two techniques have been compared. Further, optical transmission spectrophotometry has been used to investigate the optical properties of the films which have been correlated finally with the results of above structural investigations.

4.2 Preparation of samples:

TiO₂ thin films have been deposited on fused silica substrates by ABPDC magnetron sputtering technique using the system described in Chapter-2. For the present investigations, TiO₂ films were sputter deposited at six different oxygen flow rates, namely 0, 1, 3, 7, 9, 13 sccm vis-a-vis a constant argon flow rate of 50 sccm which corresponds to oxygen partial pressure of 0%, 2%, 5.6%, 12%, 15% and 21% respectively. The total pressure in the chamber was maintained at a fixed value by throttling the gate valve between the turbo pump and the deposition chamber. The detailed pulse shape of the power supply used during deposition has been given in Chapter-2. For the present study, an optimized pulse frequency of 127 KHz and optimized pulse width of 816 ns and a power level of 230 Watt were used to deposit the films. All the samples were deposited for 1 hour except the 0 sccm sample, which was deposited for 12.5 minute since the deposition rate for this film was significantly higher than that of the others. The substrates were kept at ambient during deposition; however it has

been observed that substrate temperature reaches up to 60-80°C during the process of deposition.

4.3. Grazing Incidence X-ray Diffraction measurements:

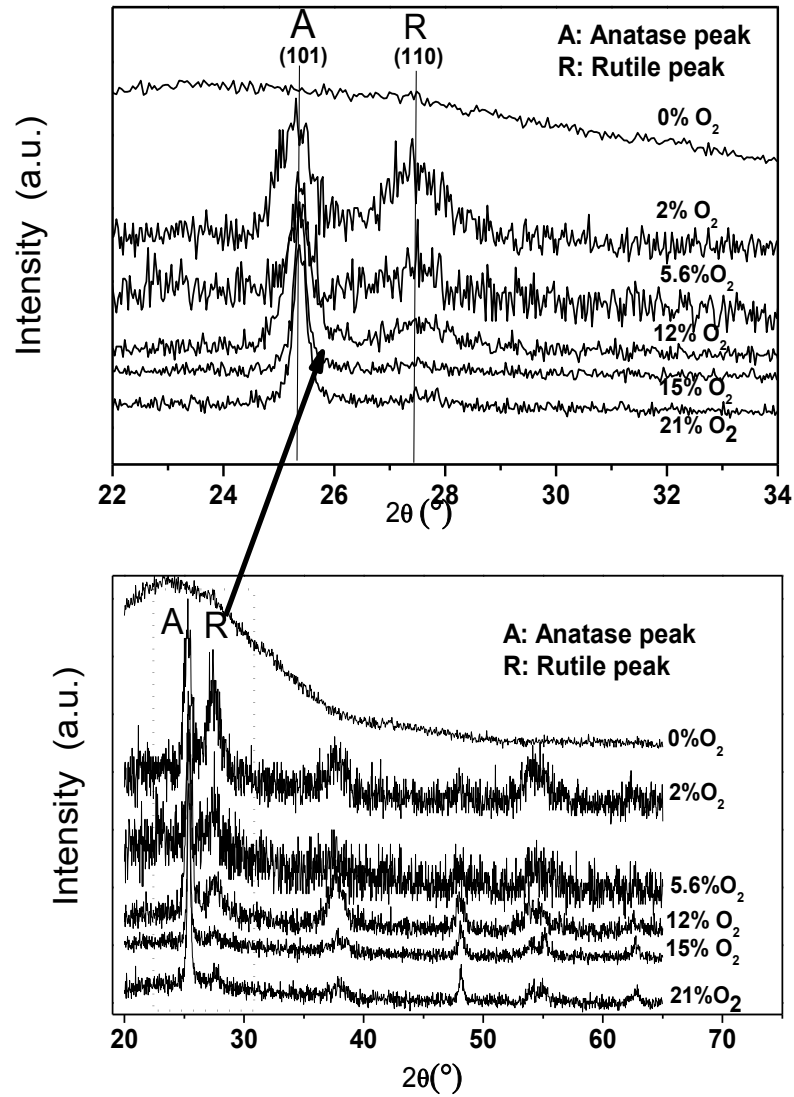


Fig.4.1: GIXRD plots of TiO₂ films deposited at various oxygen partial pressure (in percentage) used during deposition.

The grazing incidence X-ray diffraction experiments were performed on all the samples by detector scan method in the range of 2θ from 20° to 60° in step of 0.03° using a

Bruker D-8 discover diffractometer mounted on a sealed tube X-ray generator equipped with a copper target (k_{α}) operating at 3 kW output power. Fig. 4.1 depicts the GIXRD plots of the samples deposited at different oxygen partial pressures. The comparison of GIXRD plots of the samples with the standard PCPDF data [131] (PDF # 86-0147 & 84-1286) suggests that TiO_2 film deposited without oxygen in deposition ambient exhibits amorphous phase and all other samples deposited in partial oxygen ambient exhibit mixture of anatase and rutile phases. However, the intensity of the anatase phase (101) increases and that of the rutile phase (110) decreases with the increase in oxygen partial pressure.

As the deposition of anatase and rutile phase is related to the energy consideration [132], it is important to understand the energetic of the sputtered species at the substrate surface. Ti-O bonds being longer in rutile phase, Ti-O bond energy is less and hence Ti adatoms need to have higher kinetic energy on the surface of the growing films for the formation of the rutile Ti-O bonds. At lower oxygen pressure in the sputtering ambient, the deposition rate, as discussed later, is high leading to local heating of the growing surface, giving higher kinetic energy and mobility to the sputtered adatoms that ultimately leads to rutile phase formation [133]. As the oxygen partial pressure in the sputtering ambient increases, the deposition rate and hence the heating effect reduces and hence the adatoms have relatively lower kinetic energy and mobility on the growing surface leading to anatase phase formation. Apart from in reactive sputtering processes [134-135], this phenomenon has been observed in laser ablation and in pulsed laser deposition processes [136-138] also. The anatase phase fraction in the present set of samples have been estimated from the relative intensities of the anatase (101) and rutile (110) peaks following the procedure presented in ref. [139] and is plotted in fig. 4.2 as a function of oxygen partial pressure used during deposition.

It should be noted here that in the present case, the sample deposited at 0% oxygen partial pressure shows only amorphous phase in GIXRD measurements. It might be due to the fact that high deposition rate for the samples deposited at 0% oxygen partial pressure ($\sim 3.7 \text{ \AA/sec}$) prohibits the adatoms reaching on the substrate surface to find lower energy sites and this leads to amorphous TiO_2 phase. Lack of extra oxygen molecules to account for the stoichiometry may also play a crucial role in deciding the crystallinity of the deposited TiO_2 sample. With inclusion of oxygen during the deposition, sputtering rate decreases and TiO_2 grows in a crystalline phase.

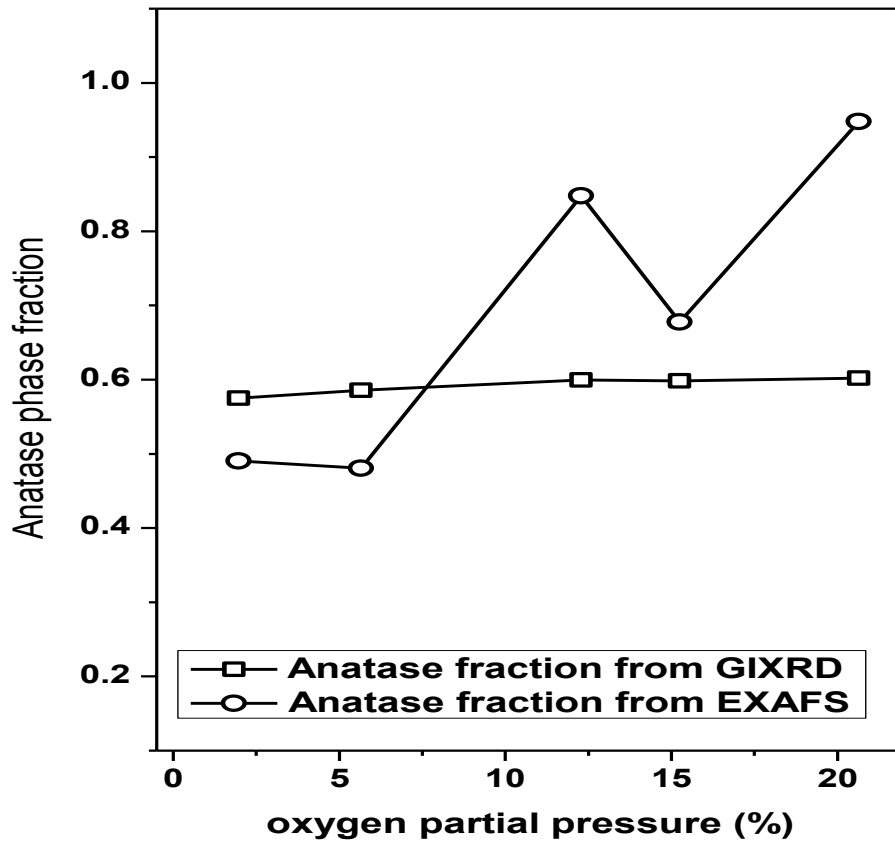


Fig.4.2: Variation of anatase phase fraction as a function of oxygen partial pressure used during deposition obtained from GIXRD and EXAFS measurements.

4.4 Optical Transmission measurements:

The optical properties of the films have been characterised by spectral transmission measurements in the range of 190 nm to 1100 nm by using the Jasco UV-VIS-NIR spectrophotometer described in Chapter-2. Fig.4.3 shows the transmission spectra of two representative TiO₂ films deposited under 0 and 21% O₂ partial pressure. It has been

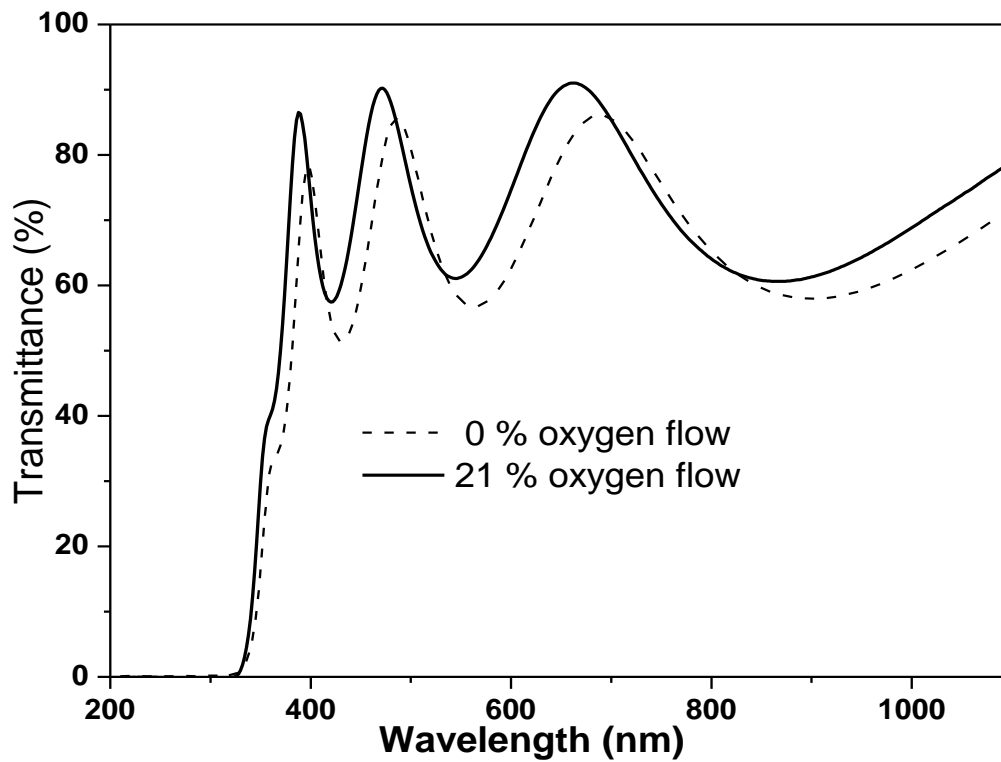


Fig. 4.3: Transmission spectra of two samples deposited at 0% (without any extra oxygen) and with 21% oxygen partial pressure in sputtering ambient.

observed that the overall transmission of the films is increased with increase in oxygen partial pressure possibly due to realisation of more and more stoichiometric films. The transmission spectra of the samples were analyzed using the method proposed by Swanepoel [64] and described in Chapter-2, to estimate thickness and wavelength dispersion of refractive index

(n) and absorption coefficient (α). The thickness of the films have been shown in Table-4.1, while the refractive indices of the samples at 550 nm as a function of oxygen partial pressure have been plotted in Fig. 4.4(a).

Table-4.1: Thickness of all the TiO₂ samples deposited under different oxygen partial pressures as estimated from transmission spectra.	
Oxygen Percentage (%)	Film Thickness (nm)
0	266 \pm 3
1.96	612 \pm 6
5.66	354 \pm 4
12.28	362 \pm 4
15.25	310 \pm 3
20.63	267 \pm 3

The band gap of the films has been obtained by plotting $(\alpha h\nu)^2$ vs. $h\nu$ curve in the region $\alpha > 10^4 \text{ cm}^{-1}$, λ and ν being the wavelength and frequency of the photon. The curve tends asymptotically towards a linear section the intersection of which to $h\nu$ axis gives direct band gap E_g of the film. Band gap values of the films as obtained above have also been plotted as a function of oxygen partial pressure in Fig. 4.4(b). It can be seen from Fig. 4.4(a) that refractive index (r.i.) of TiO₂ films varies in a non-linear fashion with the increase in oxygen partial pressure. R.I. of the non-stoichiometric Ti-rich film deposited without oxygen in sputtering ambient is found to be very high. It reduces to ~ 2.4 - 2.5 , which is a characteristic of anatase TiO₂ films, as oxygen partial pressure increases up to $\sim 12\%$. Subsequently refractive index of the films increases again to ~ 2.6 - 2.7 as oxygen partial pressure is

increased further. It can also be seen from Fig. 4.4(b) that, if the film deposited at 0% oxygen partial pressure is excluded, the band gap increases monotonically with increase in oxygen partial pressure. The increase in optical band gap with increase in oxygen partial pressure

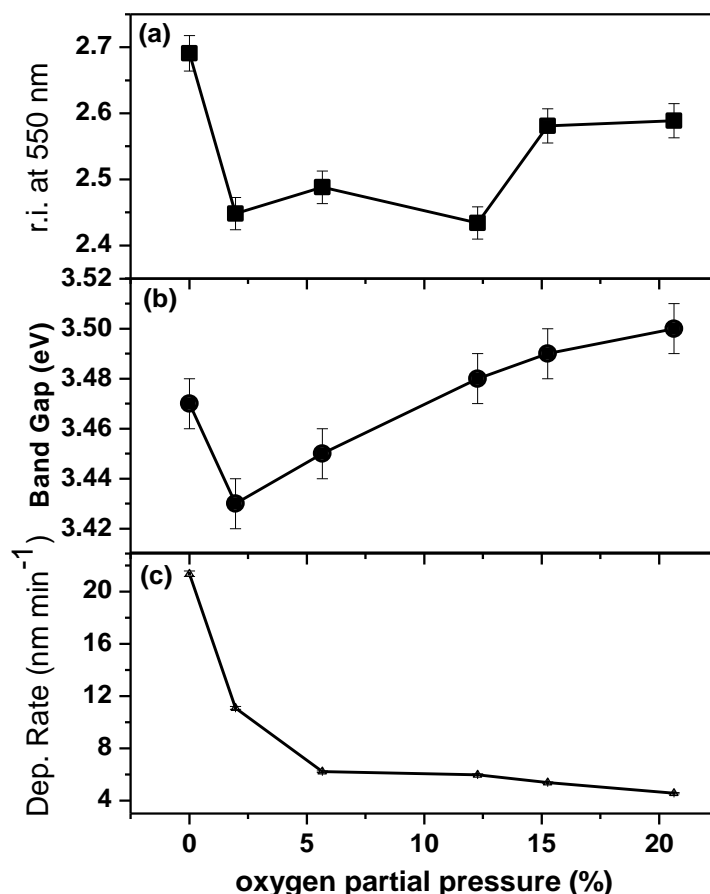


Fig.4.4: Variation of (a) refractive index @ 550 nm, (b) band gap and (c) deposition rate as obtained from transmittance measurements as a function of oxygen partial pressure (in percentage) used during deposition.

has been observed by other workers also in case of pulsed laser deposited TiO₂ films and has been attributed to realisation of more and more stoichiometric films with reduction in oxygen vacancies [138-139]. Fig.4.4(c) shows the variation in the rate of deposition of the TiO₂ films estimated from the thickness value obtained from spectrophotometric transmission measurements which shows that the deposition rate drastically decreases as oxygen partial

pressure is increased from 0% and then gradually decreases with increase in oxygen partial pressure in the range of 5.6-21%. Similar variation of the deposition or sputtering rate has been observed earlier by us in case of HfO₂ films as discussed in Chapter-3 and other workers also [85, 89]. As has already been discussed in Chapter-3, the lower sputtering efficiency of oxygen compared to that of argon causes the above gradual decrease in sputtering rate with increase in oxygen partial pressure in the range >5%. However, the drastic reduction in sputtering rate with the onset of oxygen in the sputtering ambient is due to reaction on the target surface leading to formation of oxygen-rich TiO₂ compound. The sputtering rate of TiO₂ compound is less compared to preferential sputtering of Ti in oxygen-free ambient and this also leads to metal-rich films.

4.5 EXAFS and XANES measurements:

Both EXAFS and XANES measurements of the samples have been carried out at the energy scanning EXAFS beam line (BL-9) in fluorescence mode at the INDUS-2 Synchrotron Source (2.5 GeV, 125 mA) at Raja Ramanna Centre for Advanced Technology (RRCAT), Indore, India [44, 79].as described in Chapter-2. Fig. 4.5 shows the experimental EXAFS spectra ($\mu(E)$ vs. E) of TiO₂ films deposited at different oxygen concentrations in the deposition ambient. It can be seen that though the GIXRD spectrum of the film deposited without extra oxygen in the ambient shows amorphous phase in the X-ray diffraction spectrum, the EXAFS spectrum is similar to that of other samples demonstrating the fact that the local structure in all the samples are more or less similar. Fig. 4.6 (a) shows the XANES spectra of all the samples measured in the energy range of 4950 eV to 5050 eV.

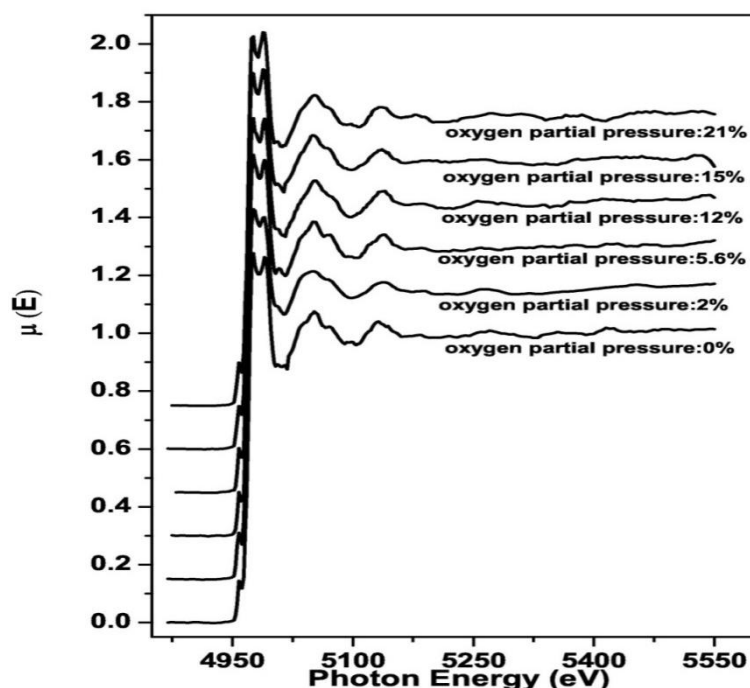


Fig.4.5: Absorption coefficient (μ) versus incident X-ray energy (E) of TiO_2 films deposited at different oxygen partial pressures.

Kravtsova et al. [140] have theoretically computed XANES spectra of both anatase and rutile TiO_2 on the basis of real space full multiple scattering theory. To compare the XANES spectra of our TiO_2 samples with the theoretically generated XANES spectra as mentioned above, we have indicated the small pre-edge peaks as A_1 , A_2 and A_3 and the peaks in the post edge region as B, C_1 , C_2 , D and E. As has been explained by Farges et al. [141] the pre-edges in six coordinated TiO_2 arises due to transition from s orbital to mixed p-d orbitals. The existence of intense B peak in most of our TiO_2 samples indicate predominant presence of anatase phase, except in case of the sample prepared at 0% oxygen, which shows flatter B peak, a characteristic of rutile phase TiO_2 . To compare with the results of Kityakarn et al. [142], in Fig. 4.6(b), we have also plotted XANES spectra of the samples prepared at 0% oxygen partial pressure and at 21% oxygen partial pressure in the region of 4980 to 5000 eV. It has been observed from the above figure that the XANES spectrum of the sample grown at

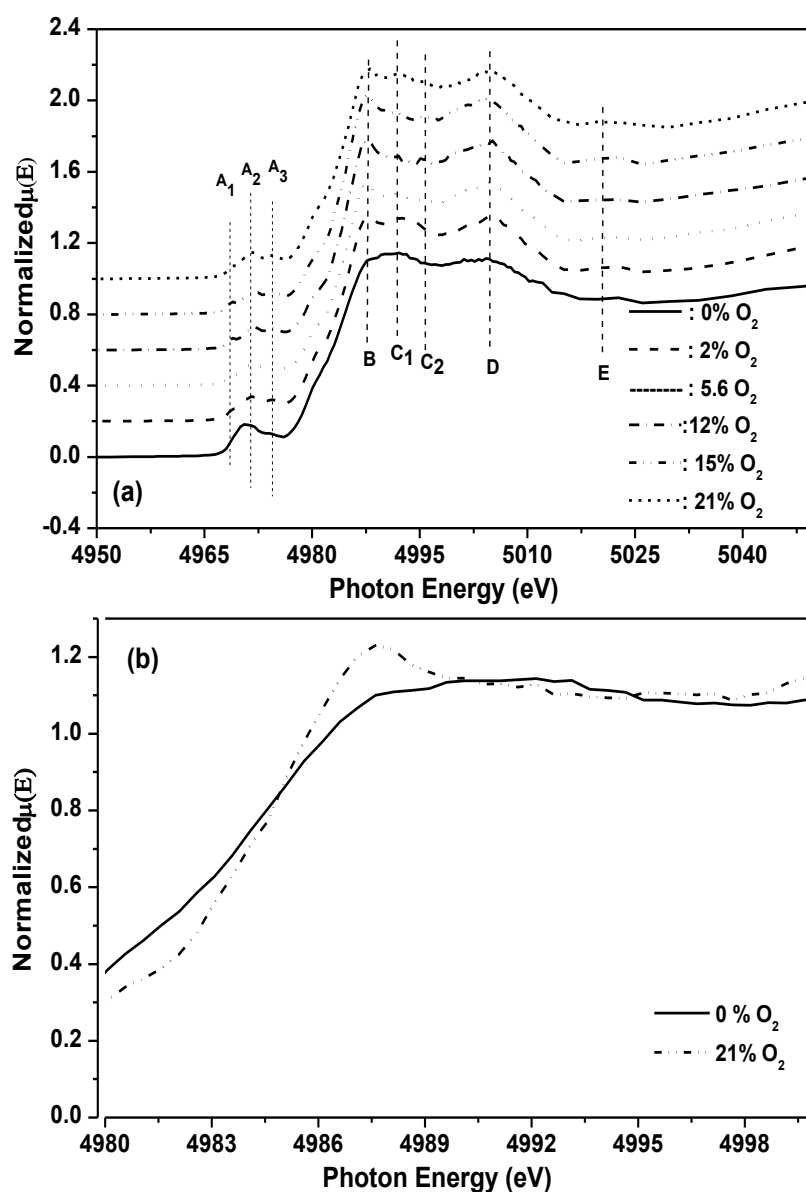


Fig.4.6: (a) XANES spectra of TiO₂ films showing various absorption peaks. (b) XANES spectra of two TiO₂ samples prepared at 0% and 21% oxygen partial pressures shown in expanded scale.

0% oxygen partial pressure shows convex curvature in the regime of 4990 to 4995 eV manifesting rutile phase while the XANES spectrum of the sample prepared at 21% oxygen partial pressure shows concave nature demonstrating the presence of predominantly anatase phase. This is consistent with the above observation that with the increase in oxygen partial pressure anatase phase content in our sample increases significantly.

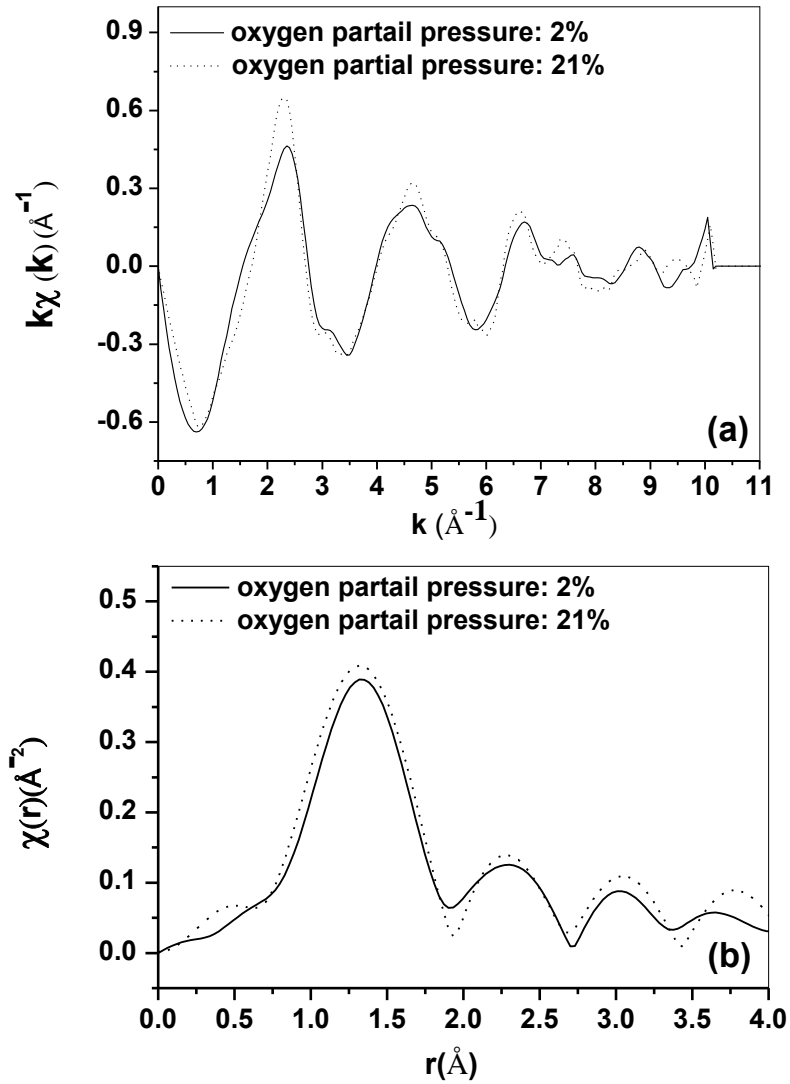


Fig.4.7: (a) $k\chi(k)$ versus k plots of the samples deposited with 2% and 21% oxygen partial pressures. (b) $\chi(r)$ versus r plots of the samples deposited with 2% and 21% oxygen partial pressures.

We have tried to further estimate the fractional percentage of anatase and rutile phases by fitting the EXAFS spectra of the samples with the theoretical spectra using the FEFF 6.0 code discussed in detail in Chapter-2. It should also be noted here that the bond distances, coordination numbers (including scattering amplitudes) and disorder (Debye-Waller) factors (σ^2), which give the mean-square fluctuations in the distances, for the individual paths have been varied while fitting. Figures 4.7(a) and (b) show $k\chi(k)$ vs k and $\chi(r)$ versus r spectra of

the samples deposited with 2% and 21% oxygen partial pressures which depict significant difference demonstrating the presence of different ratios of anatase and rutile phases in

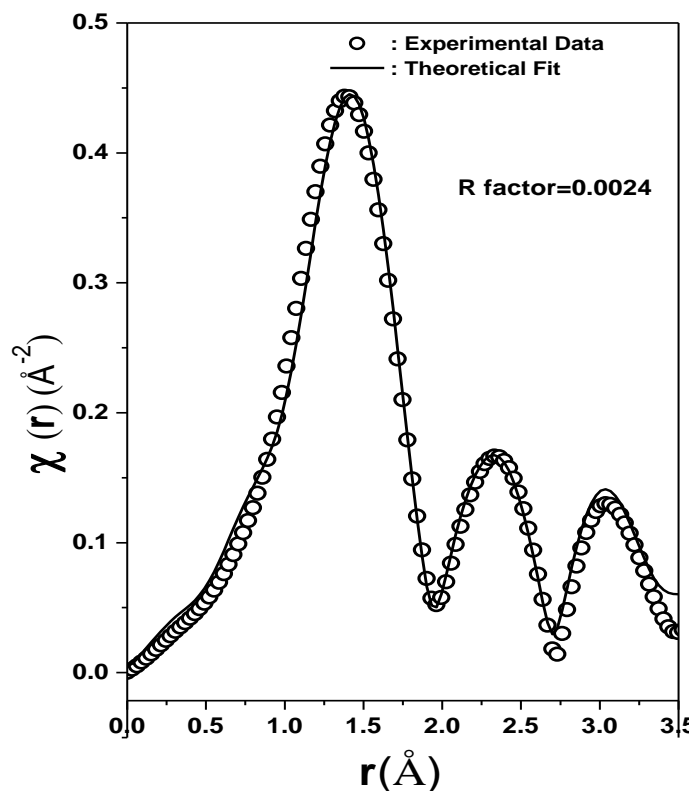


Fig.4.8: Experimental $\chi(r)$ versus r plot along with best fit theoretical plots of the TiO_2 film deposited at zero oxygen partial pressure:

ooooooo: Experimental data;

-----: Theoretical fit with rutile structure.

the samples. Since the film deposited with 0% oxygen partial pressure is expected to be of rutile structure as obtained from XANES measurement, the EXAFS spectrum of this sample has been fitted with pure rutile phase having tetragonal crystal structure with lattice parameters $a = 4.5936$, $c = 2.9586$ and space group $p4_2/mnm$ for which the structural parameters has been taken from the literature [143]. Fig. 4.8 shows the experimental $\chi(r)$ versus r spectrum of this sample along with the best fit theoretical spectrum. Theoretical

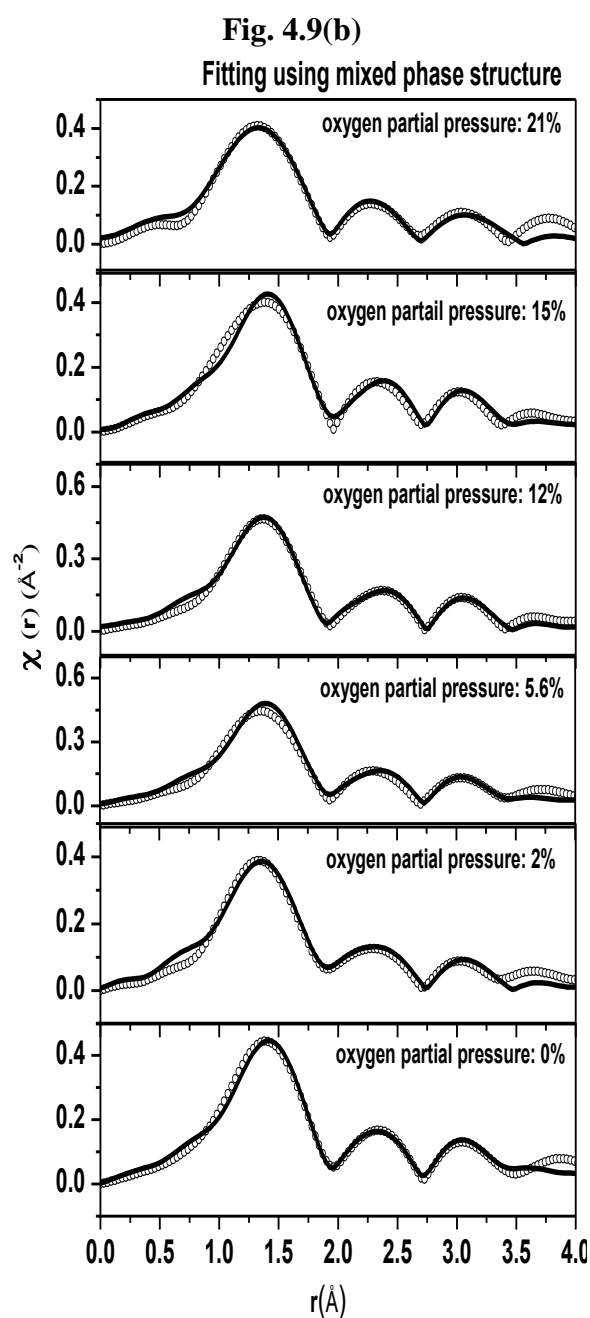
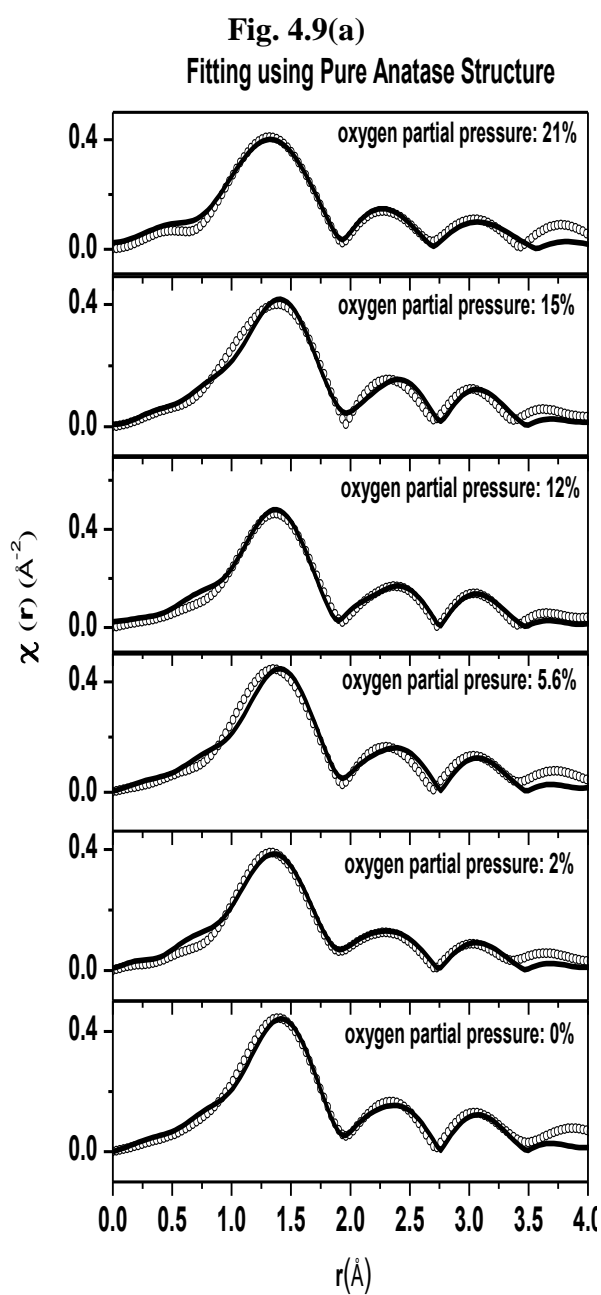


Fig. 4.9: Experimental $\chi(r)$ versus r plot along with best fit theoretical plots of TiO_2 films deposited at different oxygen partial pressures:

ooooooo : Experimental data
 : Theoretical fit assuming only anatase phase

fitting of $\chi(r)$ versus r spectra of the rest of the samples have been carried out by two methods, viz., (i) assuming only anatase structure and (ii) assuming a mixed structure of anatase and rutile phases. In the later case, the best fit parameters of the sample deposited at 0% oxygen partial pressure has been used as the parameters of the rutile phase while parameters of the anatase phase with tetragonal structure having $a = 3.785$; $c = 9.514$ and space group $41/a m d$ has been taken from the literature [144]. The parameters of the rutile phase have been kept fixed in this fitting process and only the parameters of the anatase phase and the fraction of anatase phase have been varied. It should be noted here, that since from GIXRD and XANES measurements it has been confirmed that the TiO_2 films deposited at higher oxygen partial pressures have significant anatase phase content, hence fitting of the EXAFS spectra of these samples with only rutile structure has not been attempted. Figures 4.9(a) and 4.9(b) show the experimental $\chi(r)$ versus r plots for the samples as derived from the experimentally obtained (μ vs. E) plots along with best fit theoretical curves obtained by the two methods respectively as described above. The R_{factor} for both the fitting processes for all the samples are shown in Fig.4.10 which shows that better fitting have been obtained by the 2nd method viz., assuming a mixed phase of anatase and rutile structures in the samples. The variation of the anatase phase fraction in the samples as obtained by the above fitting of EXAFS data by the 2nd method described above is shown in Fig. 4.2 along with the result obtained from GIXRD measurements. It has been observed from Fig. 4.2, that though the anatase phase fraction in the films as from GIXRD measurements is found to increase almost monotonically with oxygen partial pressure, the variation obtained from EXAFS measurements is found to be non-linear. Such a non-linear variation might apparently look unrealistic, however, it has been observed that the r.i. of the films (Fig. 4.4(a)) also varies in a

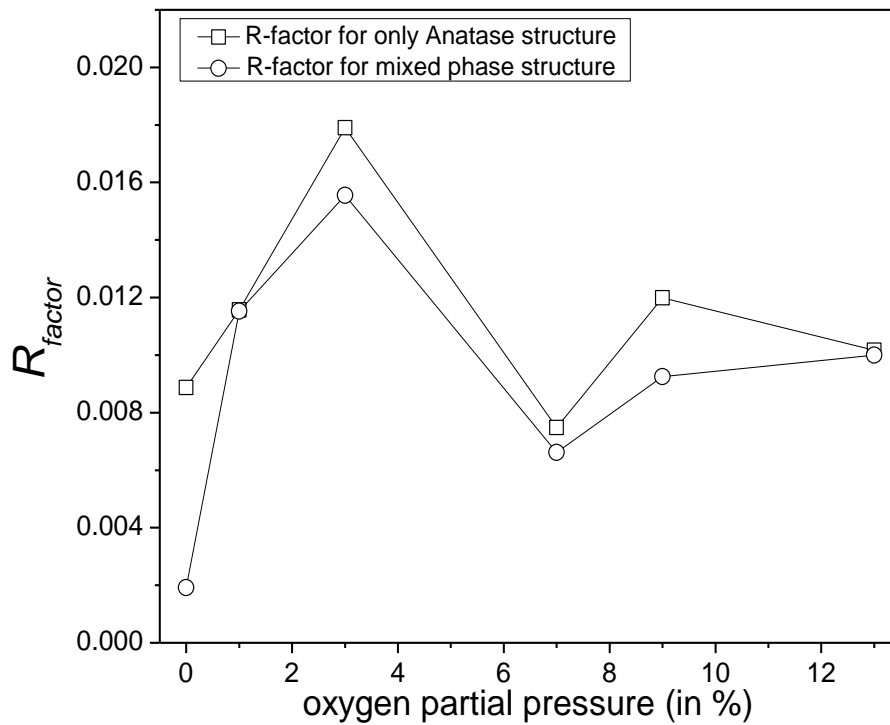


Fig.4.10: Variation of R_{factor} factor of fitting in both the cases (assuming pure anatase phase and mixed phase of anatase and rutile) as a function of oxygen partial pressure used during deposition.

non-linear fashion with increase in oxygen partial pressure used in the preparation of the samples. However, the anatase phase fraction obtained from EXAFS measurements is found to almost follow an opposite trend of variation of r.i. of the films where r.i. of the films decrease if fraction of the anatase phase increase and vice-versa. It should be noted here that refractive index of rutile-rich films should be higher than anatase-rich films since the refractive index of pure rutile-phase TiO_2 is higher than the non-linear variation of r.i. as a function of oxygen partial pressure can be due to the competition between two processes, improvement of oxygen stoichiometry of the films and reduction in mobility and kinetic energy of the adatoms reaching the surface of the growing films as oxygen partial pressure is increased. At lower oxygen partial pressure, high deposition rate and local heating of the substrate lead to high energy and mobility of the adatoms resulting in crystalline rutile

structure as discussed above, though oxygen deficiency plays a vital role in determining the quality of the films and its refractive index. At higher oxygen pressure, on the other hand, low energy of the adatoms lead to anatase phase though films are generally oxygen rich. Competition between the above two processes leads to a non-linear variation of anatase phase fraction and hence to a non-linear variation in refractive index of the films. Pin et al. [136] have obtained similar result on their PLD deposited TiO_2 thin films grown under different oxygen partial pressure where films deposited at lower oxygen partial pressure have better crystallinity but are oxygen deficient while films deposited at higher oxygen partial pressure have poor crystallinity but better stoichiometry. In their case also competition between these two processes has finally determined the structural and optical properties of TiO_2 thin films [136]. Such competition between oxygen stoichiometry and crystallinity has also been observed by Wicaksana et al. [134] for their reactive sputter deposited TiO_2 thin films deposited with different oxygen fractions in sputtering ambient.

It should be noted here that, as has been observed from Fig.4.2, the anatase phase fraction as obtained from GIXRD data for the present set of thin films shows a monotonic variation with increase in oxygen partial pressure and thus fails to explain the actual nature of variation of the macroscopic properties like refractive index of the films. This supports the observation [145] that for thin films and nanostructures with large amount of disorders, where single-phase domains are not sufficiently large, X-ray diffraction, which acts on the principle of long range order, might not give the correct phase information and for such systems, EXAFS which basically probes the local order and does not depend on the long range order can yield better result so far microscopic behavior of the samples is concerned. It has been observed by us earlier also that in case of polycrystalline/amorphous composite oxide films, where GIXRD data cannot not yield much quantitative result, EXAFS measurements can

give useful information regarding structural aspects of the samples [15, 109].

4.6 Conclusions:

In summary, a set of TiO_2 thin films has been deposited by asymmetric bipolar pulse DC sputtering technique using different oxygen partial pressures in the sputtering ambient. The structural properties of the samples have been studied by GIXRD and EXAFS measurements while the optical properties of the films have been studied by transmission spectrophotometry. The data were analysed and the following observations have been made:

(i) The refractive index of TiO_2 films varies in a non-linear fashion with increase in O_2 partial pressure in the sputtering ambient. (ii) The band gap, however increases monotonically with increase in oxygen partial pressure and this has been attributed to the realisation of more and more stoichiometric films with reduction in oxygen vacancies, as oxygen partial pressure is increased in deposition ambient. (iii) GIXRD measurements show that the anatase phase fraction in the films increases slowly and monotonically as oxygen partial pressure is increased which cannot explain the observed non-linear variation of refractive index of the films with increase in oxygen partial pressure. (iv) However, local structure investigation by EXAFS measurements shows that anatase phase fraction also varies in a non-linear fashion with increase in oxygen partial pressure and almost follows an opposite trend observed for the variation of refractive index of the films. (v) Finally, the non-linear variation of macroscopic and microscopic properties of the TiO_2 films with increase in oxygen partial pressure has been attributed to the competition between two processes during the film growth, viz., improvement of oxygen stoichiometry of the films and reduction in mobility and kinetic energy of the adatoms reaching the surface of the growing films.

CHAPTER-5

Study on Ta₂O₅ samples deposited at various oxygen partial pressures.

5.1 Introduction:

Tantalum pentoxide (Ta₂O₅) has been the focus of research for optical and electronic devices due to its excellent refractive index and dielectric properties. It is widely studied for new generation of dynamic random access memories (DRAMs) and storage devices [146]. Tantalum pentoxide can be prepared in thin film form which exhibit a very low attenuation coefficient ($\sim 10^{-4}$) in the visible wavelength region of light i.e. they are optically transparent. Depending upon the process of preparation Ta₂O₅ exhibits optical band gap around ~ 4 -4.2 eV and refractive index in the range 1.9-2.2 @ 550 nm. Due to such excellent optical properties of Ta₂O₅ and its chemical compatibility with other optical materials it also finds applications as a comprising thin film layer in various types of multilayer thin film based optical devices [23]. However, the optical properties of Ta₂O₅ thin films depend on the process parameters which control the microstructure of the deposited materials. Various deposition processes are being used to produce Ta₂O₅ thin films with required dielectric, optical and electrical properties. These deposition processes include sputtering [147], chemical vapor deposition [148], electron beam evaporation [149] and also bipolar pulsed DC sputtering technology [150].

Among the various deposition techniques, as has been described in details in previous chapters, asymmetric bipolar pulsed DC (ABPDC) sputtering technique has several

advantages over other conventional deposition techniques .We have prepared the Ta₂O₅ films by asymmetric bipolar pulsed DC (ABPDC) sputtering technique at various oxygen partial pressures which is an important parameter in controlling the properties of oxide films prepared by sputtering techniques as described earlier in this thesis . Shibata et al. [151] have deposited Ta₂O₅ films by sputtering at various O₂ to Ar ratio in the deposition ambient and has found that at an oxygen partial pressure of 20%, the dielectric constant is the highest. Zhou Ji-cheng et al. [152] have also studied the effect of sputtering pressure and substrate annealing on structural and optical properties of DC reactive magnetron sputter deposited Ta₂O₅ thin films.

Here we have tried to correlate the macroscopic observation on the optical properties of the films with the microscopic investigation by synchrotron-based Extended X-ray Absorption Fine Structure (EXAFS) measurements. To verify the trend in oxygen coordination obtained from EXAFS measurement, oxygen to tantalum ratio in the films has been estimated from Rutherford Backscattering Spectrometry (RBS).

5.2 Preparation of samples:

Ta₂O₅ thin films have been deposited on fused silica substrates by magnetron sputtering with the asymmetric bipolar pulsed DC (ABPDC) source (MKS/ENI RPG-100) to energize the magnetrons. The 10 kW ABPDC power supply has rectangular wave form as has been described in Chapter-2 in detail. For the present study, an optimized pulse frequency of 250 KHz and optimized pulse width of 496 ns were used to deposit the films. Prior to each deposition, the base pressure of 5×10^{-6} mbar in deposition chamber was achieved using a turbo molecular pump backed by a rotary pump. Argon and oxygen gas flow rates were independently controlled using two separate mass flow controllers (MKS make). Prior to all

depositions the Ta₂O₅ target was sputtered for ~300 seconds to remove surface contamination, if any, and during deposition, thickness and rate of sputtering were monitored using an online quartz crystal monitor.

For the present investigation, we have deposited a set of Ta₂O₅ thin films at various oxygen flow rates viz., 0 sccm, 4 sccm, 8 sccm, 12 sccm, 16 sccm and 20 sccm vis-à-vis a fixed Ar flow rate of 20 sccm so that oxygen partial pressure in the deposition ambient are maintained at 0%, 16.67%, 28.57%, 37.50%, 44.44% and 50% respectively. This is to be emphasized that the total gas pressure of the deposition ambient was kept fixed at 5.6×10^{-3} mbar in all the cases, whereas the O₂ partial pressure was varied by varying the oxygen inflow and the gate valve opening. All the samples were deposited for 2 hours except for the 0 sccm sample which was deposited for 28 minutes as the deposition rate in this case was very high. For preparation of the above set of samples, a power level of 150W has been used from the ABPDC power supply to energize the magnetron.

5.3 Grazing Incidence X-ray Diffraction measurements:

All the samples have been characterized by GIXRD measurements to investigate long range structure and the obtained GIXRD spectra are shown in Fig. 5.1. As the figure shows, all the Ta₂O₅ samples are amorphous in structure. This is possibly due to the low processing temperature in magnetron sputtering deposition. Earlier structural investigations made on the deposition of Ta₂O₅ thin films show that processing temperatures above 1073 K is a prerequisite for the formation of crystalline Ta₂O₅ films [153].

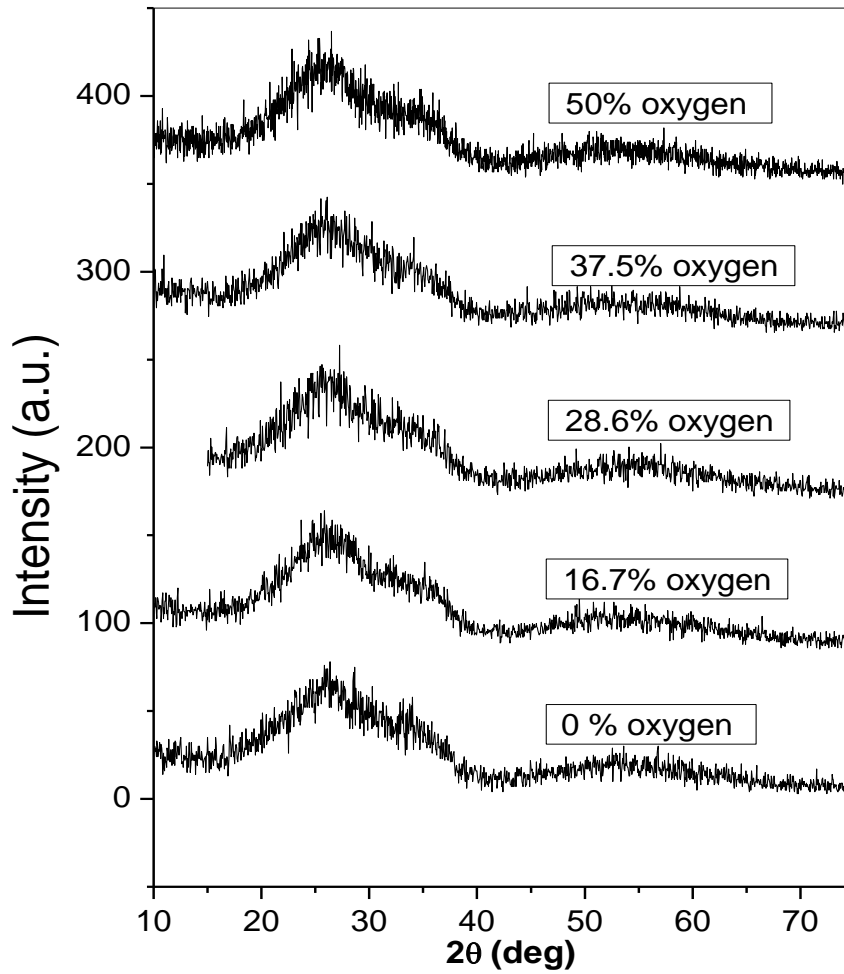


Fig.5.1: GIXRD pattern of Ta₂O₅ thin films deposited under various oxygen partial pressures used in the ambient during deposition.

5.4 Spectroscopic ellipsometry measurements:

To study the optical properties of the samples Spectroscopic ellipsometry measurements of the samples have been carried out in the range of 200-1200 nm wavelength by the rotating polarizer spectroscopic ellipsometer (GES5E by SOPRA) which has been described in Chapter-2. Fig. 5.2 shows the experimental ellipsometry spectra for a representative Ta₂O₅ film deposited with 37.5% oxygen partial pressure in sputtering ambient. The measured ellipsometry spectra are then fitted with an appropriate model assuming a realistic sample structure. The optical constants of the quartz substrates have been

supplied from standard reference [98] and the Tauc-Lorentz (TL) dispersion [68] as described in Chapter-2 has been used to describe wavelength dependent dispersion of the optical constants of the Ta_2O_5 layers. Thin film deposition by physical vapour deposition processes is in general characterized by presence of voids in the layers. For present analysis, each sample

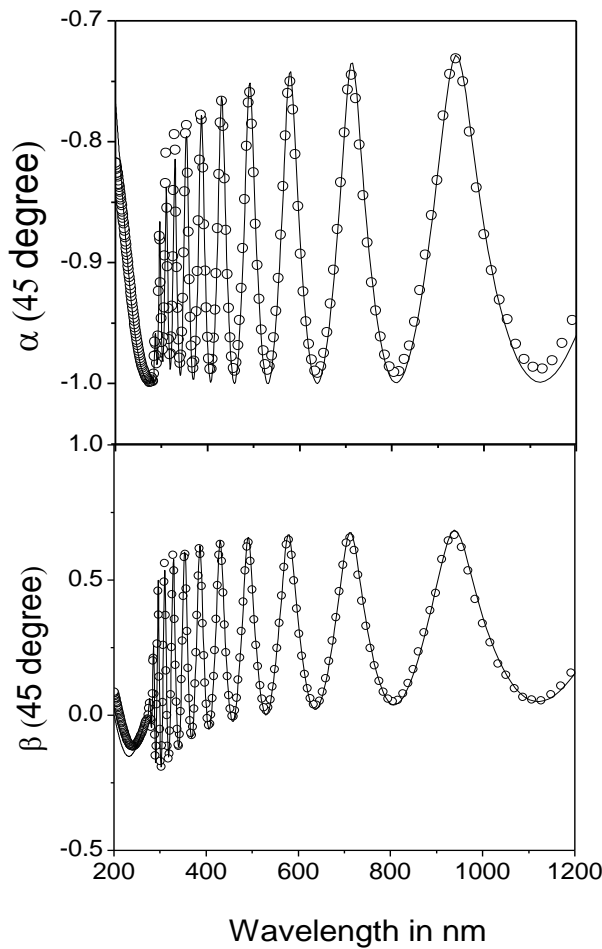


Fig.5.2: Spectroscopic ellipsometry data along with best fit theoretical simulation for a representative Ta_2O_5 film deposited with 37.5% oxygen partial pressure.

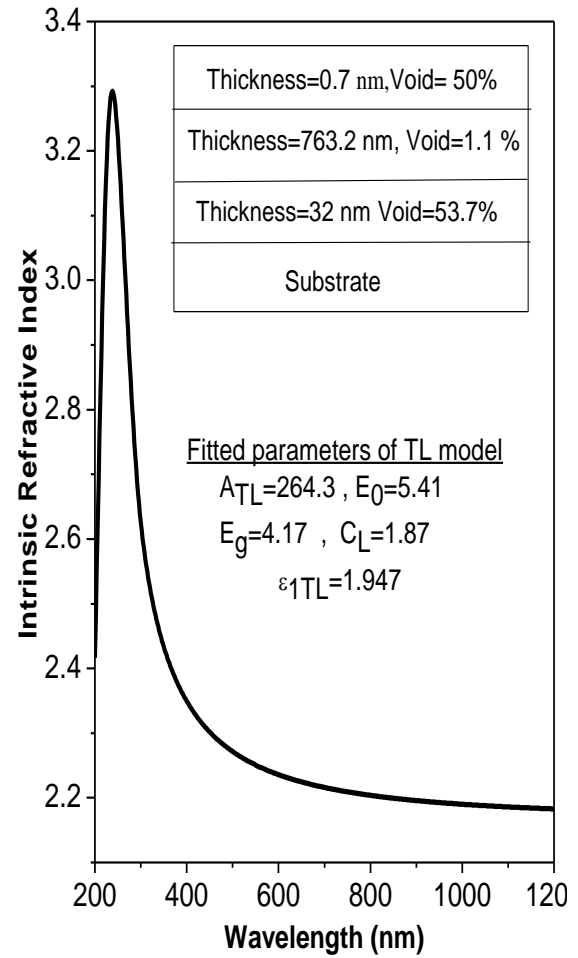


Fig.5.3: The best fit sample structure and the best fit parameters of the TL model as obtained by the fitting along with the dispersion of intrinsic refractive index generated with the best fit parameters for the representative Ta_2O_5 film deposited with 37.5% oxygen partial pressure.

has been modelled as a three-layer structure with one surface layer of 0-5 nm thickness having fixed void percentage of 50%, a bulk layer which is a homogeneous mixture of Ta₂O₅ material and certain small percentage of void and an interface layer in between film and substrate, which is again an homogeneous mixture of Ta₂O₅ material and large amount of voids. The estimation of the effective dielectric constant of the layers has been carried out using the Bruggeman Effective Medium Approximation (EMA) model mentioned in Chapter 2. Assuming the above sample structure, keeping layer thicknesses, void fractions and parameters of dispersion relation for the different layers as fitting parameters, the measured ellipsometric spectra are fitted by minimizing the Root Mean Squared Error (RMSE) value between the measured and calculated values of the ellipsometric parameters (α and β). The best fit theoretical curves for the representative Ta₂O₅ film deposited with 37.5% oxygen partial pressure in sputtering ambient is also shown in fig. 5.2 along with the experimental data. The best fit sample structures and the best fit parameters of the TL model as obtained by the fitting have been shown in fig. 5.3 along with the dispersion of intrinsic refractive index generated with the best fit parameters for the representative sample. The above exercise has been carried out on all the Ta₂O₅ samples deposited at different oxygen partial pressures and the intrinsic refractive index and band gap of the Ta₂O₅ layers have been estimated from best fit dispersion relations. Fig. 5.4(a) shows the variation of intrinsic refractive index of Ta₂O₅ at a wavelength of 550 nm while Fig. 5.4(b) shows the variation of direct band gap with respect to the variation of oxygen partial pressure used during deposition. Fig. 5.4(a) shows that the intrinsic refractive index of Ta₂O₅ decreases up to 30% oxygen partial pressure and then increases again with maximum value of refractive index obtained for films deposited with 40% oxygen partial pressure. The band gap of the samples, as shown in Fig. 5.4(b) is also found to increase up to 30% and decreases with increase in oxygen percentage beyond 40%.

The deposition rates for the samples were also calculated by dividing the estimated thickness (total thickness of all three layers in the model) by the duration of deposition and the variation of deposition rate as a function of oxygen partial pressure used during deposition has been shown in Fig. 5.4(c). It can be seen from Fig. 5.4(c) that deposition rate decreases with increase in oxygen partial pressure which is due to the lesser sputtering efficiency of

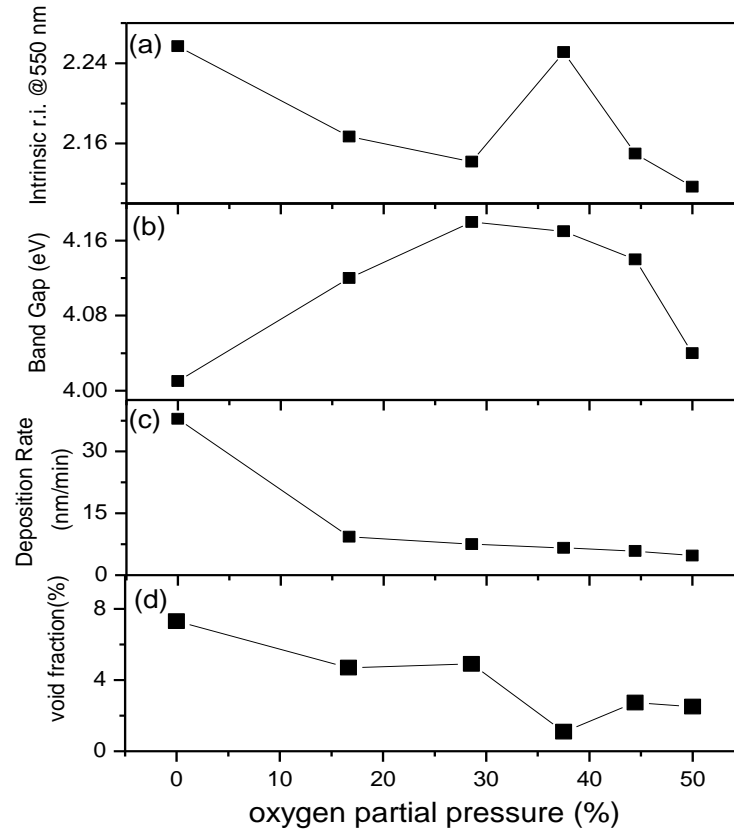


Fig.5.4: (a) Variation of intrinsic refractive index (r.i.) of Ta₂O₅ @ 550 nm as a function of oxygen partial pressure used during deposition. (b) Variation of band gap of Ta₂O₅ films as a function of oxygen partial pressure used during deposition. (c) Variation of deposition rate of Ta₂O₅ films as a function of oxygen partial pressure used during deposition. (d) Variation of void percentage of Ta₂O₅ as a function of oxygen partial pressure used during deposition.

oxygen atom compared to argon atom. The drastic reduction in sputtering rate with the onset of oxygen could be due to reaction on the target leading to oxygen rich compound formation which may lead to less sputtering of Ta₂O₅ compound compared to preferential sputtering of

Ta in case of oxygen free ambient. Similar drastic reduction in deposition rate with the onset of oxygen was observed for HfO₂ films also described in Chapter-3. Fig. 5.4(d) shows the plot of void fraction present in the bulk layers of the films as a function of oxygen percentage used during deposition. The plot shows that with the increase in oxygen percentage present during deposition there is an overall decreasing trend of void fraction. This is possibly due to decrease in rate of deposition with increasing oxygen content in the deposition chamber, so that adatoms get more time for readjustment on the surface of the growing films leading to realization of more void-free and compact films.

5.5 Extended X-ray absorption fine structure (EXAFS) measurements:

To study local structure surrounding Ta atoms in the samples, EXAFS measurements were performed around Ta L3-edge (9881 eV) using the Scanning EXAFS beam line (BL-9) at the INDUS-2, the details of which have been discussed in Chapter-2. Fig.5.5 shows the experimental EXAFS spectra (μ vs. E) of the Ta₂O₅ films deposited at different oxygen partial pressure in the deposition ambient. Fig. 5.6 shows the experimental $\chi(R)$ versus R plots for the samples following the procedure given in Chapter-2. The theoretical fitting of $\chi(R)$ versus R plots has been carried out by using orthorhombic crystal structure of β -Ta₂O₅ with space group 49. The structural parameters of β -Ta₂O₅ have been taken from the report by Aleshina et al. [154]. As seen from Fig. 5.6, the first peak of $\chi(R)$ versus R plot of each sample is located in the region of 0 to ~1.8 Å. In this region of theoretically generated $\chi(R)$ versus R spectrum, for β -Ta₂O₅ crystal structure, there are three significant paths corresponding to Ta-O bonds, all having degeneracy of 2, of which the closest Ta-O

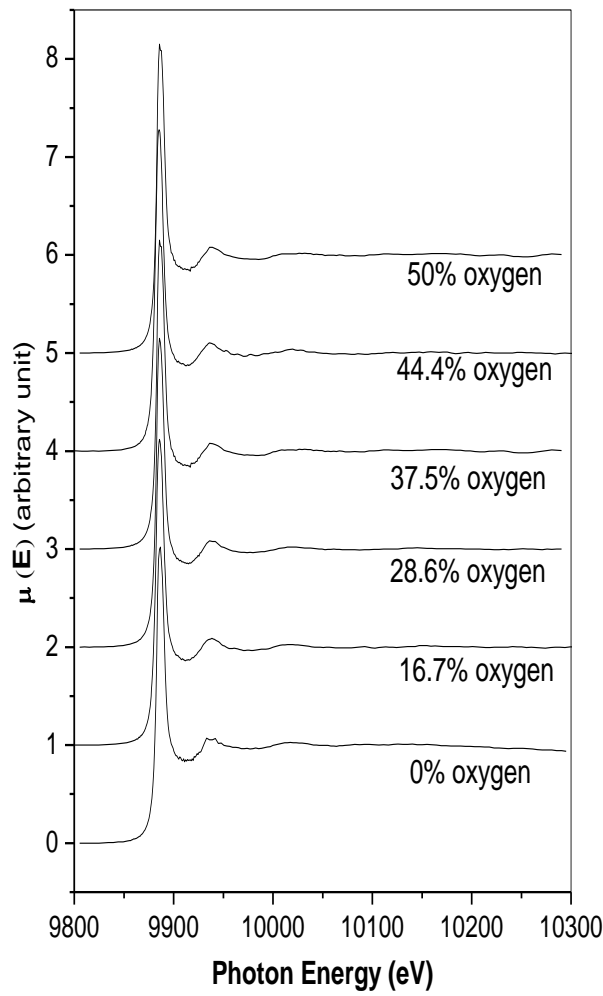


Fig.5.5: Experimental $\mu(E)$ vs. E spectra of Ta_2O_5 thin films.

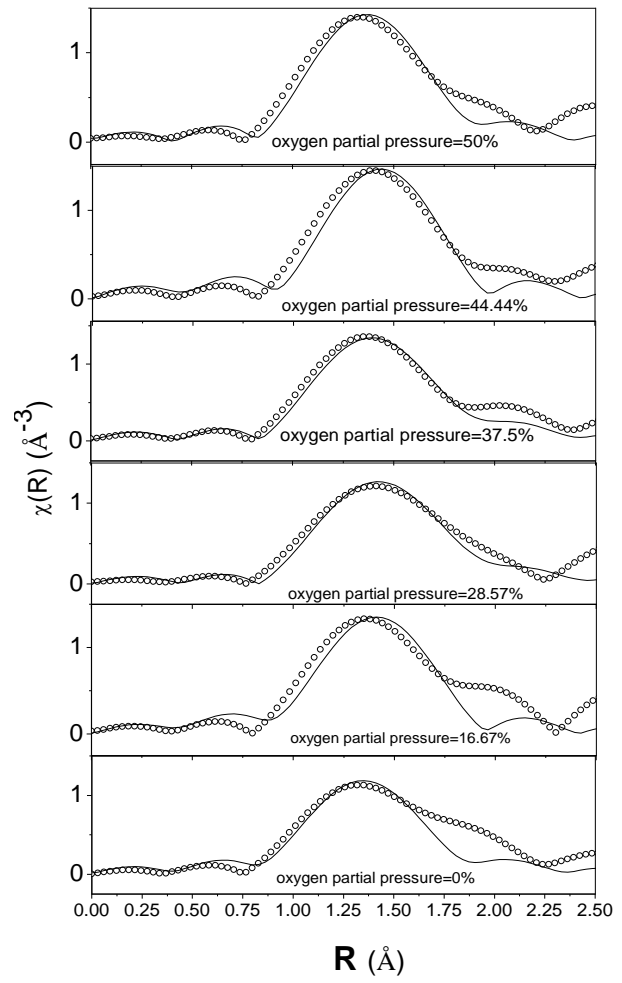


Fig. 5.6: $\chi(R)$ versus R plots for experimental and fitted EXAFS data of Ta_2O_5 thin films.

bond length is 1.839\AA and the other two are 1.949\AA and 1.983\AA . It should be noted that only the profile of the 1st major peak has been fitted neglecting the shoulders/humps appearing at higher R range in the spectra which are due to multiple scattering processes. It should also be noted here that the bond distances, co-ordination numbers (including scattering amplitudes) and disorder (Debye-Waller) factors (σ^2), which give the mean-square fluctuations in the distances for the individual paths have been varied while fitting. Fig. 5.7(a) shows the variation of the average Ta-O bond lengths for the first three Ta-O shells (R_{avg}) as

a function of oxygen partial pressure used during preparation of the samples while Fig. 5.7(b) shows similar variation of total oxygen co-ordination numbers (N_{total}) around Ta atom in the three shells. The variation of intrinsic refractive index of Ta_2O_5 with the variation in oxygen partial pressure may be explained by the results obtained from EXAFS measurements shown in Figs. 5.7(a) and (b).

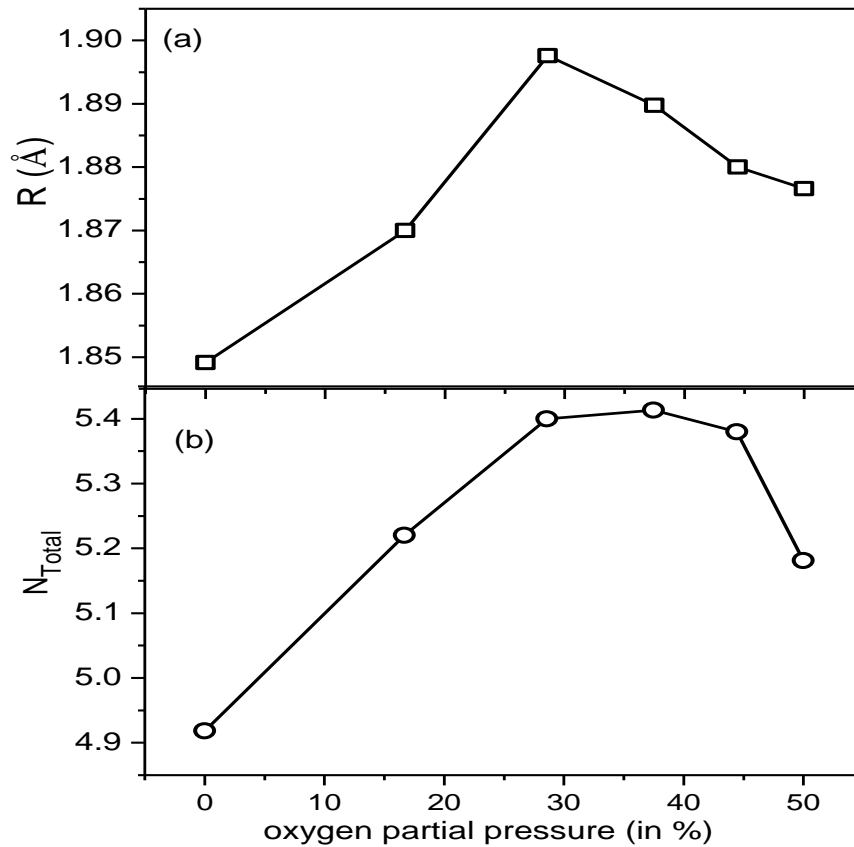


Fig.5.7: (a) Variation of average Ta-O bond length as a function of oxygen partial pressure used during deposition as obtained from EXAFS data analysis of Ta_2O_5 thin films. (b) Variation of total oxygen co-ordination number around Ta sites as a function of oxygen partial pressure used during deposition as obtained from EXAFS data analysis of Ta_2O_5 thin films.

It can be seen from Figs. 5.4(a) and 5.7(a) that intrinsic refractive index of Ta_2O_5 in the samples almost follows the reverse trend of variation of average Ta-O bond length in the samples up to ~40% oxygen partial pressure. The refractive index decreases as the average

Ta-O bond length increases up to 30% and then increases as the bond length decreases. The increase in refractive index values due to decrease in bond lengths leading to more compact microstructure of the films have been observed earlier in case of oxide thin films [15]. The decrease of refractive index beyond 40% oxygen partial pressure, however, is due to the decrease in stoichiometry in the samples which is reflected by the decrease in the total oxygen co-ordination in the Ta-O shells as shown in Fig. 5.7(b). The band gap of the samples, as shown in Fig. 5.4(b) is also found to increase up to 30% oxygen partial pressure, due to realization of more and more stoichiometric films, while it decreases with increase in oxygen percentage beyond 40% in accordance with decrease in the oxygen coordination surrounding Ta atoms.

5.6 Rutherford Back scattering (RBS) measurements:

The atomic composition of oxygen and tantalum in the tantalum oxide films has been estimated by Rutherford backscattering spectrometry experiment using proton as probe beam. The measurements were performed using 2.0 MeV proton beam obtained from 3 MV Tandetron at NCCCM, Hyderabad, India. The backscattered spectra were recorded by a silicon surface barrier detector placed at 170° angle with respect to the incident proton beam. Fig. 5.8 shows the RBS spectra of four representative films deposited under 0%, 28.57%, 37.50% and 50% oxygen partial pressures wherein the signals of Ta and O from the films and those of Si and O from the substrate (SiO_2) are clearly distinguishable. The recorded RBS spectra of all the films were simulated using the SIMNRA code [155] to extract the atomic composition of the films. Fig. 5.9(a) shows the estimated oxygen to tantalum ratio of all the Ta_2O_5 samples which has been obtained from the areal densities of Ta and O calculated by

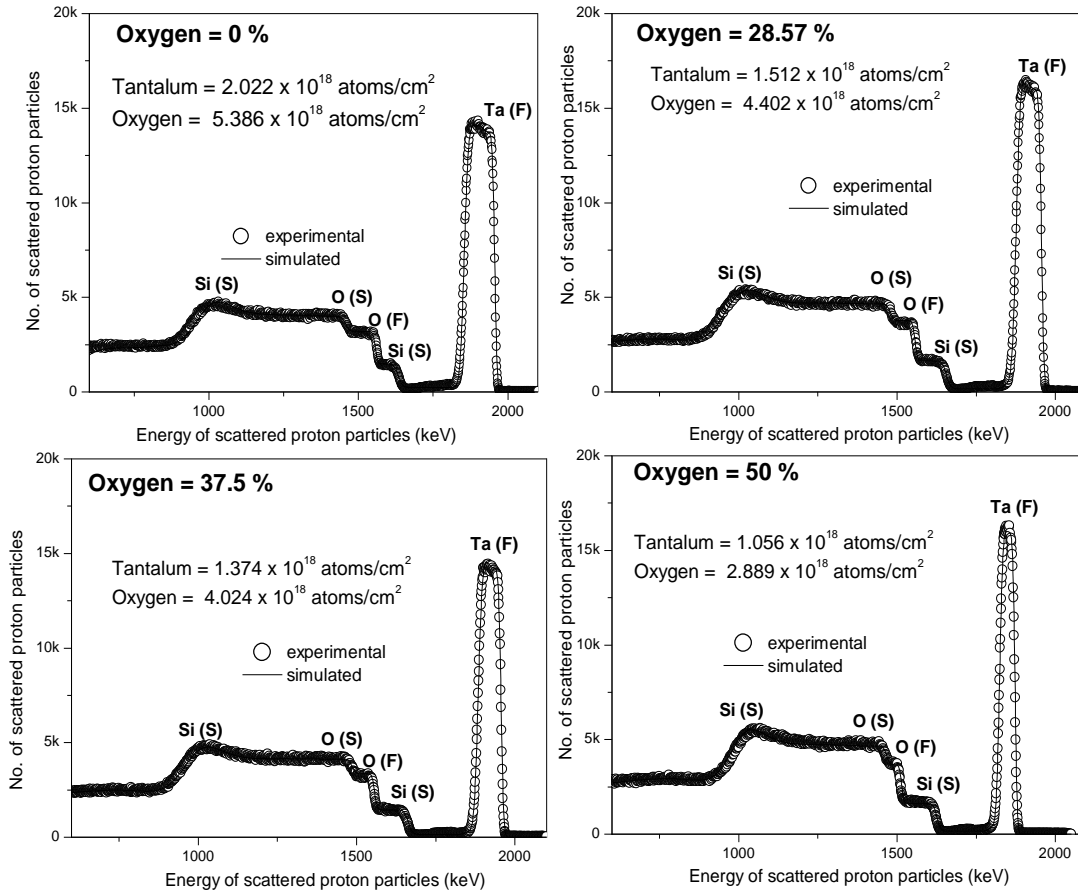


Fig.5.8: Experimental and simulated RBS spectra of Ta₂O₅ samples deposited under 0%, 28.57%, 37.5% and 50% oxygen partial pressure. The RBS front edge of different constituent elements of the film (F) and substrate (S) are indicated in the figure.

simulating the spectra. The uncertainty associated with the composition is typically about 10% which arises mainly due to the $^{16}\text{O}(\text{p,p})^{16}\text{O}$ (non-Rutherford) scattering. RBS has been employed to investigate O/Ta ratio in Ta₂O₅ films previously in various reported works [156-158]. Our estimated values of O/Ta ratio is greater than the value of (2.5) for stoichiometric Ta₂O₅, however is similar to the values obtained by Cappellani et al. [156] and Guoping et al. [157] from RBS measurement of their Ta₂O₅ films. It is evident from Fig. 5.9(a) that the oxygen content in the films is least when deposited without oxygen in the deposition ambient and oxygen content increases with the increase in oxygen percentage in deposition ambient up to 37.5% but oxygen content in the film starts decreasing with the subsequent increase in

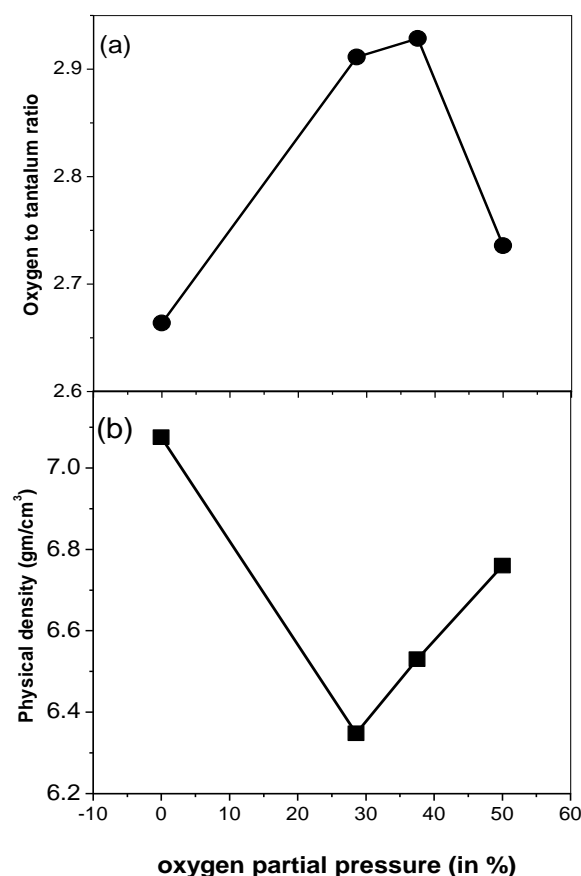


Fig.5.9: (a) Variation of oxygen to tantalum ratio obtained from RBS measurement as a function of oxygen percentage used during deposition. (b) Variation of physical density data estimated combining RBS and ellipsometry measurements as a function of oxygen percentage used during deposition.

oxygen percentage. This observation corroborates the trend in oxygen co-ordination (Fig. 5.7(b)) as estimated from EXAFS measurement of the samples. The areal densities of films obtained from backscattering measurements have further been used to calculate the physical density (atom number density in the unit of atoms/cm³) of the samples using the values of physical thicknesses of the samples estimated through ellipsometry measurements. This has been done by dividing the obtained areal density by the respective thickness obtained from ellipsometry measurement. Fig. 5.9(b) shows the trend of estimated physical density of the films with the variation in oxygen partial pressure during deposition. It shows that the physical density of the sample deposited without oxygen in the deposition ambient is high

which is due to the high Ta metal content in the film. The density has decreased substantially when deposited with 28.57% oxygen and density increases with the subsequent increase in oxygen percentage in the deposition ambient. The increase in physical density of the films in the range of 25-50% oxygen agrees with the reduction in the Ta-O bond length in this range as found from EXAFS measurements and shown in fig. 5.7(a).

5.7 Conclusions:

The changes in the optical properties of Ta₂O₅ thin films, deposited by a novel ABPDC sputtering technique, with the systematic variation of oxygen partial pressure (0-50%) used during the deposition, has been studied and investigation has been made to correlate the optical properties with the structure of the films probed by GIXRD and EXAFS. Intrinsic refractive index of the Ta₂O₅ samples, as obtained from spectroscopic ellipsometry measurements are found to decrease initially and then increases with an increase in oxygen partial pressure while band gap shows monotonic increase up to 30% oxygen partial pressure and then decreases with the subsequent increase in oxygen partial pressure. These results have been explained in the light of change in average Ta-O bond lengths and oxygen coordination around Ta sites as obtained from EXAFS measurements. The trend of variation in oxygen co-ordination as estimated from EXAFS measurements has been found to follow the variation in oxygen to tantalum ratio in the films as estimated from RBS measurement, while the variation in physical density of the films obtained from RBS measurements is found to be similar to the variation in Ta-O bond lengths obtained from EXAFS measurements.

CHAPTER-6

Study on Gd_2O_3 samples deposited at various oxygen partial pressures.

6.1 Introduction:

Rare-earth sesquioxide has drawn considerable attention in recent years for their wide applications in microelectronic, optoelectronic and optical devices [159-162] due to their excellent dielectric and optical properties. Gadolinium oxide is one such lanthanide rare-earth sesquioxide which, in one hand is a potential gate oxide material due to its good chemical compatibility, lesser interface diffusion with silicon and higher dielectric constant ($k=14$) and on other hand is an excellent optical material covering a transmitting region from 190 nm to 1600 nm and having bulk high refractive index of ~ 1.80 @ 550 nm. Gd_2O_3 finds wide applications in fabrication of optical devices such as multilayer reflecting filters [162], optical waveguides [163] etc. Over the years, a variety of studies has also been carried out on Gd_2O_3 samples both in thin film and in bulk form. For example, Gottlob et al. [164] investigated the CMOS compatibility in metal oxide semiconductor (MOS) capacitors and field effect transistors (MOSFETs) for epitaxial Gd_2O_3 . Sahoo et al. [162] have studied Gd_2O_3 films deposited by reactive electron beam evaporation and showed that the films deposited at lower substrate temperatures have higher band gaps and higher substrate temperatures yielded higher refractive indices. Apart from electronic and optical applications, pure and doped

Gd₂O₃ films have also been studied as phosphor films [165-166], scintillating films [167-168] and for neutron radiation applications [169].

As has been emphasized in earlier chapters of this thesis, among the various techniques which have been tried for the preparation of oxide films like Gd₂O₃, magnetron sputtering generally produces films having high density, low roughness and superior micro-structural properties. In the present study, we have investigated the evolution of optical, structural and other physical properties of gadolinium oxide thin film samples prepared from gadolinium oxide target by RF magnetron sputtering technique under various O₂ to Ar flow ratio in the deposition ambient. Structural characterization of the samples have been carried out by GIXRD measurements, compositional studies have been done by Rutherford Back Scattering (RBS) measurements, density and surface roughness of the films have been estimated from GIXR measurements, AFM measurements have been done for morphological studies, transmission spectrophotometry and spectroscopic ellipsometry techniques have been used for studying optical properties and finally EXAFS measurements have been carried out with synchrotron radiation in order to extract local structural information around Gd sites.

6.2 Preparation of samples:

Gd₂O₃ thin films have been deposited on fused silica substrates (1 inch dia) by RF magnetron sputtering technique using 150 watt of magnetron power in the sputtering system described in Chapter-2. For the present investigations, Gd₂O₃ films were sputter deposited at six different oxygen flow rates, viz., 0 sccm, 2 sccm, 4 sccm, 6 sccm, 12 sccm and 20 sccm along with a constant argon flow rate of 20 sccm, corresponding to oxygen partial pressure of 0%, 9.1%, 16.7%, 23.1%, 37.5% and 50% respectively. The total pressure in the chamber was maintained at a fixed value of 5.6×10^{-3} mbar by throttling the gate valve between the

turbo pump and the deposition chamber. All the samples have been deposited for 1 hour and 30 minutes while the sample with 0 sccm oxygen flow was deposited for 1 hour and 10 minutes since as has been explained later, this sample has higher deposition rate.

6.3 Grazing Incidence X-ray Diffraction (GIXRD) measurements:

GIXRD measurements of all the samples were performed in a laboratory X-ray diffractometer, equipped with a sealed tube X-ray (Cu $K\alpha$ of 1.54Å wavelength) generator operating at 3 kW output power. The same diffractometer was also used for GIXR measurements which were carried out on all the samples in 2θ range of 0-5° with step size of 0.01°. Rocking curve measurements have been done prior to each measurement for aligning the sample. Fig. 6.1 shows the measured grazing incidence X-ray diffraction data of all the Gd₂O₃ samples which show significantly broad peaks manifesting small crystallite size in the samples. Comparing the GIXRD pattern with standard database of PCPDF [131] we find that all the samples have grown in body centred cubic crystal structure. It is evident from past structural studies on gadolinium oxide [170] that this compound mainly exists in two crystallographic structures, viz., monoclinic and cubic. The cubic structure is more stable at room temperature while transformation to monoclinic phase takes place at 1200°C or higher [170]. Again cubic phase of Gd₂O₃ can exist in two phases having space group $ia-3$ and $I2_13$, both of which have co-ordination number of 6 but with different coordination geometries. Fig. 6.1 displays the experimentally measured GIXRD pattern of the samples as well as theoretical XRD patterns of two possible cubic Gd₂O₃ phases having space group $ia-3$ (PDF file number: 431014) and $I2_13$ (PDF file number: 760155). As can be seen from this figure, it is impossible to distinguish between these two phases since the samples presented here are polycrystalline in nature with relatively small grain sizes and hence the GIXRD patterns

show broad peaks (fig.6.1). Even a rocking curve measurement would not help since it would also result in a broad peak. It is hence concluded from GIXRD pattern that both the above mentioned cubic phases may exist in our samples and further structural investigations have been carried out using EXAFS measurements discussed later.

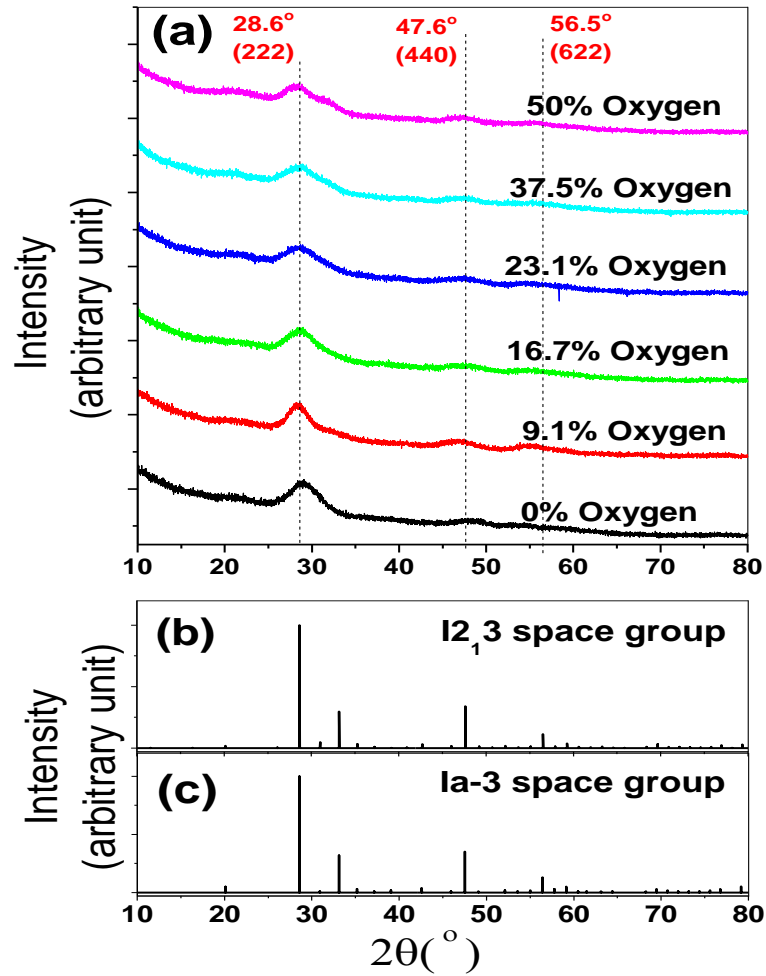


Fig.6.1: (a) GIXRD plot of all Gd_2O_3 samples deposited under different oxygen partial pressure. (b) Positions of XRD peaks for space group $I2_13$, (c) Positions of XRD peaks for space group $Ia-3$.

The above result is in contradiction with the result obtained by Li et al. [171] who found that with an increase in oxygen concentration in sputtering ambient, the crystallographic structure of Gd_2O_3 films have evolved from monoclinic to cubic phase.

However, it is to be mentioned that Li et al. prepared the samples from pure gadolinium target and under different deposition conditions viz., at 64 watt of magnetron power and 84 mm of target to substrate distance and samples were deposited on Si (100) substrate. Shoujing et al. [172] also showed that magnetron sputter deposited Gd₂O₃ films are cubic at low temperature and monoclinic at high temperature (>510°C). Comparing with PCPDF (431014) of ia3 space group and PCPDF (760155) of i213 space group, it is found that apart from the peaks indicated in fig. 6.1, there are weak peaks in few of the samples at 20.1° and 33.1° which could be due to (211) and (400) plane respectively of either of the two space groups. As is evident from (222) peak at 2θ position of 28.6°, the peak intensity and FWHM of all the samples are not the same. Further analysis of the (222) peak was carried out in order to estimate the crystallite sizes of all the samples. The peak was fitted with a combination of Lorentzian & Gaussian features. By using the well-known standard Scherrer formula [58], the average crystallite size (L in nm) is estimated as:

$$L = \frac{0.9\lambda}{B \cos \theta} \quad (1)$$

where B is the peak FWHM, θ is the Bragg angle and λ is the wavelength of incident X-ray (Cu K α 0.154 nm in the present case). The variation in calculated crystallite size as a function of oxygen partial pressure is shown in Fig.6.2. The error bars of crystallite size shown in Fig. 6.2 are calculated from the peak fitting of the GIXRD pattern. At 0% oxygen partial pressure, due to very high kinetic energies of the ad atoms and due to oxygen deficit in the adsorbed species, the film shows very small crystallite size. The crystallite size increases as oxygen is introduced in the deposition chamber because of the reduction of oxygen defects at the grain boundaries of the samples. However, as oxygen partial pressure is increased

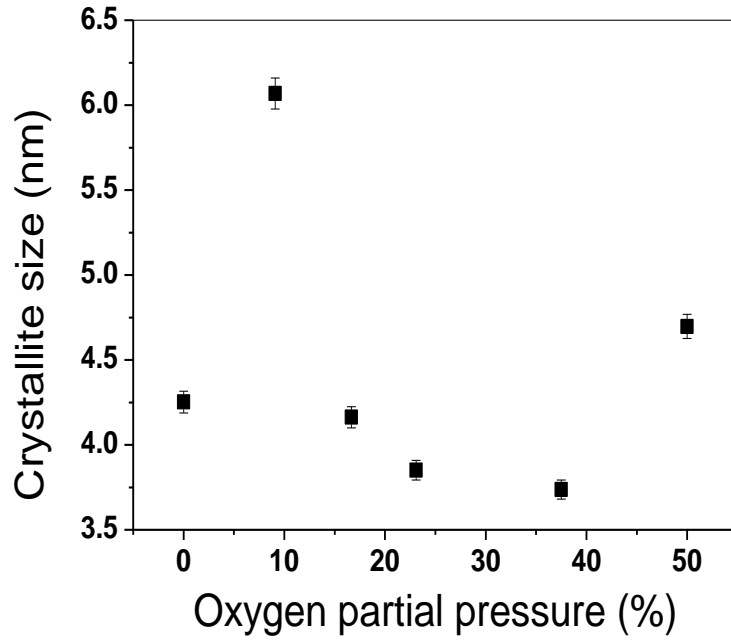


Fig.6.2: Variation of estimated crystallite size obtained from GIXRD measurement as a function of oxygen partial pressure.

from ~9.1% to ~37.5%, crystallite size decreases, while it increases again as oxygen partial pressure is increased beyond 40%. The phenomenon of grain growth in case of sputtering depends on two competitive processes, (i) sputtering of ad atoms from the target and (ii) readjustment of ad atoms on the surface of the growing film. The former is governed by the sputtering or deposition rate of the target, while the later depends on the ad atom energies. In the present case, as oxygen partial pressure increases in the sputtering ambient, ad atom energy and hence ad atom mobility decreases owing to the increased collision of sputtered atoms with the oxygen gas molecules in the deposition ambient. Reduction in kinetic energy of ad atoms prohibits them to diffuse on the surface of the films and to coalesce, thereby reducing the crystallite size. The decrease in grain size with the increase in oxygen partial pressure due to similar reason has also been observed by Liu et al. [173] while depositing ZnO-Cu films by magnetron sputtering. However at higher oxygen partial pressure (>40%), as has been discussed later, deposition rate also decreases considerably so that ad atoms get

sufficient time to coalesce and hence grain sizes increases again. Similar phenomenon of competition between the above two processes has been observed by us on the properties of ion beam sputter deposited W thin films also [174].

6.4 Rutherford Back scattering (RBS) measurements:

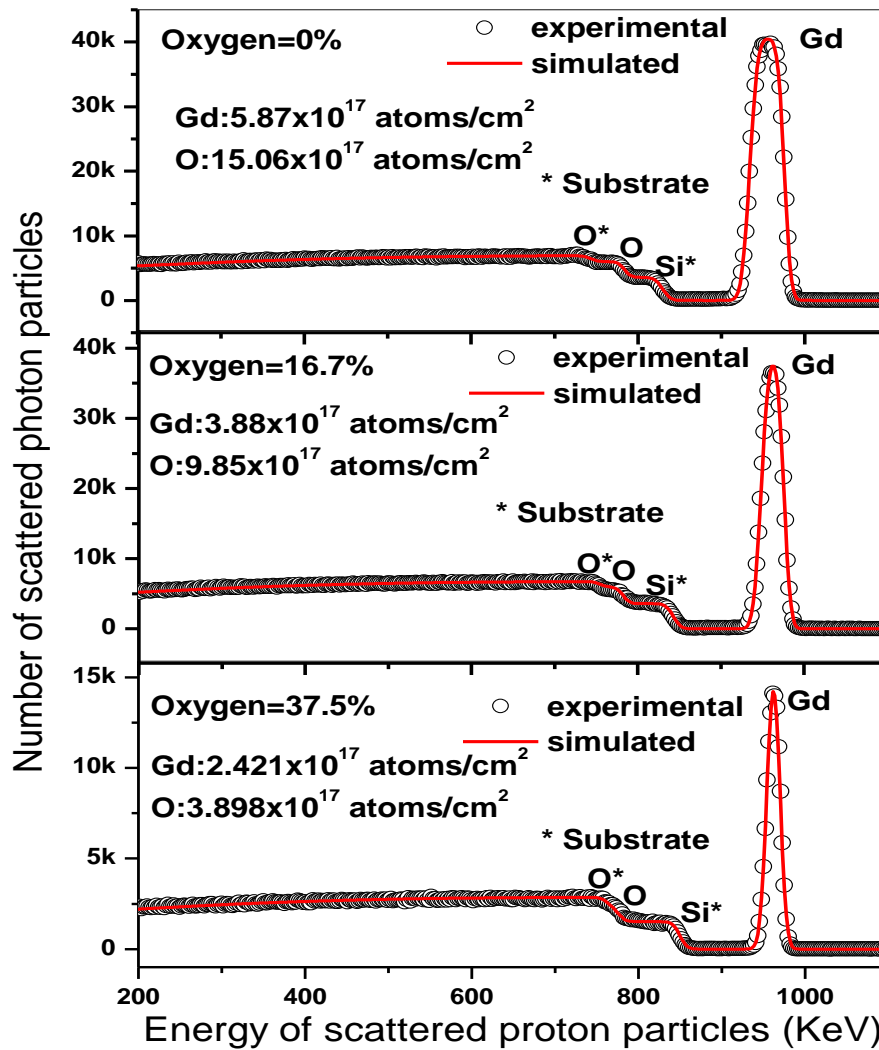


Fig.6.3: Experimental and simulated RBS spectra of Gd_2O_3 samples deposited under 0%, 16.7% and 37.5% oxygen partial pressure. The RBS front edge of different constituent elements of the film and substrate are indicated in the figure.

RBS measurements were performed using a 1.0 MeV proton beam obtained from a 3 MV tandetron at NCCCM, Hyderabad, India. The backscattered spectra were recorded by a silicon surface barrier detector placed at a 170° angle with respect to the incident proton beam. Fig. 6.3 shows the RBS spectra of three representative Gd_2O_3 films deposited with 0%, 16.7% and 37.5% oxygen partial pressure, wherein the signals of Gd and O from the films and those of Si and O from the substrate (fused silica) are clearly distinguishable.

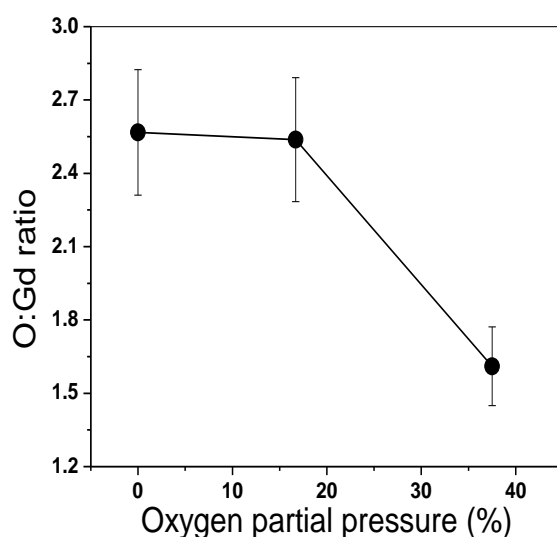


Fig. 6.4: Variation of oxygen-to-gadolinium ratio obtained from RBS measurement as a function of oxygen partial pressure.

The recorded RBS spectra of all the films were simulated using the SIMNRA code [155] to extract the atomic composition of the films in terms of areal density of O and Gd i.e., number of atoms present per unit area throughout the depth of the film. Fig. 6.4 shows the estimated oxygen-to-gadolinium atomic ratios of all the Gd_2O_3 samples as obtained using the calculated areal densities of these two elements. It can be seen from fig. 6.4 that O/Gd atomic ratios for the films deposited at lower oxygen partial pressure are significantly higher than the value (1.5) for stoichiometric Gd_2O_3 . Super-stoichiometric oxide samples estimated by RBS

technique has also been reported by us and other workers [55, 156-157]. It is clear from fig.6.4, oxygen concentration in the films decreases with an increase in oxygen partial pressure beyond 16.7%. The decrease in oxygen stoichiometry beyond certain oxygen percentage had also been observed by us in case of sputter deposited Ta₂O₅ samples [55].

6.5 Grazing Incidence X-ray reflectivity (GIXR) measurements:

Fig.6.5 depicts GIXR data of all the Gd₂O₃ samples which clearly shows that the slope of the X-ray reflectivity curve, which gives the roughness of the sample surface, monotonically decreases with an increase in oxygen partial pressure from 9.1% to 50%, while the sample prepared at 9.1% oxygen partial pressure exhibits similar slope as that of the sample deposited without oxygen flow. In order to get a more quantitative idea about the

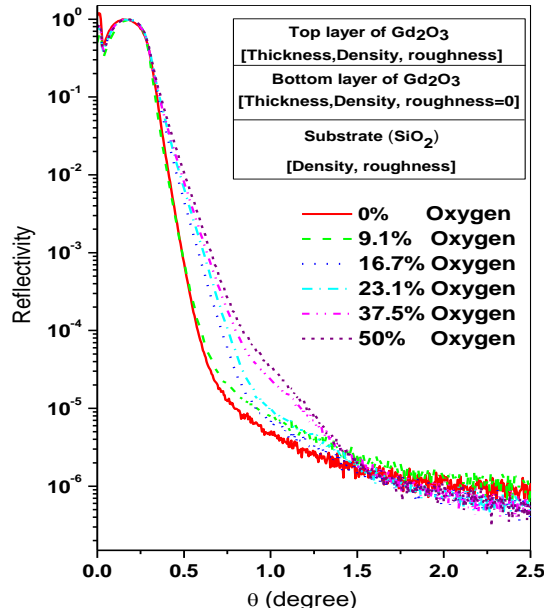


Fig.6.5: Measured GIXR curves of all Gd₂O₃ samples deposited under different oxygen partial pressures. (Inset shows the layer structure model employed to fit the experimental GIXR spectra).

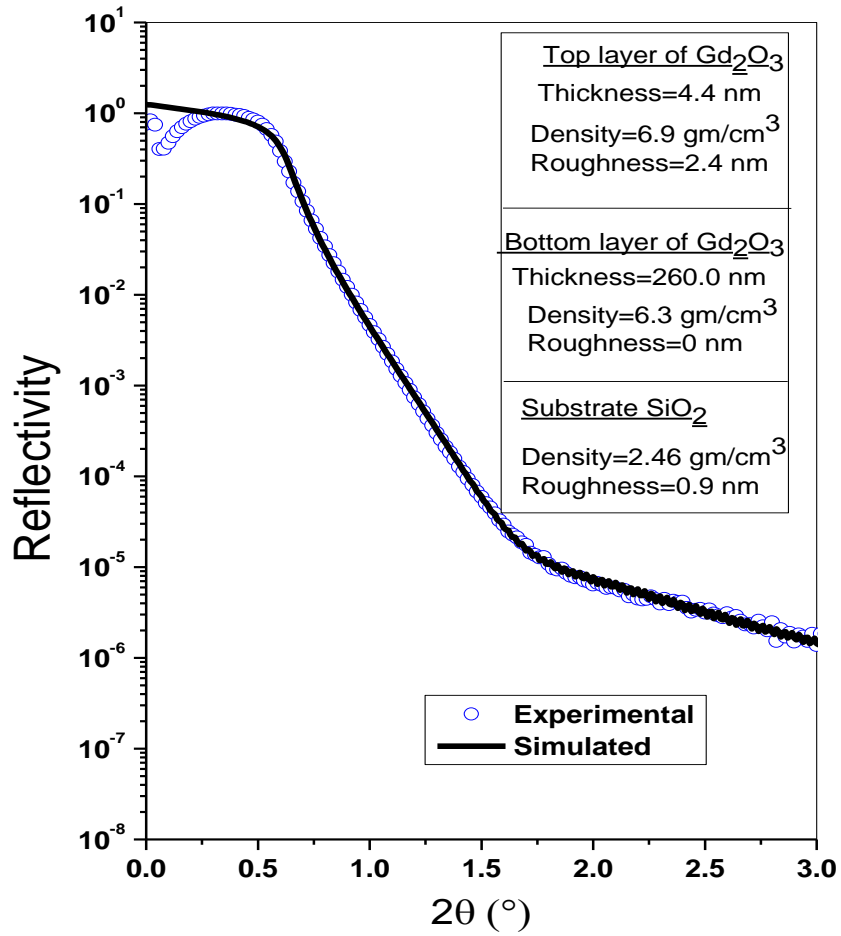


Fig.6.6: Experimental GIXR curve along with best fit theoretical simulation for a representative Gd_2O_3 sample deposited at 16.7% oxygen partial pressure. (Inset shows layer structure model obtained by analysing the GIXR data of the same sample).

surface roughness of the samples, all the GIXR data have been fitted theoretically using “IMD” code [61] under the “XOP” software package following Parratt’s formalism [62] as described in detail in Chapter-2. A two-layer model as shown in the inset of fig. 6.5 was necessitated to achieve best fitting in which the top layer was introduced to represent the surface roughness of the film and the bottom layer represents the density and thickness of the bulk of the sample. For the present set of samples the χ^2 values are ~ 0.01 manifesting good quality fit of the data assuming above model. Here it should be mentioned that a single layer model was also tried to fit the GIXR data but that did not give satisfactory fitting quality.

The experimental GIXR curve along with the best fitted simulated curve is shown in fig. 6.6 for a representative Gd_2O_3 sample deposited at 16.7% oxygen partial pressure and the best fit sample structure is also shown in the inset. Two or multiple layer model has previously been used by many others [175-177] also to represent depth inhomogeneity in a single layer thin

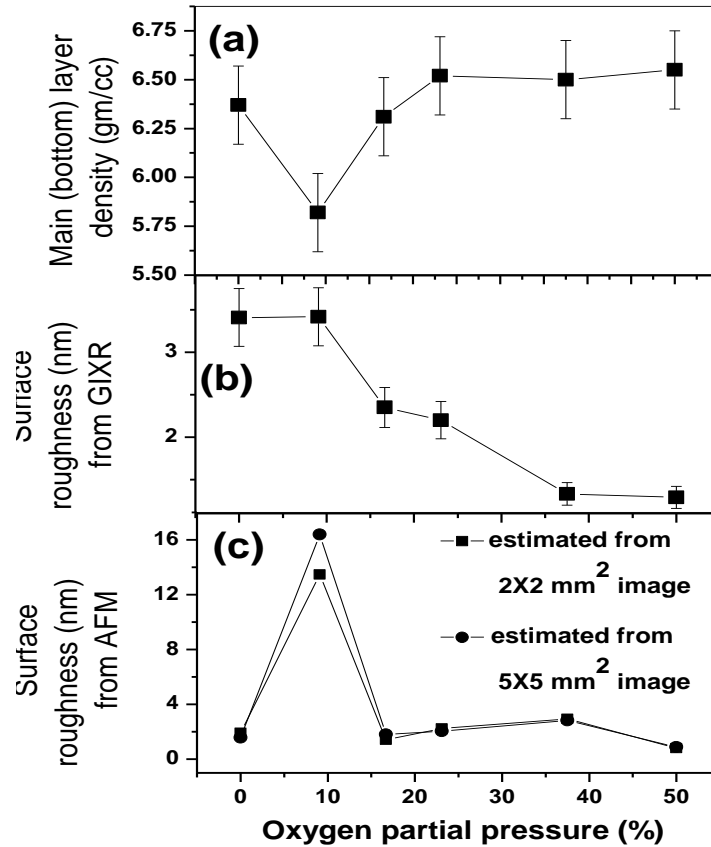


Fig. 6.7: (a) Variation of (a) main (bottom) layer density obtained from GIXR fitting, (b) Surface roughness obtained from GIXR fitting, (c) Surface roughness (RMS) estimated from AFM measurement as a function of oxygen partial pressure.

film. Since the interference oscillation of the GIXR data could not be resolved, the same cannot be used for accurate determination of the thicknesses of the sample. Instead, thicknesses of the samples obtained from spectroscopic ellipsometry measurements, discussed later, have been used as an approximate initial guess of bottom layer (main layer) thickness. The roughness on bottom layer has been assumed to be zero since both top and bottom layers are of same Gd_2O_3 material and they have grown continuously. The variation

of the estimated bottom layer (main layer) density and the top layer roughness as a function of oxygen partial pressure have been shown in figures 6.7(a) and 6.7(b) respectively. As is evident from Fig. 6.7(a), densities of all the samples are slightly less compared to the bulk Gd_2O_3 density of 7.41 gm/cm^3 [170], which is expected for sputter deposited films. It can be seen from fig. 6.7(a) that the density of the films first decreases as oxygen partial pressure is increased, because of the decrease in the kinetic energies of the ad atoms reaching on the substrates due to collision with oxygen ions. However, the density is found to increase again as the oxygen partial pressure is increased beyond 10%. This might be due to realisation of more and more stoichiometric films (with less oxygen and higher metallic content) as oxygen partial pressure is increased in the sputtering ambient as can be seen from fig. 6.4. From Fig. 6.7(b), it can be seen that with an increase in oxygen partial pressure from 9.1% to 50%, surface roughness decreases. This is due to the decrease in thickness of the films with the increase in oxygen partial pressure as estimated from transmission and ellipsometry measurements discussed later. The increase in surface roughness with the increase in film thickness has already been established through dynamic scaling theory [178]. However, in the present case, surface roughness does not increase further when oxygen partial pressure decreases from 9.1% to 0%. This is because without oxygen partial pressure the ad atom energies increase drastically since there is no collision [179] of the ad atoms with the neutral oxygen atoms which is otherwise present in finite oxygen partial pressure. The enhanced kinetic energies of the ad atoms at 0% oxygen partial pressure help in smoothening the film surface through the breaking of columnar structures

6.6 Atomic Force Microscopy (AFM) measurements:

Surface morphology of all the Gd_2O_3 samples were measured by Atomic force microscope (NT-MDT, SOLVER-PRO) using Si cantilever tips (resonant frequency ~ 190

kHz) in non-contact mode. Both $2 \times 2 \mu\text{m}^2$ and $5 \times 5 \mu\text{m}^2$ images were recorded in the central region of the films. Fig.6.8 displays both $2 \times 2 \mu\text{m}^2$ and $5 \times 5 \mu\text{m}^2$ AFM images of all the samples. RMS roughnesses of the samples were estimated from statistical variation of surface height for both sets of images and are shown in Fig.6.7 (c). It can be seen from fig. 6.7(b) and fig. 6.7(c) that beyond $\sim 10\%$ oxygen partial pressure surface roughness values measured by both AFM and GIXR techniques decrease with increase in oxygen partial pressure. Furthermore, if we disregard the data for the sample deposited at 9.1% oxygen partial pressure, the values of surface roughness obtained from GIXR and AFM measurements almost agree with each other. The issue of agreement of the surface roughness value obtained from GIXR and AFM measurements has been discussed in detail by Su et.al.[180] who have concluded that these two values may not necessarily match with each other since (i) the techniques covers different regions of power spectral density curve, in case of AFM, it is limited by the tip width vis-a-vis the scanned area while in GIXR measurement it is limited by the coherence length of the X-ray beam and (ii) AFM cannot distinguish between low density contamination spikes on the surfaces which are not considered by GIXR measurement. Possibly for the above reasons, the values of roughness measured by two techniques are quite different for the sample prepared at 9.1 % oxygen partial pressure.

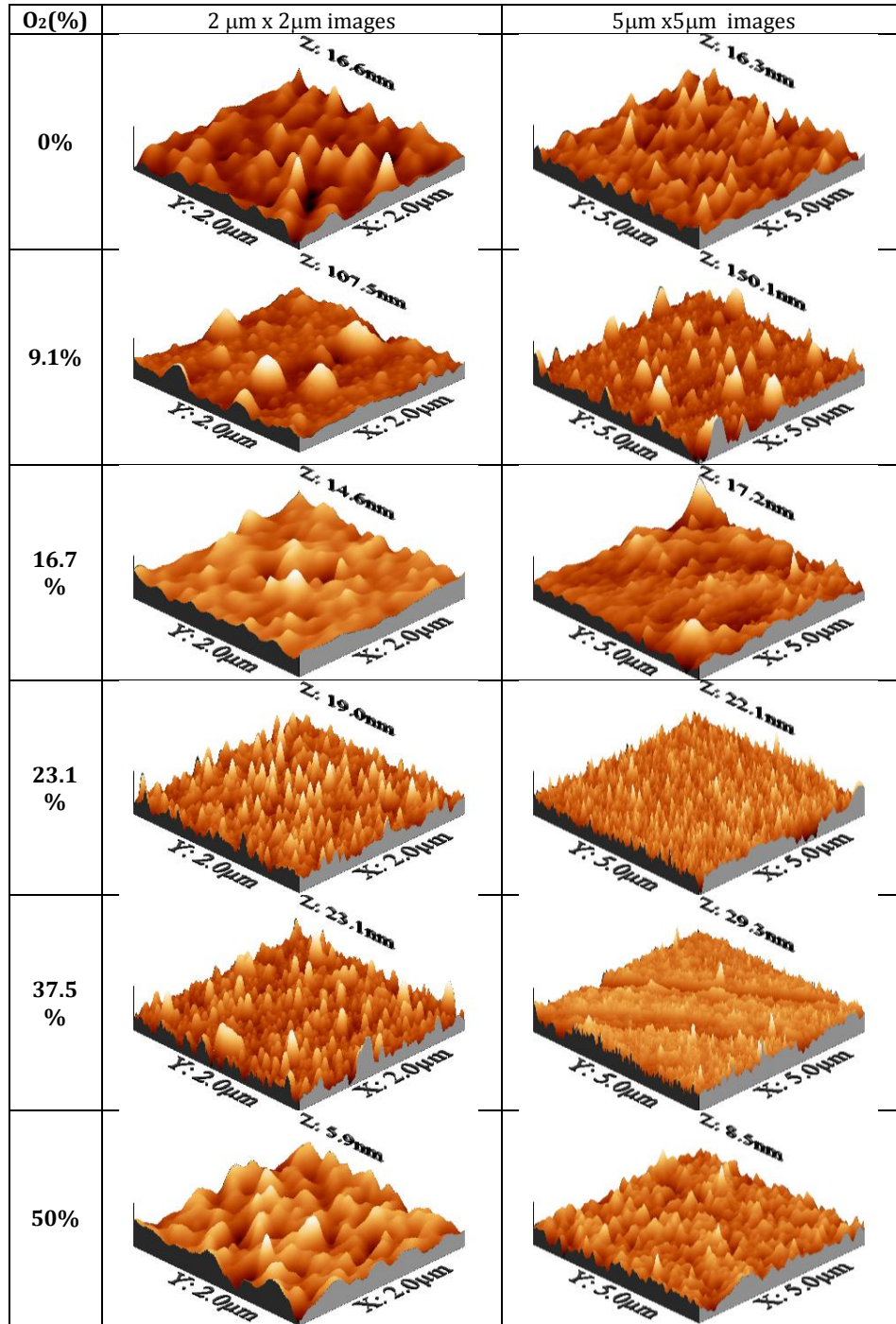


Fig.6.8: 3D AFM micrographs of all the Gd₂O₃ samples deposited under different oxygen partial pressures (x and y axes are in μm , z axis is in nm unit).

6.7 Transmittance spectrophotometry measurements:

The optical properties of the films have been characterised by spectral transom mission measurements by using a UV-VIS-NIR spectrophotometer. Fig.6.9 shows the transmission spectrum of a representative Gd_2O_3 film deposited on fused silica substrate under 16.7% oxygen partial pressure. The transmission spectra of the samples were analyzed using the

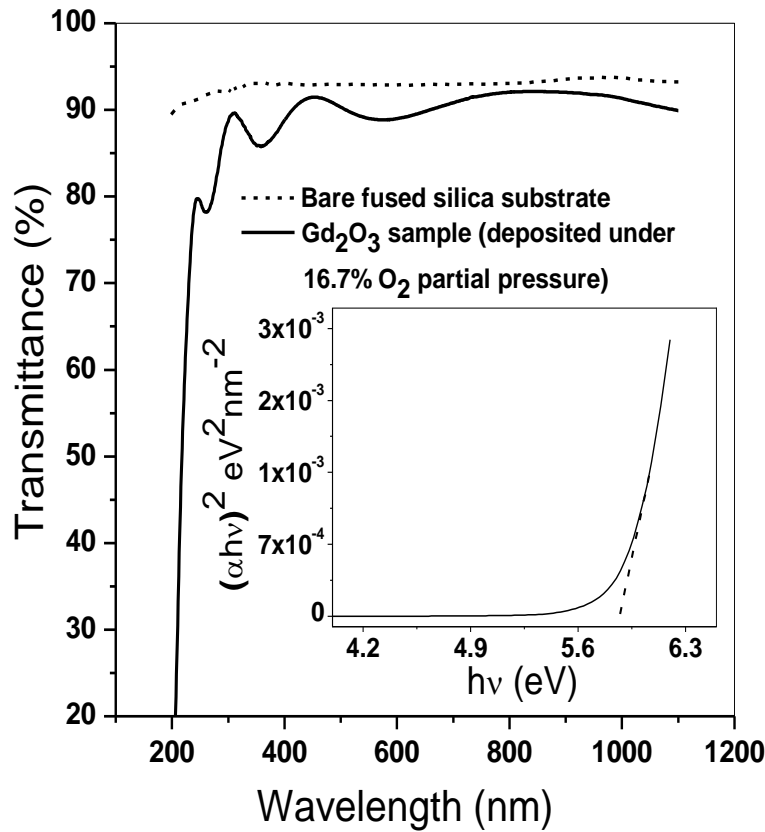


Fig.6.9: Experimental transmission spectrum of bare fused silica substrate and of one representative Gd_2O_3 sample deposited on fused silica substrate under 16.7% oxygen partial pressure. (Inset shows $(\alpha h\nu)^2$ vs. $h\nu$ curve for the sample.)

method proposed by Swanepoel [64] to estimate thickness and wavelength dependent dispersion of refractive index (n) and absorption coefficient (α). The deposition rates of the films estimated using the thickness obtained from transmission measurement and deposition time are shown in Fig. 6.10(a), while the refractive indices of the samples at 550 nm as a function of oxygen partial pressure have been plotted in Fig. 6.10(b). The band gap of the

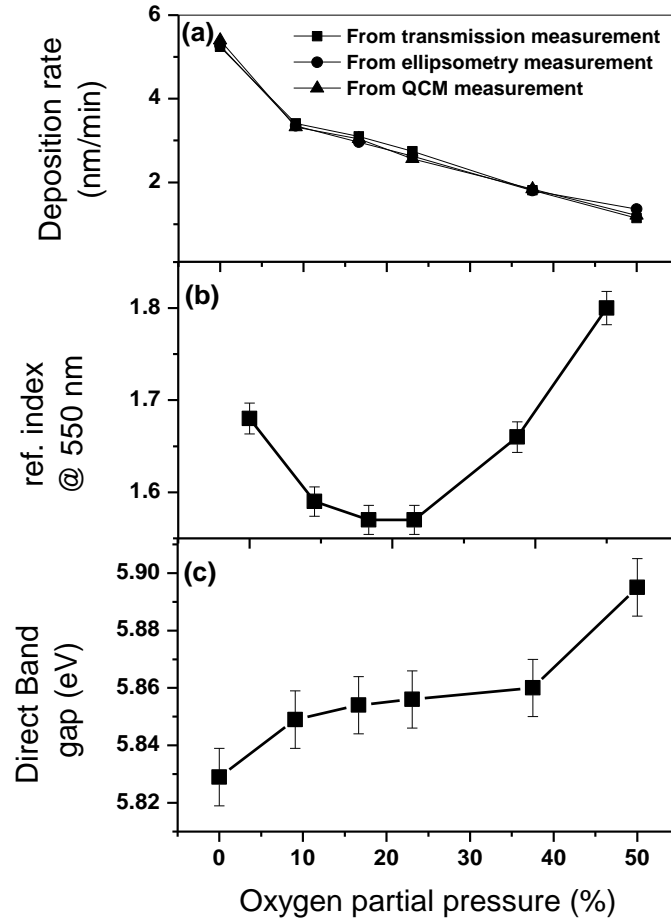


Fig.6.10: Variation of (a) deposition rate (b) refractive index at 550 nm (c) direct band gap estimated from transmission measurement as a function of oxygen partial pressure. (a) also shows the variation of deposition rate obtained from spectroscopic ellipsometry measurement and in-situ measurement by quartz crystal monitor.

films has been determined [181] by plotting $(\alpha h\nu)^2$ vs. $h\nu$ curve in the region $\alpha > 10^4 \text{ cm}^{-1}$, ν being the frequency of the photon. The curve tends asymptotically towards a linear section, the intersection of which to $h\nu$ axis gives direct band gap E_g of the film as shown in the inset of Fig. 6.9 for a representative Gd_2O_3 film deposited under 16.7% oxygen partial pressure. Band gap values of the films as obtained above have also been plotted as a function of oxygen partial pressure in Fig. 6.10(c). The error in estimated thickness and refractive index in this method is $\sim 1\%$ as suggested by Swanepoel [64], while the error in band gap has been estimated to be $\pm 0.01 \text{ eV}$ based on the wavelength resolution of the

spectrophotometer used in transmission measurement. The refractive index and band gap values obtained in these films are similar to that reported by other workers also [182-183].

Fig. 6.10(a) shows that the deposition rate drastically decreases as oxygen partial pressure is increased from 0% to 9.1% and then gradually decreases with an increase in oxygen partial pressure in the range of 9.1-50%. Similar variation in the deposition rate has been observed by us for other oxide samples also and the reason has been explained in Chapter-3. . It can be seen from fig. 6.7(a) and fig. 6.10(b), that both the main layer density obtained from GIXR measurement and refractive index obtained from transmission measurements initially decrease as oxygen partial pressure is increased from 0 to 10%, while at higher oxygen partial pressure both the quantities show an increasing trend. Fig. 6.10(c) shows that the band gap is increased with the onset of oxygen, though with further increase in oxygen it does not increase much and gets saturated. The increase in band gap with the increase in oxygen partial pressure is due to the evolution of stoichiometric Gd_2O_3 films as shown in fig.

6.8 Spectroscopic Ellipsometry measurements:

Spectroscopic ellipsometry measurements of all the samples have been carried out in the wavelength range of 200-900 nm by the rotating polarizer spectroscopic ellipsometer (GES5E by SOPRA) at 70° angle of incidence as described in Chapter-2. The details of the ellipsometric data analysis has been presented in Chapter-2. In this case, the sample layer structure model used for simulating theoretical ellipsometric spectra consists of one bulk layer without void and one interface layer, having a mixture of void and material between the substrate and the bulk layer, where optical constants of the bulk material (Gd_2O_3) are assumed to follow the Tauc-Lorentz dispersion model [68] which is common for such oxide dielectric films and has been described briefly in Chapter-2. It should be noted that generally

while analysing the spectroscopic ellipsometric data of such physical vapour deposited thin film samples, sample structures with a top layer having 50% void above the bulk layer is also assumed [55, 184] to take care of the surface roughness present in the films. However, it has been observed that in this case good quality fitting of the ellipsometric data can be obtained without considering the surface roughness layer or in other words inclusion of the surface roughness layer in the sample structure does not improve the fitting quality further. This may be because of the fact that as has been observed from GIXR and AFM measurements (shown in fig. 6.7(b) and 6.7(c) respectively), the surface roughness values of most of the samples are in the range of 1-2 nm which is 1% of the total thickness of the films. However, the sample deposited with 9.1% oxygen partial pressure has relatively higher surface roughness and a surface roughness layer has been added to fit the spectroscopic ellipsometric data of this sample. The estimated thickness of the interface layer of the samples is found to be in the range of 16 to 90 nm, the void percentage of the interface layer varies in the range 5 to 23% while the main layer thickness is found to be in the range of 106 nm to 374 nm. Fig. 6.10(a) also shows the calculated deposition rate as derived by dividing the thickness obtained from ellipsometry measurement with the deposition time which shows similar trend as obtained from the transmission data and these data also agree with the average deposition rates observed in the quartz crystal monitor during deposition of the samples, which have also been shown in fig. 6.10(a). Fig. 6.11(a) shows the variation of intrinsic refractive index of the main layer @ 550 nm as a function of oxygen partial pressure. As can be seen from Fig. 6.11(a), the intrinsic refractive index of the films, which is a basic property of the material and does not have the effect of voids, first decreases from a high value for the film deposited with 0% oxygen partial pressure which is a metal rich film to the film deposited with 9.1%

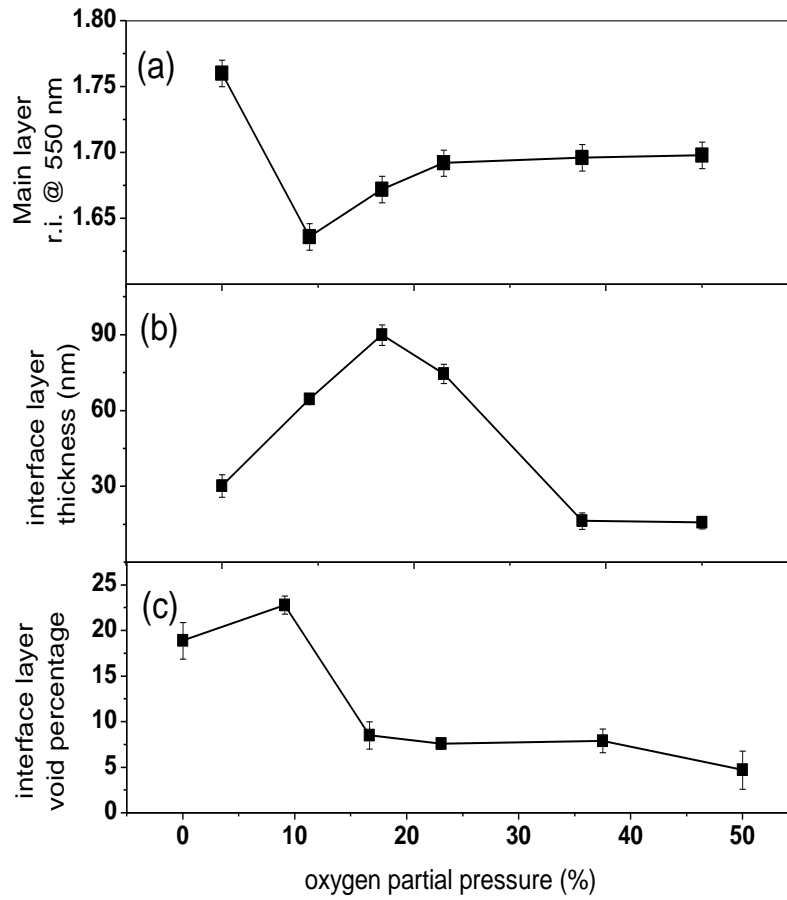


Fig.6.11: Variation of (a) intrinsic refractive index @ 550 nm (b) interface layer thickness and (c) interface layer void percentage estimated from spectroscopic ellipsometry data as a function of oxygen partial pressure.

oxygen partial pressure and subsequently increases with a further increase in oxygen partial pressure. Fig. 6.11(b) & (c) show the variation of thickness and void percentage of the interface layer. It should be noted that the variation in the void fraction (Fig.6.11(c)) in interface layer as a function of oxygen partial pressure follow the reverse trend of the variation of the density (Fig. 6.7(a)) of the films as obtained from GIXR measurements, which is as expected. Here it should be noted that Fig. 6.10(b) represents the effective refractive index of the samples @ 550 nm as obtained from transmittance measurement, while Fig. 6.11(a) represents the refractive index of the bulk material of the film excluding voids as obtained from spectroscopic ellipsometry.

6.9 Extended X-ray Absorption Fine Structure measurements:

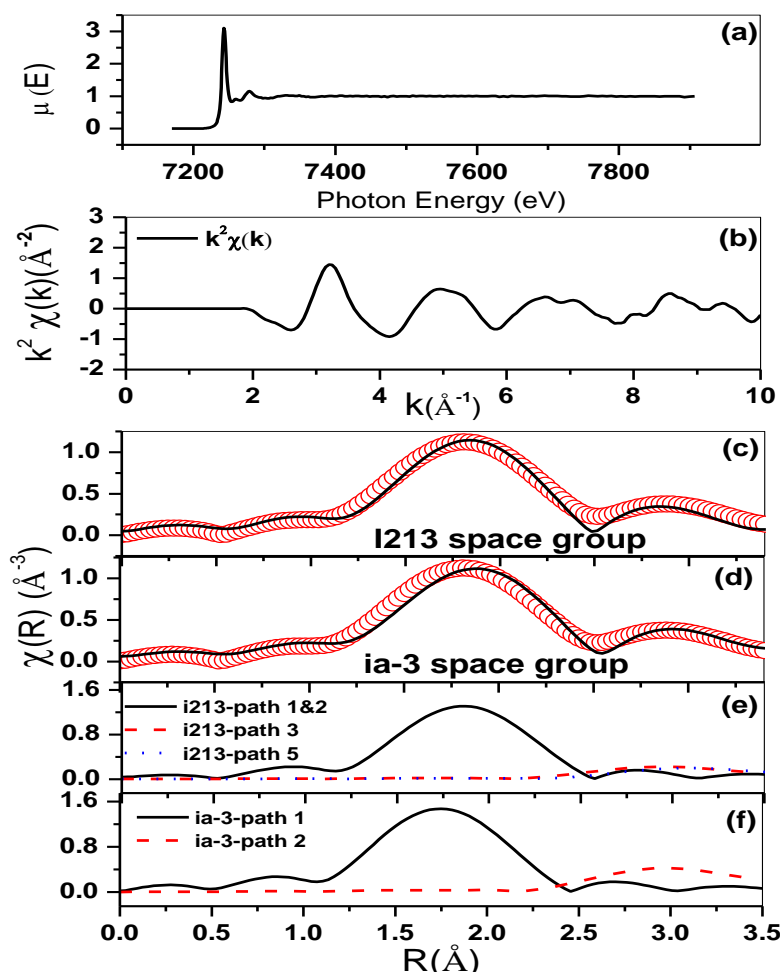


Fig.6.12: (a) Experimental EXAFS spectrum (μ vs. E), (b) Reduced $k^2\chi(k)$ vs. k plot, (c) Fourier transformed EXAFS spectrum ($\chi(R)$ versus R) along with best-fit theoretical simulation assuming body centered cubic Gd_2O_3 phase having space group $I2_13$, (d) Fourier transformed EXAFS spectrum ($\chi(R)$ versus R) along with best-fit theoretical simulation assuming body centered cubic Gd_2O_3 phase having space group $ia-3$ for a representative Gd_2O_3 sample deposited at 9.09% oxygen partial pressure, (e) theoretical paths of $I2_13$ space group and (f) theoretical paths of $ia-3$ space group.

EXAFS measurements of the Gd_2O_3 samples have been carried out at the energy scanning EXAFS beam line (BL-09) in fluorescence mode at the INDUS-2 Synchrotron Source (2.5 GeV, 125 mA) at Raja Ramanna Centre for Advanced Technology (RRCAT), Indore, India as described in Chapter-2. In order to investigate the local structures surrounding Gd sites, X-ray absorption coefficient (α) is measured as a function of energy of

X-ray around the Gd L3 edge energy (7243 eV). The EXAFS data has been analysed using the methodology described in Chapter-2.

Table-6.1: Scattering paths used for fitting assuming BCC crystal structure having space group I2₁3.			
	Degen eracy	R _{eff}	Amp
Path-1 (Gd-O2)	3	2.396	100
Path-2 (Gd-O1)	3	2.410	98.49
Path-3 (Gd-Gd3)	3	3.509	46.94
Path-5 (Gd-Gd2)	3	3.658	43.22

Table-6.2: Scattering paths used for fitting assuming BCC crystal structure having space group ia-3.			
	Degeneracy	R _{eff}	Amp
Path-1 (Gd-O1)	6	2.281	100
Path-2 (Gd-Gd2)	6	3.553	41.93

As discussed earlier in the context of GIXRD result, cubic phase of Gd₂O₃ is most probable in room temperature and also since we have obtained the signature of cubic Gd₂O₃ phase only from GIXRD measurement of the present Gd₂O₃ samples, we have explored the two possible body centred cubic Gd₂O₃ phases having space group I2₁3 (199) and ia-3 (206) for analysing the EXAFS data. The theoretical standards for cubic Gd₂O₃ phases having space group I2₁3 (199) and ia-3 (206) were created using lattice parameters and Wyckoff positions obtained from literature [185-186]. The scattering paths used for simulating EXAFS spectra of space group I2₁3 (199) have been tabulated in Table-6.1. While fitting with this

model, paths 1 and 2, which represent the first two oxygen shells were combined and were represented by a single scattering path with degeneracy 6. Also, path-3 and path-5 have been combined after fitting to represent an equivalent Gd-Gd shell. As for space group ia-3 (206) model, the scattering paths used for simulating EXAFS spectra have been tabulated in Table-6.2. In this case path-1 and path-2 individually represents the first Gd-O and Gd-Gd shell respectively. Experimental EXAFS spectrum (μ vs. E), reduced $k^2\chi(k)$ vs. k plot and Fourier transformed EXAFS spectrum ($\chi(R)$ versus R) for a representative Gd_2O_3 sample deposited at 9.1% oxygen partial pressure are shown in fig. 6.12(a)-(b). Figures 6.12(c) and (d) show best fit theoretical $\chi(R)$ versus R plots obtained using both the space groups along with the experimental data of the representative sample, while fig.6.12 (e) and (f) shows the theoretical paths for the corresponding space groups. The above exercise has been carried out on all the samples and fig. 6.13 depicts the R_{factor} values achieved by fitting using both the models for all the samples. It can be seen that R_{factor} values are less for the fitting with the ia-3 space group model compared to that obtained with $I2_13$ space group model for most of the samples. Figures 6.14(a)-(d) (left side) and 6.14(a)-(d) (right side) show the variation of the bond length and mean square displacement (σ^2) corresponding to the nearest Gd-O shell and next nearest Gd-Gd shells obtained from EXAFS data analysis using $I2_13$ and ia-3 space group models respectively. It can be seen from the above figures that though the results for the first Gd-O shell obtained from EXAFS fitting of both the space group models are similar, the results for the 2nd shell (Gd-Gd shell) are different. It should be noted here that the values of the best fit coordination numbers are similar within the error bar of $\pm 10\%$ and have not been plotted here. It has been observed that the variation of Gd-Gd bond length as a function of oxygen partial pressure used during deposition of the samples using the ia-3 space group model gives more reasonable result, since in this case the Gd-Gd bond increases significantly

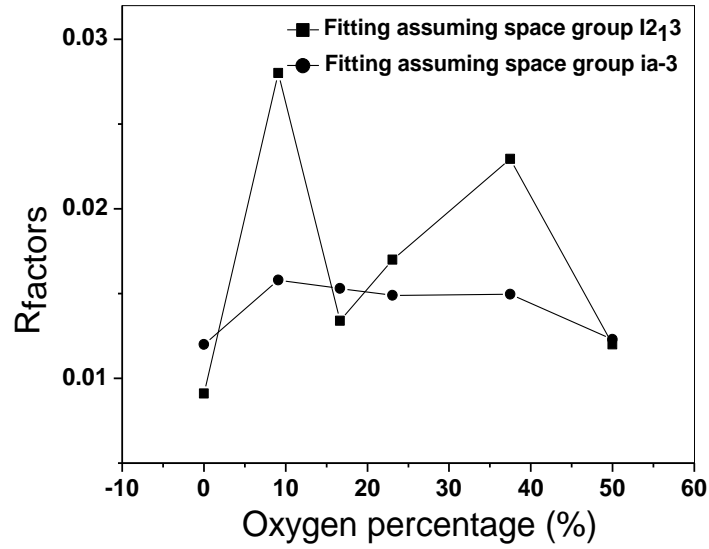


Fig. 6.13: Variation of R_{factor} assuming body centred cubic Gd_2O_3 phase having space group $I2_13$ and $ia-3$ model as a function of oxygen partial pressure.

in case the sample deposited with 9.1% oxygen partial pressure, as can be seen from fig.6.14(c) (right side), which signifies less compact structure, less density and low intrinsic refractive index of the films. This is reflected in the variation of intrinsic refractive index of the films obtained from spectroscopic ellipsometry data and shown in fig. 6.11(a). Similar increase in the intrinsic refractive index in thin film systems due to a decrease in bond length and vice-versa has also been observed earlier by us in several other oxide systems also [187-188]. However, Gd-Gd bond length variation obtained by fitting using the space group $I2_13$ shows a decrease in Gd-Gd bond length for the film deposited with 9.1% oxygen partial pressure, as can be seen from fig.6.14(c) (left side). Moreover goodness of fitting of EXAFS spectra, as dictated by R_{factor} values shown in fig. 6.13, is better for $ia-3$ space group. Thus from the above studies it can be concluded that the films have assumed cubic structure with the space group of $ia-3$.

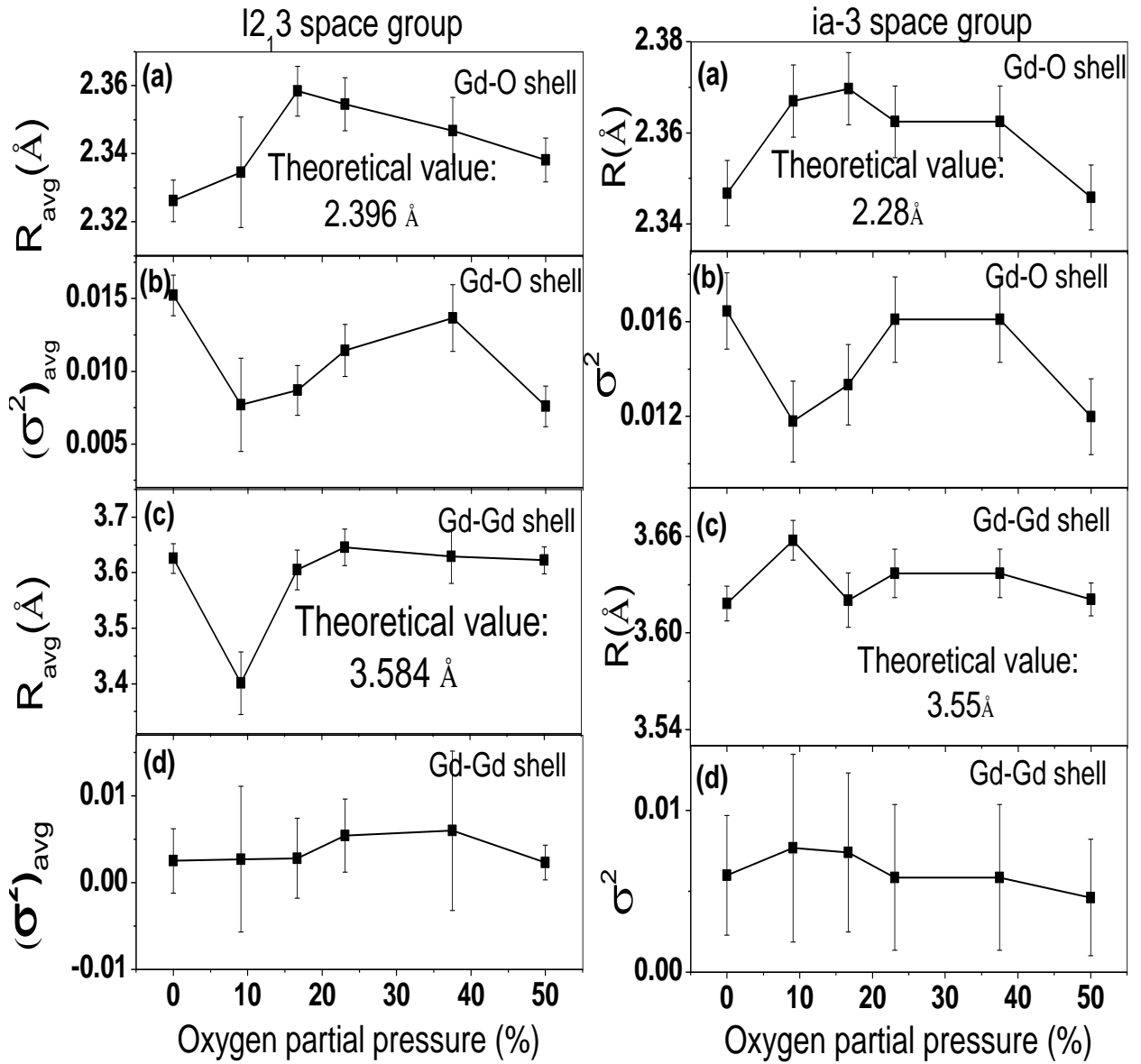


Fig.6.14: Variation of (a) average Gd-O bond length (b) average Debye-Waller factor of Gd-O bonds (c) average Gd-Gd bond length and (d) average Debye-Waller factor of Gd-Gd bonds as a function of oxygen partial pressure as obtained from EXAFS data analysis assuming Gd₂O₃ cubic phase having space group I_{2,3} (left panel) and space group ia-3 (right panel).

6.10 Conclusion:

A set of Gd₂O₃ thin films has been deposited on quartz substrates by RF magnetron sputtering under a mixed ambient of argon and oxygen at various oxygen partial pressures. GIXRD measurements show that all the thin film samples are grown in cubic phases, while

GIXR measurements show that the films have low surface roughness which decreases as oxygen partial pressure is increased in the sputtering ambience. Similar variation is also observed for the surface roughness value obtained from AFM measurements. RBS measurements show that the films deposited at lower oxygen partial pressure are oxygen-rich while relatively stoichiometric films are realised at higher oxygen partial pressure. The density of the films, obtained from GIXR measurements is found to vary in a non-linear fashion with the films deposited at 9.1% oxygen partial pressure having the lowest density, the overall refractive index obtained from transmission measurements follow the similar variation as bulk density as expected. Spectroscopic ellipsometry measurements show that the low density of the sample prepared with 9.1% oxygen partial pressure is due to the presence of high concentration of voids in this sample. EXAFS measurements have yielded information regarding the local structure around Gd sites. Comparing the nature of variation of Gd-Gd bond length of the samples obtained from EXAFS measurements, as a function of oxygen partial pressure, with that of the intrinsic refractive index of the Gd_2O_3 material present in the films, as obtained from the spectroscopic ellipsometric measurements, it could be concluded that these films assume $ia-3$ space group of cubic crystalline structure. Thus by applying complementary characterisation techniques, it has been possible to explain several macroscopic properties of this technologically important thin film system from microscopic structural information.

CHAPTER-7

Study of Gd doped ZrO_2 samples

7.1 Introduction:

Zirconia (ZrO_2) has been extensively studied in various forms due to its diverse applications such as a refractory material, oxygen sensor, bioceramic, or thermal barrier coating, amongst others [24-25]. Structure-wise, pure ZrO_2 is monoclinic from room temperature to 1440 K, tetragonal between 1440 and 2650 K and cubic up to its melting point of 2950 K [189]. Zirconia exhibits high anionic conductivity when doped with aliovalent cations due to the generation of oxygen ion vacancies required for charge compensation [190]. Doped zirconia systems are especially important in catalytic applications, either as supports or as electrolytes in solid oxide fuel cells (SOFCs) [26-27]. Apart from imparting relevant ionic conductivity, doping also stabilizes the cubic fluorite phase of zirconia, at the operating temperatures of the solid oxide fuel cell. Yttria-stabilized zirconia (YSZ) typically with 8 mol% Y doped in ZrO_2 , is the most common material used in SOFCs [191-192]. However, the use of YSZ for SOFC application is seriously limited by the fact that it requires relatively high temperatures of around 1100–1300K to achieve adequate ionic conduction. The high temperature of operation raises the issue of material stability and compatibility. Thus, the search for alternate materials having equivalent ionic conductivity at lower temperature is going on to enable operation of solid oxide fuel cells at intermediate

temperatures of 900-1000 K. Along with many other alternate dopants, Gadolinium (Gd) is one of the most promising dopants in ZrO_2 system on which several works have already been reported [28-29].

Apart from above mentioned applications, zirconium oxide has wide range of optical applications also. Due to its high transparency in the entire visible and near infrared region and stability with other refractory materials, ZrO_2 is often used as a comprising layer in multilayer interference coating based optical devices such as in anti-reflection coating, broadband interference filters and active electro-optical devices [1]. Additionally, ZrO_2 is the most frequently used material for fabricating high power laser mirrors [193] and to generate passive [3] and active [2] waveguides. Doped and composite forms of ZrO_2 have also drawn considerable attention due to their suitable optical properties. Y_2O_3 -doped ZrO_2 has been studied for its optical properties by Sanchez-Gonzalez et al. [181] and Boulouz et al. [194]. Band gap tuning of ZrO_2 has been demonstrated by varying Sn concentration in ZrO_2 - SnO_2 nanocomposite by Lakshmi et al. [195] and by varying Au doping concentration in ZrO_2 by John Berlin et al. [196], while Kul'kova et al. [197] demonstrated how oxygen vacancies produce additional states near the Fermi level and affects the optical properties of zirconia.

The important issue being addressed in this context is the position of oxygen vacancies due to aliovalent doping in ZrO_2 . Our group has earlier employed Extended X-ray absorption fine structure (EXAFS) studies at Zr K and Gd L_3 -edges to find out the positions of oxygen vacancies in ZrO_2 samples prepared by co-precipitation route [198, 199]. It has been observed from the above studies that Gd doping creates oxygen vacancies near the host Zr atoms and ~9 mol% Gd^{3+} is the optimum doping percentage for creation of maximum oxygen vacancies. The above observation regarding the position of oxygen vacancies agree with the findings by

several other researchers also [200-201]. However, there are few other studies where it has been reported that Gd doping creates oxygen vacancies near the dopant (Gd) sites [28-29].

In order to have more insight into the mechanism of creation of oxygen vacancies in the Gd doped system, and also to seek confirmation of our previously mentioned findings in case of thin film systems, in the present study we have carried out EXAFS measurements on a set of Gd^{3+} doped ZrO_2 thin films prepared by magnetron sputtering technique. Apart from EXAFS measurements the films have also been subjected to other standard structural and optical characterizations.

7.2 Preparation of samples:

ZrO_2 thin films with 0, 7, 9, 11 and 13% of Gd doping were prepared by RF magnetron sputtering technique by directly sputtering pure/doped ZrO_2 targets in the home-made RF magnetron sputtering system described in Chapter-2. For the deposition of the present set of samples RF power of 100 W was used for sputtering under a mixed ambient at 2.5×10^{-4} mbar pressure with 8 sccm O_2 flow and 24 sccm Ar flow rates. External oxygen flow was provided during sputtering in order to ensure proper oxygen stoichiometry in the films.

Grazing incidence X-ray diffraction (GIXRD) measurements have been carried out on all the films using $\text{Cu } K\alpha$ ($\lambda=1.5418\text{\AA}$) radiation incident at a grazing angle of 0.55° while the diffracted beam intensity was recorded in 2θ range of 10° - 90° with step size of 0.01° . Optical transmission measurements have been carried out in the wavelength range of 190 to 1100 nm in steps of 2 nm in the UV-Visible-NIR spectrophotometer (JASCO V-630) while spectroscopic ellipsometry measurements were carried out in the wavelength range of 250 to 1000 nm by the rotating polarizer spectroscopic ellipsometer described in Chapter-2.

Extended X-ray Absorption Fine Structure (EXAFS) measurements on representative Gd doped ZrO_2 thin film samples have been carried out in fluorescence mode at Zr K-edge and Gd L_3 -edges at the Energy-Scanning EXAFS beam line (BL-9) at the INDUS-2 Synchrotron Source (2.5 GeV, 100 mA) at Raja Ramanna Centre for Advanced Technology (RRCAT), Indore, India as mentioned in Chapter-2. EXAFS measurements were performed at Zr K-edge in the range of 17841 eV to 18800 eV and at Gd L_3 -edge in the range of 7160 eV to 7730 eV in fluorescence mode.

7.3 Grazing Incidence X-ray reflectivity (GIXR) measurements:

Figs.7.1 (a), (b) and (c) show the GIXRD spectra of the fused silica substrate, pure ZrO_2 film and four numbers of Gd doped ZrO_2 films respectively. Fig. 7.1(a) shows that the fused silica substrate is amorphous with a hump at 21.64° . Fig. 7.1(b) shows that the GIXRD pattern of pure ZrO_2 film which, when compared with standard database of PCPDF [131] shows that the sample has grown in monoclinic (PDF file number: 861451) crystal structure except for the fact that the second most intense peak corresponding to (111) plane ($2\theta = 31.48^\circ$) is missing which was otherwise present in pure ZrO_2 target (not shown here). Comparing the GIXRD pattern of the doped samples as shown in Fig. 7.1(c), with standard database of PCPDF (PDF file number: 811551) [131] we find that all the doped thin film samples have predominantly cubic crystal structure. It should be mentioned here that XRD spectra of the pure and all the doped ZrO targets (not shown here) replicate the XRD pattern of monoclinic ZrO_2 crystal structure. Thus it is seen that even though both doped and undoped ZrO_2 target materials from which the samples have been prepared exhibit monoclinic crystal structure, the doped thin film samples have stabilized in cubic phase while

the undoped ZrO_2 sample remains in monoclinic phase. In our earlier work also [199] we have found that Gd doped ZrO_2 nanocrystalline samples have distorted cubic phase.

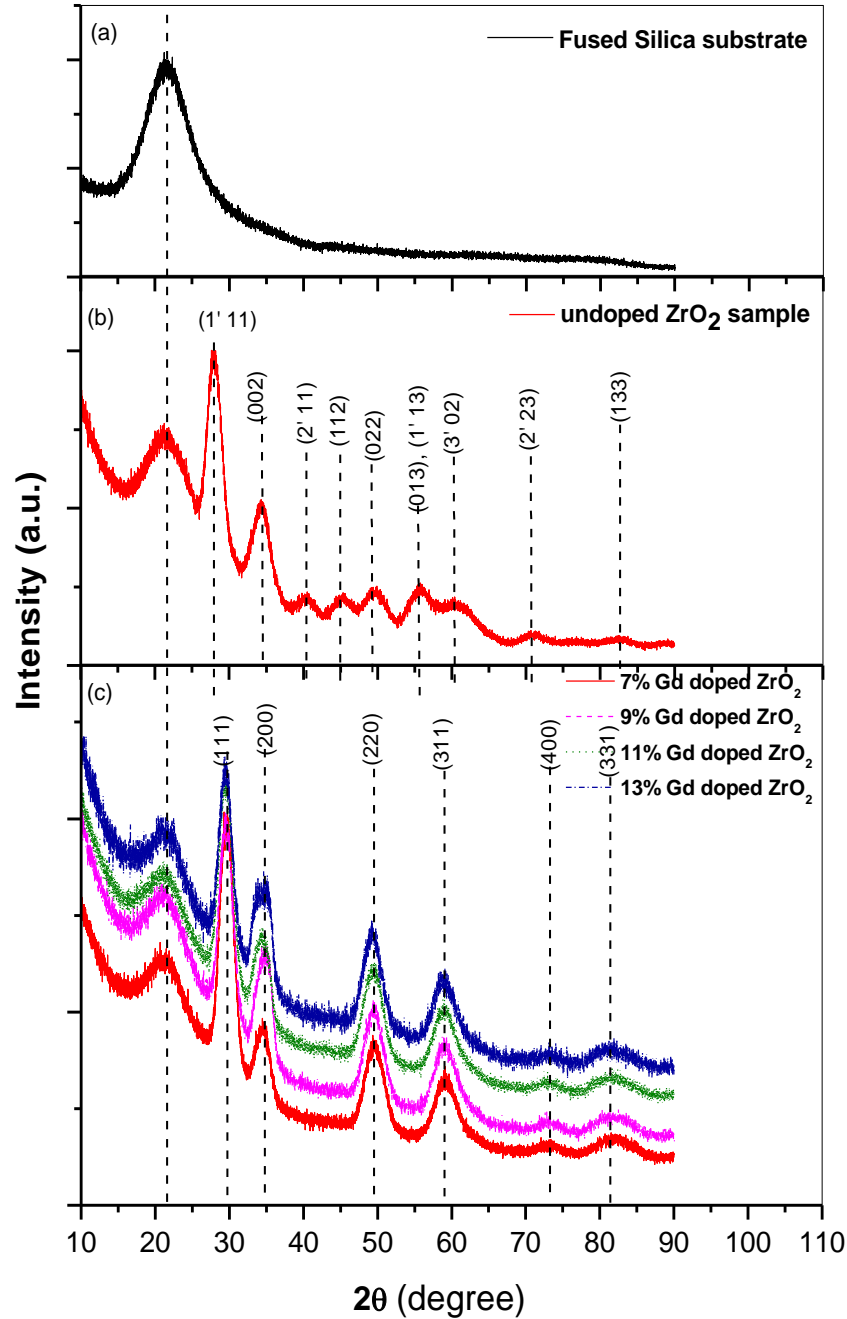


Fig. 7.1: (a) GIXRD plot of fused silica substrate, (b) GIXRD plot of undoped ZrO_2 thin film and (c) GIXRD plots of 7%, 9%, 11% and 13% Gd doped ZrO_2 thin films.

7.4 Spectroscopic Ellipsometry measurements:

For detailed optical characterizations, the spectroscopic ellipsometry measurement has been carried out on all the films. It has been observed that for the best fit of the ellipsometric data each sample had to be modelled as a two-layer structure with one bulk layer without any void and one interfacial layer in-between the bulk layer and substrate having certain void percentage. Such structures are very common for oxide thin film samples deposited by PVD techniques [55]. It has been assumed that the refractive index (r.i.) of the bulk ZrO_2 material

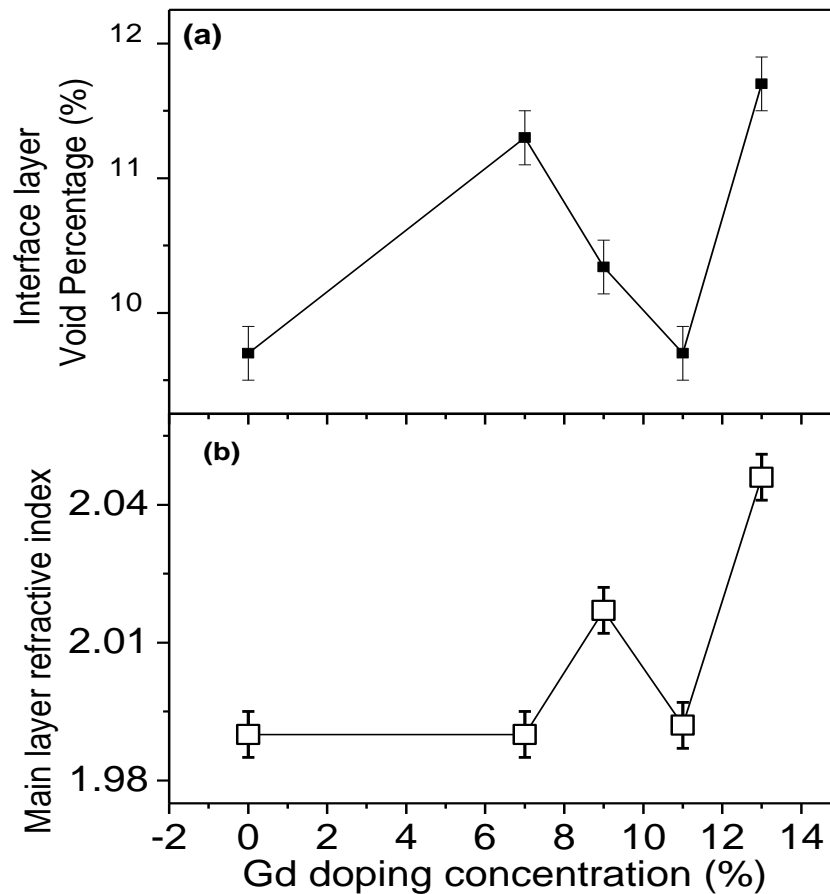


Fig. 7.2: (a) Variation of void percentage of interface layer in all the samples obtained from spectroscopic ellipsometry measurement.

(b) Variation of main layer refractive index of all the samples at 550 nm obtained from ellipsometry measurement.

follows the Tauc-Lorentz dispersion relation [68], mentioned in Chapter-2, which has been found to be followed by similar oxide samples in several other cases also [85, 184]. Fig.7.2 (a) depicts the variation of void percentage present in the interface layer as a function of Gd doping concentration in the samples which shows that void fraction in the interface layer decreases in the Gd doping concentration range of 7-11%, while it increases significantly beyond 11% Gd doping. The r.i. of main layer of the films, as depicted in fig. 7.2(b) has also been found to increase considerably beyond 11% Gd doping. The significant increase in r.i. and void fraction of the films beyond 11% Gd doping shows the metal-rich and void-prone poor quality of the films beyond 11% Gd doping.

The optical transmission spectra of the doped and undoped ZrO₂ thin films have been analyzed by the algorithm prescribed by Swanepoel [64] to extract effective r.i. and absorption coefficient of the films. The obtained absorption spectra of all the samples have been shown in Fig. 7.3(a). From the straight line interpolation of absorption spectrum (in the region $\alpha \geq 10^4 \text{ cm}^{-1}$) we have calculated the band gap of the samples using Tauc's formula [181] given by: $(\alpha h\nu)^p = A(h\nu - E_g)$; where $p=2$ gives the direct band gap and $p=1/2$ gives indirect band gap. Fig. 7.3(a) shows that unlike other samples, pure ZrO₂ thin film has two slopes in its absorption spectrum which signifies the presence of indirect band gap in this sample. The estimated indirect band gap value of pure ZrO₂ thin film is 5.10 eV, whereas the direct band gap of the same sample is 5.69 eV. The variation of the direct band gap values of the samples as a function of Gd doping concentration estimated for all the samples is shown in fig. 7.3(b) and it has been found that the direct band gap also decreases drastically beyond 11% Gd doping concentration manifesting poor quality of the films in this Gd concentration regime. The estimated effective r.i. of the films at 550 nm is shown in Fig.7.3(c) as a function of Gd doping concentration, which shows that there is an optimum (~9%) Gd concentration

for which the r.i. is the highest. The low interface void percentage and medium bulk layer r.i. for the samples with Gd doping in the range 9-11%, as has been obtained from ellipsometric measurement, causes the maximum overall effective r.i. for 9% Gd doped sample, while it decreases significantly beyond 11% Gd concentration.

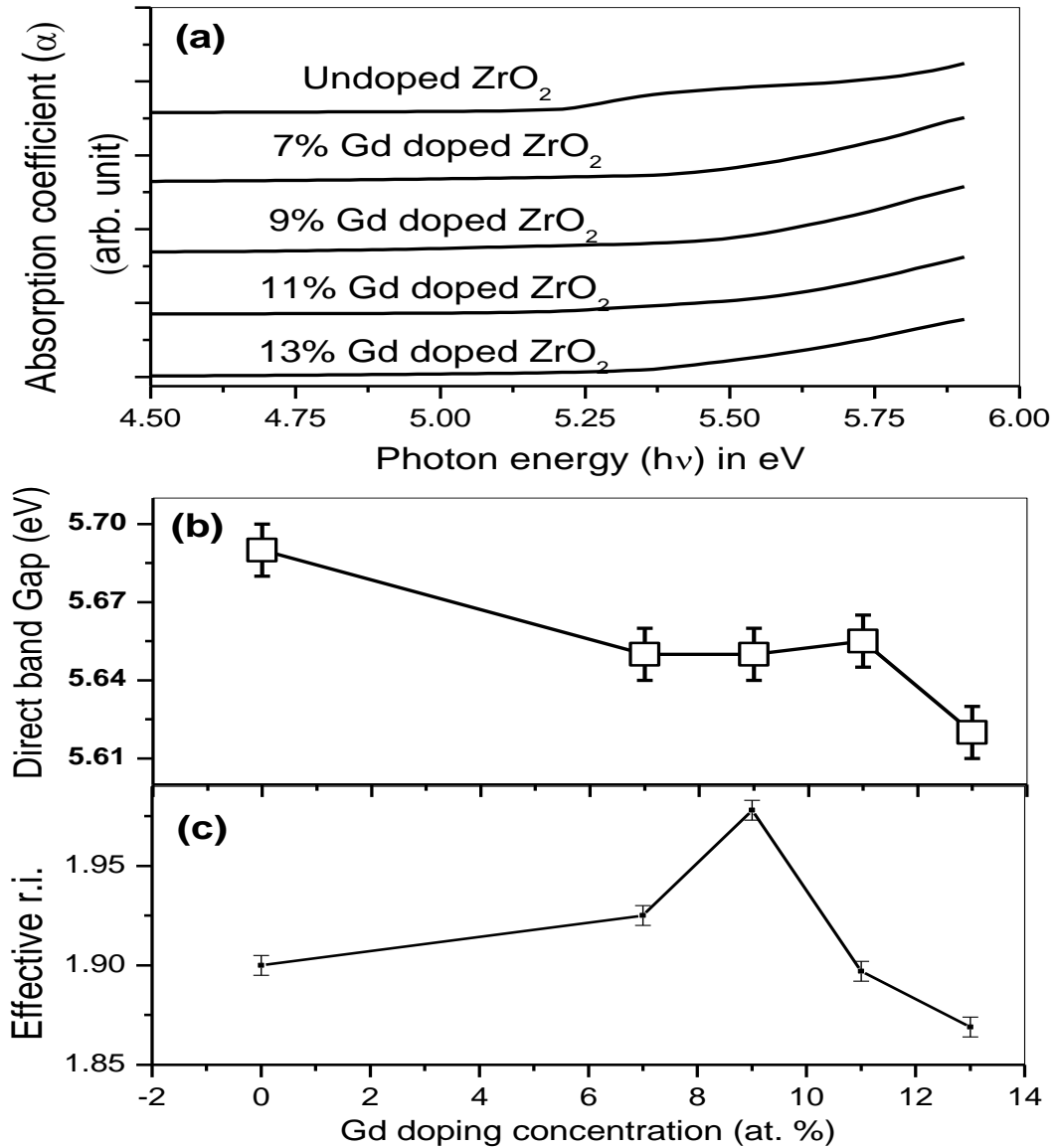


Fig. 7.3: (a) Absorption coefficient (α) versus energy ($h\nu$) plots in optical region obtained from transmission measurement for all the samples. (b) Variation of direct band gap calculated from absorption spectra as a function of Gd doping concentration. (c) Variation of effective refractive index of all the samples at 550 nm obtained from transmittance measurement.

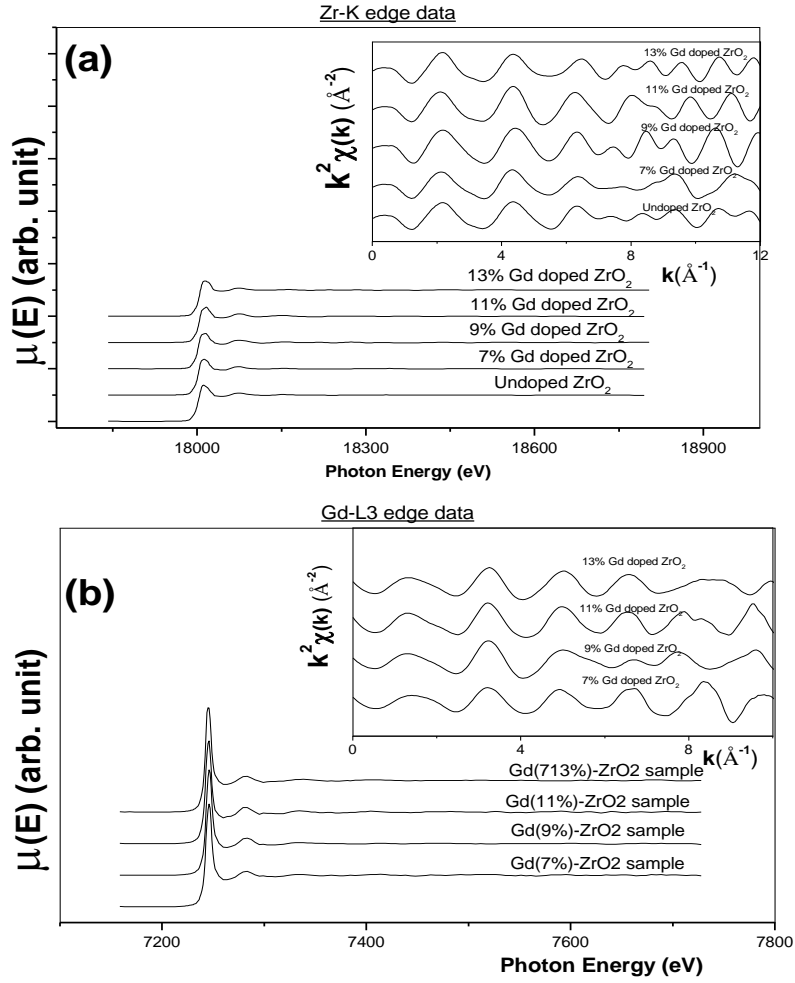


Fig. 7.4: (a) Absorption coefficient ($\mu(E)$) versus incident X-ray energy (E) of undoped as well as Gd doped ZrO_2 thin films measured at Zr K-edge. Inset: $k^2\chi(k)$ vs. k plots of the samples.
 (b) Absorption coefficient ($\mu(E)$) versus incident X-ray energy (E) of all Gd doped ZrO_2 thin films measured at Gd L_3 -edge. Inset: $k^2\chi(k)$ vs. k plots of the samples.

7.5 Extended X-ray Absorption Fine Structure measurements:

As has been mentioned earlier, the samples have also been characterized by EXAFS measurements to investigate the local structure surrounding Zr and Gd sites. Figs. 7.4(a) and (b) show the experimental EXAFS spectra (μ vs. E) of the doped and undoped ZrO_2 films

measured at Zr K-edge and Gd L₃-edges respectively. $k^2 \chi(k)$ vs. k plots for the undoped and doped ZrO₂ thin films derived from the Zr K edge and Gd L₃ edge data have been shown in the inset of Figs. 7.4 (a) and 7.4(b) respectively.

7.5.1 Zr K-edge data:

$\chi(R)$ versus R plots for the samples as derived above from the experimentally derived (μ vs. E) plots of Zr K-edge following the formalism described above have been fitted with the theoretically simulated spectra. Since, from the GIXRD measurements, pure ZrO₂ film has been found to be monoclinic while Gd doped thin film samples are found to be cubic, experimental $\chi(R)$ versus R plots have been fitted with both monoclinic and cubic structures for all the samples. The parameters of crystal structure for monoclinic and cubic ZrO₂ have been taken from literature values [202-203]. Fig. 7.5(a) shows the experimental $\chi(R)$ versus R plots along with the best fit theoretical spectra generated assuming monoclinic crystal structure. As indicated by various other workers also for the doped ZrO₂ systems [28-29, 201], the first two peaks of $\chi(R)$ versus R plots (phase uncorrected) in the range 1-2 Å have been attributed to Zr-O bonds while the more distant peaks ~3Å are attributed to the Zr-Zr bonds. Table-7.1 displays the scattering paths used for fitting assuming monoclinic crystal structure. As can be seen from the above table, monoclinic ZrO₂ has 7 oxygen atoms at slightly different distances in the immediate neighbourhood of Zr site, which have been approximated as a single oxygen shell with degeneracy of 7. Similarly, three Zr shells in the next nearest sites having total degeneracy of 5, have been approximated as a single Zr shell having degeneracy of 5.

Table-7.1: Scattering paths used for fitting Zr K-edge data with Monoclinic Phase of ZrO₂.			
	Degeneracy	R _{eff}	Amp
Path-1 (Zr-O2)	1	1.745	100
Path-2 (Zr-O2)	1	1.860	85.65
Path-3 (Zr-O1)	1	2.049	67.39
Path-4 (Zr-O1)	1	2.087	64.32
Path-5 (Zr-O1)	1	2.164	58.69
Path-6 (Zr-O2)	1	2.918	26.40
Path-7 (Zr-O2)	1	2.961	25.33
Path-11 (Zr-Zr1)	1	3.350	26.01
Path-13 (Zr-Zr1)	2	3.451	48.11
Path-15 (Zr-Zr1)	2	3.476	47.20

Table-7.2: Scattering paths used for fitting Zr K-edge data with cubic phase of ZrO₂.			
	Degeneracy	R _{eff}	Amp
Path-1 (Zr-O)	8	2.202	100
Path-3 (Zr-Zr)	12	3.596	54.77
Path-6 (Zr-O)	24	4.217	44.37

Fig. 7.5(b) shows the experimental $\chi(R)$ versus R plots along with the best fit theoretical spectra generated assuming cubic crystal structure. It should be noted here that as obtained by Cole et al.. [29], the FT-EXAFS spectra of cubic ZrO₂ is characterised by only one peak for oxygen shell in the range of 1-2.5 Å while in case of tetragonal ZrO₂, as mentioned by Li and Chen [201], this peak is split into two which is a characteristic of the tetragonal structure. In the case of the bulk ZrO₂ samples prepared by co-precipitation method reported earlier [198-199]; it had been observed that the first Zr-O peak in the FT-EXAFS spectra is split into two peaks indicating tetragonal structure of ZrO₂.

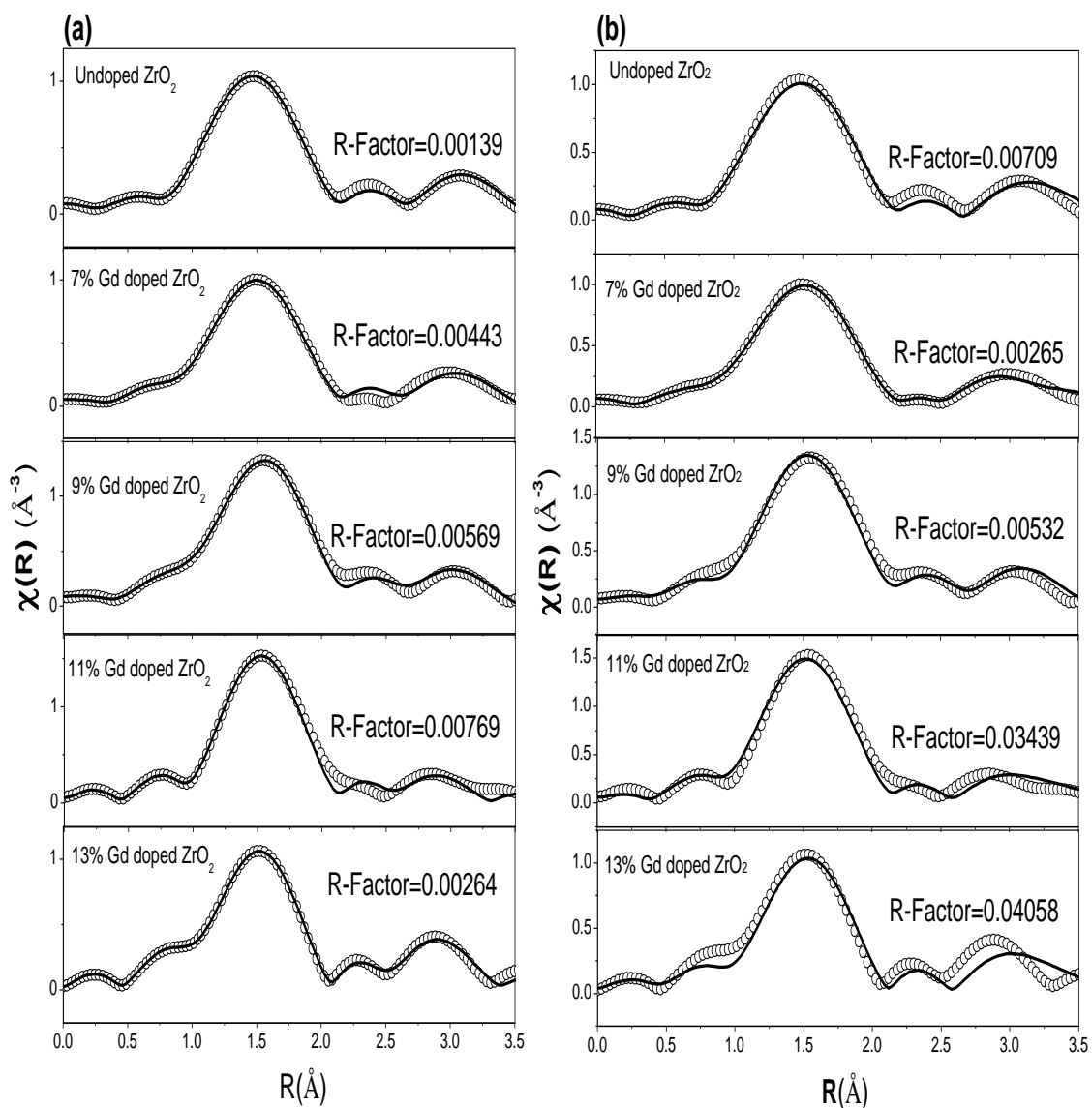


Fig. 7.5: (a) Experimental $\chi(R)$ versus R plots along with best fit theoretical plots of undoped as well as Gd doped ZrO_2 samples measured at Zr K-edge assuming Monoclinic Phase of ZrO_2 .

o-o-o-o: Experimental Data; -----: Theoretical fit.

(b) Experimental $\chi(R)$ versus R plots along with best fit theoretical plots of undoped as well as Gd doped ZrO_2 samples measured at Zr K-edge assuming Cubic Phase of ZrO_2 .

o-o-o-o: Experimental Data; -----: Theoretical fit

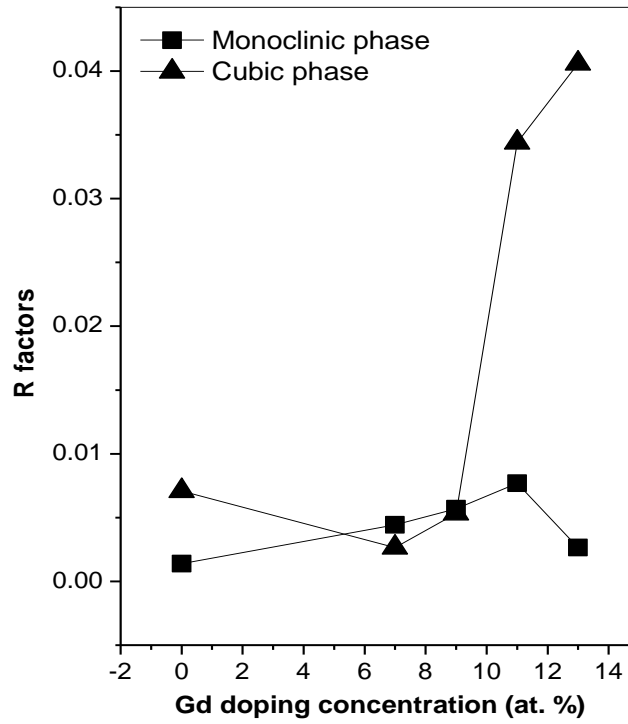


Fig. 7.6: Variation of R_{factor} in case of fitting of Zr K-edge data assuming Monoclinic and Cubic phase of ZrO_2 as a function of Gd doping concentration.

Detail structural characterisation of cubic ZrO_2 [204] reveals that oxygen atoms are displaced from their ideal positions by up to 0.05 nm along the 100 or 111 axes, and the structure corresponds to the P43m space group of tetragonal structure instead of the Fm3m space group which is a characteristic of the cubic fluorite structure. However, for the present set of Gd doped ZrO_2 thin film samples it has been observed that the first Zr-O peak does not get split into two confirming cubic structure of the samples. As for the cubic phase model, the first peak in the Zr K-edge FT-EXAFS spectrum has been fitted with a single oxygen shell with degeneracy of 8 and the second peak has been fitted with one Zr shell having degeneracy of 12 and another oxygen shell having degeneracy of 24 as shown in Table 7.2.

The values of R_{factor} obtained for both the cases i.e., fitting with monoclinic and cubic structure have been compared in Fig. 7.6 for all the films. It can be seen from Fig. 7.6 that

R_{factor} values for the undoped ZrO_2 film is lower in case of fitting with monoclinic structure than while fitting with cubic crystal structure which is as expected. It has also been seen that for films with Gd doping up to a concentration of 9%, fitting with cubic crystal phase yields lower R_{factor} value than fitting with monoclinic phase. However, in case of ZrO_2 thin films prepared with Gd doping concentration higher than 9%, the R_{factor} value increases significantly manifesting poor quality fitting with cubic structure, compared to that with monoclinic structure. This proves the fact that for higher Gd doping concentration the films no longer retain cubic structure.

It should be noted here that there is a discrepancy observed in the results obtained from EXAFS and GIXRD measurements. Though GIXRD measurements, discussed earlier, show that all the doped ZrO_2 thin films have cubic structure; EXAFS results conclude that samples with more than 9% Gd doping are having monoclinic structure. However, as has been observed by other workers also [145, 205] it should be noted that for thin film and nanocrystalline systems with large amount of disorders, where single-phase domains are not sufficiently large, X-ray diffraction, which acts on the principle of long range order, might not give the correct phase information and for such systems, EXAFS which basically probes the local order and does not depend on the long range order can yield better result so far microscopic behaviour of the samples is concerned. We have also observed that for pulse DC magnetron sputter deposited TiO_2 films, as described in Chapter-4, the anatase to rutile phase ratio obtained from GIXRD data shows a monotonic variation with increase in oxygen partial pressure and thus fails to explain the actual non-linear nature of variation of the macroscopic properties like refractive index of the films, while phase fraction obtained from EXAFS measurements could correctly explain the behaviour. There are also many reports [206-208]

where presence of small secondary phases in nanocrystalline and thin film systems have been detected by EXAFS while they remain undetected in XRD measurements.

Fig. 7.7 shows the variation of the total co-ordination numbers (N_{Total}) and the average Debye-Waller factor (σ_{Avg}^2) obtained for the nearest neighbour oxygen shell as a function of Gd doping concentration, where the values for 0%, 11% and 13% Gd doped samples have been taken from best fit results of monoclinic structure while the corresponding values for 7% and 9% Gd doped samples have been taken from the best fit result of the cubic structure. It can be seen from Fig. 7.7 that oxygen coordination in doped samples is significantly less

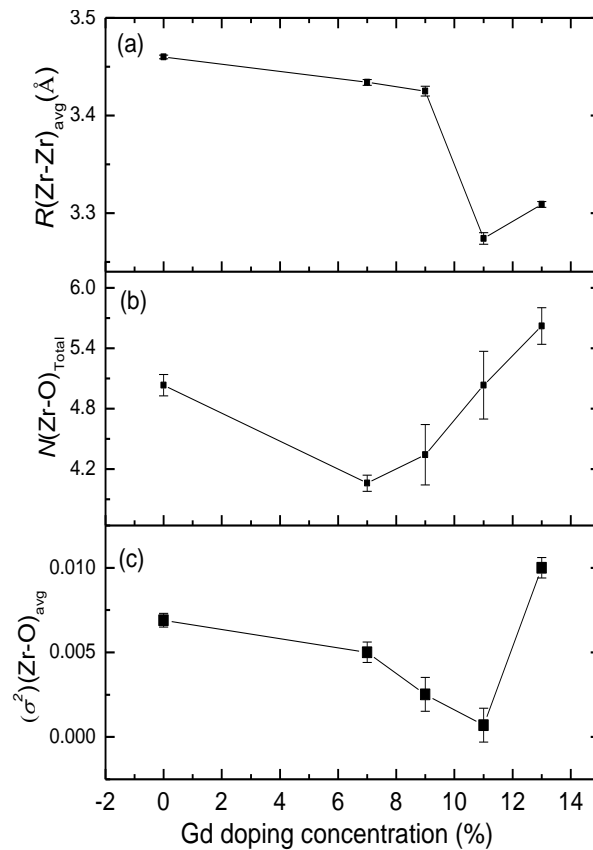


Fig. 7.7:(a) Variation of average Zr-Zr distance as a function of Gd doping concentration(b) Variation of total oxygen co-ordination number around core Zr sites as a function of Gd doping concentration.(c) Variation of average Debye Waller factors of Zr-O bonds as a function of Gd doping concentration.

compared to the undoped sample manifesting the presence of oxygen vacancies near the Zr sites for samples up to Gd doping of 9%, above which oxygen coordination increases significantly. Debye-Waller factor also increases considerably above 11% Gd doping concentration showing poor quality of the samples. Thus it has been observed that Gd doping up to 9-11% is suitable for replacing Zr in ZrO₂ matrix and for creation of oxygen vacancies, beyond which Gd gets precipitated and does not go to the lattice. This conclusion agrees with our findings on ZrO bulk samples prepared by co-precipitation method [198-199] and this is further established by Gd L₃-edge measurement of the present samples as described below. It should be mentioned here that there is no significant variation in the average Zr-O distance due to Gd doping over the whole range of doping concentration (not shown here).

7.5.2 Gd L₃-edge data:

Based on the results obtained above for the Zr K-edge EXAFS data, the FT-EXAFS data measured at Gd L₃-edge of 7-13% Gd doped ZrO₂ samples have been analyzed using two theoretical models (i) cubic ZrO₂ phase where core Zr atom has been replaced by Gd atom and (ii) cubic Gd₂O₃ structure surrounding the Gd environment. Such an approach to modelling has been reported by other authors as well [201]. For the latter model we have used the crystal structure parameters of cubic Gd₂O₃ having space group of *ia*-3 [186]. For both the models, the scattering paths used for fitting are shown in Table-7.3 and Table-7.4 respectively. Figs. 7.8(a) & (b) show the experimental $\chi(R)$ versus R plots along with the

Table-7.3: Scattering paths used for fitting Gd L₃-edge data with Cubic Phase of ZrO₂, core Zr being replaced by Gd.			
	Degeneracy	R _{eff}	Amp
Path-1 (Gd1-O1)	8	2.202	100
Path-3 (Gd1-Zr1)	12	3.596	54.41
Path-6 (Gd1-O1)	24	4.217	51.61

Table-7.4: Scattering paths used for fitting Gd L₃-edge data with cubic Gd₂O₃ structure.			
	Degeneracy	R _{eff}	Amp
Path-1 (Gd1-O1)	6	2.281	100
Path-2 (Gd1-Gd2)	6	3.553	41.93

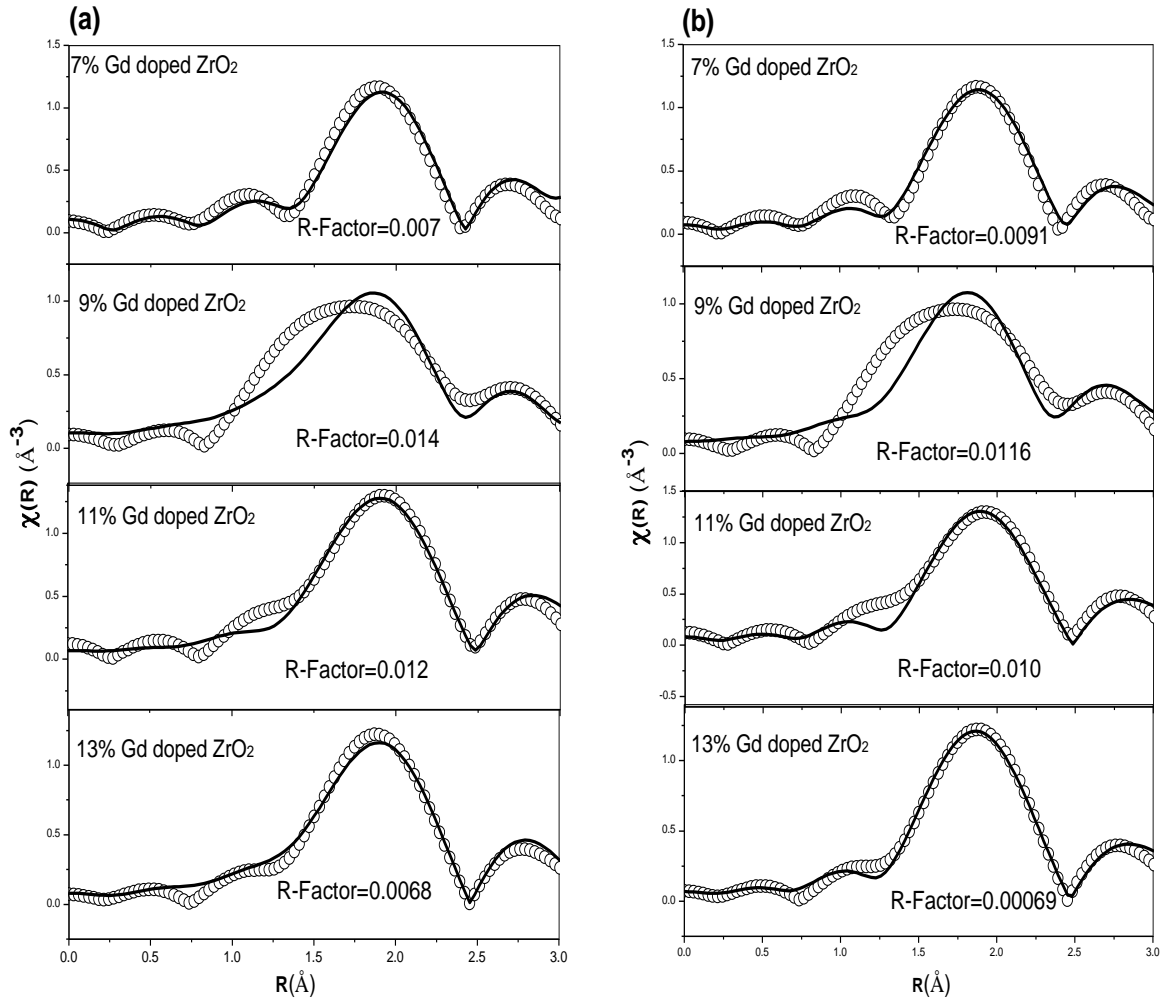


Fig.7.8(a):Experimental versus plots along with best fit theoretical plots of Gd doped ZrO₂ samples measured at Gd L₃-edge assuming Cubic Phase of ZrO₂, core Zr site being replaced by Gd. o-o-o-o: Experimental Data; -----: Theoretical fit.

(b): Experimental versus plots along with best fit theoretical plots of Gd doped ZrO₂ samples measured at Gd L₃-edge assuming Cubic Phase of Gd₂O₃. o-o-o-o: Experimental Data; -----: Theoretical fit.

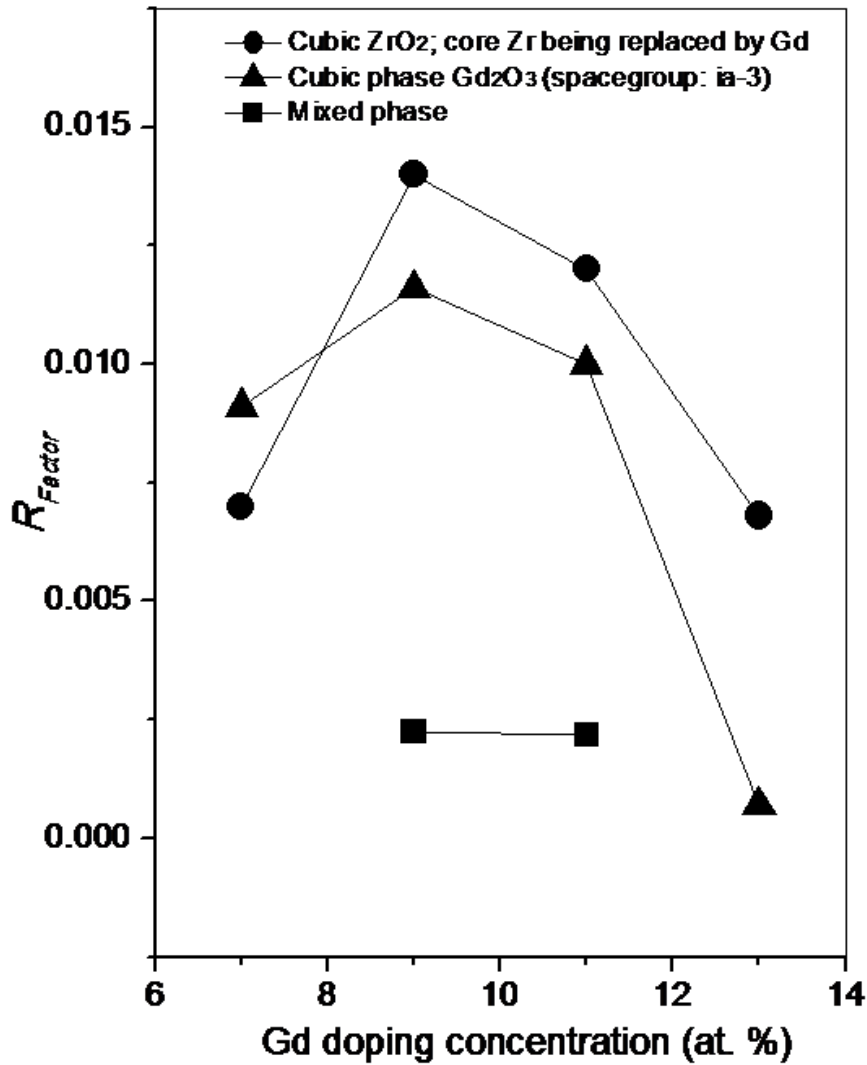


Fig. 7.9: Variation of R_{factor} in case of fitting of Gd L_3 -edge data as a function of Gd doping concentration assuming (i) Cubic Phase of ZrO_2 , core Zr site being replaced by Gd, (ii) Cubic Phase of Gd_2O_3 , and (iii) mixed phase for the 9% and 11% Gd doped samples

best fit theoretical plots assuming the above two models respectively, while the R_{factor} values obtained in the two cases have been compared in Fig. 7.9. It has been observed that the R_{factor} value is lower for the former model in case of the ZrO_2 sample with 7% Gd doping concentration, while it is significantly less for the latter model in case of the sample with 13% Gd doping concentration. This confirms the above conclusion that with doping concentration higher than 11%, Gd atoms do not go in the ZrO_2 lattice; rather they get precipitated out as a

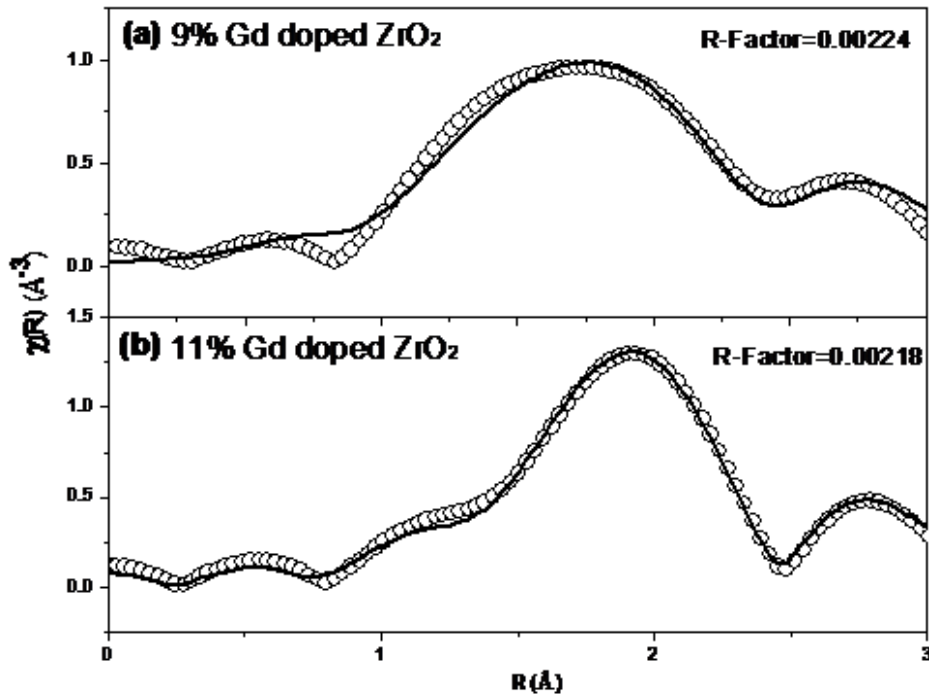


Fig.7.10: Experimental $\chi(R)$ versus R plots along with best fit theoretical plots of (a) 9% Gd doped ZrO_2 sample and (b) 11% Gd doped ZrO_2 sample measured at Gd L_3 -edge assuming mixed phase model.
o-o-o-o: Experimental Data; -----: Theoretical fit.

separate cubic Gd_2O_3 phase. However, as can be observed from Fig.7.9, the FT-EXAFS data for the 9% or 11% Gd doped samples cannot be fitted reasonably well with either of the above two models and it has been observed that the fitting quality for these two samples improves significantly if these data are fitted with a mixed phase structure considering the scattering paths from both the models. Fig.7.10(a) and (b) show the experimental $\chi(R)$ versus R plots of the above two samples along with the best fit theoretical plots obtained using the mixed phase model while the respective R_{factor} values have been shown in Fig. 7.9. The relative contributions of the two structures in the 1st peak of the FT-EXAFS spectra of the samples have been considered to be their relative concentrations in the respective samples. It has been observed that the contribution of the Gd_2O_3 cubic phase is 31% for the

9% Gd doped sample and for the 11% Gd doped sample it is 54%. This is consistent with the fact that at still higher concentration of Gd, the Gd environment in the samples becomes completely Gd_2O_3 -like. It should be mentioned here that the fitting quality of the 7% and 13% Gd doped samples, however do not improve with a mixed phase model structure.

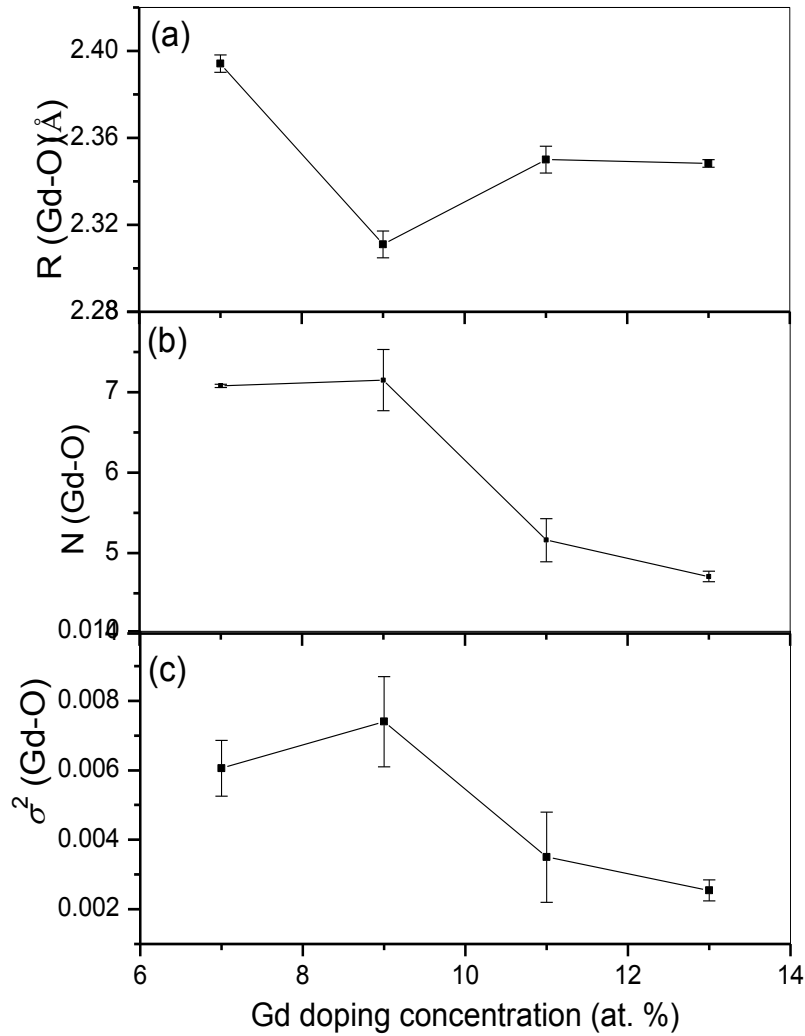


Fig.7.11: (a) Variation of Gd-O bond length as a function of Gd doping concentration.
(b) Variation of oxygen co-ordination around Gd site as a function of Gd doping concentration.
(c) Variation of Debye Waller factors of Gd-O bonds as a function of Gd doping concentration

The average bond length (R_{Avg}), total co-ordination numbers (N_{Total}) and the average Debye-Waller factor (σ_{Avg}^2) obtained for the nearest neighbour oxygen shell has been shown

in Fig. 7.11 as a function of Gd doping concentration. Here for the 7% Gd doped sample, the values have been taken from the fitting result of the first model, that for the 13% Gd doped sample, have been taken from the fitting result of the second model, while for the 9% and 11% Gd doped samples the values have been taken from the fitting result of the mixed phase model. It shows that for the samples with 7% and 9% Gd doping concentration, oxygen coordination is close to their bulk value of 8 showing that oxygen vacancies are created near Zr sites rather than near Gd site.

The EXAFS results also corroborate with the results of optical measurements on the samples described above, which shows that beyond 11% doping concentration, Gd doping yields samples with higher void fraction, lower band gap and lower effective refractive index. It should also be noted that the intrinsic r.i. as obtained from spectroscopic ellipsometry measurements and displayed in fig. 7.2(b) is significantly high for samples with Gd doping concentration higher than 11%, since Zr-Zr bond length reduces considerably at this doping concentration as can be found from Fig.7.7 (a). Similar increase in intrinsic refractive index due to a decrease in bond length has also been observed earlier by us in several other oxide systems also [15, 109, and 187].

7.6 Conclusion:

ZrO₂ thin films with 0, 7, 9, 11 and 13% of Gd doping were prepared by RF magnetron sputtering technique by sputtering pure/doped ZrO₂ targets under mixed ambient of Ar and O₂. It has been observed from spectroscopic ellipsometry and optical transmission measurements that the void fraction present in the films increases significantly beyond Gd doping concentration of 11% causing a decrease in the effective refractive index of the films. It has also been observed from GIXRD measurements that though the undoped ZrO₂ film is

having monoclinic structure, Gd doping stabilises the films in cubic structure, which is different from the results obtained earlier by us on bulk ZrO_2 samples prepared by co-precipitation route. This is further confirmed by EXAFS measurements on the samples at Zr K edge which shows that better fitting of the FT-EXAFS data could be obtained with cubic structure up to a Gd doping concentration of 9%, beyond which, however, better fitting of the data are obtained with monoclinic structure. EXAFS measurements at Zr K edge and Gd L_3 edges further confirm that Gd dopants replace Zr atoms in ZrO_2 matrix up to 9-11% doping concentration with creation of oxygen vacancies near Zr sites, however above 11% Gd doping, Gd precipitates out as a separate Gd_2O_3 phase. This corroborates with our earlier results on bulk ZrO_2 samples and also explains the observed optical properties of the thin films that Gd doping beyond 11% yields samples with higher void fraction, lower band gap and lower effective refractive index.

CHAPTER-8

Local structural investigation of refractory oxide thin films near to laser damage threshold

8.1 Introduction:

The study of laser induced damage mechanism and effort to increase the damage threshold is a continuing challenge because as improved laser-damage-resistant optical materials and better fabrication technologies are developed, laser designers increase the system operating energies and powers to the limits of these new materials. The motivation behind this is simply economics; the higher the damage resistance of the optics, the greater the laser output energy that can be achieved for a given investment [209].

Generally, for laser damage experiment, pulsed laser with pulse width ranging from femtosecond to nanosecond lasers are employed in order to deposit maximum laser energy on the sample in a span of very short time interval to effectively increase the laser power. Numerous studies have been made to understand the damage mechanism in different regime of pulse width [210]. Three prime mechanisms [211] that drive laser induced damage process are (i) thermal process resulting from absorption of the laser energy in the material, (ii) dielectric process occurring when the electric field density is high enough to strip electrons from lattice, (iii) multiphoton ionization, which is a special case of the second mechanism and occurs when the energy is high enough such that the stripped electrons are raised to

higher energy levels instantaneously [212]. Usually for long pulse duration the thermal process generally describes the damage phenomena, but in the short pulse regime the damage process can be expressed according to the other two mechanisms [212]. In the long pulse regime, where the thermal process is dominant, laser induced damage is a combination of three processes, the absorption of the radiation [213], transport of the absorbed energy away from the absorption site i.e. thermal conductivity [211], and the thermo-mechanical response like dissipation of pressure buildup resulting from absorption at the defect sites [214]. Interestingly, Dawei Zhang et al. [215] demonstrated that the absorption measured by CW: YAG laser may always not represent the absorption in actual laser damage experiment by Nd: YAG laser since nodular defects in dielectric thin films which are insensitive to CW: YAG laser can play major role when being subjected to Nd: YAG laser.

On the other hand, tailoring of material properties by purposeful laser irradiation [216] is another attractive area of research in the same domain. Miru Noh et al. [217] obtained improvement in crystallinity of indium tin oxide films with the increase in laser power while annealing with excimer laser. Effect of combination of post deposition annealing and laser conditioning on evolution of Laser Induced Damage Threshold (LIDT) for Ta₂O₅ samples has been studied by Cheng Xu et al. [218]. Jianke Yao et al. [219] investigated the reason behind improvement of LIDT by thermal annealing of TiO₂/SiO₂ multilayer reflector and found that improved stoichiometry is the main reason of absorption reducing and LIDT rising after annealing. The improvement of LIDT due to annealing for both Ta₂O₅ and Ta₂O₅/SiO₂ films is mainly attributed to the improvement in stoichiometry and reduction in structural defects [220-221].

Although, many efforts have been made to investigate how stoichiometry [219] or long ranged order structure [214] plays role in describing laser damage process, to the best of

our knowledge effort to understand laser damage mechanism from local structural point of view has not been made so far. The study aims at understanding laser induced damage mechanism of refractory oxide samples visualizing TiO_2 , Ta_2O_5 , HfO_2 and Gd_2O_3 samples by local structural investigation employing EXAFS technique.

8.2 Preparation of samples:

Dielectric refractory oxide thin films samples of TiO_2 , Ta_2O_5 , HfO_2 and Gd_2O_3 have been deposited on 2 inch diameter BK-7 substrate in the homemade RF magnetron sputtering system described in Chapter-2. All the samples were deposited with approximately 200 nm thicknesses with prior calibration of quartz crystal monitor. All the depositions were carried out by directly sputtering oxide targets with magnetron energizing power of 100 W in non-reactive environment. Prior to actual deposition, the targets were pre-sputtered for 30 minutes in order to remove surface contamination, if any, present on top of the sputtering targets. The duration of deposition was 42 minutes for HfO_2 , 60 minutes for Ta_2O_5 , 100 minutes for TiO_2 and 80 minutes for Gd_2O_3 samples to have similar thickness.

8.3 Laser irradiation of samples:

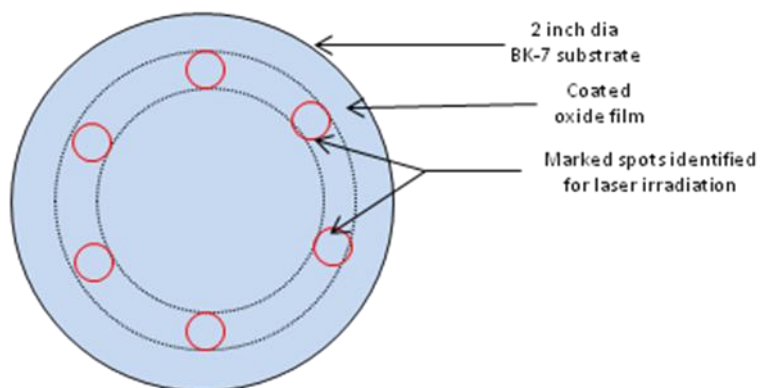


Fig. 8.1: Schematic of marked zones on sample surface. to carry out laser damage experiment

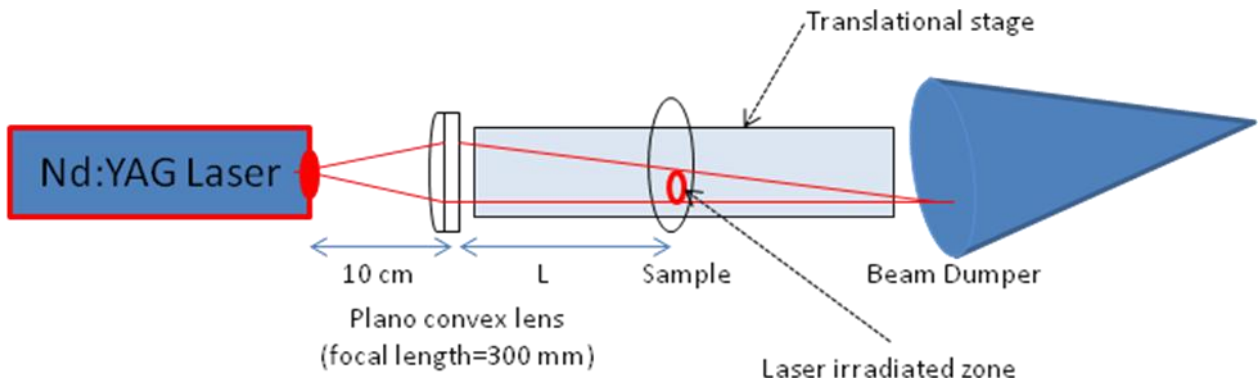
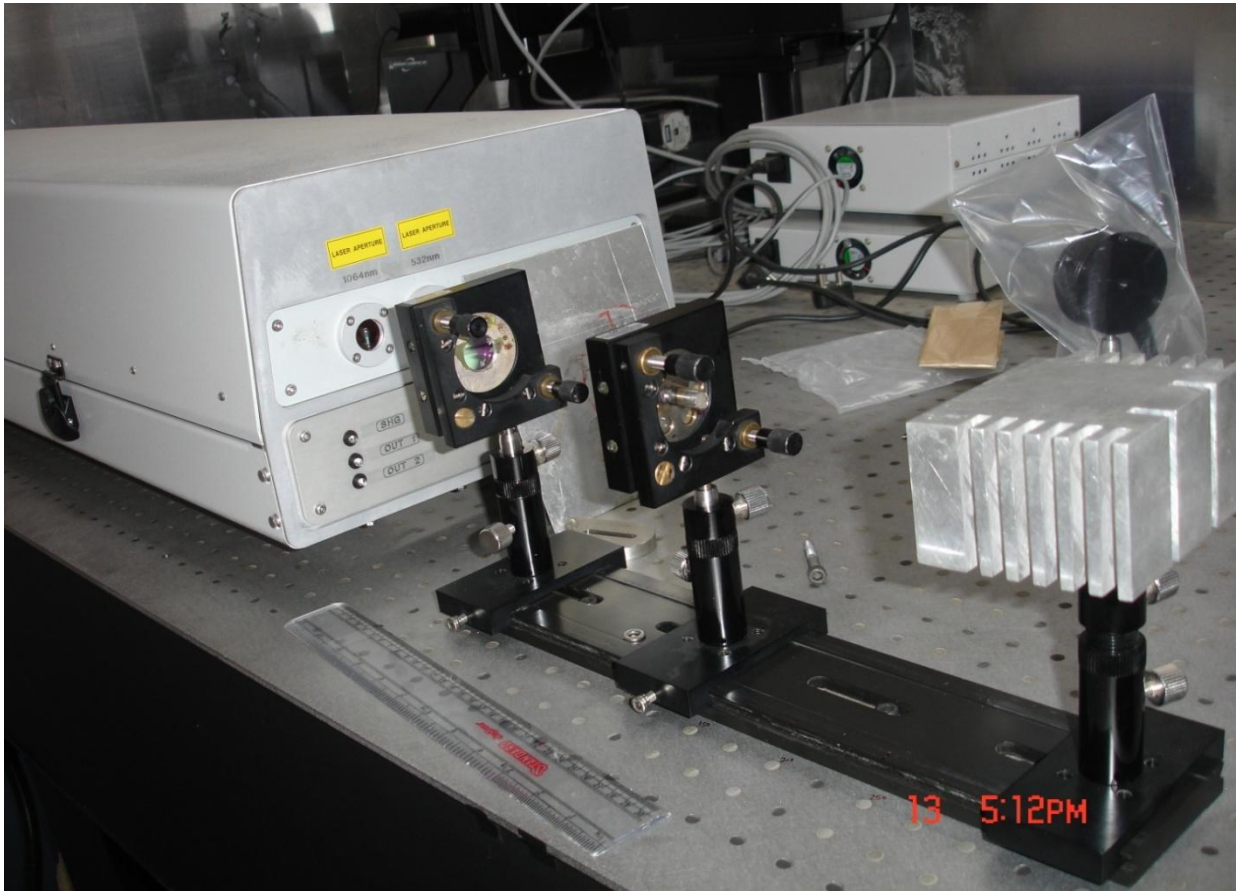


Fig.8.2: (a) Photograph and (b) schematic of Laser irradiation experimental set-up.

Each sample was deposited on 2 inch diameter glass substrate. At fixed radius (~17 mm) of the circular sample, several spots of 5 mm diameters have been marked on opposite

Table-8.1: Experimental condition (Pulse repetition rate was 1 Hz for all the experiments) Diameter of laser illumination zone, D; Laser peak energy E_p						
Material	Fixed Parameters	Varied parameters				Starting point of damage as visually observed on trial sample
TiO₂	L=15 cm, $E_p=0.19$ J D=5 mm, Fluence= 0.95 J/cm ² .	10 shots	15 shots	23 shots	30 shots	Damage started at around 20 shots.
Ta₂O₅	L=15 cm, $E_p=0.41$ J D=5 mm, Fluence= 2.06 J/cm ²	10 shots	20 shots	30 shots	40 shots	Damage started at around 16 shots.
HfO₂	L=17.5 cm, $E_p=0.76$ J D=4.2 mm, Fluence= 5.58 J/cm ²	05 shots	10 shots	20 shots	30 shots	Damage started at around 12 shots.
Gd₂O₃	L=25 cm, No. of shots=5, D=1.7 mm	$E_p = 0.29$ J Fluence= 13.2 J/cm ²	$E_p = 0.41$ J Fluence= 18.6 J/cm ²	$E_p = 0.53$ J Fluence= 24.4 J/cm ²	$E_p = 0.76$ J Fluence= 34.9 J/cm ²	Damage started at laser power level > 150 W i.e. at > 13.2 J/cm ² .

to the coated surface, for laser irradiation at varying conditions. A schematic of marked zones on the sample surface is shown in Fig. 8.1 where laser irradiation experiment was carried out. The arrangement of laser damage experiment is shown in Fig. 8.2. The laser source (Make: Quanta System Laser) used for the experiment was an Nd:YAG pulsed laser having pulse width of ~10 ns and fundamental wavelength of 1064 nm and source beam diameter of 1 cm. As shown in fig. 8.2, the laser falls on the sample through a plano-convex lens. Both the lens

and the sample holders are mounted on a translational stage in order to adjust the distance (L) between plano-convex lens and the sample to vary the laser spot size as well as laser fluence on the sample surface for a given laser power. The distance 'L' has been optimized and kept fixed during laser irradiation of one set of samples, thereby fixing the area of laser irradiated zone. The actual laser fluence during the experiment depends on the distance 'L' as well as on the set laser peak energy. Prior to each experiment, the laser peak energy has been measured using power meter at different set power levels of laser source and calibrated. The detailed experimental conditions along with the laser peak energy and fluence for each set of samples have been tabulated in Table-8.1. For TiO_2 , Ta_2O_5 and HfO_2 samples, the laser fluence was optimized to 0.95 J/cm^2 , 2.06 J/cm^2 and 5.58 J/cm^2 respectively and different locations on the sample were irradiated with varying number of pulse shots. On the other hand, for Gd_2O_3 samples it was observed that laser damage does not occur up to 13 J/cm^2 even with very large number of pulse shots and at fluence $>13 \text{ J/cm}^2$ damage starts just on exposure of 2-3 shots. Hence for Gd_2O_3 set of samples, the number of shots was kept constant at 5 and the fluence was varied from ~ 13 - 35 J/cm^2 in order to study the damage mechanism around the damage threshold.

8.4 Characterization of laser irradiated samples:

The optical microscope imaging was carried out on irradiated samples by optical microscope (Make: Dino-Lite Digital Microscope, Model: AM7013) for imaging the damage morphology. The images of irradiated zones were recorded at magnification of 1 and 2.5 of the objective lens which yields the morphology of (1.7 mm X 2.3 mm) and (0.8 mm X 1.1 mm) size on the sample surface. Post laser irradiation experiment, grazing incidence X-ray diffraction (GIXRD) measurements were performed in a laboratory X-ray diffractometer,

equipped with a sealed tube X-ray (Cu $K\alpha$ of 1.54Å wavelength) generator operating at 3 kW output power. The same diffractometer was also used for grazing incidence X-ray reflectivity (GIXR) measurements which were carried out on all the samples in 2θ range of 0-4° with step size of 0.01°. Rocking curve measurements have been done prior to each measurement for aligning the sample. During the above measurements, slit width of the diffractometer was adjusted to cover only the laser irradiated region of the sample.

All the irradiated samples have also been characterized by X-ray Absorption Spectroscopy (XAS) measurements with synchrotron radiation which comprises of both X-ray Near Edge Structure (XANES) and Extended X-ray Absorption Fine Structure (EXAFS) techniques [45] at Energy Scanning EXAFS beam line (BL-9) of INDUS-2 SRS as described in Chapter-2. The incident X-ray beam spot size was reduced to 2 mm (horizontal) x 1 mm (vertical) by increasing radius of curvature of second crystal of DCM to make it incident on the damaged spot. The X-ray energy range scanned for Ta₂O₅ samples was in the range of 9820 eV to 10590 eV around Ta L3-edge (9881 eV), for HfO₂ was in the range of 9480 eV to 10230 eV around Hf L3-edge (9561 eV) and for Gd₂O₃ samples was in the range of 7175 eV to 7935 eV around Gd L3-edge (7243 eV). However, the TiO₂ samples could not be characterized by EXAFS since the absorption edge of Ti K-edge (4966 eV) is very near to the energy edge of various impurity elements present in the BK-7 substrate on which the samples were deposited. Thus for the TiO₂ samples measurements have been carried out only in the XANES region of 4890 to 5125 eV.

8.5 Results and discussions:

8.5.1 Titanium di-oxide samples:

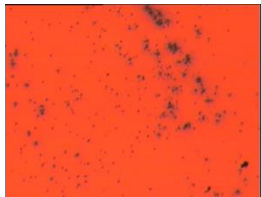
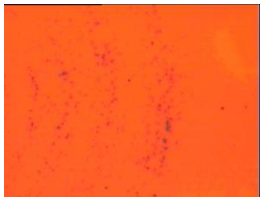
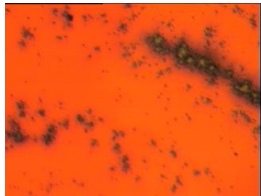
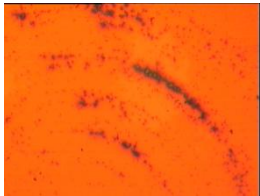
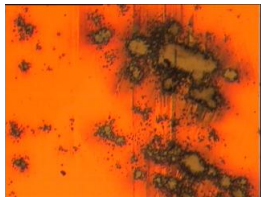
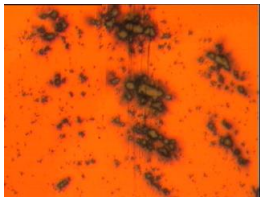
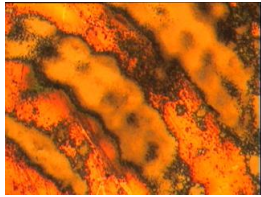
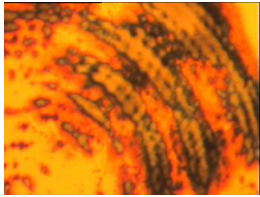
No. of pulse shots	Magnification 2.5 (0.8 mm X 1.1 mm)	Magnification 1 (1.7 mm X 2.3 mm)
10 shots		
15 shots		
23 shots		
30 shots		

Fig.8.3: Optical microscopic images of laser irradiated TiO₂ sample spots after undergoing laser irradiation of 0.95 J/cm²

The optical microscopic images of laser irradiated zones of TiO₂ samples are displayed in Fig.8.3 which shows the evolution of morphology with the increase in number of shots. The change begins with the formation of small holes after 10 shots and then increased numbers of holes along the circular line creates arc of damaged holes. Beyond 23 shots the

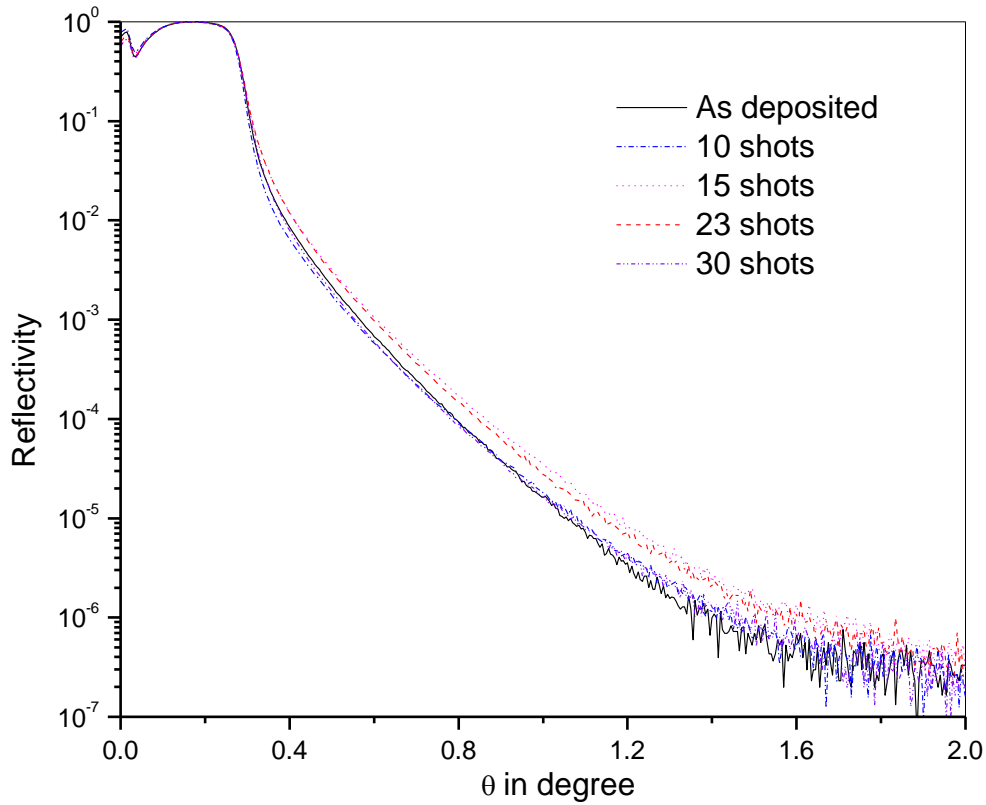


Fig. 8.4: GIXR spectra of as-deposited and all laser irradiated TiO₂ sample spots.

arcs of holes have got merged with one another and have got diffused due to melting. Recrystallization beyond 23 shots as evident from GIXRD pattern, discussed later, might be the reason of very high absorption due to increase in optical path length [213] in the interfaces of grains which ultimately results in increase in higher local heating and rapid damage of the sample.

GIXR spectra of all the irradiated TiO₂ samples along with the as-deposited sample have been depicted in fig. 8.4. As can be seen from fig. 8.4, there is no significant difference in density among the TiO₂ samples irradiated by variable number of shots. Only there is a slight change in slope of reflectivity curve which signifies minor change in surface morphology. Fig. 8.5 shows the recorded GIXRD pattern of all the laser irradiated TiO₂ sample spots along with that of the as-deposited sample. The comparison of measured GIXRD pattern with the standard PCPDF file (PCPDF file No: 860147) suggests that the as-

deposited as well as laser irradiated samples exhibit rutile phase of TiO_2 . This is contrary to our earlier published report [105], presented in Chapter-4, in which amorphous nature of magnetron sputtered TiO_2 thin films were observed when grown without flow of oxygen. This could have happened due to higher deposition rate (3.7 \AA sec^{-1}) at 230W magnetron power used earlier as compared to the present deposition rate of $\sim 0.3 \text{ \AA sec}^{-1}$ at magnetron power of 100 W. As can be further observed from fig. 8.5, the peak height of the rutile crystallographic plane (110) detected for the samples decreases with initial increase of number of laser pulse shots. However beyond 23 shots, the crystallinity has started improving.

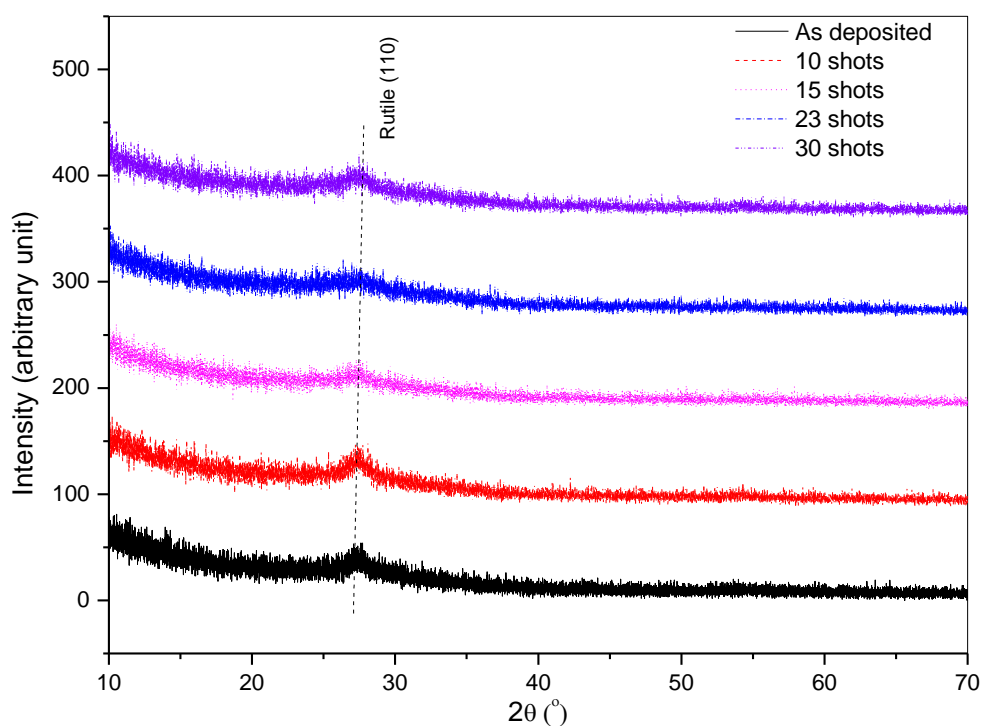


Fig. 8.5: GIXRD spectra of all the laser irradiated TiO_2 sample spots along with that of the as deposited sample spot.

XANES spectra of as-deposited and laser irradiated TiO_2 samples are shown in Fig. 8.6(a). Pre-edges as observed in the XANES spectra have also been marked in the same figure. As has been explained by Farges et al.. [141] the pre-edges in six-coordinated TiO_2

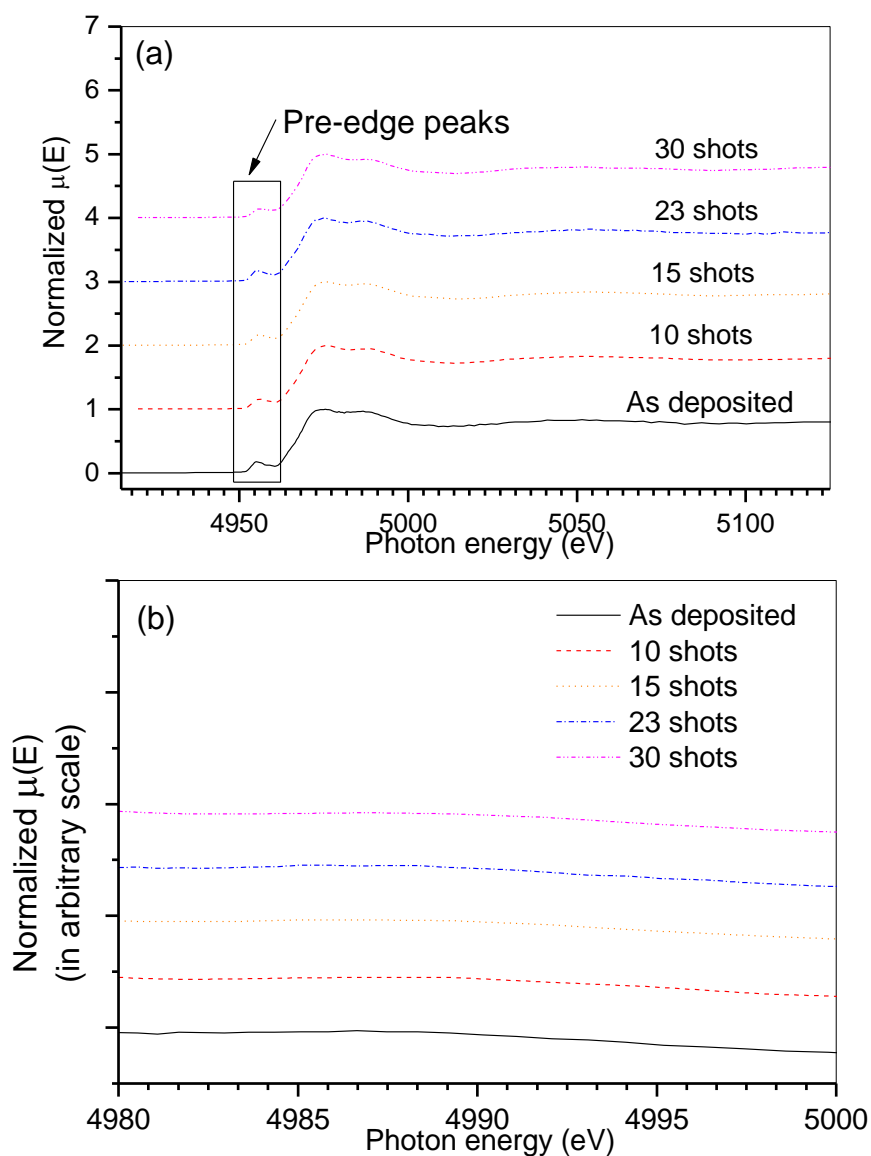


Fig. 8.6: (a) XANES spectra of as deposited and laser irradiated TiO₂ sample spots. (b) Expanded XANES spectra in the region of 4980–5000 eV.

arises due to transition from ‘s’ orbital to mixed p–d orbitals. To compare with the results of Kityakarn et al., [142], in Fig. 8.6(b), we have also expanded XANES spectra in the region of 4980–5000 eV. It has been observed from Fig. 8.6(b) that the XANES spectrum of all the samples show convex curvature in the regime of 4990–4995 eV manifesting rutile phase. This is consistent with the observation made by GIXRD measurement which also predicts rutile phase of TiO₂. Fig. 8.7 shows the pre-edge region of the XANES spectra in the same

scale which shows that the pre-edges peak intensity decreases with increase in laser irradiation up to 23 shots and beyond which it increases again. This implies that up to 23 pulse shots there is a transition from distorted octahedral to amorphous geometry [222] and beyond 23 pulse shots it again returns to distorted octahedral geometry.

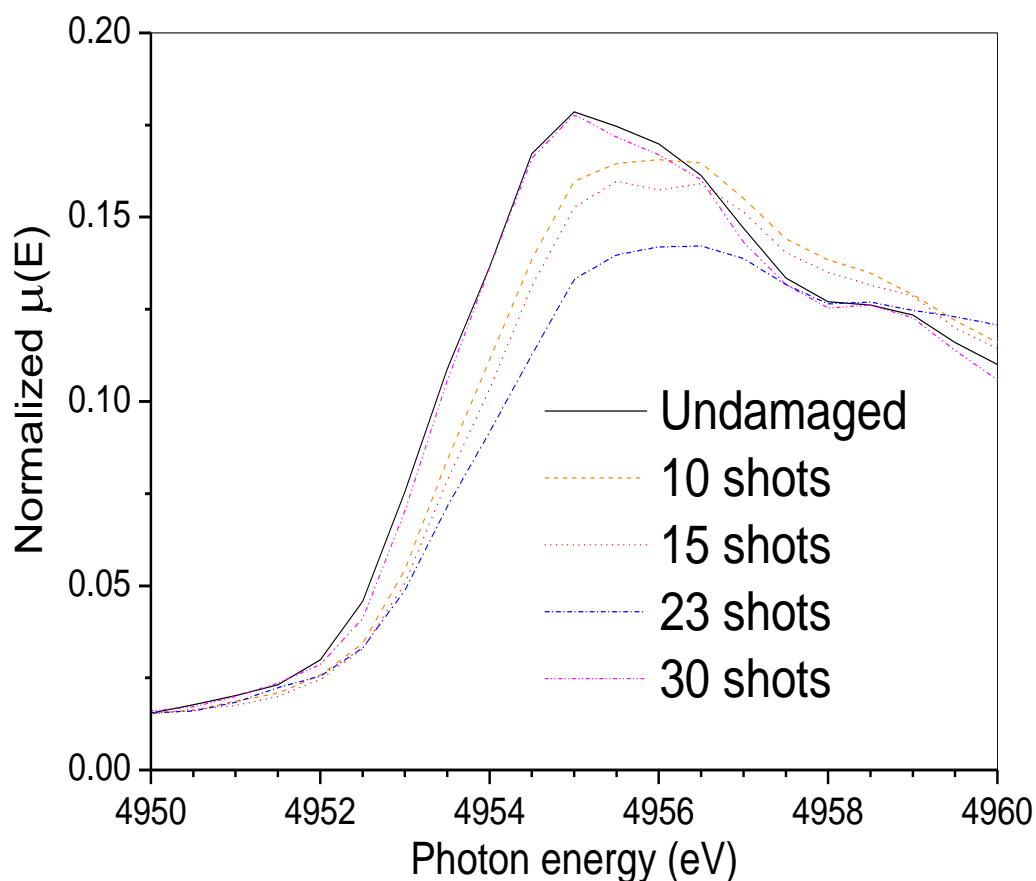


Fig. 8.7: (a) Pre-edge region of the XANES spectra of as-deposited and laser irradiated TiO_2 sample spots.

8.5.2 Tantalum pentoxide samples:

The evolution of laser irradiation morphology of Ta_2O_5 samples as obtained from optical microscopic imaging has been displayed in Fig. 8.8. It shows visible damage from 20 pulse shots onwards and the damaged morphologies are in the form of elongated scratch along the arc of circular laser beam profile. The elongated scratches get fatter as the number

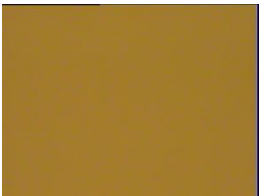
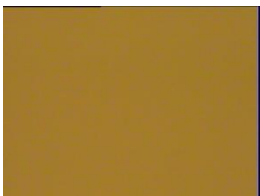

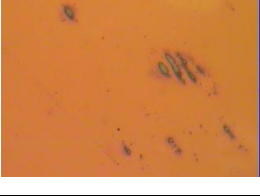
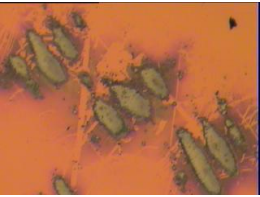
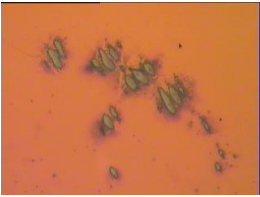
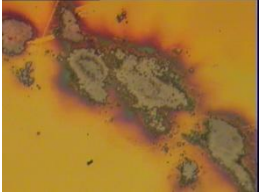
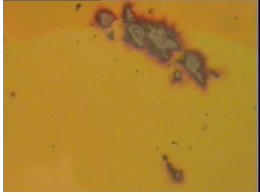
No. of pulse shots	Magnification 2.5 (0.8 mm X 1.1 mm)	Magnification 1 (1.7 mm X 2.3 mm)
10 shots		
20 shots		
30 shots		
40 shots		

Fig.8.8: Optical microscopic images of laser irradiated Ta₂O₅ sample spots after undergoing laser irradiation of 2.06 J/cm².

of shots increases and the scratches start overlapping with one another when the number of to 40. GIXR spectra of all the irradiated Ta₂O₅ sample spots along with the as-deposited sample have been depicted in Fig. 8.9. As can be seen from this figure, there is no significant difference in density or surface roughness among the Ta₂O₅ samples with increase in the number of laser shots. GIXRD spectra of as-deposited and all the irradiated Ta₂O₅ samples are shown in Fig. 8.10 which indicates amorphous nature of the film and it shows no change upon irradiation of sample by laser pulse or by increasing number of laser irradiation shots.

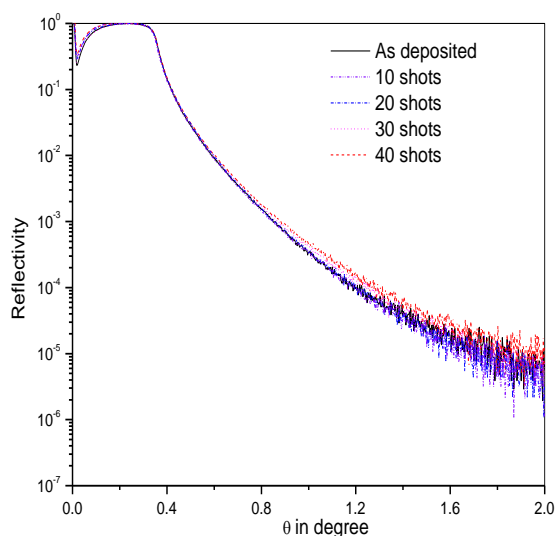


Fig. 8.9: GIXR spectra of as deposited and all laser irradiated Ta₂O₅ sample spots.

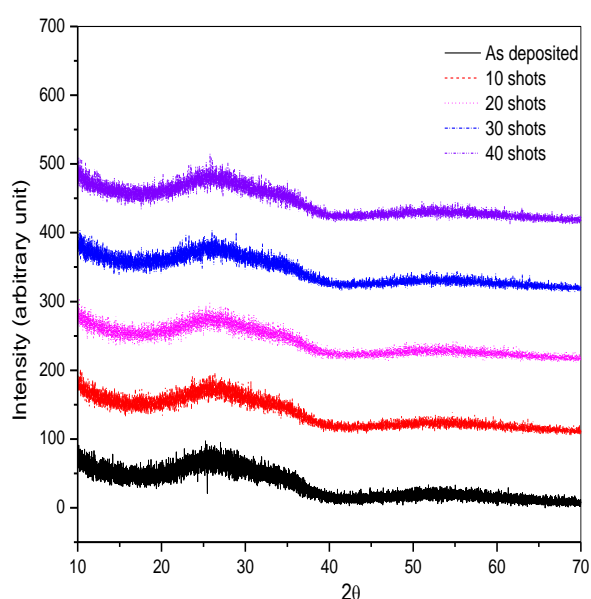


Fig. 8.10: GIXRD spectra of as deposited and all laser irradiated Ta₂O₅ sample spots.

Fig. 8.11 shows normalized EXAFS spectra of all the Ta₂O₅ samples measured around Ta L3-edge (9881 eV) in the energy range of 9820 to 10590 eV. Measured EXAFS spectra have been processed as described in Chapter--2 and Fourier transformed EXAFS spectra have been derived. The first shell (1-2 Å) of the FT-EXAFS spectra have been fitted assuming β -Ta₂O₅ phase (space group: Pccm). Scattering paths for β -Ta₂O₅ structure were generated using the structural parameters given in the literature [154] and the contributing single scattering paths in R range of 1-2 Å are displayed in Table-8.2. While fitting, two closely located Ta-O shells at R_{eff} of 1.949 Å and 1.983 Å have been represented by a single co-ordination shell with degeneracy 4. Post fitting, the bond parameters obtained from path-1 and path 2 have been averaged out to arrive at a single set of bond parameters for Ta-O co-ordination shell. Fig. 8.12 displays the experimental and fitted FT-EXAFS spectra for the

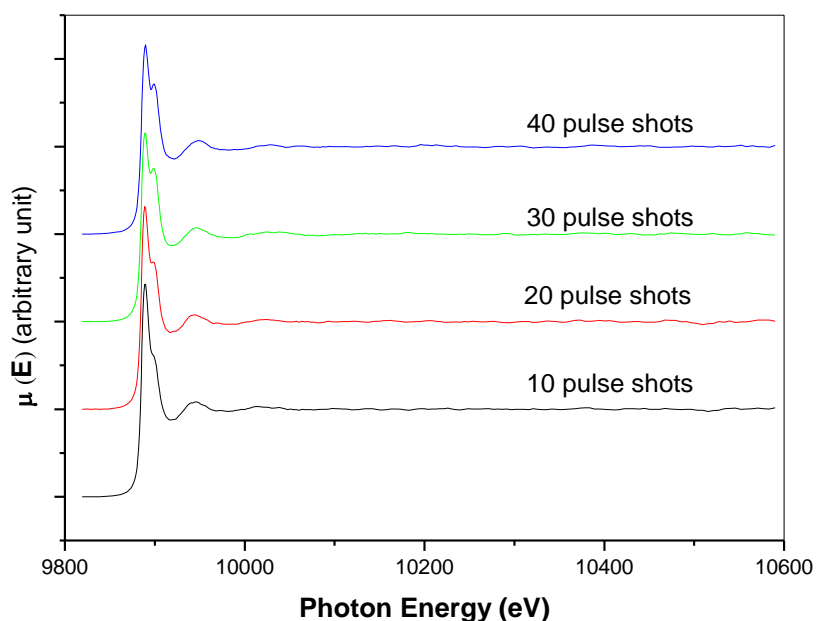


Fig. 8.11: Measured normalized EXAFS spectra of as-deposited and all laser irradiated Ta₂O₅ sample spots.

Table-8.2: Scattering paths used for fitting Ta₂O₅ EXAFS data assuming orthorhombic crystal structure having β-Ta₂O₅ phase (space group: Pccm)			
	degeneracy	R _{eff}	Amp
Path-1 (Ta1-O1)	2	1.839	100
Path-2 (Ta1-O3)	2	1.949	87.46
Path-3 (Ta1-O2)	2	1.983	83.94

all the laser irradiated Ta₂O₅ sample spots while fig. 8.13 shows the plot of average Ta-O bond length, oxygen co-ordination number and average disorder of Ta-O bonds as obtained by analyzing Ta₂O₅ EXAFS spectra, as a function of no. of shots. As can be seen from this figure, Ta-O bond length increases with the increase in number of pulse shots from 10 to 15 and subsequently the bond length remains almost stable with the further increase of number

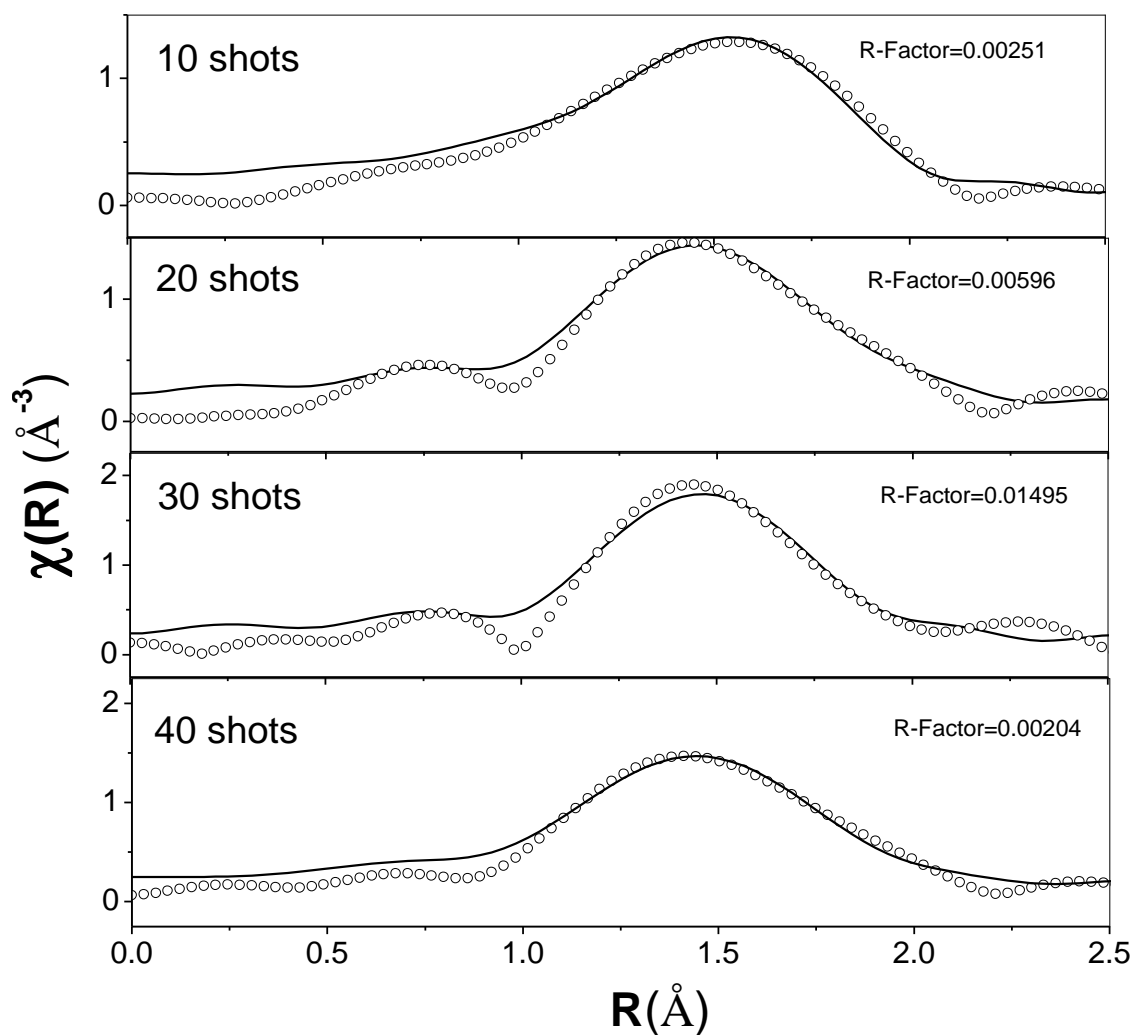


Fig. 8.12: Experimental and fitted FT-EXAFS spectra for all the laser irradiated Ta_2O_5 samples.

of shots. On the other hand, oxygen co-ordination is found to increase monotonically with the increase in number of shots. Referring to fig. 8.8, it can be observed that in spite of the fact that the damaged spot size increases with the increase in number of shots, the bond length has increased prior to damage (i.e. from 10 shots to 20 shots), which is as expected since the lattice gets expanded due to laser heating prior to the onset of damage, however after the onset of damage bond length remains almost stable with the increase in number of shots.

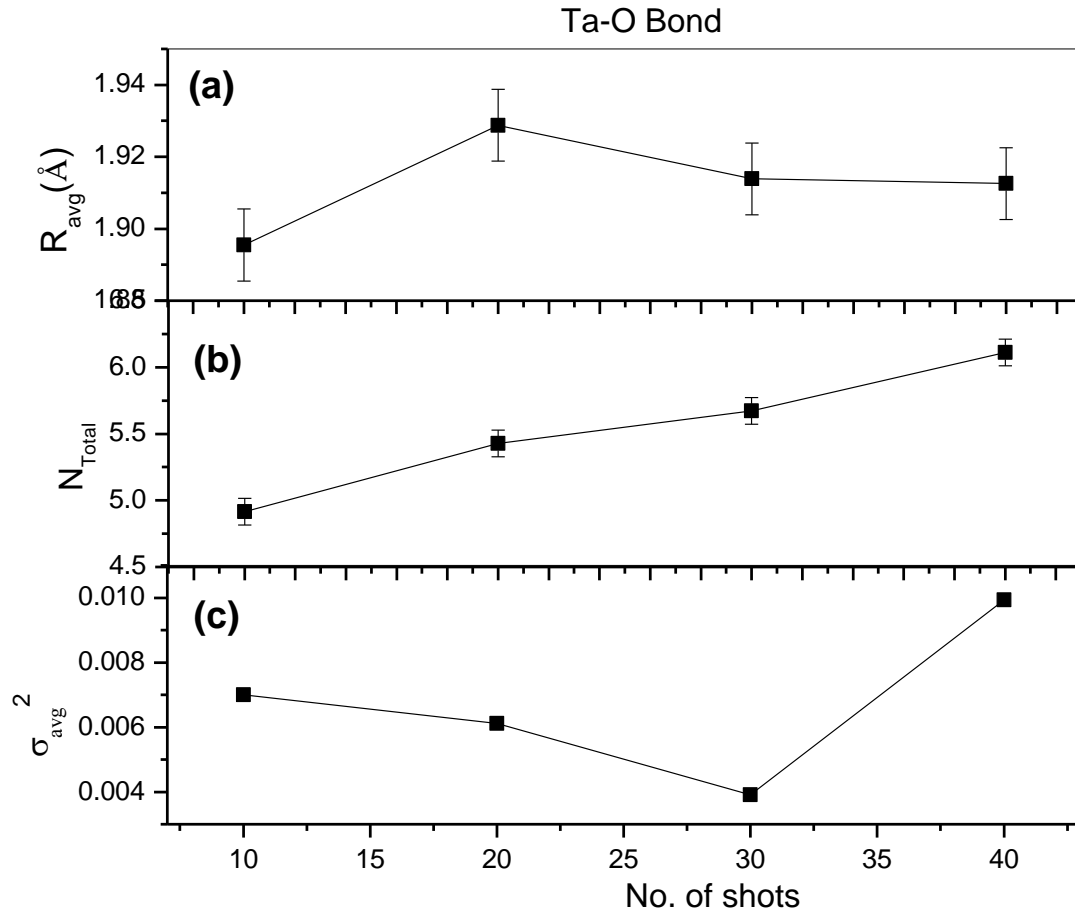


Fig. 8.13: Plot of (a) average Ta-O bond length, (b) oxygen co-ordination number and (c) average disorder of Ta-O bonds obtained from EXAFS.

This can be ascribed to the monotonic increase in oxygen stoichiometry with the increase in number of shots. The increased oxygen stoichiometry helps in reducing heat absorption from laser beam [219] and thus prevents the increase of Ta-O bond length. The monotonic increase of oxygen co-ordination with the increase in number of pulse shots could be due to the oxygen adsorption of the sample from atmosphere [223] which increases as the interaction time of laser beam and sample increases with the increase in number of shots.

8.5.3 Hafnium di-oxide samples:

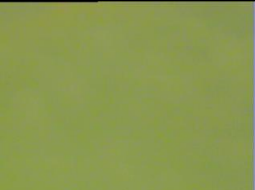
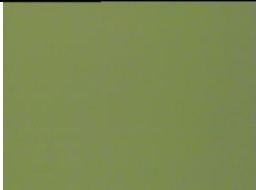


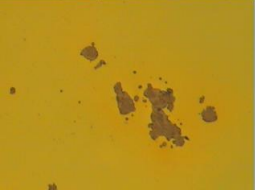

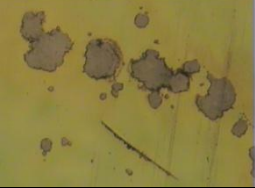

No. of pulse shots	Magnification 2.5 (0.8 mm X 1.1 mm)		Magnification 1 (1.7 mm X 2.3 mm)	
05 shots				
10 shots				
20 shots				
30 shots				

Fig.8.14: Optical microscopic images of laser irradiated HfO₂ sample spots after undergoing laser irradiation of 5.58 J/cm².

The evolution of laser irradiation morphology of HfO₂ samples as obtained from optical microscopic imaging has been displayed in fig. 8.14. Fig. 8.15 displays the measured GIXR data of as-deposited and all laser irradiated HfO₂ sample spots and the plots have been zoomed in the θ range of 0-1° and shown in the inset of the same figure. The figure shows no substantial change in density while there is a substantial change in surface morphology as dictated by the difference in slope of the spectra beyond critical angle. To further investigate the surface morphology of the samples the GIXR data has been analyzed assuming a realistic sample structure. The trend of variation of surface roughness obtained by analyzing the GIXR

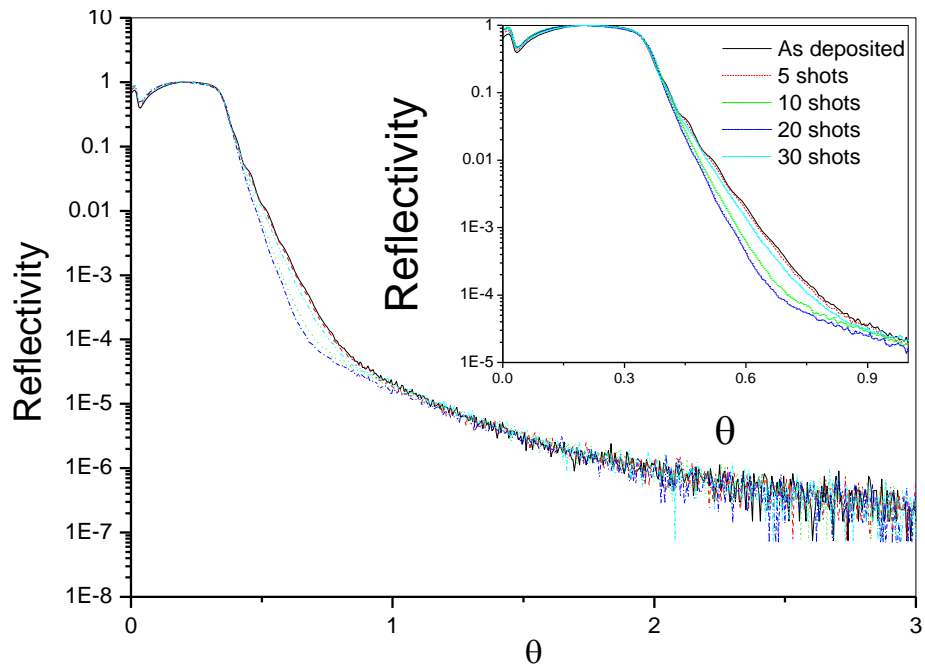


Fig. 8.15: Measured GIXR spectra of as-deposited and all laser irradiated HfO_2 samples.

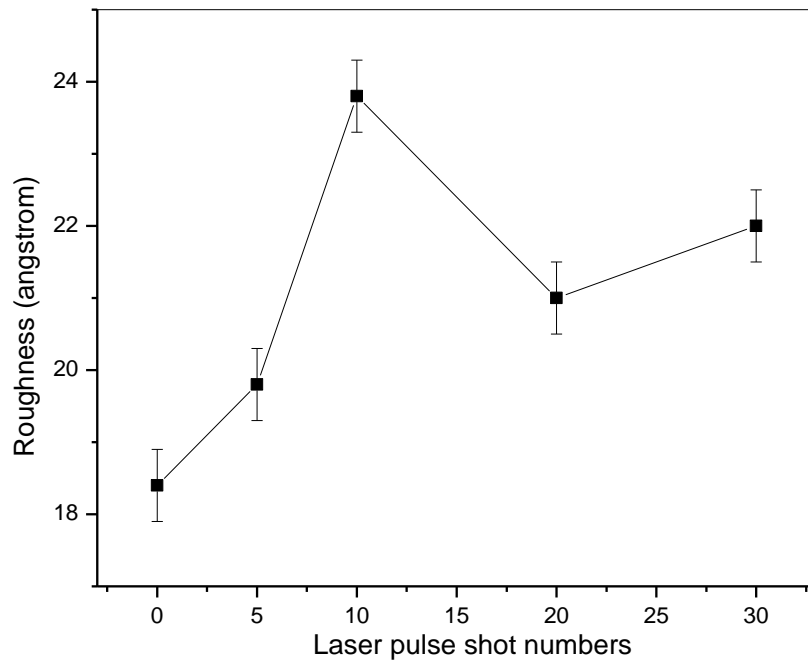


Fig. 8.16: Variation of roughness of laser irradiated spots of HfO_2 as obtained analyzing the GIXR data.

data has been shown in fig. 8.16. Typical error in estimation of surface roughness by GIXR measurement is $\pm 0.5 \text{ \AA}$ [224]. A representative sample layer structure model used for analysis has been shown in the inset of same figure. The increase in surface roughness with the laser treatment is generally observed in laser treatment literature [225] as has been observed in present case up to 10 shots of laser pulse. However, beyond 10 shots, the surface roughness no longer increases but decreases slightly which is possibly due to laser annealing [226]. This is to be recollected from optical microscopic images shown in fig. 8.14 that the laser induced damage has started occurring beyond 10 shots.

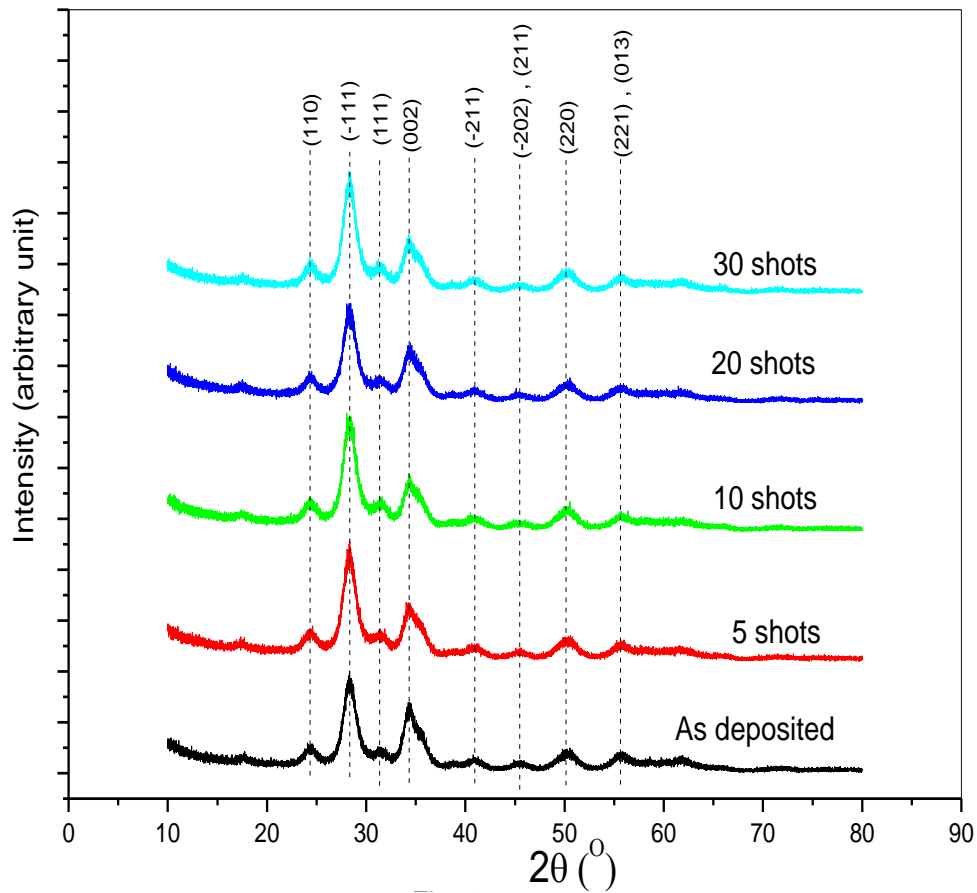


Fig. 8.17: Measured GIXRD spectra of as-deposited as well as laser irradiated HfO₂ sample spots.

Measured GIXRD spectra for all the as-deposited as well as the laser irradiated samples are shown in fig.8.17. The spectra were compared with standard database of JCPDS

and the peak positions are found to resemble with that of standard monoclinic HfO_2 material (PCPDF 78-0050). However, the obtained peaks are broad which is generally resulted from finite crystallite size or strain in the lattice. Williamson-Hall (W-H) analysis [227] has been carried out to eliminate the broadening due to strain and to extract average crystallite size from all the GIXRD peaks. The representative Williamson-Hall plot of as deposited HfO_2 sample has been shown in fig. 8.18(a). The obtained values of crystallite size have been plotted in fig. 8.18(b) which shows that crystallite size decreases with the increases in laser pulse shots which might be due to the disintegration of larger crystallites into smaller one with the increase in laser pulse shots.

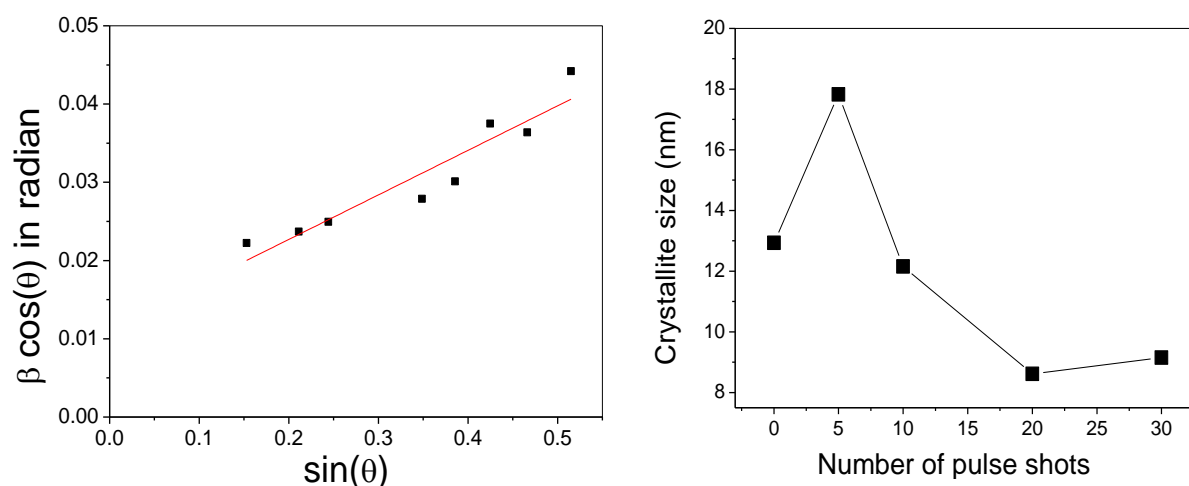


Fig. 8.18(a): Representative Williamson-Hall plot for as deposited HfO_2 sample.

Fig.8.18 (b): Plot of variation of crystallite size with increase in number of pulse shots as obtained from GIXRD.

Fig. 8.19 shows the measured EXAFS data for all the laser irradiated HfO_2 sample spots around Hf L3-edge (9561 eV) in the range of 9480 to 10230 eV. Measured EXAFS data have been processed as described in Chapter-2 and Fourier transformed EXAFS spectra have been derived. The obtained Fourier transformed EXAFS spectra have been fitted

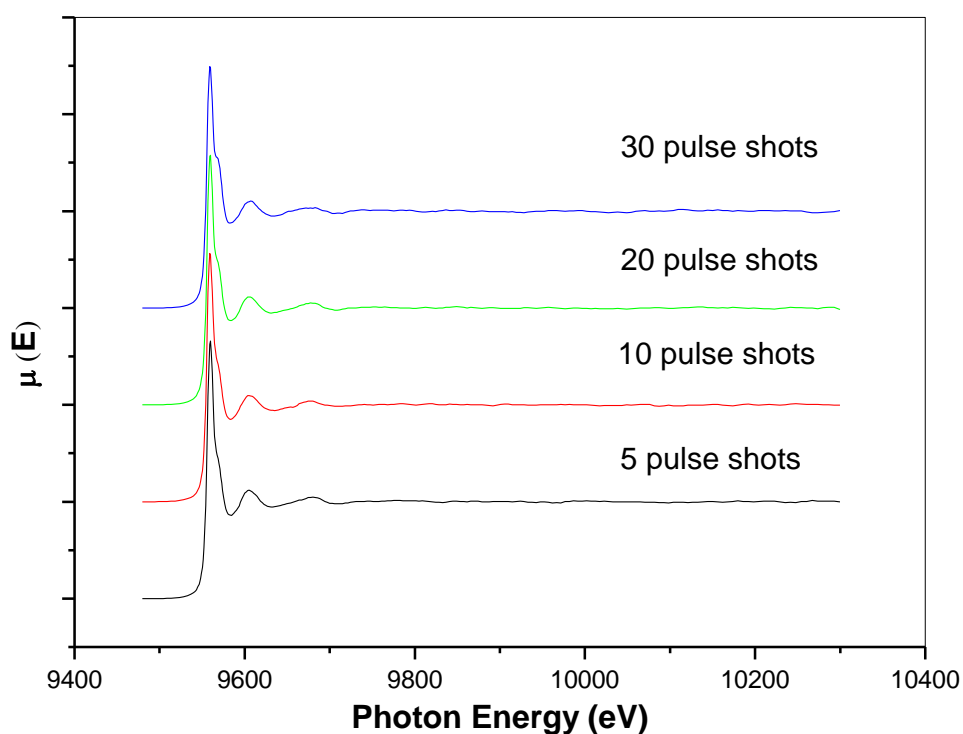


Fig. 8.19: Measured EXAFS spectra for all the laser irradiated HfO₂ sample spots

in the R range of 1.2-3.3 Å assuming monoclinic crystal structure (space group: P21/c) as obtained from GIXRD measurement. Scattering paths were generated for the same structure using the structural parameters given in the literature [103] and the contributing single scattering paths in R range of 1.2-3.3 Å are displayed in table-8.3. To reduce the number of variable parameters, while fitting, all these scattering paths have been represented by three major paths visualizing Path-5(Hf-O) with degeneracy 7, path-11(Hf-Hf) with degeneracy 7 and path-45 (Hf-Hf) with degeneracy 4.

Table-8.3: Scattering paths used for fitting HfO₂ EXAFS data assuming monoclinic crystal structure (space group: P21/c).

Model of structure	Path No.	Degeneracy	R _{effective} (Å ⁰)	Amplitude	Scattering paths considered
Monoclinic	Path-1	1	2.054	100	[+] O1_1 [+]
	Path-2	1	2.063	99.01	[+] O1_2 [+]
	Path-3	1	2.138	90.78	[+] O2_1 [+]
	Path-4	1	2.147	89.91	[+] O1_3 [+]
	Path-5	1	2.162	88.34	[+] O2_2 [+]
	Path-6	1	2.213	83.45	[+] O2_3 [+]
	Path-7	1	2.217	83.08	[+] O2_4 [+]
	Path-8	1	3.346	35.91	[+] Hf_1 [+]
	Path-11	2	3.398	69.59	[+] Hf_2 [+]
	Path-12	2	3.404	69.32	[+] Hf_3 [+]
	Path-14	1	3.425	34.23	[+] Hf_4 [+]
	Path-21	1	3.528	32.15	[+] Hf_5 [+]
	Path-45	2	3.929	50.47	[+] Hf_6 [+]
	Path-51	2	4.017	47.90	[+] Hf_7 [+]

Fig. 8.20 displays the experimental and fitted FT-EXAFS spectra for all the laser irradiated HfO₂ samples. After analyzing the EXAFS data the obtained average bond length, co-ordination number and average disorder for Hf-O bond (represented by path 5) have been plotted in fig. 8.21 and that for Hf-Hf bond (represented by path 11) have been plotted in fig. 8.22 as a function of number of laser shots.

It is to be observed that with the initial increase in number of shots (<10shots), both

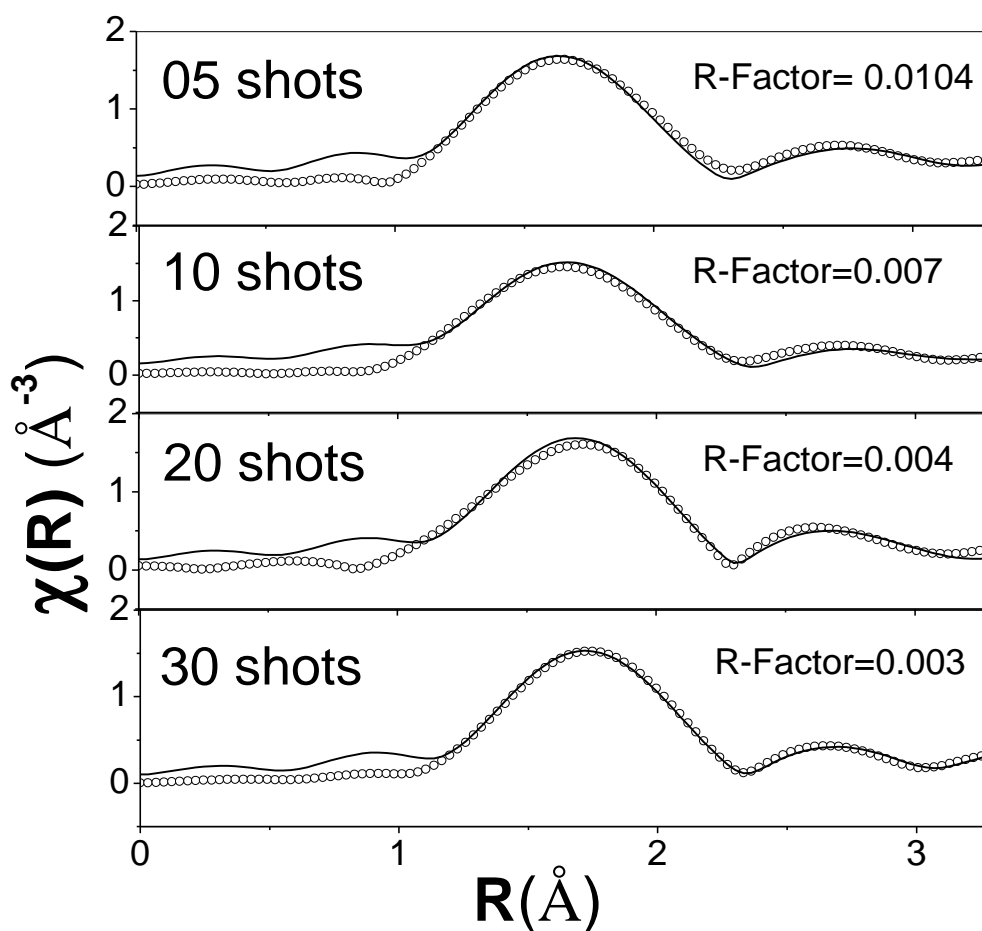


Fig. 8.20: Experimental and fitted FT-EXAFS spectra for all the laser irradiated HfO_2 sample spots.

Hf-O and Hf-Hf bond length expands due to absorption of laser energy by the lattice, oxygen co-ordination increases due to adsorption of oxygen by the sample. It can be seen that the results of the oxygen coordination shell in case of the HfO_2 samples are opposite to that observed for that of Ta_2O_5 samples, where beyond the onset of laser damage the oxygen coordination decreases, possibly due to desorption of oxygen from the samples. This in turn causes enhancement of heat absorption by the samples from the laser radiation and hence Hf-O bond length increases monotonically with an increase in no. of shots.

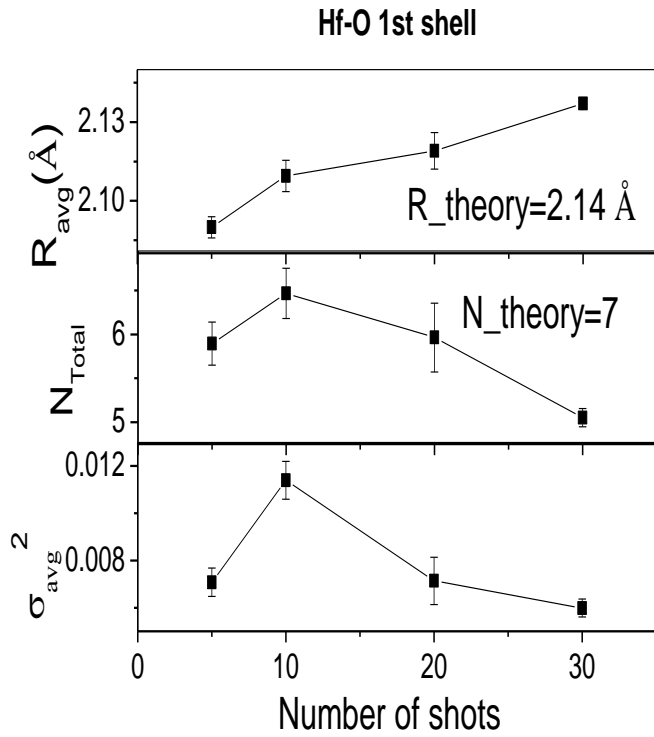


Fig. 8.21: Plot of estimated bond parameters for Hf-O co-ordination shell

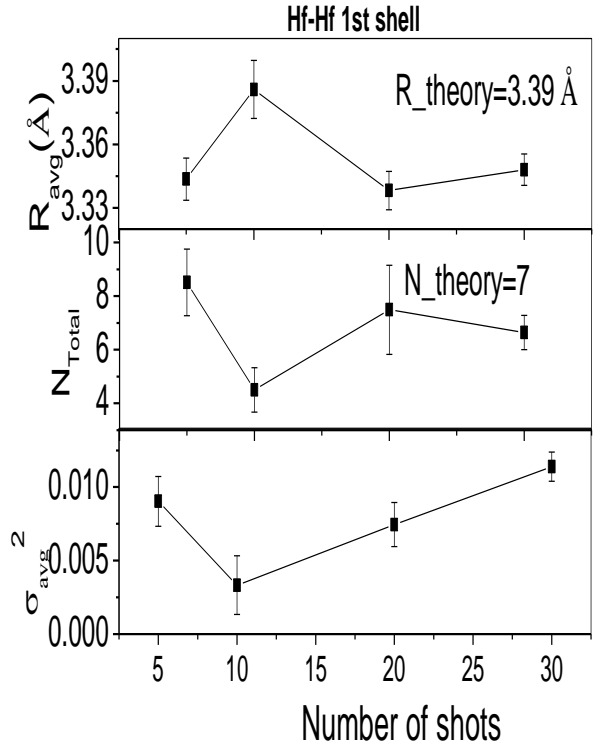


Fig. 8.22: Plot of estimated bond parameters for Hf-Hf co-ordination shell

8.5.4 Gadolinium oxide samples:

The evolution of laser irradiation morphology of Gd_2O_3 samples as obtained from optical microscopic imaging has been displayed in Fig. 8.23. GIXR spectra of all the irradiated Gd_2O_3 samples along with the as-deposited sample have been depicted in fig. 8.24. The variation of critical angle has been shown in the inset of the same figure.

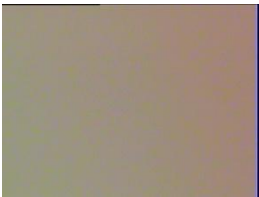
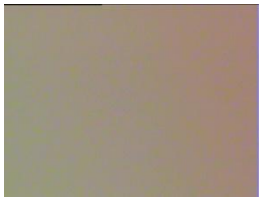





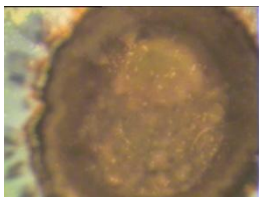
Laser fluence	Magnification 2.5 (0.8 mm X 1.1 mm)	Magnification 1 (1.7 mm X 2.3 mm)
13.2 J/cm ²		
18.6 J/cm ²		
24.4 J/cm ²		
34.9 J/cm ²		

Fig. 8.23: Optical microscopic images of laser irradiated Gd₂O₃ sample spots after undergoing laser irradiation of varying fluencies.

Measured GIXRD spectra for all the as-deposited as well as laser irradiated sample spots are shown in fig. 8.25. The spectra were compared with standard database of JCPDS and it is found that the peak position at 29.4° and 47.5° can be ascribed to (222) and (440) plane of either ia-3 space group (PCPDF 431014) and I213 space groups (PCPDF 760155)

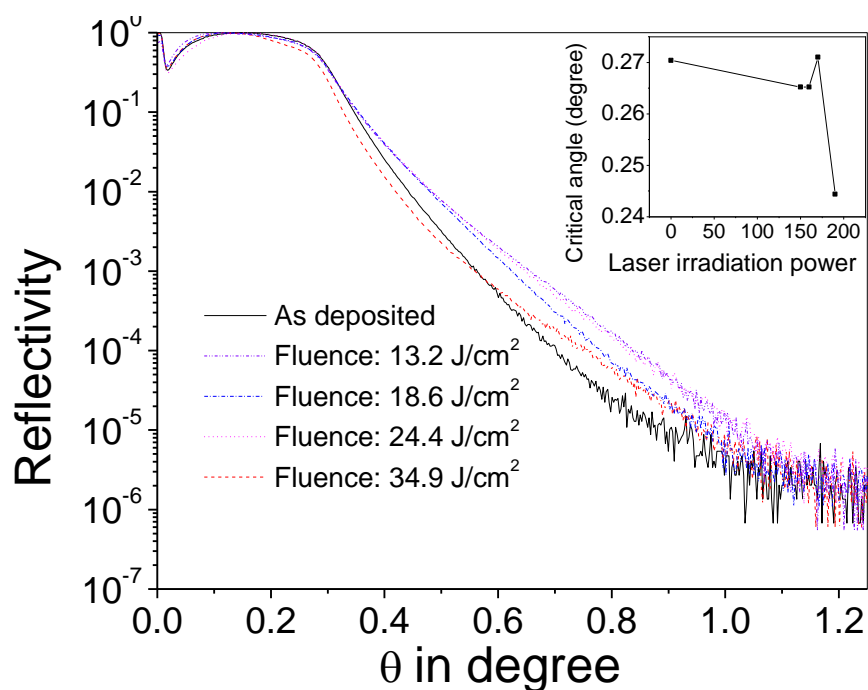


Fig. 8.24: GIXR spectra of all the laser irradiated Gd_2O_3 samples along with the as-deposited sample.

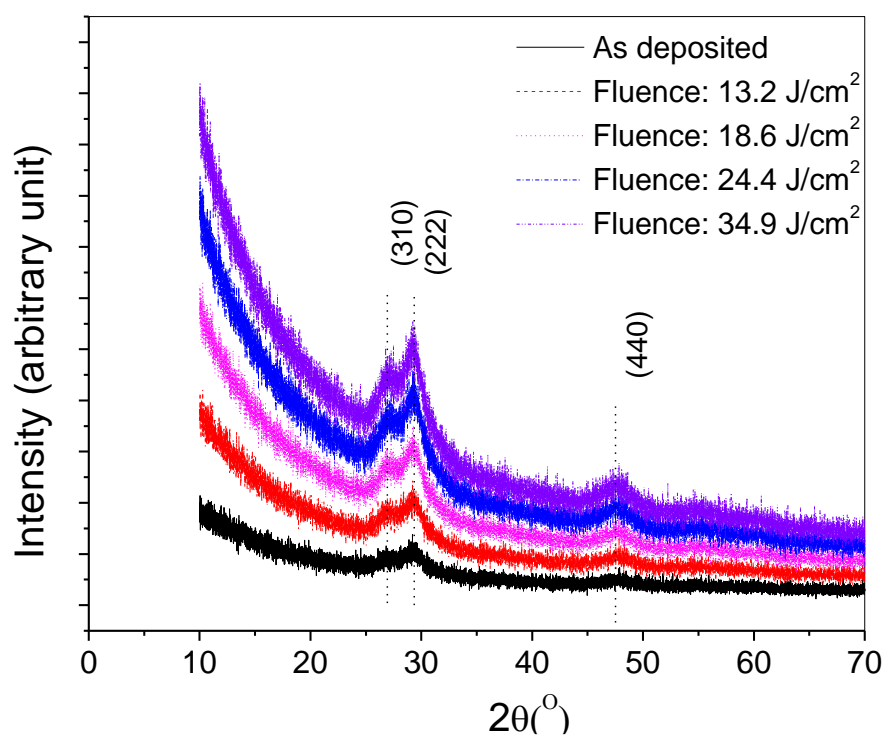


Fig. 8.25: GIXRD spectra of all the laser irradiated Gd_2O_3 samples along with the as-deposited sample spots.

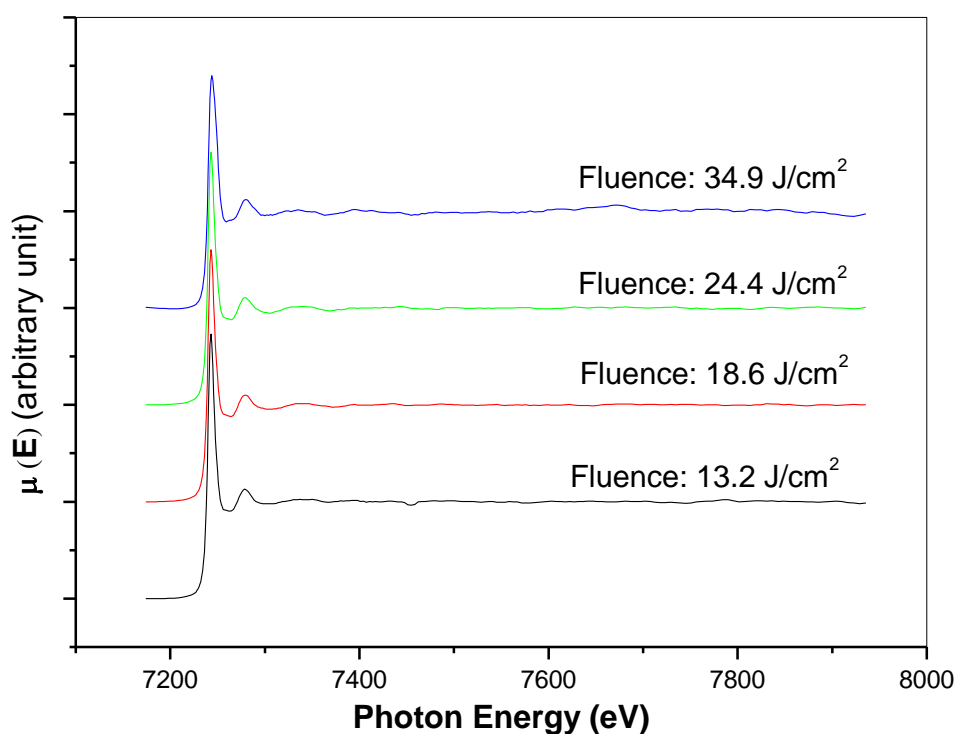


Fig. 8.26: Measured normalized EXAFS spectra of as deposited and all laser irradiated Gd_2O_3 sample spots

respectively having body centered cubic (BCC) crystallographic structure. Additional peak at 26.9° as observed in measured GIXRD pattern can be ascribed to (310) plane of I213 space group alone. Overall, GIXRD measurement suggests that all the Gd_2O_3 samples exhibit either ia-3 or i213 or both the space groups.

Fig. 8.26 shows the measured EXAFS data for all the laser irradiated Gd_2O_3 samples around Gd L3-edge (7243 eV) in the range of 7175 to 7935 eV. Measured EXAFS spectra have been processed as earlier and Fourier transformed EXAFS spectra have been derived. The obtained Fourier transformed EXAFS spectra have been fitted in the R range of 1.2-3.4 Å assuming both i213 and ia-3 space groups as obtained from GIXRD measurement. Scattering paths for i213 space groups were generated using the structural parameters given

Table-8.4: Scattering paths used for fitting Gd L3-edge $\chi(R)$ versus R data assuming BCC crystal structure having space group $I2_13$.			
	Degeneracy	R_{eff}	Amp
Path-1 (Gd-O2)	3	2.396	100
Path-2 (Gd-O1)	3	2.410	98.49
Path-3 (Gd-Gd3)	3	3.509	46.94
Path-5 (Gd-Gd2)	3	3.658	43.22

Table-8.5: Scattering paths used for fitting Gd L3-edge $\chi(R)$ versus R data assuming BCC crystal structure having space group $ia-3$.			
	Degeneracy	R_{eff}	Amp
Path-1 (Gd-O1)	6	2.281	100
Path-2 (Gd-Gd2)	6	3.553	41.93

in the literature [185] and the contributing single scattering paths in R range of 1.2-3.4 Å are displayed in table-8.4. While fitting, two closely located Gd-O shells at R_{eff} of 2.396 Å and 2.410 Å have been represented by a single co-ordination shell with degeneracy 6 and average bond parameters have been calculated for Gd-O shell. For Gd-Gd shells also, post fitting, the parameters of two nearby coordination shells have been averaged out to arrive at a single set of parameters. As for $ia-3$ space group model, the scattering paths were generated using the structural parameters given in the literature [186] and the contributing single scattering paths in R range of 1.2-3.4 Å are displayed in Table-8.5. The bond parameters of these scattering paths were varied and simulated EXAFS spectra were fitted with the processed EXAFS spectra from measured data.

Fig. 8.27 displays the experimental and fitted EXAFS spectra for all the laser irradiated Gd_2O_3 samples assuming both the models. The qualities of fitting using both the models were computed by evaluating R-factor [78] and are displayed in fig. 8.28 for comparison. It can be observed from fig. 8.28 that quality of fitting for all the samples are

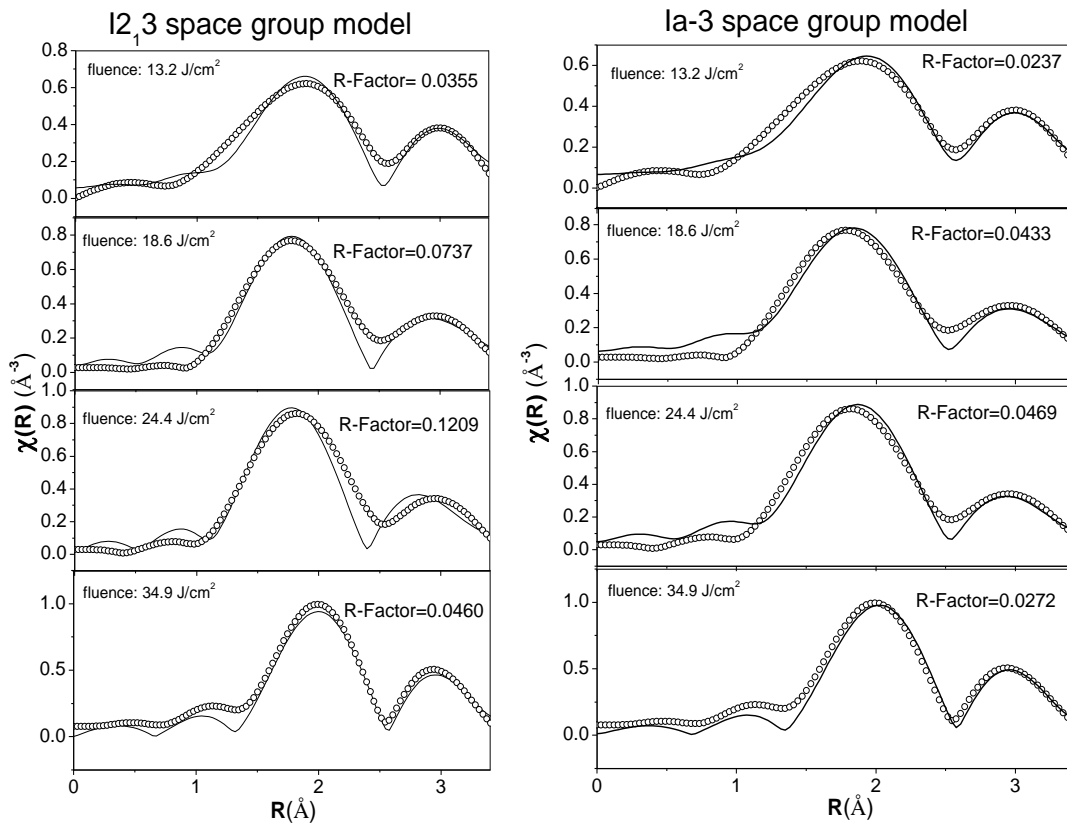


Fig. 8.27: Experimental and fitted FT-EXAFS spectra for all the laser irradiated Gd_2O_3 samples.

better using ia-3 model. So, local structural investigation indicates the possibility of formation of ia-3 space group even though long range structural investigation by GIXRD measurement indicates better signature of I213 space group. In present study, the local structural information obtained using ia-3 space group models have been presented in Fig. 8.29 and 8.30 which respectively depict the trend of variation of Gd-O and Gd-Gd bonding parameters. As can be seen from fig. 8.29, the results are similar to the case of HfO_2 samples, where Gd-O bond length increases continuously beyond the onset of damage, manifesting expansion of the lattice along with decrease in oxygen coordination. The decrease in oxygen coordination acts as oxygen defect in the lattice and causes enhancement of heat absorption by the samples from the laser radiation.

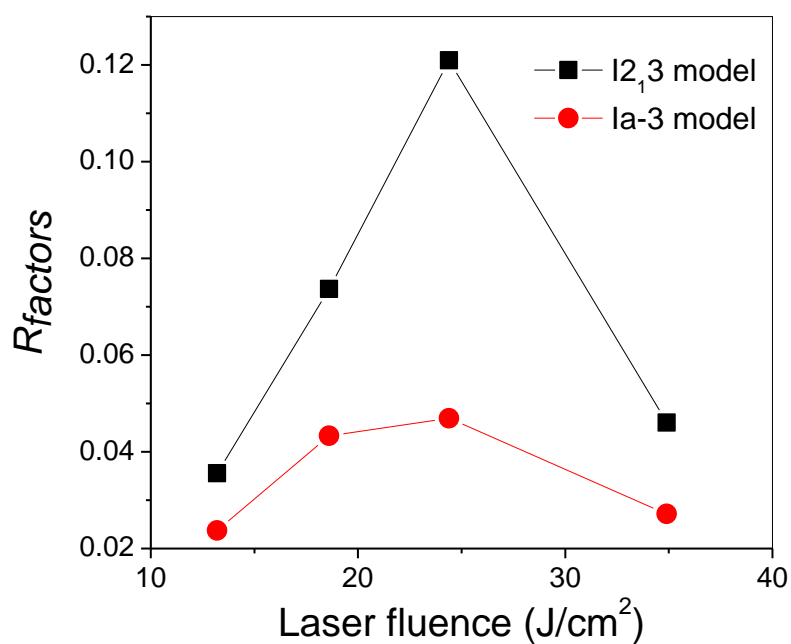


Fig. 8.28: R-factor of fitting using I_{2,3} and ia-3 space group model.

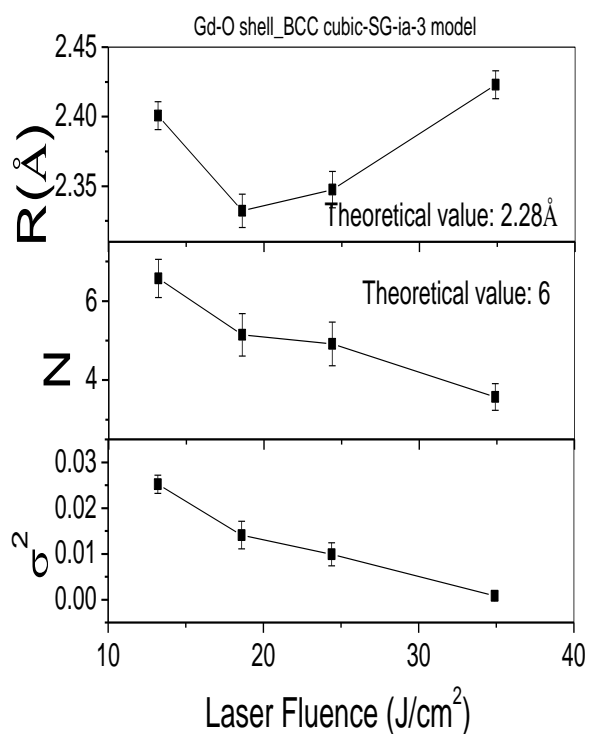


Fig. 8.29: Plot of estimated bond parameters for Gd-O co-ordination shell

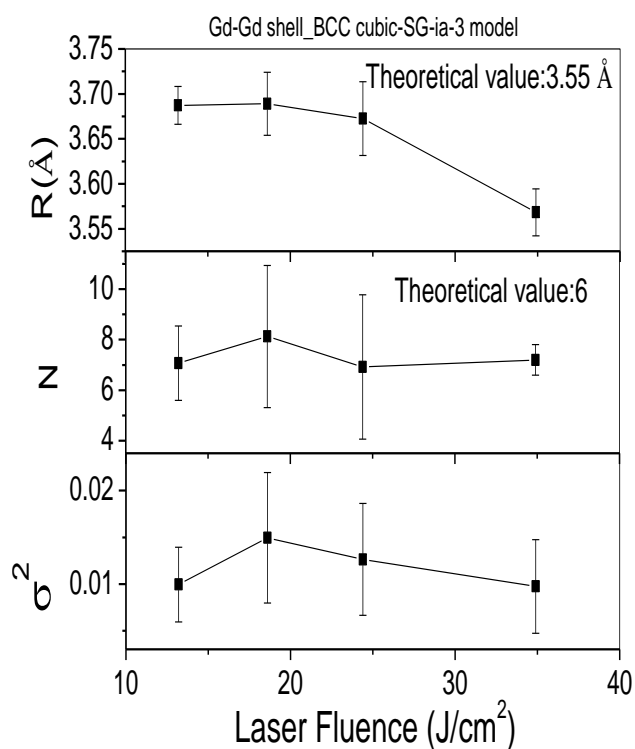


Fig. 8.30: Plot of estimated bond parameters for Gd-Gd co-ordination shell

8.6 Conclusion:

Four refractory oxide samples visualizing TiO_2 , Ta_2O_5 , HfO_2 and Gd_2O_3 samples have been irradiated with nanosecond pulse laser of 1064nm with varying irradiation around their damage threshold. The evolution of macro/micro structural properties with the increase in laser irradiation has been investigated employing mainly EXAFS and GIXRD technique and the following observations could be made. In case of TiO_2 samples, it is observed that up to 23 pulse shots there is a transition from distorted octahedral to amorphous nature and beyond 23 pulse shots it again returns back to distorted octahedral geometry due to recrystallization by laser irradiation. In case of Ta_2O_5 samples, films remain in amorphous phase even with the increase of no. of shots and. Ta-O bond length increases initially and then remains constant. Here monotonic increase in oxygen stoichiometry with the increase in number of shots helps in reducing heat absorption from laser beam and prevents Ta-O bond length to expand further. In case of HfO_2 samples, the samples remain monoclinic though crystallite size decreases beyond damage threshold. Contrary to the case of Ta_2O_5 samples, in case of HfO_2 samples, Hf-O bond expansion take place monotonically with increase in number of shots even beyond the onset of laser damage. This is due to the fact that in this case oxygen coordination decreases continuously with the increase of pulse shots number which causes enhancement of heat absorption by the samples. In case of Gd_2O_3 samples also, it is found that with the increase in laser fluence, Gd-O bond length increases continuously beyond the onset of damage, manifesting expansion of the lattice along with decrease in oxygen coordination.

CHAPTER-9

Summary and future work plan

9.1 Introduction:

Metal oxide thin films can be prepared by sputtering techniques in two manners, either by sputtering metallic targets along with addition of oxygen flow to cause reactive sputtering or by directly sputtering of metal oxide targets. In direct sputtering of metal oxide targets also, addition of oxygen flow in deposition ambient is required as the bombarding Ar^+ ions do not necessarily sputter the target species in form of molecules. In fact there is always a chance of dissociation of target molecules in its constituent atoms/ions as the energetic Ar^+ ions collide with the target surface. These sputtered atoms or ions again form oxide molecules of target material and get deposited on the substrate. In the process there can be loss of oxygen which may lead to non-stoichiometric film. Therefore it is always recommended to purge in some amount of oxygen flow in deposition ambient even in case of sputtering metal oxide targets. But then the quantity of oxygen inflow has to be properly optimized since this oxygen not only influences the stoichiometry of the deposited film but also affects the effective sputtering rate since oxygen and argon has very different sputtering yields. Moreover oxygen pressure in deposition ambient controls the kinetic energy of the ad atoms as these ad atoms undergo collision with oxygen atoms before reaching to the substrate. All these factors make oxygen to argon flow ratio in deposition ambient a very crucial parameter which influences, along with other properties, the stoichiometry, surface morphology and crystallinity of the deposited oxide thin films.

In this chapter, the results of studies made on various refractory oxide thin films deposited under varying oxygen to argon flow ratio and substrate biasing during magnetron sputtering have been summarized. The results on Gd doped ZrO_2 sample deposited under varying doping percentage has been concluded. The results of evolution of local structural properties with the laser irradiation of oxide thin film samples have also been summarized.

9.2 Summary on study of HfO_2 samples:

HfO_2 thin films have been deposited on fused silica substrates by RF magnetron sputtering technique under varying oxygen partial pressure in the range of 0-60%; one set without any substrate bias and another set with substrate kept under pulse DC substrate biasing. From detailed characterizations of these thin film samples following major observations have been made:

- (i) All the HfO_2 films were polycrystalline with predominantly monoclinic crystal structure and crystallinity of the films gets degraded with increase in oxygen partial pressure during deposition.
- (ii) For films deposited without oxygen and with 9.1% oxygen partial pressure, the densities are high but band gaps are low and overall refractive index as obtained from optical transmission measurements are high manifesting oxygen deficiency and high Hf content in the films.
- (iii) The density of the films deposited with substrate bias is found to be higher than that for the films deposited without substrate bias since enhanced bombardment of Ar^+ ions on the growing films in the negative half cycle of the pulsed bias leads to more compact and denser films. For films deposited at >15% oxygen partial pressure without any substrate bias, density shows an overall increasing trend with oxygen partial pressure, however for the other set

deposited with substrate bias, density does not increase, rather decreases slightly. This is attributed to the fact that for the later set of films, as oxygen partial pressure is increased, enhanced bombardment of the growing films by negative oxygen ions in the positive half cycle leads to oxygen rich low density films.

(iv) The variation of density and void content in the films have got reflected in the variation of overall optical properties of the HfO_2 films as obtained from transmission measurements. Refractive index of the films deposited with >15% oxygen partial pressure and without substrate bias show an overall increasing trend with increase in oxygen partial pressure, due to increase in density. However, for the set of films deposited with substrate bias, refractive index does not increase significantly since density does not increase due to enhancement of void content in the films.

(v) Finally we conclude that stoichiometric HfO_2 films with high band gap, high refractive index and low void content can be obtained with 15-30% oxygen partial pressure and with a substrate bias of 50 watt pulse DC on the substrate.

(vi) The information obtained from EXAFS measurement has been found to be correlated with the variation of intrinsic refractive index of the deposited material. For the set of HfO_2 films deposited without substrate bias, the variation of intrinsic refractive index of the films with oxygen partial pressure could be explained in terms of the variation of Hf-Hf bond lengths estimated from the EXAFS modelling. It has been observed that the film having lowest Hf-Hf bond length manifests the highest refractive index due to increase in compactness and density. However, for the set of films deposited with substrate bias it has been observed that refractive index does not follow the trend of variation of Hf-Hf bond length. Rather for this set of films, oxygen coordination surrounding Hf sites plays a major role. In this case, Ar^+ ion bombardment -ve cycle of PDC substrate bias causes oxygen loss

from the sample resulting in lower refractive index in the range of 20-40%, where as beyond 40% oxygen partial pressure, oxygen ion bombardment predominates which results in improved stoichiometric and high refractive index film. Thus EXAFS measurement and analysis provides a microscopic explanation of the macroscopic behaviour of intrinsic refractive index of the oxide films.

9.3 Summary on study of TiO₂ set samples:

This study was made on a set of TiO₂ thin films deposited by asymmetric bipolar pulse DC sputtering technique using different oxygen partial pressures in the range of 0 to 21%. The structural properties of the samples have been studied by GIXRD and EXAFS measurements while the optical properties of the films have been studied by transmission spectrophotometry. The data were analysed and the following observations have been made:

(i) The band gap increases monotonically with increase in oxygen partial pressure and this has been attributed to the realisation of more and more stoichiometric films with reduction in oxygen vacancies, as oxygen partial pressure is increased in deposition ambient. (ii) The refractive index of TiO₂ films varies in a non-linear fashion with increase in O₂ partial pressure in the sputtering ambient. (iii) GIXRD measurements show that all the films have grown in mixed phase of anatase and rutile; and the anatase phase fraction in the films increases continuously as oxygen partial pressure is increased which cannot explain the observed non-linear variation of refractive index of the films with increase in oxygen partial pressure. (iv) However, local structure investigation by EXAFS measurements shows that anatase phase fraction also varies in a non-linear fashion with increase in oxygen partial pressure and almost follows an opposite trend observed for the variation of refractive index of the films. (v) Finally, the non-linear variation of macroscopic and microscopic properties of

the TiO₂ films with increase in oxygen partial pressure has been attributed to the competition between two processes during the film growth, viz., improvement of oxygen stoichiometry of the films and reduction in mobility and kinetic energy of the adatoms reaching the surface of the growing films.

9.4 Summary on study of Ta₂O₅ samples:

This study has been made on a set of Ta₂O₅ thin films, deposited by ABPDC sputtering technique with the systematic variation of oxygen partial pressure (0-50%) used during the deposition, to see if it is possible to correlate the optical properties with the structure of the films probed by GIXRD and EXAFS. Intrinsic refractive index of the Ta₂O₅ samples, as obtained from spectroscopic ellipsometry measurements are found to decrease initially and then increases with an increase in oxygen partial pressure while band gap shows monotonic increase up to 30% oxygen partial pressure and then decreases with the subsequent increase in oxygen partial pressure. These results have been explained in the light of change in average Ta-O bond lengths and oxygen coordination around Ta sites as obtained from EXAFS measurements. The trend of variation in oxygen co-ordination as estimated from EXAFS measurements has been found to follow the variation in oxygen to tantalum ratio in the films as estimated from RBS measurement, while the variation in physical density of the films obtained from RBS measurements is found to be similar to the variation in Ta-O bond lengths obtained from EXAFS measurements.

Tantalum pentoxide is an important optical material which finds application in various multilayer thin film based optical devices. The above study will be helpful to have an insight into the dependence of the parameters of sputtering process on the optical properties of the films and hence in the optimization of these parameters to obtain optical quality films.

9.5 Summary on study of Gd_2O_3 samples:

Under this study, a set of Gd_2O_3 thin films has been deposited on quartz substrates by RF sputtering under a mixed ambient of argon and oxygen at various oxygen partial pressures in the range 0-50%. GIXRD measurements show that all the thin film samples are grown in cubic phases, while GIXR measurements show that the films have low surface roughness which decreases as oxygen partial pressure is increased in the sputtering ambience. Similar variation is also observed for the surface roughness value obtained from AFM measurements. RBS measurements show that the films deposited at lower oxygen partial pressure are oxygen rich while relatively stoichiometric films are realised at higher oxygen partial pressure. The density of the films, obtained from GIXR measurements is found to vary in a non-linear fashion with the films deposited at 9.1% oxygen partial pressure having the lowest density, the overall refractive index obtained from transmission measurements follow the similar variation as bulk density as expected. Spectroscopic ellipsometry measurements show that the low density of the sample prepared with 9.1% oxygen partial pressure is due to the presence of high concentration of voids in this sample. EXAFS measurements have yielded information regarding the local structure around Gd sites. Comparing the nature of variation of Gd-Gd bond length of the samples obtained from EXAFS measurements, as a function of oxygen partial pressure, with that of the intrinsic refractive index of the Gd_2O_3 material present in the films, as obtained from the spectroscopic ellipsometric measurements, it could be concluded that these films assume $ia-3$ space group of cubic crystalline structure. Thus by applying complementary characterisation techniques, it has been possible to explain several macroscopic properties of this technologically important thin film system from microscopic structural information.

9.6 Summary of study made with the variation of oxygen partial pressure:

From all the studies made on four refractory oxide thin films namely HfO_2 , TiO_2 , Ta_2O_5 and Gd_2O_3 prepared by sputtering technique at varying oxygen partial pressures, the following general observations could be made.

1. With the onset of oxygen flow in deposition ambient the deposition rate decreases drastically and with further increase in oxygen partial pressure the deposition rate decreases gradually. The gradual decrease in sputtering rate with increase in oxygen partial pressure might be due to the fact that sputtering efficiency of oxygen is less than that of argon. However, the large decrease in sputtering rate with onset of oxygen ambient cannot be solely due to the lower sputtering efficiency with oxygen. This can be attributed to reaction on the target surface leading to oxygen-rich compound formation that would result in sputtering of material in form of compound compared to preferential sputtering of metal in oxygen-free ambient.
2. The direct band gap as estimated from transmission measurements shows an overall increasing trend with increase in oxygen partial pressure in all cases. This is probably due to the fact that the thin films deposited without oxygen suffers from oxygen deficiency in the sample thereby leading to metal rich low band gap thin film. With the increase in oxygen partial pressure due to realization of stoichiometric oxide films the band gap increases.
3. In all cases, refractive index of the film without oxygen flow is high due to metal rich film formation. With the onset of oxygen refractive index decreases and then varies in a non-linear fashion with further increase in oxygen partial pressure due to various competitive phenomena in the deposition process.

4. The optical properties of all the studied thin film samples prepared in varying oxygen partial pressures have been found to be correlated with local structural properties in different way in different type optical materials. For example for HfO_2 set of thin films deposited without substrate biasing, the variation of intrinsic refractive index of the films with oxygen partial pressure was found to be correlated with the variation of Hf-Hf bond lengths estimated from the EXAFS measurements. It has been observed that the film having lowest Hf-Hf bond length manifests the highest refractive index due to increase in compactness and density. However, for the set of films deposited with substrate bias it has been observed that refractive index shows correlation with rather oxygen coordination surrounding Hf sites. For the set of TiO_2 samples, the non-linear variation of refractive index with respect to oxygen partial pressure could be explained, at least in limited range ($\sim 5\text{-}15\%$), based on the anatase to rutile phase ratio obtained from local structural analysis. For the set of Ta_2O_5 samples, the variation of refractive index was found to be related with Ta-O bond length up to around 40% oxygen partial pressure beyond which refractive index is found to have been correlated with oxygen co-ordination number around Ta sites. For the set of Gd_2O_3 samples, the trend of refractive index is found to be correlated with Gd-Gd bond length when these bond lengths are extracted assuming $ia-3$ space group instead of $i2_13$ space group which is another possible crystallographic phase of Gd_2O_3 . Thus EXAFS measurement and analysis provides a microscopic explanation of the macroscopic behaviour of refractive index of the studied refractory oxide films in one or other ways.

9.7 Summary on study of Gd doped ZrO_2 set of samples

In this study, ZrO_2 thin films with 0, 7, 9, 11 and 13% of Gd doping were prepared by RF magnetron sputtering technique by sputtering pure/doped ZrO_2 targets under mixed

ambient of Ar and O₂. It has been observed from spectroscopic ellipsometry and optical transmission measurements that the void fraction present in the films increases significantly beyond Gd doping concentration of 11% causing a decrease in the effective refractive index of the films. It has also been observed from GIXRD measurements that though the undoped ZrO₂ film is having monoclinic structure, Gd doping stabilises the films in cubic structure. This is further confirmed by EXAFS measurements on the samples at Zr K edge which shows that better fitting of the FT-EXAFS data could be obtained with cubic structure up to a Gd doping concentration of 9%, beyond which, however, better fitting of the data are obtained with monoclinic structure. EXAFS measurements at Zr K edge and Gd L₃ edges further confirm that Gd dopants replace Zr atoms in ZrO₂ matrix up to 9-11% doping concentration with creation of oxygen vacancies near Zr sites, however above 11% Gd doping, Gd precipitates out as a separate Gd₂O₃ phase. This corroborates the observed optical properties of the thin films that Gd doping beyond 11% yields samples with higher void fraction, lower band gap and lower effective refractive index.

9.8 Summary on study of local structure investigation on refractory oxide thin films near laser damage threshold:

Four refractory oxide thin film samples viz., TiO₂, Ta₂O₅, HfO₂ and Gd₂O₃ have been irradiated with nanosecond pulse laser of 1064nm with varying irradiation around their damage threshold. The evolution of macro/micro structural properties with the increase in laser irradiation has been investigated employing mainly EXAFS and GIXRD technique and the following observations could be made. In case of TiO₂ samples, it is observed that up to 23 pulse shots there is a transition from distorted octahedral to amorphous nature and beyond 23 pulse shots it again returns back to distorted octahedral geometry due to recrystallization

by laser irradiation. In case of Ta_2O_5 samples, films remain in amorphous phase even with the increase of no. of shots and Ta-O bond length increases initially and then remains constant. Here monotonic increase in oxygen stoichiometry with the increase in number of shots helps in reducing heat absorption from laser beam and prevents Ta-O bond length to expand further. In case of HfO_2 samples, the samples remain monoclinic though crystallite size decreases beyond damage threshold. Contrary to the case of Ta_2O_5 samples, in case of HfO_2 samples, Hf-O bond expansion take place monotonically with increase in number of shots even beyond the onset of laser damage. This is due to the fact that in this case oxygen coordination decreases continuously with the increase of pulse shots number which causes enhancement of heat absorption by the samples. In case of Gd_2O_3 samples also, it is found that with the increase in laser fluence, Gd-O bond length increases continuously beyond the onset of damage, manifesting expansion of the lattice along with decrease in oxygen coordination.

9.9 Future work plan:

This thesis work establishes EXAFS as a useful technique to investigate the microstructural properties of oxide thin films and their correlations with the macroscopic properties which can directly be exploited in their technological applications. One limitation of this work has been that no depth dependent structural information of the films has been presented here. However, recently, a grazing incidence X-ray Absorption Spectroscopy (GIXAS) measurement facility has been set up at the Energy Scanning EXAFS beam line at INDUS-2 SRS by employing a 2-circle goniometry with 5-axis sample stage in the experimental station of the beam line. In this facility it will be possible to change the grazing angle of incidence of the synchrotron X-ray on the sample and hence its penetration depth

inside the sample. It will also be possible to detect the fluorescence EXAFS and reflectivity signals simultaneously from the same sample spot by two detectors. Thus this set-up would provide depth dependent XAFS measurement facility on thin films. This work will further be extended to carry out non-destructive structural investigation on interfaces of the multilayer structures prepared using these oxide films.

The work on structural investigation of the films near their laser damage threshold will also be extended to in-situ study where the films will be irradiated by the laser while EXAFS data are measured so that real-time changes in the bond length etc.in the sample due to laser irradiation can be carried out.

References

1. S. Korkmaz, S. Pat, N. Ekem, M. Zafer Balbag, and S. Temel, "Thermal treatment effect on the optical properties of ZrO₂ thin films deposited by thermionic vacuum arc," *Vacuum*, 86, 1930–1933 (2012).
2. M. Zevin and R. Reisfeld, "Preparation and properties of active waveguides based on zirconia glasses," *Opt. Mater.* 8, 37–41 (1997).
3. R. Brenier, C. Urlacher, J. Mugnier, and M. Brunel, "Stress development in amorphous zirconium oxide films prepared by sol-gel processing," *Thin Solid Films* 338, 136–141 (1999).
4. <http://www.animations.physics.unsw.edu.au/jw/light/non-reflective-coatings.html>.
5. <https://www.digitaltrends.com/cool-tech/scientists-develop-cheap-spray-on-solar-cells/>.
6. Y. Liu, P. H. Daum, "Relationship of refractive index to mass density and self-consistency of mixing rules for multicomponent mixtures like ambient," *Journal of Aerosol Science* 39, 974–986 (2008).
7. S. Kasap, P. Capper, "Springer Handbook of Electronic and Photonic Materials", Stürtz GmbH, Würzburg (2007).
8. https://en.wikipedia.org/wiki/Abbe_number.
9. L. Properzi, A. Di Cicco, L. Nataf, F. Baudelet & T. Irifune, "Short-range order of compressed amorphous GeSe₂," *Scientific Reports* 5, 1 (2015).
10. G. D. Wilk, R. M. Wallace, and J. M. Anthony, "High- κ gate dielectrics: Current status and materials properties considerations," *J. Appl. Phys.* 89, 5243 (2001).
11. R. K. Nahar, V. Singh, and A. Sharma, "Study of electrical and microstructure properties of high dielectric hafnium oxide thin film for MOS devices," *J. Mater. Sci.-Mater. Electron.* 18, 615 (2007).
12. T. Kanashima, T. Tada, and M. Okuyama, "Preparation and characterization of HfO₂ thin films by photo-assisted MOCVD," *J. Phys. IV* 132, 279 (2006).
13. J. Yuan, H. Qi, Y. Zhao, Z. Fan, and J. Shao, "Influence of purity of HfO₂ on reflectance of ultraviolet multilayer," *Chin. Opt. Lett.* 6, 222 (2008).
14. R. B. Tokas, N. K. Sahoo, S. Thakur, and N. M. Kamble, "A comparative morphological study of electron beam co-deposited binary optical thin films of HfO₂:SiO₂ and ZrO₂:SiO₂," *Curr. Appl. Phys.* 8, 589 (2008).
15. N. C. Das, N. K. Sahoo, D. Bhattacharyya, S. Thakur, N. M. Kamble, D. Nanda, S. Hazra, J. K. Bal, J. F. Lee, Y. L. Tai, and C. A. Hsieh, "Correlation between local structure and refractive index of e-beam evaporated HfO₂-SiO₂ composite thin films" *J. Appl. Phys.* 108, 023515 (2010).
16. P. Eiamchai, P. Chindaudom, A. Pokaipisit, and P. Limsuwan, "A spectroscopic ellipsometry study of TiO₂ thin films prepared by ion-assisted electron-beam evaporation," *Curr. Appl. Phys.* 9, 707–712 (2009).
17. K. Jiang, A. Zakutayev, J. Stowers, M. D. Anderson, J. Tate, D. H. McIntyre, D. C. Johnson, and D. A. Keszler, "Low-temperature, solution processing of TiO₂ thin films and fabrication of multilayer dielectric optical elements," *Solid State Sci.* 11, 1692–1699 (2009).
18. L. Miao, L. F. Su, S. Tanemura, C. A. J. Fisher, L. L. Zhao, Q. Liang, and G. Xu, "Cost-effective nanoporous SiO₂-TiO₂ coatings on glass substrates with antireflective and self-cleaning properties," *Appl. Eng.* 112, 1198–1205 (2013).

19. P. M. Perillo and D. F. Rodriguez, "A room temperature chloroform sensor using TiO₂ nanotubes," *Sens. Actuators B* 193, 263–266 (2014).
20. F. Meng, X. Song, and Z. Sun, "Photocatalytic activity of TiO₂ thin films deposited by RF magnetron sputtering," *Vacuum* 83, 1147–1151 (2009).
21. W. S. Shih, S. J. Young, L. W. Ji, W. Water, T. H. Meen, K. T. Lam, J. Sheen, and W. C. Chu, "Thin film transistors based on TiO₂ fabricated by using radio-frequency magnetron sputtering," *J. Phys. Chem. Solids* 71, 1760–1762 (2010).
22. P.-C. Yao, J.-L. Chiang, and M.-C. Lee, "Application of sol–gel TiO₂ film for an extended-gate H⁺ ion-sensitive field-effect transistor," *Solid State Sci.* 28, 47–54 (2014).
23. K. Koc, F. Z. Tepehan, and G. G. Tepehan, "Antireflecting coating from Ta₂O₅ and SiO₂ multilayer films," *J. Mater. Sci.* 40, 1363–1366 (2005).
24. I. Birkby and R. Stevens, "Applications of zirconia ceramics," *Key Eng. Mater.* 122–124, 527–552 (1996).
25. J. W. Fergus, "Doping and defect association in oxides for use in oxygen sensors," *J. Mater. Sci.* 38, 4259–4270 (2003).
26. R. M. Ormerod, "Solid oxide fuel cells," *Chem. Soc. Rev.* 32, 17–28 (2003).
27. P. D. L. Mercera, J. G. van Ommen, E. B. M. Doesburg, A. J. Burggraaf, and J. R. H. Ross, "Stabilized tetragonal zirconium oxide as a support for catalysts: evolution of the texture and structure on calcination in static air," *Appl. Catal.* 78, 79–96 (1991).
28. V. A. Sadykov, V. V. Kriventsov, E. M. Moroz, Y. V. Borchert, D. A. Zyuzin, V. P. Kolko, T. G. Kuznetsova, V. P. Ivanov, S. Trukhan, A. I. Boronin, E. M. Pazhentov, N. V. Mezentseva, E. B. Burgina, and J. R. H. Ross, "Ceria-zirconia nanoparticles doped with La or Gd: effect of the doping cation on the real structure," *Solid State Phenom.* 128, 81–88 (2007).
29. M. Cole, C. R. A. Catlows, and J. P. Dragun, "EXAFS studies of doped-ZrO₂ systems," *J. Phys. Chem. Solids* 51, 507–513 (1990).
30. Jong Geol Lee, Hyun Gi Kim, Sung Soo Kim, "Defect-sealing of Al₂O₃/ZrO₂ multilayer for barrier coating by plasma-enhanced atomic layer deposition process," *Thin Solid Films* 577, 143–148 (2015).
31. C. T. Kuo and R. Kwor, "Study of sputtered HfO₂ thin films on silicon," *Thin Solid Films* 213, 257 (1992).
32. M. G. Blanchin, B. Canut, Y. Lambert, V. S. Teodorescu, A. Barau, and M. Zaharescu, "Structure and dielectric properties of HfO₂ films prepared by a sol–gel route," *J. Sol-Gel Sci. Technol.* 47, 165 (2008).
33. J. Kim, S. Kim, H. Jeon, M. H. Cho, K. B. Chung, and C. Bae, "Characteristics of HfO₂ thin films grown by plasma atomic layer deposition," *Appl. Phys. Lett.* 87, 053108 (2005).
34. T. Moria, M. Fujiwarab, R. R. Manorya, I. Shimizuc, T. Tanakab, and S. Miyakea, "HfO₂ thin films prepared by ion beam assisted deposition," *Surf. Coat. Technol.* 169, 528 (2003).
35. D. E. Morton and T. R. Jensen, "OSA technical digest series," in *Optical Interference Coatings*, Banff, Canada, 15 July 2001 (Optical Society of America) (2001), paper MB6.
36. P. R. Sagdeo, D. D. Shinde, J. S. Misal, N. M. Kamble, R. B. Tokas, A. Biswas, A. K. Poswal, S. Thakur, D. Bhattacharyya, N. K. Sahoo and S. C. Sabharwal, "Deposition and characterization of titania–silica optical multilayers by asymmetric bipolar pulsed dc sputtering of oxide targets," *J. Phys. D Appl. Phys.* 43, 045302 (2010).
37. S. Berg and T. Nyberg, "Fundamental understanding and modeling of reactive sputtering processes," *Thin Solid Films* 476, 215 (2005).

38. D. H. Kuo, C. H. Chien, and C. H. Huang, "Zirconia and zirconia-silica thin films deposited by magnetron sputtering," *Thin Solid Films*, 420, 47 (2002).
39. W. Kwasny, L. A. Dobrzanski, M. Pawlyta, and W. Gulbinski, "Fractal nature of surface topography and physical properties of the coatings obtained using magnetron sputtering," *J. Mater. Process. Technol.* 157, 188 (2004).
40. Z.W. Ma, L.X. Liu, Y.Z. Xie, Y.R. Su, H.T. Zhao, B.Y. Wang, X.Z. Cao, X.B. Qin, J. Li, Y.H. Yang, E.Q. Xie, "Spectroscopic ellipsometry and positron annihilation investigation of sputtered HfO₂ films," *Thin Solid Films* 519, 6349 (2011).
41. W. Kern and K. K. Schuegraf, "Handbook of Thin Film Deposition Processes and Techniques: Principles, Methods, Equipment and Applications", 2nd ed. (William Andrew Publishing/Noyes, Norwich, New York) (2002).
42. H. Kersten, H. Deutsch, H. Steffen, G. M. W. Kroesen, and R. Hippler, "The energy balance at substrate surfaces during plasma processing," *Vacuum* 63, 385 (2001).
43. A. Belkind, W. Song, G. McDonough, and R. Scholl, "The energy balance at substrate surfaces during plasma processing," in 45th Annual SVC Technical Conference (Society of Vacuum Coaters) p. 184 (2002).
44. S. Basu, C. Nayak, A. K. Yadav, A. Agrawal, A. K. Poswal, D. Bhattacharyya, S. N. Jha, and N. K. Sahoo, "A comprehensive facility for EXAFS measurements at the INDUS-2 synchrotron source at RRCAT, Indore, India," *J. Phys.: Conf. Ser.* 493, 012032 (2014).
45. D. C. Konigsberger and R. Prince, *X-Ray Absorption: Principles, Applications, Techniques of EXAFS, SEXAFS and XANES* (Wiley) (1988).
46. M. Newville, B. Ravel, D. Haskel, J. J. Rehr, E. A. Stern, and Y. Yacoby, "Analysis of multiple-scattering XAFS data using theoretical standards," *Physica B* 208–209, 154–156 (1995).
47. Krishna Seshan, "Deposition Processes and Techniques", Noyes Publications, Norwich, New York, U.S.A. (2002).
48. https://en.wikipedia.org/wiki/Sputter_deposition.
49. E. Alfonso, J. Olaya, G. Cubillos, "Thin film growth through sputtering technique and its applications, Crystallization-Science and Technology", InTech, Croatia p. 401–402 (2012).
50. S. Rosnagel, "Sputtering and Sputter Deposition", in K. Seshan, "Handbook Of Thin-Film Deposition Processes And Techniques", Noyes Publication, Norwich, New York, U.S.A (2002).
51. K. Wasa, I. Kanno, H. Kotera, "Handbook of sputter deposition technology: Fundamentals and applications for functional thin films, nanomaterials and MEMS", 2nd edn. (Elsevier, Amsterdam) (2012)
52. https://www.plasma-universe.com/Electric_glow_discharge.
53. M. Ohring, "The Materials Science of Thin Films", Academic Press, San Diego New York Boston p. 120(1992).
54. J. W. Lee, J. J. Cuomo, and M. Bourham, "Plasma characteristics in pulsed direct current reactive magnetron sputtering of aluminum nitride thin films," *J. Vac. Sci. Technol. A* 22, 260–263 (2004).
55. S. M. Haque, P. R. Sagdeo, D. D. Shinde, J.S. Misal, S.N. Jha, D. Bhattacharyya and N.K. Sahoo, "Extended X-ray Absorption Fine Structure (EXAFS) measurements on Asymmetric Bipolar Pulse direct current magnetron sputtered Ta₂O₅ thin films," *Applied Optics* 54, 6744 (2015).
56. E. Hollands, D. S. Campbell, "The mechanism of reactive sputtering," *Journal of Materials Science* 3, 544-552 (1968).

57. D. A. Golosov, "Balanced magnetic field in magnetron sputtering systems," *Vacuum* 139, 109–116 (2017).
58. B. D. Cullity and S. R. Stock, "Elements of X-Ray Diffraction", 3rd edn., Pearson education Ltd. UK (2001).
59. R. W. James, "The Optical Principles of Diffraction of X-Rays", Cornell University Press, New York (1965).
60. <https://www.rigaku.com/en/service/software/globalfit>.
61. D. L. Windt, "IMD Version 4.1.1," 2000, <http://www.rxcollc.com/idl/index.html>.
62. L. G. Parratt, "Surface studies of solids by total reflection of X-rays," *Phys. Rev.* 95, 359–369 (1954).
63. J. C. Manifacier, J. Gasiot, and J. P. Fillard, "A simple method for the determination of the optical constants n , k and the thickness of a weakly absorbing thin film", *J. Phys. E* 9, 1002–1004 (1976).
64. R. Swanepoel, "Determination of the thickness and optical constants of amorphous silicon", *J. Phys. E.* 16, 1214–1222 (1983).
65. R. M. A. Azzam and N. M. Bashara, "Ellipsometry and Polarized Light" North-Holland, Amsterdam (1977).
66. H. Fujiwara, "Spectroscopic Ellipsometry: Principles and Applications", Wiley (2003).
67. A. Biswas, D. Bhattacharyya, N.K. Sahoo, B.S. Yadav, S.S. Major, R.S. Srinivasa, "Spectroscopic ellipsometry studies of GaN films deposited by reactive rf sputtering of GaAs target", *Journal of Applied Physics*, 103, 083541 (2008).
68. G.E. Jellison Jr., F.A. Modine, "Parameterization of the optical functions of amorphous materials in the interband region", *Appl. Phys. Lett.* 69, 371 (1996).
69. K. Oura, V.G. Lifshits, A.A. Saranin, A.V. Zotov, et al., "Surface Science: An Introduction", Springer-Verlag (2003). (ISBN 3-540-00545-5).
70. http://neutron.ujf.cas.cz/vdg/methods_rbs.html.
71. <https://voer.edu.vn/m/photon-energies-and-the-electromagnetic-spectrum/15d6c4d0>
72. M. Newville, Fundamentals of XAFS, Consortium for Advanced Radiation Sources, University of Chicago, Chicago (2004).
73. <http://hyperphysics.phy-astr.gsu.edu/hbase/quantum/compton.html>.
74. https://en.wikipedia.org/wiki/Compton_scattering.
75. <http://electrons.wikidot.com/pair-production-and-annihilation>.
76. <http://slideplayer.com/slide/597594/>.
77. G. Bunker, "Introduction to XAFS", Cambridge University Press, Cambridge CB2 8RU, UK, p. 2 (2010).
78. S. D. Kelly, D. Hesterberg, and B. Ravel, "Analysis of soils and minerals using X-ray absorption spectroscopy," in A. L. Ulery and R. Drees, "Methods of Soil Analysis-Part 5 Mineralogical Methods", *Soil Sci. Soc. Am.*, pp. 387–464 (2008).
79. A. K. Poswal, A. Agrawal, A. K. Yadav, C. Nayak, S. Basu, S. R. Kane, C. K. Garg, D. Bhattacharyya, S. N. Jha, and N. K. Sahoo, "Commissioning and first results of scanning type EXAFS beamline (BL-09) at INDUS-2 synchrotron source," *AIP Conf. Proc.* 1591, 649–651 (2014).
80. G. Aygun, A. Cantas, Y. Simsek, and R. Turan, *Thin Solid Films* 519, 5820 (2011).

81. P. M. Babu, B. Radhakrishnaa, G. V. Rao, P. S. Reddy, and S. Uthanna, "Bias voltage dependence properties of DC reactive magnetron sputtered indium oxide films," *J. Optoelectron. Adv. Mater.* 6, 205 (2004).
82. H. Kim, D. H. Jung, B. Park, K. C. Yoo, J. J. Lee, and J. H. Joo, "The effect of the substrate bias voltage and the deposition pressure on the properties of diamond-like carbon produced by inductively coupled plasma assisted chemical vapor deposition," *Surf. Coat. Tech.* 193, 255 (2005).
83. M. Chandrasekhar, S. V. J. Chandra, and S. Uthanna, "The effect of the substrate bias voltage and the deposition pressure on the properties of diamond-like carbon produced by inductively coupled plasma assisted chemical vapor deposition," *Indian J. Pure Ap. Phy.* 47, 49 (2009).
84. S. Jun, P. D. Rack, T. E. McKnight, A. V. Melechko, and M. L. Simpson, "Direct-current substrate bias effects on amorphous silicon sputter-deposited films for thin film transistor fabrication," *Appl. Phys. Lett.* 87, 132108 (2005).
85. Sk. M. Haque, P. R. Sagdeo, S. Balaji, S. Kumar, D. Bhattacharyya, D. Bhattacharyya, N. K. Sahoo, "Effect of substrate bias and oxygen partial pressure on properties of RF magnetron sputtered HfO₂ thin films," *J. Vac. Sci. Technol. B* 32, 03D104-1 (2014).
86. <http://www.ams.ethz.ch/research/material/iba/rbs>.
87. S. Kumar, G. L. N. Reddy, and V. S. Raju, "Hydrogen storage in Pd capped thermally grown Mg films: Studies by nuclear resonance reaction analysis," *J. Alloy. Compd.* 476, 500 (2009).
88. A.G. Sisonyuk, "A posteriori error of the transmission interference method of thin film refractive index calculation," *J. Phys. D Appl. Phys.* 29, 1068 (1996).
89. W. D. Sproul, D. J. Christie, and D. C. Carter, "Control of reactive sputtering processes," *Thin Solid Films* 491, 1 (2005).
90. S. Heiroth, R. Ghisleni, T. Lippert, J. Michler, and A. Wokaun, "Optical and mechanical properties of amorphous and crystalline yttria-stabilized zirconia thin films prepared by pulsed laser deposition," *Acta. Meta.* 59, 2330 (2011).
91. B. Ayupov, K. Zherikova, N. Gelfond, and N. Morozova, "Optical properties of MOCVD HfO₂ films," *Phys. Status Solidi a* 206, 281 (2009).
92. T. Tan, Z. Liu, H. Lu, W. Liu, and H. Tian, "Structure and optical properties of HfO₂ thin films on silicon after rapid thermal annealing," *Optical Materials* 32, 432 (2010).
93. T. J. Brighta, J. I. Watjen, Z. M. Zhang, C. Muratore, and A. A. Voevodin, "Optical properties of HfO₂ thin films deposited by magnetron sputtering: From the visible to the far-infrared," *Thin Solid Films* 520, 6793 (2012).
94. P. Chindaudom, and K. Vedam, "Studies on inhomogeneous transparent, optical coatings on transparent substrates by spectroscopic ellipsometry," *Thin Solid Films* 234, 439 (1993).
95. J. S. Parramon, M. Modreanu, S. Bosch, and M. Stchakovsky, "Optical characterization of HfO₂ by spectroscopic ellipsometry: Dispersion models and direct data inversion," *Thin Solid Films* 516, 7990 (2008).
96. G. He, L.Q. Zhu, M. Liu, Q. Fang, and L. D. Zhang, "Optical and electrical properties of plasma-oxidation derived HfO₂ gate dielectric films," *Appl. Surf. Sci.* 253, 3413 (2007).
97. B. Drevillon, "Phase modulated ellipsometry from the ultraviolet to the infrared: in situ application to the growth of semiconductors," *Prog. Crystal Growth and Charact.* 27, 1-87 (1993).
98. E. D. Palik, "Handbook of Optical Constants of Solids", Academic Press, Orlando, (1985).

99. "Optical Characterisation of Real Surfaces and Films", edited by K. Vedam, in "Physics of Thin Films", edited by M.H. Frasncombe and J.L. Vossen, Academic Press, San Diego, Vol. 19 (1994).
100. M. Zaharescu, V. S. Teodorescu, M. Gartner, M. G. Blanchin, A. Baraua, and M. Anastasescu, "Correlation between the method of preparation and the properties of the sol-gel HfO_2 thin films," *J. Non-Cryst. Solids* 354, 409 (2008).
101. Y. Lu, O. Bui, S. Hall, and P. K. Hurley, "Optical and electrical characterization of hafnium oxide deposited by MOCVD," *Microelectron. Reliab.* 45, 965 (2005).
102. H. Wei, Z. Lu, D.S.H. Chan, and B. Jin Cho, "Cubic-Structured HfO_2 With Optimized Doping of Lanthanum for Higher Dielectric Constant," *Electron Device Letters* 30, 623 – 625 (2009).
103. X. Zhao and D. Vanderbilt, "First-principles study of structural, vibrational, and lattice dielectric properties of hafnium oxide," *Physical Review B* 65, 233106 (2002).
104. O. Ohtaka, T. Yamanaka, S. Kume, N. Hara, H. Asano, and F. Izumi, "Structural Analysis of Orthorhombic HfO₂ by Neutron Powder Diffraction," *J. Am. Ceram. Soc.* 78, 233-237 (1995).
105. S M. Haque, P. R. Sagdeo, A. Sagdeo, S. N. Jha, D. Bhattacharyya, and N. K. Sahoo, "Effect of oxygen partial pressure on properties of asymmetric bipolar pulse dc magnetron sputtered TiO_2 thin films," *Appl. Optics* 54, 3817-3825, (2015).
106. M. Vargas, N.R. Murphy and C.V. Ramana, "Structure and optical properties of nanocrystalline hafnium oxide thin films," *Optical Materials* 37, 621–628 (2014).
107. A. Thaveedetrakul, N. Witit-anun and V. Boonamnuayvitaya, "The role of target-to-substrate distance on the DC magnetron sputtered zirconia thin films bioactivity," *Appl. Surf. Sci.* 258, 2612-2619 (2012).
108. Z. Zhang, C. Bao, S. Ma, L. Zhang and S. Hou, "Effects of deposition power and pressure on the crystallinity of Al-doped ZnO thin films at glass substrates by low temperature RF magnetron sputtering", *J. Aus. Cer. Soc.*, 48, 214-222 (2012).
109. N. C. Das, N. K. Sahoo, D. Bhattacharyya, S. Thakur, D. Nanda, S. Hazra, J. K. Bal, J. F. Lee, Y. L. Tai, and C. A. Hsieh, "Modifications of local structures of Gd_2O_3 on incorporation of SiO_2 ," *J. Appl Phys.* 110, 063527 (2011).
110. P. Eiamchai, P. Chindaudom, A. Pokaipisit, P. Limsuwan, "A spectroscopic ellipsometry study of TiO_2 thin films prepared by ion-assisted electron-beam evaporation," *Curr. Appl. Phys.* 9, 707-712 (2009).
111. K. Jiang, A. Zakutayev, J. Stowers, M. D. Anderson, J. Tate, D. H. McIntyre, D. C. Johnson, D. A. Keszler, "Low-temperature, solution processing of TiO_2 thin films and fabrication of multilayer dielectric optical elements," *Sol. St. Sci.* 11, 1692-1699 (2009).
112. L. Miao, L. F. Su, S. Tanemura, C. A.J. Fisher, Li Li Zhao, Q. Liang, G. Xu, "Cost-effective nanoporous SiO_2 - TiO_2 coatings on glass substrates with antireflective and self-cleaning properties," *Appl. En.* 112, 1198-1205 (2013).
113. P. M. Perillo, D.F. Rodriguez, "A room temperature chloroform sensor using TiO_2 nanotubes," *Sensors and Actuators B* 193, 263-266 (2014).
114. F. Meng, X. Song, Z. Sun, "Photocatalytic activity of TiO_2 thin films deposited by RF magnetron sputtering," *Vacuum* 83, 1147-1204 (2009).
115. W.S. Shih, S.J. Young, L. W. Ji, W. Water, T.H. Meen, K.T. Lam, J. Sheen, W.C. Chu, "Thin film transistors based on TiO_2 fabricated by using radio-frequency magnetron sputtering," *J. Phys. Chem. Sol.* 71, 1760-1762 (2010).

116. P. C. Yao, J. L. Chiang, M. C. Lee, "Application of sol-gel TiO₂ film for an extended-gate H⁺ ion-sensitive field-effect transistor," *Solid State Sciences* 28, 47-54 (2014).
117. S. F. Wang, Y. F. Hsu, Y. S. Lee, "Microstructural evolution and optical properties of doped TiO₂ films prepared by RF magnetron sputtering," *Cer. Int.* 32, 121-127 (2006).
118. H. Q. Jiang, Q. Wei, Q. X. Cao, X. Yaob, "Spectroscopic ellipsometry characterization of TiO₂ thin films prepared by the sol-gel method," *Cer. Int.* 34, 1039-1042 (2008).
119. M. L. Lee, C. Y. Su, Y. H. Lin, S. C. Liao, J. M. Chen, T. P. Perng, J. W. Yeh, H. C. Shih, "Atomic layer deposition of TiO₂ on negative electrode for lithium ion batteries," *J. Power Sour.* 244, 410-416 (2013).
120. D. Li, M. Carette, A. Granier, J.P. Landesman, A. Goullet, "Spectroscopic ellipsometry analysis of TiO₂ films deposited by plasma enhanced chemical vapor deposition in oxygen/titanium tetraisopropoxide plasma," *Thin Solid Films* 522, 366-371 (2012).
121. M. N. Iliev, V.G. Hadjiev, A.P. Litvinchuk, "Raman and infrared spectra of brookite (TiO₂): Experiment and theory," *Vibrat. Spect.* 64, 148-152(2013).
122. M. Addamo, M. Bellardita, A. Di Paola and L. Palmisano, "Preparation and photoactivity of nanostructured anatase, rutile and brookite TiO₂ thin films," *Chem. Commun.* 4943-4945 (2006).
123. K. S. Lin, H. W. Cheng, W. R. Chen and J. F. Wu, "Synthesis, characterization and application of anatase-typed Titania nanoparticles," *J. Environ. Eng. & Manag.* 20, 69-76 (2010).
124. C. Ohara, T. Hongo, A. Yamazaki, T. Nagoya, "Synthesis and characterization of brookite/anatase complex thin film," *Appl. Surf. Sci.* 254, 6619-6622 (2008).
125. D. Mardare, V. Nica, Cristian-Mihail Teodorescu, D. Macovei, "Fe-doped TiO₂ thin films," *Surf. Sci.* 601 (2007) 4479-4483.
126. M. P. Moret, R. Zallen, D. P. Vijay, S. B. Desu, "Brookite-rich titania films made by pulsed laser deposition," *Thin Solid Films* 366, 8-10 (2000).
127. H. J. Jung, "Characterization of TiO₂ nanocrystalline films for high performance dye-sensitized solar cells," *Transac. Elect. Electron. Mater.* 12, 123-126 (2011).
128. O. Duyar, F. Pacido, H. Z. Durusoy, "Optimization of TiO₂ films prepared by reactive electron beam evaporation of Ti₃O₅," *J. Phys. D: Appl. Phys.* 41, 095307 (2008).
129. F. Flory, E. Pelletier, G. Albrand, Y. Hu, "Surface optical coatings by ion assisted deposition techniques: study of uniformity," *Appl. Opt.* 28, 2952-2959 (1989).
130. P. Singh, D. Kaur, "Room temperature growth of nanocrystalline anatase TiO₂ thin films by dc magnetron sputtering," *Physica B: Cond. Matter* 405, 1258-1266 (2010).
131. <http://www.icdd.com/> (JCPDS - International Centre for Diffraction Data).
132. H. Zhang, J. F. Banfield, "New kinetic model for the nanocrystalline anatase-to-rutile transformation revealing rate dependence on number of particles," *Am. Mineral.* 84, 528-535 (1999).
133. A. N. Pargellis, "Evaporating and sputtering: Substrate heating dependence on deposition rate," *J. Vac. Sci. Technol. A* 7, 27-30 (1989).
134. D. Wicaksana, A. Kobayashi, A. Kinbara, "Process effects on structural properties of TiO₂ thin films by reactive sputtering," *J. Vac. Sci. Technol. A* 10, 1479-1482 (1992).
135. A. Buranawong, N. Witt-Anun, S. Chaiyakun, "Total pressure and annealing temperature effects on structure and photo-induce hydrophilicity of reactive DC sputtered TiO₂ thin films," *Eng. J.* 16, 79-90 (2012).

- 136.M. Pin, G. Lee, W. Lee, E. Choi , Y. Yoo, "Effects of Oxygen Working Pressure on Structural and Optical Properties of TiO₂ Films Grown on Glass Substrate," Jap. J. Appl. Phys. 51, 09MF12 (2012).
- 137.S. J. Wang, W.T. Chang, J.Y. Chou, M.K. Wie, M.S. Wong, "Preparation of TiO₂ thin films by laser ablation for photocatalytic applications," J. Vac. Sci. Technol A 26, 898-902 (2008).
- 138.H. Long, G. Yang, A. Chen, Y. Li, P. Lu, "Growth and characteristics of laser deposited anatase and rutile TiO₂ films on Si substrates," Thin Solid Films 517, 745-749 (2008).
- 139.F. C. Gennari, D.M. Pasquevich, "Kinetics of the anatase–rutile transformation in TiO₂ in the presence of Fe₂O₃," J. Mater. Sci. 33, 1571-1578 (1998).
- 140.A. N. Kravtsova, A. V. Soldatov, M. Nachtegaal, M. W. Tew, J. A. van Bokhoven, "Influence of the muffin-tin approximation on the simulation of titanium K-edge X-ray absorption spectra of TiO₂ (rutile and anatase phases)," Physica B 405, 724–726 (2010).
- 141.F. Farges, G. E. Brown Jr., J. J. Rehr, "Ti K-edge XANES studies of Ti coordination and disorder in oxide compounds: Comparison between theory and experiment," Phys. Rev. B, 56, 1809-1819 (1997).
- 142.S. Kityakarn, A. Worayingyong, A. Suramitr, M. F. Smith, "Ce-doped nanoparticles of TiO₂: Rutile-to-brookite phase transition and evolution of Ce local-structure studied with XRD and XANES," Mater. Chem. Phys. 139, 543-549 (2013).
- 143.<http://cars9.uchicago.edu/atomsdb/TiO2-rut.inp>.
- 144.<http://cars9.uchicago.edu/atomsdb/TiO2-ana.inp>.
- 145.M. F. Smith, W. Klysubun, S. Kityakarn, A. Worayingyong, S.B. Zhang, S-H. Wei, D. Onkaw, P. Songsiriritthigul, S. Rujirawat, S. Limpijumnong, "Determination of phase ratio in polymorphic materials by x-ray absorption spectroscopy: The case of anatase and rutile phase mixture in TiO₂," J. Appl. Phys. 105, 024308 (1)-024308(4) (2009).
- 146.K. A. McKinley, N.P. Sandier, "Tantalum pentoxide for advanced DRAM applications," Thin Solid Films 290-291, 440-446 (1996).
- 147.P. Jain, J. S. Juneja, V. Bhagwat, E. J. Rymaszewski, T. M. Lu, T. S. Cale, "Effects of substrate temperature on properties of pulsed dc reactively sputtered tantalum oxide films," J. Vac. Sci. Technol. A 23, 512-519 (2005).
- 148.F. Jolly, M. Passacantando, V. Salerni, L. Lozzi, P. Picozzi, S. Santucci, "Structural and electrical properties of Ta₂O₅ thin films deposited on Si(100) from Ta(OC₂H₅)₅ precursor," J. Non-Cryst. Solids 322, 233-239 (2003).
- 149.O. A. Azim, M. M. Abdel-Aziz, I. S. Yahia, "Structure and optical analysis of Ta₂O₅ deposited on infrasil substrate," Appl. Surf. Sci. 255, 4829-4835 (2009).
- 150.V. Ligatchev, E. Rusli, L-B Keng, L-F Khuen, Y. Rumin, J. Zhao, "Structure and optical analysis of Ta₂O₅ deposited on infrasil substrate," Technical Proceedings of the 2005 NSTI Nanotechnology Conference and Trade Show 2, 381-384 (2005).
- 151.S. Shibata, "Dielectric constants of Ta₂O₅ thin films deposited by r.f. sputtering," Thin Solid Films 277, 1-4 (1996).
- 152.Z. Ji-cheng, L. Di-tian, L. You-zhen, L. Zheng, "Effect of sputtering pressure and rapid thermal annealing on optical properties of Ta₂O₅ thin films," Trans. Nonferrous Met. Soc. China 19, 359-363 (2009).
- 153.C. Xu, Q. Xiao, J. Ma, Y. Jin, J. Shao, Z. Fan, "High temperature annealing effect on structure, optical property and laser-induced damage threshold of Ta₂O₅ films," Appl. Surf. Sci. 254, 6554-6559 (2008).
- 154.L. A. Aleshina, S. V. Loginova, "Rietveld Analysis of X-ray Diffraction Pattern from β-Ta₂O₅ Oxide," Crystallography Reports 47, 415-419 (2002).

155. M. Mayer, "SIMNRA User's Guide", Report IPP 9/113, Max-Planck-Institut für Plasmaphysik, Garching, Germany, (1997).
156. A. Cappellani, J.L. Keddie, N.P. Barradas, S.M. Jackson, "Processing and characterisation of sol-gel deposited Ta₂O₅ and TiO₂-Ta₂O₅ dielectric thin films," *Solid-State Electronics* 43, 1095-1099 (1999).
157. C. Guoping, L. Lingzhen, Z. Suixin, Z. Haokang, "Structures and properties of a Ta₂O₅ thin film deposited by dc magnetron reactive sputtering in a pure O₂ atmosphere," *Vacuum*, 41, 1204-1206 (1990).
158. D. K. Murti, Roger Kelly, Z.L. Liao, J.M. Poate, "Structural and compositional changes in ion-bombarded Ta₂O₅," *Surface Science* 81, 571-588 (1979).
159. M. Hong, J. Kwo, A. R. Kortan, J. P. Mannaerts, and A. M. Sergent, "Epitaxial Cubic Gadolinium Oxide as a Dielectric for Gallium Arsenide Passivation," *Science* 283, 1897 (1999).
160. J. Kwo, M. Hong, A. R. Kortan, K. T. Queeney, Y. J. Chabal, R. L. Opila, Jr., D. A. Muller, S. N. G. Chu, B. J. Sapjeta, T. S. Lay, J. P. Mannaerts, T. Boone, H. W. Krautter, J. J. Krajewski, A. M. Sergent, and J. M. Rosamilia, "Properties of high k gate dielectrics Gd₂O₃ and Y₂O₃ for Si," *J. Appl. Phys.* 89, 3920 (2001).
161. V. Mikhelashvili, G. Eisentsein, and F. Edelmann, "Characteristics of electron-beam-gun-evaporated Er₂O₃ thin films as gate dielectrics for silicon," *J. Appl. Phys.* 90, 5447 (2001).
162. N. K. Sahoo, S. Thakur, M. Senthikumar, D. Bhattacharyya, N.C. Das, "Reactive electron beam evaporation of gadolinium oxide optical thin films for ultraviolet and deep ultraviolet laser wavelengths," *Thin Solid Films* 440, 155–168 (2003).
163. H. Guo, X. Yang, T. Xiao, W. Zhang, L. Lou, J. Mugnier, "Structure and optical properties of sol-gel derived Gd₂O₃ waveguide films," *Applied Surface Science* 230, 215–221 (2004).
164. H. D. B. Gottlob, T. Echtermeyer, T. Mollenhauer, J.K. Efavi, M. Schmidt, T. Wahlbrink, M.C. Lemme, H. Kurz, M. Czernohorsky, E. Bugiel, H.J. Osten, A. Fissel, "CMOS integration of epitaxial Gd₂O₃ high-k gate dielectrics," *Solid-State Electronics* 50, 979–985 (2006).
165. S. Y. Seo, S. Lee, H.D. Park, N. Shin, K.S. Sohn, "Luminescence of pulsed laser deposited Gd₂O₃: Eu 3+ thin film phosphors on quartz glass substrates," *J. Appl. Phys.* 92, 5248 (2002).
166. J.S. Bae, J.H. Jeong, S.S. Yi, J.C. Park, "Improved photoluminescence of pulsed-laser-ablated Y₂O₃: Eu 3+ thin-film phosphors by Gd substitution," *Appl. Phys. Lett.* 82, 3629 (2003).
167. A. Garcia-Murillo, C.L. Luyer, C. Dujardin, T. Martin, C. Garapon, C. Pedrini, J. Mugnier, "Elaboration and scintillation properties of Eu³⁺-doped Gd₂O₃ and Lu₂O₃ sol-gel films," *Nucl. Instrum. Meth. A* 486, 181 (2002).
168. A. Garcia-Murillo, C.L. Luyer, C. Garapon, C. Dujardin, E. Bernstein, C. Pedrini, J. Mugnier, "Optical properties of europium-doped Gd₂O₃ waveguiding thin films prepared by the sol-gel method," *Opt. Mater.* 19, 161 (2002).
169. D. A. Grave, Z. R. Hughes, J. A. Robinson, T. P. Medill, M. J. Hollander, A. L. Stump, M. Labella, X. Weng, D. E. Wolfe, "Process-structure-property relations of micron thick Gd₂O₃ films deposited by reactive electron-beam physical vapor deposition (EB-PVD)," *Surface & Coatings Technology* 206, 3094–3103 (2012).
170. A. F. Wells, *Structural Inorganic Chemistry*, Clarendon/Oxford University, (1984).
171. Y. L. Li, N. F. Chen, J. P. Zhou, S. L. Song, L. F. Liu, Z. G. Yin, C. L. Cai, "Effect of the oxygen concentration on the properties of Gd₂O₃ thin films," *Journal of Crystal Growth* 265, 548–552 (2004).

172. YUE. Shoujing, W. Feng, W. Yi, Y. Zhimin, T. Hailing, D. Jun, "Phase control of magnetron sputtering deposited Gd_2O_3 thin films as high- κ gate dielectrics," *Journal of Rare Earths* 26, 371 (2008).
173. H. Liu, P. Zhou, L. Zhang, Z. Liang, H. Zhao, Z. Wang, "Effects of oxygen partial pressure on the structural and optical properties of undoped and Cu-doped ZnO thin films prepared by magnetron co-sputtering," *Materials Letters* 164, 509–512 (2016).
174. A. Biswas and D. Bhattacharyya, "Ion energy dependence of interface parameters of ion beam sputter deposited W/Si interfaces," *Nuclear Instruments and Methods in Physics Research B* 268, 1594–1600 (2010).
175. A. Kossoy, D. Simakov, S. Olafsson, K. Leosson, "Determining surface coverage of ultra-thin gold films from X-ray reflectivity measurements," *Thin Solid Films* 536, 50–53 (2013);
176. A. Jurkevičiūtė, A. Lazauskas, T. Tamulevičius, A. Vasiliauskas, D. Peckus, Š. Meškinis, and S. Tamulevičius, "Structure and density profile of diamond-like carbon films containing copper: study by X-ray reflectivity, transmission electron microscopy, and spectroscopic ellipsometry," *Thin Solid Films* 630, 48–58 (2017).
177. K. J. S. Sokhey, S. K. Raib, G. S. Lodha, "Oxidation studies of niobium thin films at room temperature by X-ray reflectivity," *Applied Surface Science* 257, 222–226 (2010).
178. S. M. Haque, A. Biswas, D. Bhattacharya, R.B. Tokas, D. Bhattacharyya, N.K. Sahoo, "Surface roughness and interface width scaling of magnetron sputter deposited Ni/Ti multilayers," *Journal of Applied Physics* 114, 103508 (1-9) (2013).
179. Y. M. Tao, S. Y. Ma, H. X. Chen, J. X. Meng, L. L. Hou, Y. F. Jia, X. R. Shang, "Effect of the oxygen partial pressure on the microstructure and optical properties of ZnO:Cu films," *Vacuum* 85, 744–748 (2011).
180. H. C. Su, C. H. Lee, M. Z. Lin, and T. W. Huang, "A Comparison between X-ray Reflectivity and Atomic Force Microscopy on the Characterization of a Surface Roughness," *Chi. J. Phys.* 50, 291 (2012).
181. J. Sa´nchez-Gonza´lez, A. Di´az-Parralejo, A.L. Ortiz, F. Guiberteau, "Determination of optical properties in nanostructured thin films using the Swanepoel method," *Applied Surface Science* 252, 6013–6017 (2006).
182. M. Mishra, P. Kuppasami, S. Ramya, V. Ganesan, A. Singh, R. Thirumurugesan, E. Mohandas, "Microstructure and optical properties of Gd_2O_3 thin films prepared by pulsed laser deposition," *Surface & Coatings Technology* 262, 56–63 (2015).
183. J. Gryglewicz, P. Firek, J. Jaśiński, R. Mroczynski, J. Szmidt, "Characterization of thin Gd_2O_3 magnetron sputtered layers," *Proc. of SPIE* 8902, 89022M-1 (2013).
184. S. M. Haque, K. Divakar Rao, J.S. Misal, R.B. Tokas, D.D. Shinde, J.V. Ramana, S. Rai, and N. K. Sahoo, "Study of hafnium oxide thin films deposited by RF magnetron sputtering under glancing angle deposition at varying target to substrate distance," *Applied Surface Science* 353, 459–468 (2015).
185. W. H. Zachariasen, "The crystal structure of the modification c of the sesquioxides of the rare earth metals, and of Indium and Thallium," *Norsk Geologisk Tidsskrift* 9, 310–316 (1927).
186. A. M. Pires, M. R. Davolos, C. O. P. Santos, E. B. Stucchi, and J. Flor, "New X-ray powder diffraction data and Rietveld refinement for Gd_2O_3 monodispersed fine spherical particles," *Journal of Solid State Chemistry* 171, 420–423 (2003).
187. S. M. Haque, C. Nayak, D. Bhattacharyya, S. N. Jha, And N. K. Sahoo, "Extended x-ray absorption fine structure measurements on radio frequency magnetron sputtered HfO_2 thin films deposited with different oxygen partial pressures," *Appl. Optics* 55, 2175–2181 (2016).

- 188.S. M. Haque, S. Tripathi, S.N. Jha, D. Bhattacharyya and N. K. Sahoo, "EXAFS studies on Gd doped ZrO₂ thin films deposited by r.f. magnetron sputtering," *Appl. Optics* 55, 7355 (2016).
- 189.C. J. Howard, R. J. Hill, and B. E. Reichert, "Structures of ZrO₂ polymorphs at room temperature by high-resolution neutron powder diffraction," *Acta Cryst.* B44, 116-120 (1988).
- 190.M. O. Zacate, L. Minervini, D. J. Bradfield, R. W. Grimes, and K. E. Sick-afus, "Defect cluster formation in M₂O₃-doped cubic ZrO₂," *Sol. St. Ionics* 128, 243-254 (2000).
- 191.I. Kosacki, T. Christopher, M. Rouleau, P. F. Becher, J. Bentley, and D. H. Lowndes, "Nanoscale effects on the ionic conductivity in highly textured YSZ thin films," *Sol. St. Ionics* 176, 1319-1326 (2005).
- 192.S. S. Chopade, C. Nayak, D. Bhattacharyya, S. N. Jha, R.B. Tokas, N.K. Sahoo, M. N. Deo, A. Biswas, S. Rai, K. H. T. Raman, G. M. Rao, N. K. Pandey and D. S. Patil, "RF Plasma enhanced MOCVD of Yttria Stabilized Zirconia thin films using octanedionate precursors and their characterization," *Appl. Surface Science* 355, 82-92 (2015).
- 193.I. M. Thomas, "Preparation of dielectric highly reflective (HR) mirrors from colloidal oxide suspensions containing organic polymer binders," *SPIE* 2288, 50 (1994).
- 194.M. Boulouaz, F. Tcheliobod, and A. Boyer, "Electrical and optical properties of magnetron-sputtered Y₂O₃ stabilized ZrO₂ thin films," *Journal of the European Ceramic Society* 17, 1741-1748 (1997).
- 195.J. S. Lakshmi, I. J. Berlin, J. K. Thomas, P. V. Thomas, and K. Joy, "Band gap tuning and improved optical properties of ZrO₂-SnO₂ nanocomposite thin films prepared by sol-gel route," *IOP Conf. Series:Materials Science and Engineering* 23, 012030 (1-6) (2011).
- 196.I. John Berlin, and K. Joy, "Optical enhancement of Au doped ZrO₂ thin films by sol-gel dip coating method," *Physica B* 457, 182–187 (2015).
- 197.S. E. Kul'kova, and O. N. Muryzhnikova, "Electronic structure and optical properties of zirconia," *Inorganic Materials* 36, 38-42 (2000).
- 198.S. Basu, S. Varma, A. N. Shirsat, B. N. Wani, S. R. Bharadwaj, A. Chakrabarti, S. N. Jha, and D. Bhattacharyya, "Extended X-ray absorption fine structure study of Gd doped ZrO₂ systems," *Journal of Applied Physics* 113, 043508 (1-4) (2013).
- 199.S. Basu, S. Varma, A. N. Shirsat, B. N. Wani, S. R. Bharadwaj, A. Chakrabarti, S. N. Jha, and D. Bhattacharyya, "X-ray absorption spectroscopy of doped ZrO₂ systems," *Journal of Applied Physics* 111, 053532 (1-9) (2012).
- 200.T. Uehara, K. Koto, S. Emura, and F. Kanamaru, "EXAFS study of the fluorite and pyrochlore compounds in the system ZrO₂-Gd₂O₃," *Solid State Ionics* 23, 331–337 (1987).
- 201.P. Li, I. W. Chen, and J. E. P. Hahn, "Effect of dopants on zirconia stabilization—an x-ray-absorption study: I, Trivalent dopants," *J. Am. Ceram. Soc.* 77, 118–128 (1994).
- 202.D. K. Smith, and H. W. Newkirk, "The crystal structure of baddeleyite (monoclinic ZrO₂) and its relation to the polymorphism of ZrO₂," *Acta Cryst.* 18, 983-991 (1965).
- 203.G. Fadda, L. Colombo and G. Zanzotto, "First-principles study of the structural and elastic properties of zirconia," *Phys. Rev. B* 79, 214102 (1-13) (2009).
- 204.<http://sundoc.bibliothek.uni-halle.de/diss-online/01/01H078/> for A. Tikhonovsky, "Plastic Deformation of Cubic Zirconia Single Crystals-The Onfluence of the Orientation of Compression Axis and Yttria Stabilizer Content", Online university publications of the University of Halle-Wittenberg at the University and State Library Saxony-Anhalt (2001).

205. P. S. Lysaght, J. C. Woicik, M. A. Sahiner, P. D. Kirsch, G. Bersuker, B.-H. Lee, and R. Jammy, "Physical characteristics of HfO_2 dielectrics at the Physical Scaling Limit," VLSI Technology, Systems and Applications, International Symposium, p. 156-157 (2008).
206. I. Bilecka, L. Luo, I. Djerdj, M.D. Rossell, M. Jagodič, Z. Jagličić, Y. Masubuchi, S. Kikkawa and M. Niederberger, "Microwave-Assisted Nonaqueous Sol-Gel Chemistry for Highly Concentrated ZnO -Based Magnetic Semiconductor Nanocrystals," J. Phys. Chem. C 115, 1484-1495 (2011).
207. R. Knut, J.M. Wikberg, K. Lashgari, V.A. Coleman, G. Westin, P. Svedlindh and O. Karis, "Magnetic and electronic characterization of highly Co-doped ZnO : An annealing study at the solubility limit," Phys. Rev. B 82, 094438 (1-7) (2010).
208. S. Basu, D. Inamdar, S. Mahamuni, A. Chakrabarti, C. Kamal, G. Kumar, S.N. Jha and D. Bhattacharya, "Local Structure Investigation of Co and Mn Doped ZnO Nanocrystals and its Correlation with Magnetic Properties," The Journal of Physical Chemistry, Part C 118, 9154-9164 (2014).
209. J. H. Campbell, "Damage Resistant Optical Glasses for High Power Lasers: A Continuing Glass Science and Technology Challenge", First International Workshop on Glass and the Photonics Revolution, Germany (2002).
210. B. C. Stuart, M. D. Feit, S. Herman, A. M. Rubenchik, B. W. Shore, and M. D. Perry, "Nanosecond-to-femtosecond laser-induced breakdown in dielectrics", Physical Review B 53, 1749-1761 (1996).
211. A. Bananej, A. Hassanpour, H. Razzaghi, M. V. Zade, A. Mohammadi, "The effect of porosity on the laser induced damage threshold of TiO_2 and ZrO_2 single layer films," Optics & Laser Technology 42, 1187-1192 (2010).
212. R. M. Wood, "Laser-induced damage of optical materials" Bristol, Philadelphia: Institute of Physics Publishing, (2008).
213. Q. Zhang, F. Pan, J. Luo, Q. Wu, Z. Wang, Y. Wei, "Optical and laser damage properties of $\text{HfO}_2/\text{Al}_2\text{O}_3$ thin films deposited by atomic layer deposition," Journal of Alloys and Compounds 659, 288-294 (2016).
214. D. Zhang, J. Shao, Y. Zhao, S. Fan, R. Hong and Z. Fan, "Laser-induced damage threshold of ZrO_2 thin films prepared at different oxygen partial pressures by electron-beam evaporation," J. Vac. Sci. Technol. A 23-1, 197-200 (2005).
215. D. Zhang, S. Fan, W. Gao, H. He, Y. Wang, J. Shao, Z. Fan and H. Sun, "Study on absorbance and laser damage threshold of HfO_2 films prepared by ion-assisted reaction deposition," Chinese Optics Letters 2, 305-307 (2004).
216. J. M. Fairfield, G. H. Schwuttke, "Silicon diodes made by laser irradiation," Solid-State Electronics 11, 1175-1176 (1968).
217. M. Noh, I. Seo, J. Park, J. S. Chung, Y. S. Lee, H. J. Kim, Y. J. Chang, J. H. Park, M. G. Kang, C. Y. Kang, "Spectroscopic ellipsometry investigation on the excimer laser annealed indium thin oxide sol-gel films," Current Applied Physics 16, 145-149 (2016).
218. C. Xu, D. Li, H. Fan, J. Deng, J. Qi, P. Yi, Y. Qiang, "Effects of different post-treatment methods on optical properties, absorption and nanosecond laser-induced damage threshold of Ta_2O_5 films," Thin Solid Films 580, 12-20 (2015).
219. J. Yao, J. Shao, H. He, Z. Fan, "Effects of annealing on laser-induced damage threshold of $\text{TiO}_2/\text{SiO}_2$ high reflectors," Applied Surface Science 253, 8911-8914 (2007).
220. C. Xu, P. Yi, H. Fan, J. Qi, Y. Qiang, J. Liu, C. Tao, D. Li, "Correlations between the oxygen deficiency and the laser damage resistance of different oxide films," Appl. Surf. Sci. 289, 141 (2014).

221. Y. Zhao, Y. Wang, H. Gong, J. Shao, Z. Fan, "Annealing effects on structure and laser induced damage threshold of Ta₂O₅/SiO₂ dielectric mirrors," *Appl. Surf. Sci.* 210, 353 (2003).
222. A. K. Yadav, Sk M. Haque, S. Tripathi, D. Shukla, Md. A. Ahmed, D. M. Phase, S. Bandyopadhyay, S. N. Jha and D. Bhattacharyya, "Investigation of Fe doped ZnO thin films by X-ray absorption spectroscopy," *RSC Adv.* 6, 74982 (2016).
223. B. C. T. Khac, K. J. Jeon, S. T. Choi, Y. S. Kim, F. W. DelRio, and K. H. Chung, "Laser-Induced Particle Adsorption on Atomically Thin MoS₂," *ACS Appl. Mater. Interfaces* 8, 2974–2984 (2016).
224. I. Kojima And B. Li, "Structural characterization of thin films by x-ray reflectivity," *Rigaku Journal* 16, 31 (1999).
225. O. Kirmali, H. Akin, A. Kapdan, "Evaluation of the surface roughness of zirconia ceramics after different surface treatments," *Acta Odontologica Scandinavica* (2013). (DOI: 10.3109/00016357.2013.853320)
226. N. C. Kerr, D. C. Emmony, "The Effect of Laser Annealing on Laser-induced Damage Threshold," *Journal of Modern Optics* 37, 787-802 (1990).
227. A. Khorsand Zak, W.H. A. Majid, M.E. Abrishami, R. Yousefi, "X-ray analysis of ZnO nanoparticles by Williamson-Hall and size-strain plot Methods," *Solid State Sciences* 13, 251-256 (2011).

Appendices

Appendix-A

Swanepoel method

Swanepoel method also known as envelope method is used to estimate thickness and optical constants of single layer thin film deposited on transparent thick substrate as shown in fig. A.1. A brief account of the methodology is described below.

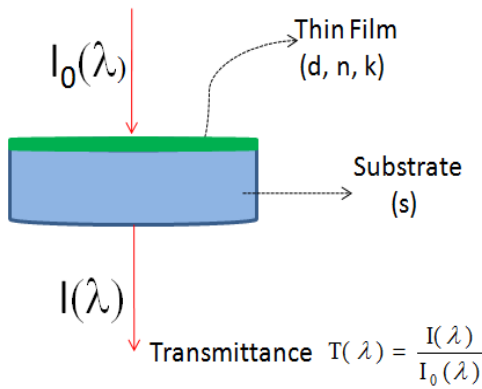


Figure-A.1: Single layer thin film deposited on a thick substrate

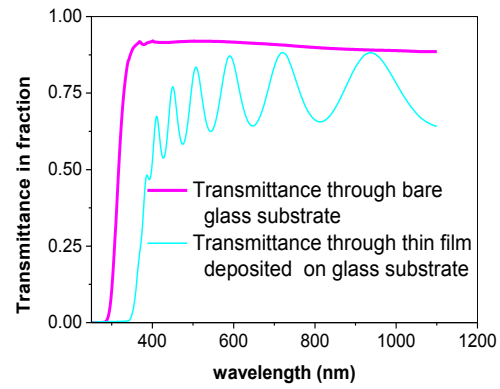


Figure-A.2: A typical transmittance spectrum of single layer thin film

Transmittance through such single layer thin film system is given by [1] -

$$T = \frac{Ax}{B - Cx \cos(\varphi) + Dx^2} = T(\lambda, n, d, k) \quad (\text{A.1})$$

$$\left. \begin{aligned} \text{where } A &= 16n^2s, \quad B = (n-1)^3(n+s^2), \\ C &= 2(n^2-1)(n^2-s^2), \quad D = (n-1)^3(n-s^2) \end{aligned} \right\} \quad (\text{A.1.1})$$

$$\text{and} \quad \varphi = 4\pi nd / \lambda \quad (\text{A.1.2})$$

$$\text{and} \quad x = \exp(-\alpha d) \text{ with } \alpha = 4\pi k / \lambda \quad (\text{A.1.3})$$

The expression of T as given by equation (A.1) is under the approximation that the substrate is transparent and the absorption in thin film is less enough such that $k^2 \ll n^2$. A typical transmittance spectrum through such thin film system is shown in Fig. A.2. As we can see from equation (A.1) that, for a given experimental transmittance spectrum $T_{\text{exp}}(\lambda)$, three unknowns visualizing film thickness (d), refractive index $n(\lambda)$ and attenuation coefficient $k(\lambda)$ are to be calculated simultaneously out of only one equation. So, basically this is an underdetermined problem. This underdetermined problem is deterministically solved by envelope method which is based on the construction of continuous envelope curve through the group of points where extrema of interference fringes occurs.

Envelope of maxima and minima is drawn by interpolating or extrapolating the maxima and minima points respectively or by using envelope drawing algorithm [2-3], as shown in the Fig. A.3.

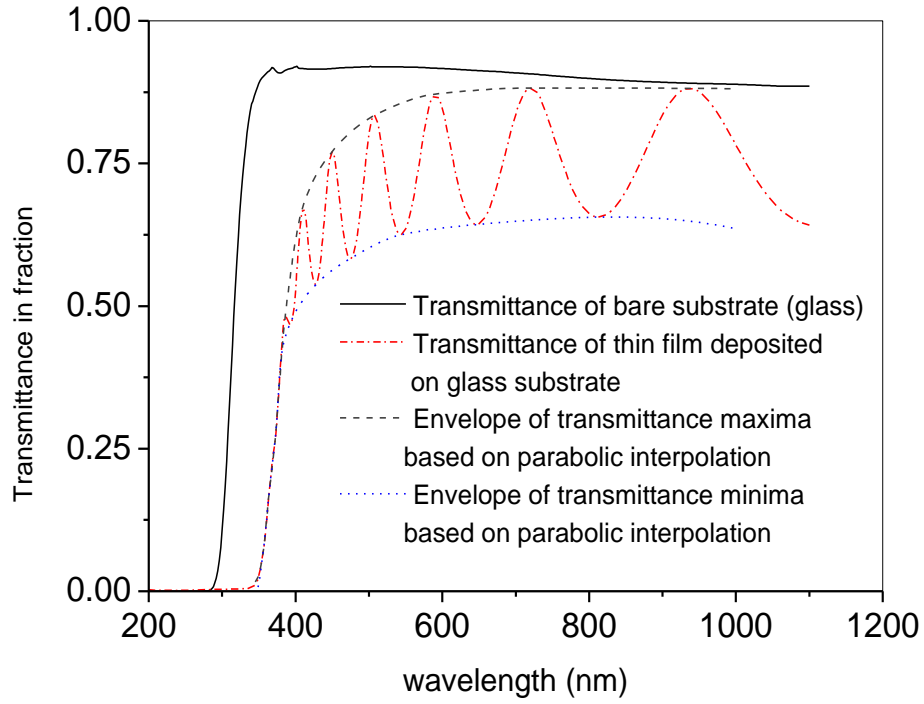


Figure-A.3: Typical transmission spectrum of thin-film and it's envelope

Theoretical expression for the envelope of maxima and minima (as shown in Fig. A.3) are given by [1]-

$$T_M = \frac{Ax}{B - Cx + Dx^2} \quad (\text{A.2})$$

$$T_m = \frac{Ax}{B + Cx + Dx^2} \quad (\text{A.3})$$

From equations (A.2) and (A.3), we get

$$\left(\frac{1}{T_m} - \frac{1}{T_M} \right) = \frac{2C}{A} \quad (\text{A.4})$$

Substituting the expression for C and A from equation (A.1.1) into equation (A.4), and after little manipulation, we get

$$n = [N + (N^2 - s^2)^{1/2}]^{1/2} \quad (\text{A.5})$$

$$\text{where } N = 2s \frac{T_M - T_m}{T_M T_m} + \frac{s^2 + 1}{2}.$$

From equation (A.5), one can calculate refractive index at extrema wavelength of the spectrum by using the envelope curves shown in Fig. A.3.

The condition of extrema occurring at wavelength, λ is given by-

$$2nd = m\lambda \quad (\text{A.6})$$

m is integer for maxima and half-integer for minima, d is the thickness of the film.

By using the condition of extrema given in equation (A.6), thickness d can be calculated from any two consecutive extrema (one maxima and another subsequent minima) visualizing

$$d = \frac{\lambda_1 \lambda_2}{4(n_2 \lambda_1 - n_1 \lambda_2)} \quad (\text{A.7})$$

Now to average out the thicknesses calculated from all set of consecutive extrema, and for the order number correction by approximating to nearest integer or half-integer, a graphical method as described below is used.

Assuming, m_1 to be of the order number of the first extrema, equation (A.6) can be written as-

$$\begin{aligned} 2nd &= \left(m_1 + \frac{l}{2} \right) \lambda \\ \Rightarrow l/2 &= 2d(n/\lambda) - m_1 \end{aligned} \quad (\text{A.8})$$

where $l = 0, 1, 2, 3, \dots$. The straight line $(l/2)$ vs. (n/λ) is plotted with the value of n as calculated using equation (2.5) for tangent points of experimental transmission spectrum. ' d ' is calculated from the slope of the straight line and ' m_1 ' is calculated from the intersection of the straight line with the ordinate axis as shown in Figure-A.4.

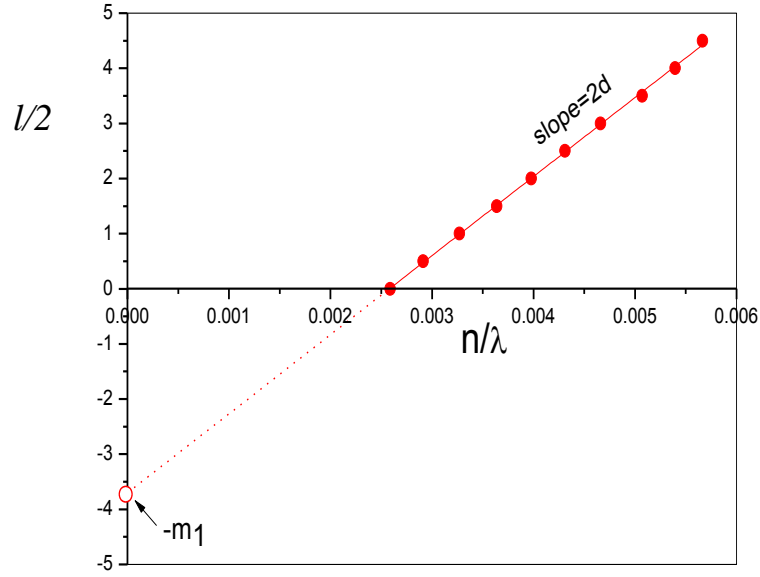


Figure-A.4: plot of $l/2$ vs. n/λ

The order numbers of all other extrema are calculated based on the order number of first extrema. With this exact order numbers, m and calculated values of d , the value of n is re-calculated using equation (A.6) at all extrema wavelength. Substitution of this calculated d and n in the expression of either (A.2) or (A.3) yields the value of attenuation coefficient, k .

Appendix-B

Tauc-Lorentz dispersion model

The measured spectroscopic ellipsometry data of thin film or bulk material are used to describe the sample based on a model of single or multiple layers of the given material. The layers are represented by wavelength dependent dielectric functions called dispersion relations that help to evaluate the material's optical properties by adjusting specific fit parameters. Following section deals with one such widely used dispersion formula known as Tauc-Lorentz dispersion [4] formula.

Jellison and Modine developed this model (1996) using the Tauc joint density of states and the Lorentz oscillator. The standard Lorentzian expression [5] of imaginary part of dielectric constant $\varepsilon_2 (= 2nk)$ for a single electronic transition is:

$$\varepsilon_2(E) = 2nk = \frac{A_L E_0 C_L E}{(E^2 - E_0^2)^2 + C_L^2 E^2} \quad (\text{B.1})$$

where, E_0 is the peak transition energy, while A_L and C_L determine the strength and broadening of the transition respectively.

The joint density of states for an amorphous material as suggested by Tauc[6] is given by:

$$\varepsilon_2(E) = \frac{A_T (E - E_g)^2}{E^2} \quad (\text{B.2})$$

Assuming the amorphous material to be a collection of non-interacting atoms one obtains the following parametric expression for the imaginary part of the dielectric constant of the material (ε_2) by directly multiplying eqn. (C.1) with eqn. (C.2).

$$\begin{aligned}\varepsilon_{2TL}(E) &= \frac{A_{TL}E_0C_L(E-E_g)^2}{\{(E^2-E_0^2)+C_L^2E^2\}E}, & E > E_g \\ &= 0 & E \leq E_g\end{aligned}\quad (B.3)$$

The expression for real part of dielectric constant can be obtained by Kramers-Kronig analysis as:

$$\begin{aligned}\varepsilon_{1TL}(E) &= \varepsilon_{1TL}(\infty) + \frac{1}{2} \frac{A_{TL}}{\pi} \frac{C_L}{\xi^4} \frac{a_{ln}}{\alpha E_0} \ln \left[\frac{(E_0^2 + E_g^2 + \alpha E_g)}{(E_0^2 + E_g^2 - \alpha E_g)} \right] - \frac{A_{TL}}{\pi \xi^4} \frac{a_{atan}}{E_0} \left[\pi - a \tan \left(\frac{2E_g + \alpha}{C_L} \right) + \right. \\ &\quad \left. \tan^{-1} \left(\frac{-2E_g + \alpha}{C_L} \right) \right] \\ &\quad + 2 \frac{A_{TL}}{\pi \xi^4} \frac{E_0}{\alpha} \left\{ E_g \left(E^2 - \gamma_{TL}^2 \right) \left[\pi + 2 \tan^{-1} \left(2 \frac{\gamma_{TL}^2 - E_g^2}{\alpha C_L} \right) \right] \right\} \\ &\quad - \frac{A_{TL}E_0C_L}{\pi \xi^4} \frac{E^2 + E_g^2}{E} \ln \left(\frac{|E - E_g|}{E + E_g} \right) + 2 \frac{A_{TL}E_0C_L}{\pi \xi^4} E_g \ln \left[\frac{|E - E_g|(E + E_g)}{\sqrt{(E_0^2 - E_g^2)^2 + E_g^2 C_L^2}} \right]\end{aligned}\quad (B.4)$$

where,

$$a_{ln} = (E_g^2 - E_o^2)E^2 + E_g^2 C_L^2 - E_o^2(E_o^2 + 3E_g^2)$$

$$a_{atan} = (E^2 - E_o^2)(E_o^2 + E_g^2) + E_g^2 C_L^2$$

$$\xi^4 = (E^2 - \gamma^2)^2 + \frac{\alpha^2 C_L^2}{4}$$

$$\alpha = \sqrt{4E_o^2 - C_L^2}/2$$

$$\gamma_{TL} = \sqrt{E_o^2 - C_L^2}/2$$

Thus in the TL model the dispersion of optical constants can be described by the five parameters

$$A_{TL}, C_L, E_o, E_g \text{ and } \varepsilon_{1TL}(\infty).$$

References:

1. R. Swanepoel, “Determination of the thickness and optical constants of amorphous silicon”, J. Phys. E. 16, 1214–1222 (1983).
2. B. S. Richardsa, A. Lambertz, A.B. Sproul, “Determination of the optical properties of non-uniformly thick non-hydrogenated sputtered silicon thin films on glass”, Thin Solid Films, 460, 247–255 (2004).
3. M. McClain, A. Feldman, D. Kahaner and X. Ying, “An algorithm and computer program for the calculation of envelope curves”, Computers in Physics, page-45 (1991).
4. G.E. Jellison Jr., F.A. Modine, “Parameterization of the optical functions of amorphous materials in the interband region”, Appl. Phys. Lett. 69, 371 (1996).
5. F. Wooten, “Optical Properties of Solids”, Academic, New York, (1972)
6. J. Tauc, R. Grigorovici, and A. Vancu, “Optical Properties and Electronic Structure of Amorphous Germanium”, Phys. Status Solidi 15, 627 (1966).

=====OOO=====